INFORMATION TO USERS

While the most advanced technology has been used to photograph and reproduce this manuscript, the quality of the reproduction is heavily dependent upon the quality of the material submitted. For example:

- Manuscript pages may have indistinct print. In such cases, the best available copy has been filmed.

- Manuscripts may not always be complete. In such cases, a note will indicate that it is not possible to obtain missing pages.

- Copyrighted material may have been removed from the manuscript. In such cases, a note will indicate the deletion.

Oversize materials (e.g., maps, drawings, and charts) are photographed by sectioning the original, beginning at the upper left-hand corner and continuing from left to right in equal sections with small overlaps. Each oversize page is also filmed as one exposure and is available, for an additional charge, as a standard 35mm slide or as a 17"x 23" black and white photographic print.

Most photographs reproduce acceptably on positive microfilm or microfiche but lack the clarity on xerographic copies made from the microfilm. For an additional charge, 35mm slides of 6"x 9" black and white photographic prints are available for any photographs or illustrations that cannot be reproduced satisfactorily by xerography.

Pan, Xiaohe

ELECTRONIC STRUCTURE AND CHEMICAL ACTIVITY OF MODIFIED METAL SURFACES

City University of New York PH.D. 1987

PLEASE NOTE:

In all cases this material has been filmed in the best possible way from the available copy. Problems encountered with this document have been identified here with a check mark ✓.

1. Glossy photographs or pages _____
2. Colored illustrations, paper or print _____
3. Photographs with dark background ✓
4. Illustrations are poor copy _____
5. Pages with black marks, not original copy ✓
6. Print shows through as there is text on both sides of page _____
7. Indistinct, broken or small print on several pages ✓
8. Print exceeds margin requirements _____
9. Tightly bound copy with print lost in spine _____
10. Computer printout pages with indistinct print _____
11. Page(s) _____ lacking when material received, and not available from school or author.
12. Page(s) _____ seem to be missing in numbering only as text follows.
13. Two pages numbered _____. Text follows.
14. Curling and wrinkled pages _____
15. Dissertation contains pages with print at a slant, filmed as received ✓
16. Other _____

_____

_____

University
Microfilms
International

ELECTRONIC STRUCTURE AND CHEMICAL ACTIVITY OF MODIFIED METAL SURFACES

by

XIAOHE PAN

A dissertation submitted to the Graduate Faculty in Physics in partial fulfillment of the requirements for the degree of Doctor of Philosophy, The City University of New York.

1987

This manuscript has been read and accepted for the Graduate Faculty in Physics in satisfaction of the dissertation requirement for the degree of Doctor of Philosophy.

January 8, 1987
Date

Myron Strongin
Chair of Examining Committee

January 29, 1987
Date

Joel I. Gersten
Executive Officer

Arthur Damask

Leonard Roelling

Kelvin Lynn

Supervisory Committee

The City University of New York

ABSTRACT

ELECTRONIC STRUCTURE AND CHEMICAL ACTIVITY OF MODIFIED METAL SURFACES

Xiaohe Pan

The City University of New York

November, 1986

Angle-resolved synchrotron radiation photoemission has been used, together with k-resolved inverse photoemission, low-energy electron diffraction, and Auger electron spectroscopy, to study the occupied and unoccupied electronic states, the morphology, and the chemical activity of Ni, Pd, and Pt overlayers on Nb(110) and Ta(110) substrates.

The strong adlayer-substrate bonding leads to the formation of highly strained commensurate Pd and Pt layers in the early growth stage. However, Ni agglomerates and forms incommensurate structures because the additional lattice mismatch cannot be overcome by the adsorbate-substrate bonding. In the photoemission studies of these metal-metal systems, the adlayer derived bonding interface resonance is observed at a higher binding energy part of the *d*- band below the Fermi level (E_F). The dominance of this bonding interface resonance and the absence of *d*- states near E_F makes the valence band electronic structure of Pt and Pd monolayer noble-metal-like. Chemisorption studies at 300 K show that CO does not chemisorb on the surface of a monolayer of Pt or Pd on Nb(110). However, both dissociative and molecular CO adsorption occurs on Nb(110) covered by a equivalent monolayer of Ni.

K-resolved inverse photoemission identifies an antibonding interface resonance at 1.6 eV above E_F for a monolayer of Pd on Nb(110). This mainly Nb-derived interface state is confirmed by the dispersion of two-dimensional band structure along the surface normal and surface Brillouin zone. The experiments further show that the interface bond weakens as the thickness of the overlayers increases. Together with the photoemission results, a further insight into the physical and chemical properties of these transition metal-metal systems can be achieved by a simple picture of *d*-*d* hybridization between the adlayer and substrate with a bonding level below E_F and an antibonding level above E_F.

Acknowledgements

In my graduate career there are many people who have made my experience one which I will remember forever and to those people I wish to express my most sincere gratitude.

First, I should take this opportunity to express my extreme gratitude to my advisor Myron Strongin for originally suggesting this project, and especially for his support, help, advice and continual source of ideas throughout the past four years. Myron's scientific intuition and unique experimental styles has contributed greatly to my evolution as a scientist.

I feel quite fortunate in having a chance to work in Brookhaven National Laboratory (BNL), and especially at the National Synchrotron Light Source (NSLS). I will always remember that it was Arthur Damask who introduced me into this great institution and made my dream come true. I would like to thank him and his family again for being so kind and warm to me.

Another special reward of this thesis has been the opportunity to work with Peter Johnson, a great physicist and easy to work with. I thank Peter Johnson for the good time I had working with him.

A lot of help was given by the staff members in Physics Department at BNL. Foremost is Steve Hulbert, who was there during a large fraction of those late nights, giving me so much help and I can not thank him enough for his support. Mark Ruckman and M. L. Shek both were very helpful in my work.

I thank Kelvin Lynn and members of his group for many discussion and support. Of course, I can not forget Fran Loeb for his excellent technical support and his friendship.

I give special thanks to my parents, Su-in Lee and Chaoxian Pan, and brother Xiaopin for their continuing encouragement and support.

Finally, I thank my friends Henry Chen, Phillip Shou, Donmin Chen, K. G. Huang, Rong Li, and H. Chen for their friendship and support.

Financial support for this work came from U.S. Department of Energy under contract DE-AC-02-76CH00016.

Brookhaven National Laboratory, New York.

November, 1986

CONTENTS

List of Tables

List of Figures

Chapter 1.
Introduction

1.1. Objective

The purpose of this thesis is to extend our knowledge on complex systems like modified metal surfaces. By combining various advanced surface-sensitive techniques to study systematically Ni, Pt, Pd overlayers on Nb(110) and Ta(110) surfaces at different temperatures, we hope to obtain a better understanding of the electronic structures, geometrical structures and the chemical properties of metal-metal interfaces and surfaces. Obviously, to solve these problems completely would require much more experimental and theoretical work. The present attempt is to make full use of all the newly developed techniques and equipment available to test various ideas and principles which might explain or predict the phenomena of metal thin-films and overlayers.

1.2. Why Study Modified Metal Surfaces ?

The physical and chemical properties of metal surfaces have been studied for many years [1-2]. Traditionally, surface science has been the study of pure metal-vacuum or pure metal-gas interface phenomena. The rapid development of new surface-sensitive and ultra-high vacuum techniques has made possible the recent extensive studies of the electronic and chemical properties of modified metal surfaces, such as the metal-metal interfaces, the metal-semiconductor interfaces and alkali metal promoted surfaces. These studies have had a strong impact on both the microelectronic and the chemical industries. When the dimensions of electronic devices becomes comparable with the electronic characteristic length, interface phenomena begin to dominate their performance. In chemistry, the systematic progress in corrosion resistance and heterogeneous catalysis requires a step-by-step understanding of surface chemical reactions [3]. Synchrotron radiation, with its tunability, polarization and high intensity, has a great advantage for surface science studies. Using a monochromator one can tune the photon energy to produce photoelectrons with a minimum mean free path to enhance the surface sensitivity. One can also tune the photon energy to scan the component of electron momentum perpendicular to the surface, thereby permitting measurements of the complete bulk band dispersion. The polarization dependence of photoelectron emission can be used to determine the orientation of molecules absorbed

on a surface and the direction of chemical bonds. Synchrotron radiation, together with other surface-sensitive techniques like low-energy electron diffraction (LEED), Auger electron spectroscopy (AES), electron-energy-loss spectroscopy (EELS), and k-resolved inverse photoemission (KRIPES), will greatly advance our knowledge of the chemical composition of surface, the local structure arrangement both in terms of adsorbate-substrate registry and order-disorder phenomena, the electronic structure of clean surfaces and adsorbate layers, the nature and strength of surface bonding, kinetics and mechanism of adsorbtion, desorption and catalytic reactions at the surfaces.

1.3. Historical Review

Studies of metal films grown on other metal crystalline substrates started not long ago but have attracted more and more attention recently. Previous investigation have shown that the chemical activity of an ultra-thin metal overlayers can be modified to be different from the bulk of the substrate, the bulk of the overlayer metals or different from both that of the substrate or overlayer metals. Several results relevant to this work are: (1) no CO chemisorption at room temperature on Ta(110), W(110) or Au(111) covered by a monolayer of Pd [4-6], (2) a large increase in the reaction rate of cyclohexane dehydrogenation to benzene for Pt(100) covered by a Au monolayer or for Au(111) covered by a Pt monolayer [7], and (3) a large increase in the hydrogen uptake for Nb(110) covered by a few monolayers of Pd [8-9]. The origin of the enhanced reactivity of the metal overlayers was attributed to the modified metal surface structure, such as large hollows existing between the overlayer atoms or steps with the edge atoms that are more active than the atoms in a smooth plane. The novel chemical behavior of the monolayer of Pd was interpreted as the result of the low electron density of states at the Fermi level (E_F).

1.4. Experimental Approach

In order to achieve our goal of gaining new insights into the nature of metal thin film or overlayers, a series of experiments have been developed to combine the application of multiple structure-sensitive electron spectroscopies with *in-situ* metal film growth. Using synchrotron radiation, complemented by the conventional surface-sensitive techniques such as the He discharge lamp photoemission spectroscopy, LEED and AES, we have studied the electronic structure and the morphology of the overlayers of three late transition-metals and their chemical properties on the Nb(110) and Ta(110) surfaces throughout the coverage region from submonolayer to the point at which bulk crystallographic ordering appears in

the overlayers. We are particularly interested in fcc(111)-bcc(110) metal epitaxy for their large lattice mismatch at the interface between the two crystal structures. The electronic and chemical properties of supported Pd overlayers have previously been studied by photoemission, low-energy electron diffraction, and Auger electron spectroscopy [10–14]. A great deal of work was done in this Laboratory by other scientists. The present thesis extends the previous program to include two extreme cases in group-VIII transition-metals and to study systematically and more carefully the trends of the electronic and chemical properties of metal overlayers at different temperatures. The metal overlayers investigated in this study were the transition metals Pt, Pd and Ni on which CO is strongly molecular chemisorbed. Even with this similar chemical property, the interaction of Ni-Ni atoms on Nb(110) or Ta(110) substrate are very different from that of Pt-Pt and Cu-Cu atoms. The different behavior of these group-VIII transition-metals as overlayers on the surface of group-VB transition-metals makes our study more interesting. Surface self migration cohesive energy and activation energy of Pt are both 30% larger than that of Ni [15]. However, the effect of overlayer metal electronegativity and atomic radius may play a more important role in the epitaxial and electronic trends. Compared with Ni, the electronegativity of Pt is very different from the Nb or Ta substrate and the atomic radius is relatively similar to the substrate metals. Ideally, the large difference in electronegativity implies a stronger adsorbate-substrate interaction and large atomic radius of the adsorbates suggests easier surface diffusion. These effects might determine the Pt layer-by-layer or Ni three-dimensional island formation of the overlayer growth.

Finally k-resolved inverse photoemission is applied for the first time to the investigation of the electronic bonding and antibonding states on metal-metal interfaces. The observation of electronic unoccupied antibonding interface states for a Pd monolayer on Nb(110) confirms the electronic bonding and antibonding model and leads to a simple intuitive picture of the metal-metal interactions.

Chapter 2.
Experimental Techniques

2.1. Introduction

In order to understand such a complex system as ultrathin metal overlayers, a wide variety of surface-sensitive techniques must be used to study systematically the electronic structures, atomic structures and chemical properties. The experimental program was carried out in three stages. The investigation of occupied electronic structures, the epitaxial and chemical properties of Ni and Pt overlayers on Ta(110) substrate by angle-resolved synchrotron radiation photoemission at low temperatures were performed at National Synchrotron Light Source (NSLS) U7 beam line. The studies of unoccupied electronic structures, the bonding and antibonding states of Pd overlayers on Nb(110) substrate by k-resolved inverse photoemission were carried out on a inverse photoemission system with a normal incidence grating spectrometer at the Surface Physics Laboratory of Brookhaven National Laboratory (BNL). The experiment of Ni and Pt overlayers on the Nb(110) substrate and other ground work, such as sample preparation and evaporation source calibration, were conducted in a UHV system at the Surface Physics Laboratory of Brookhaven National Laboratory (BNL).

The U7 beam line at NSLS was designed for angle-resolved ultraviolet photoemission spectroscopy (ARUPS) and surface-extended x-ray absorption fine structure (SEXAFS) experiments. The experimental system shown in Fig. 1 consists of two major parts: the monochromator and the experimental chamber. The optical configuration has a three-element plane-grating grazing monochromator which has a scan range of 15-1200 eV photon energy with a resolution of $\Delta\lambda/\lambda = 1 \times 10^{-2}$. The experimental apparatus includes a VG APES 400 hemispherical analyzer with a resolution of $\Delta E/E = 0.01$. Mounted on two-axis goniometer is a cryostat manipulator with z movement and z-axis rotation which has the ability to cool the sample to liquid helium temperature (20 K) in about an hour. There is also a LEED/AES facility, a high pressure gas doser and several metal evaporation sources. The UHV system is pumped by a ion pump, a cryogenic pump and a 150 l/s turbomolecular pump. The base pressure of the sample chamber is 9×10^{-11} Torr. A photograph of the experimental chamber is shown in Fig. 2.

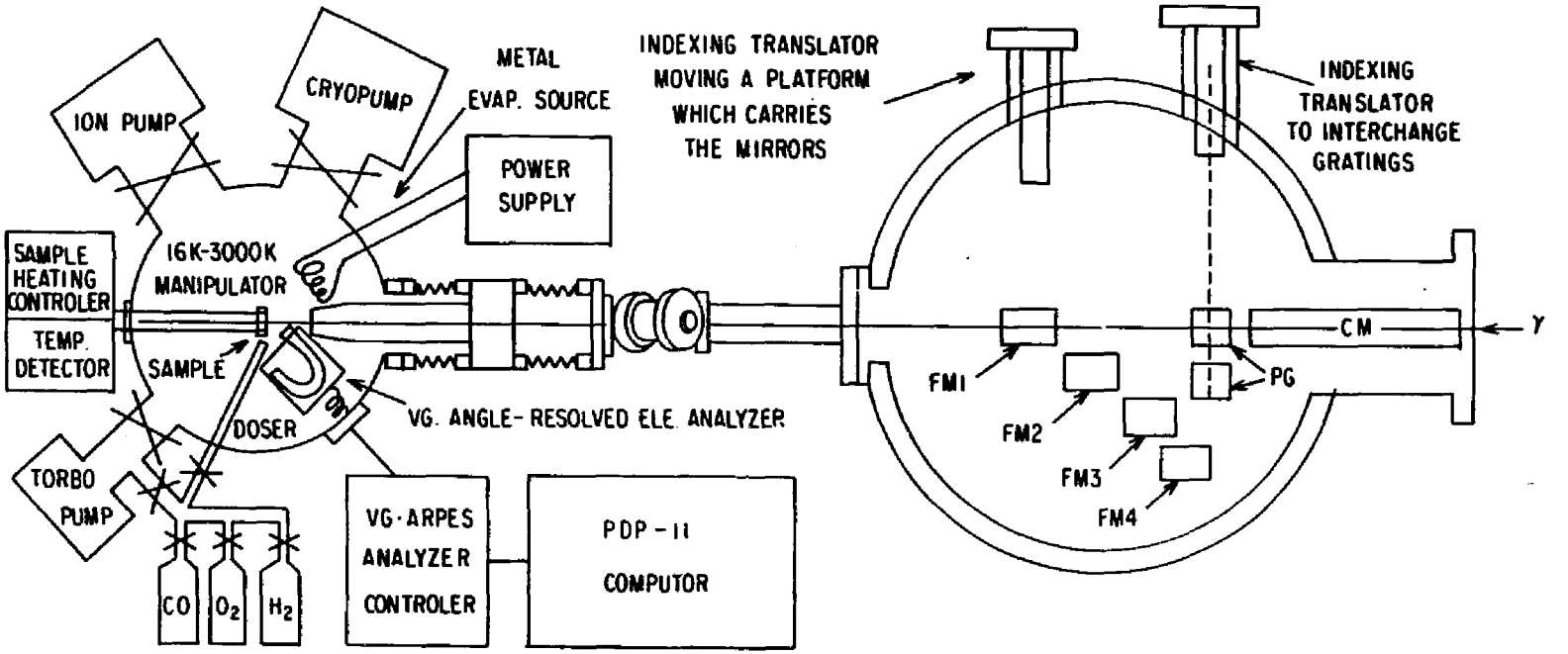

Figure 1: Schematic drawing of the U7 beamline experimental set-up used for low temperatures photoemission at National Synchrotron Light Source (NSLS).

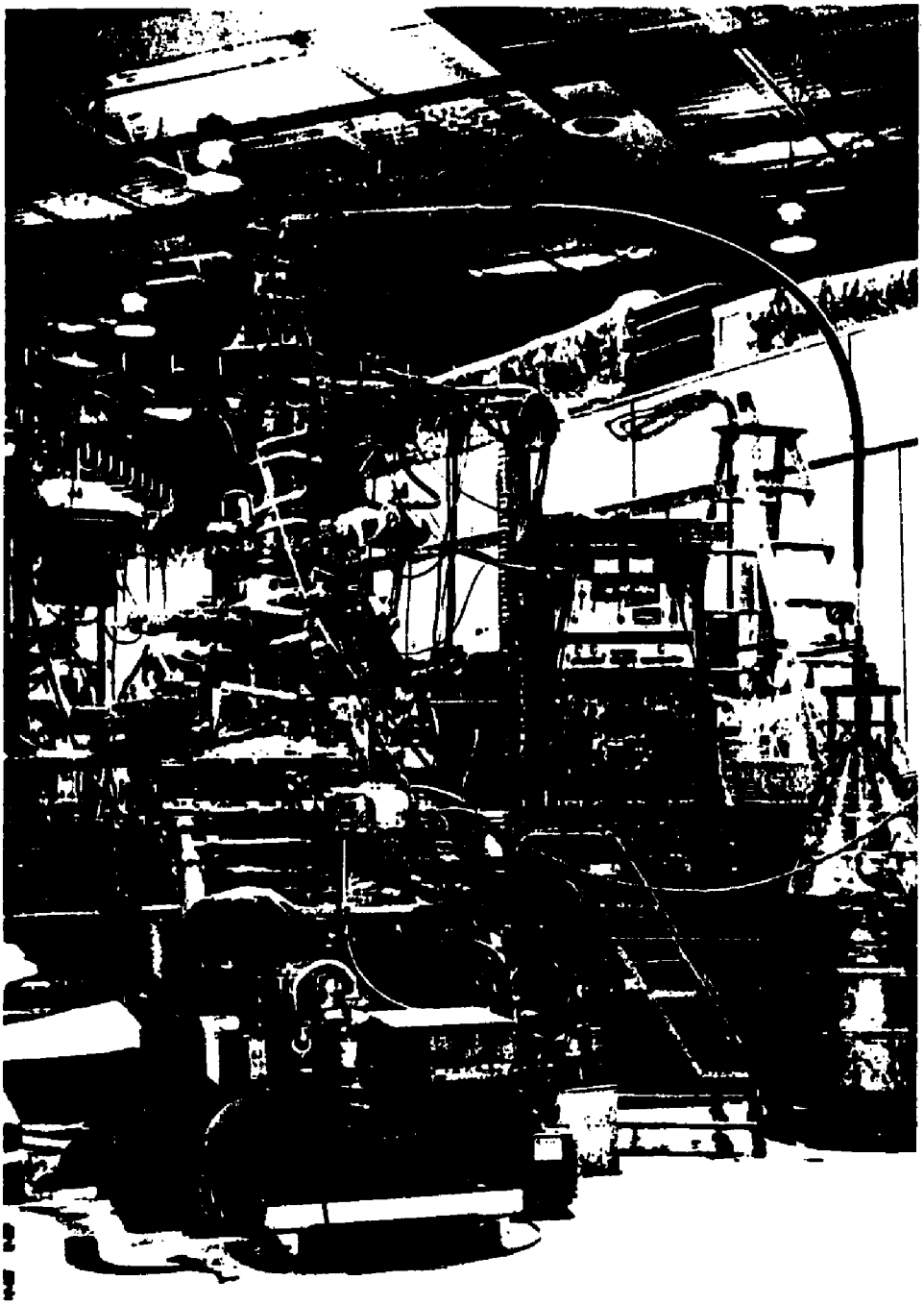

Figure 2: Photograph of the U7 beamline experimental set-up used for low temperatures photoemission at National Synchrotron Light Source (NSLS).

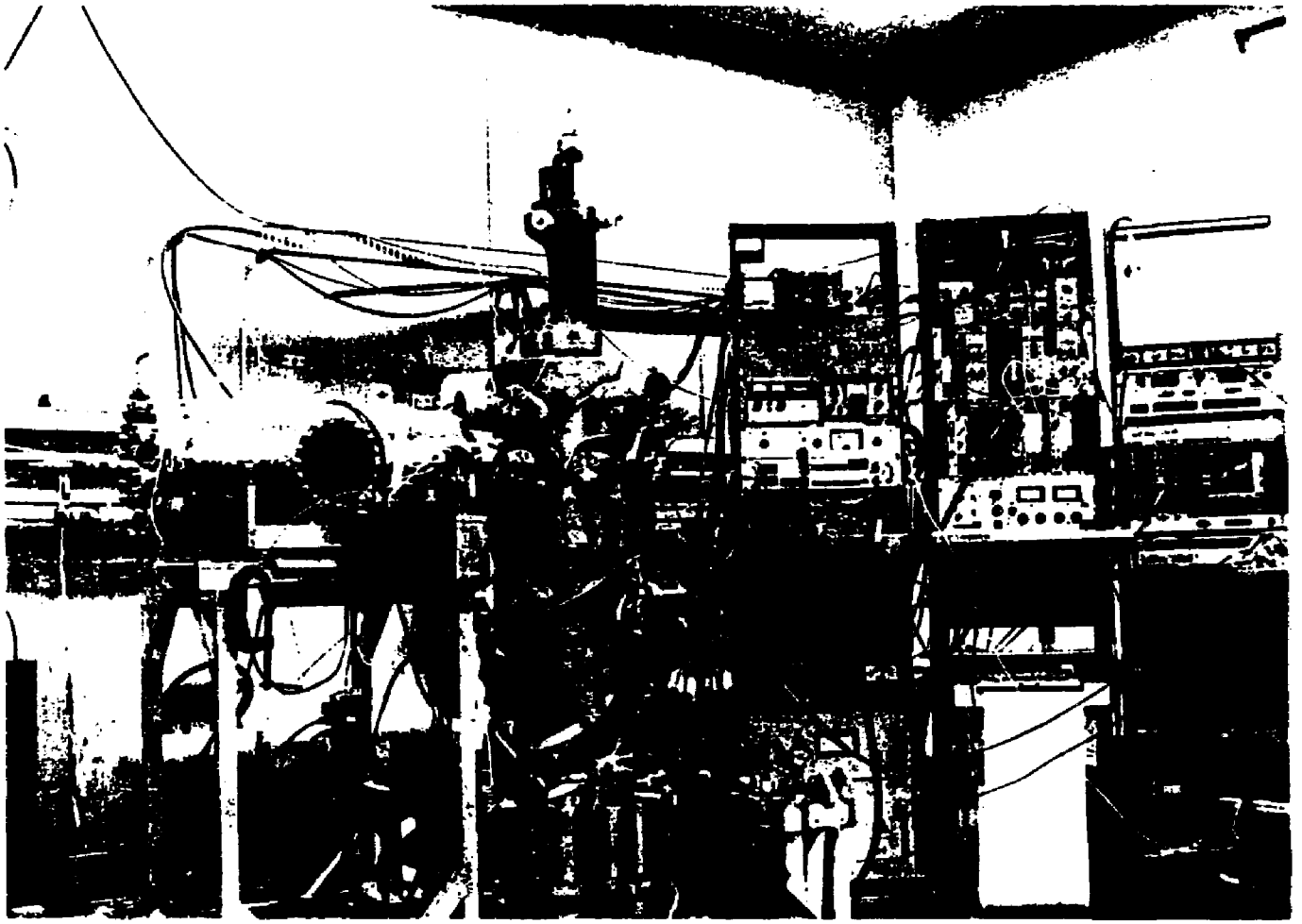

Figure 3: Photograph of the experimental set-up for k-resolved inverse photoemission at Surface Physics Group of Brookhaven National Laboratory (BNL).

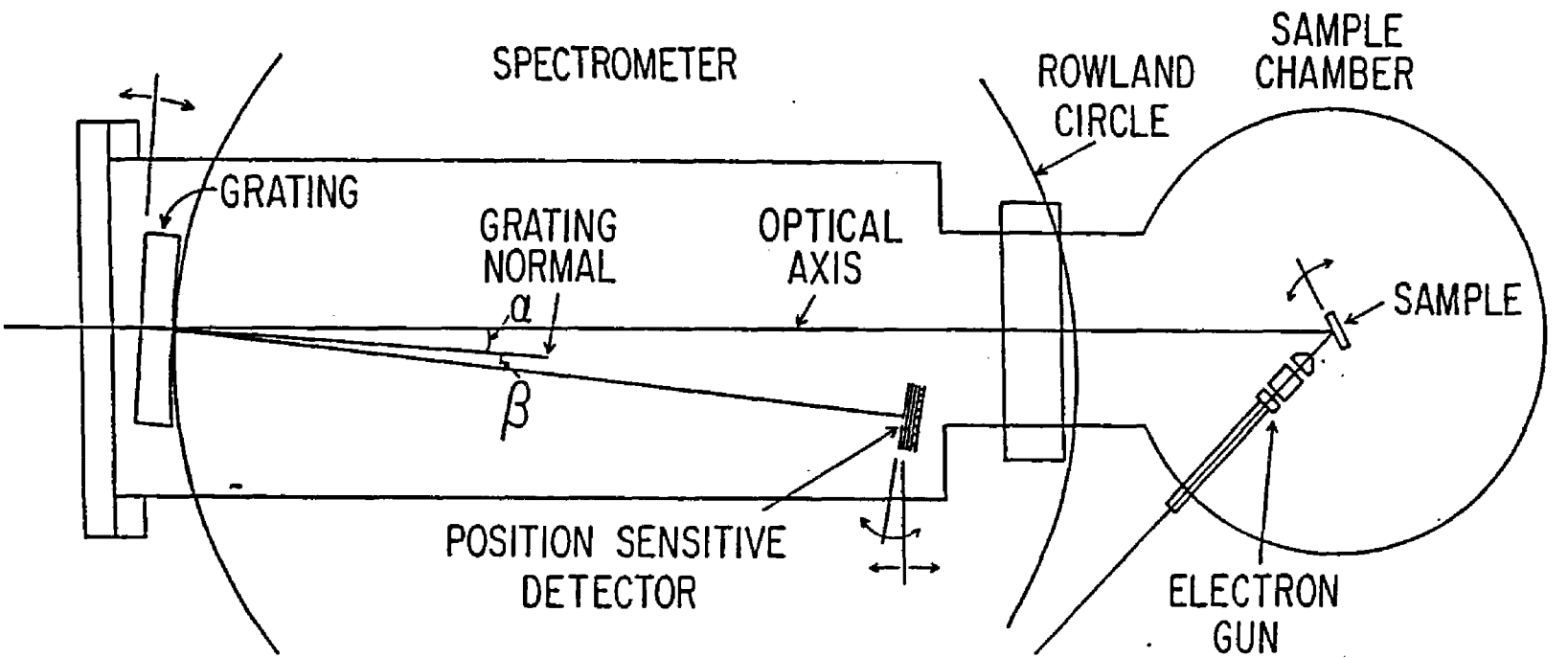

Figure 4: Schematic drawing of experimental set-up for k-resolved inverse photoemission in Surface Physics Group, BNL. Courtesy of P. D. Johnson.

The inverse photoemission system shown in Fig. 3 consists of a normal incidence grating spectrometer which covers the range of 10-30 eV photon energy, a low-energy high-brightness electron gun with a 5° full width angular convergence, a Varian LEED/AES optics, a PHI gracing incident electron gun, a Vecco rate/thickness controller, and a VG mass spectrometer for gas analysis. The UHV system is pumped by a 400 l/s ion pump and a 60 l/s turbomolecular pump with a base pressure 5×10^{-11} Torr. The schematic drawing of experimental set-up for k-resolved inverse photoemission is shown in Fig. 4.

The photoemission system in the Surface Physics Laboratory (shown in Fig. 5) has the traditional surface-sensitive analysis abilities. The system includes a gas-discharge lamp which can produce either the HeI(21.2eV), the HeII(40.8eV), the NeI(16.8eV), the NeII(26.9eV), or the NeIII(30.4eV) resonance lines, an Al anode x-ray source which produces 1800 eV photons, a double pass cylindrical mirror electron energy analyzer with an internal electron gun for UPS/XPS and EELS, a four grid retarded field LEED/AES optics for low energy electron diffraction, a single pass cylindrical mirror electron energy analyzer with an internal electron gun for Auger electron spectroscopy, a Vecco rate/thickness controller for metal thin film evaporation, a UTI mass spectrometer for gas analysis, a high pressure gas doser for chemisorption studies, and a three dimensional sample manipulator for sample alignment. By use of a 400 l/s ion pump and a 60 l/s turbomolecular pump, the UHV chamber can reach a pressure as low as 4×10^{-11} Torr. A schematic drawing of experimental set-up is shown in Fig. 6.

In the following sections I will describe the physical principles and the detailed experimental implementation of the primary surface-sensitive techniques used for this thesis. The sample preparation and ultra-high vacuum techniques will also be discussed.

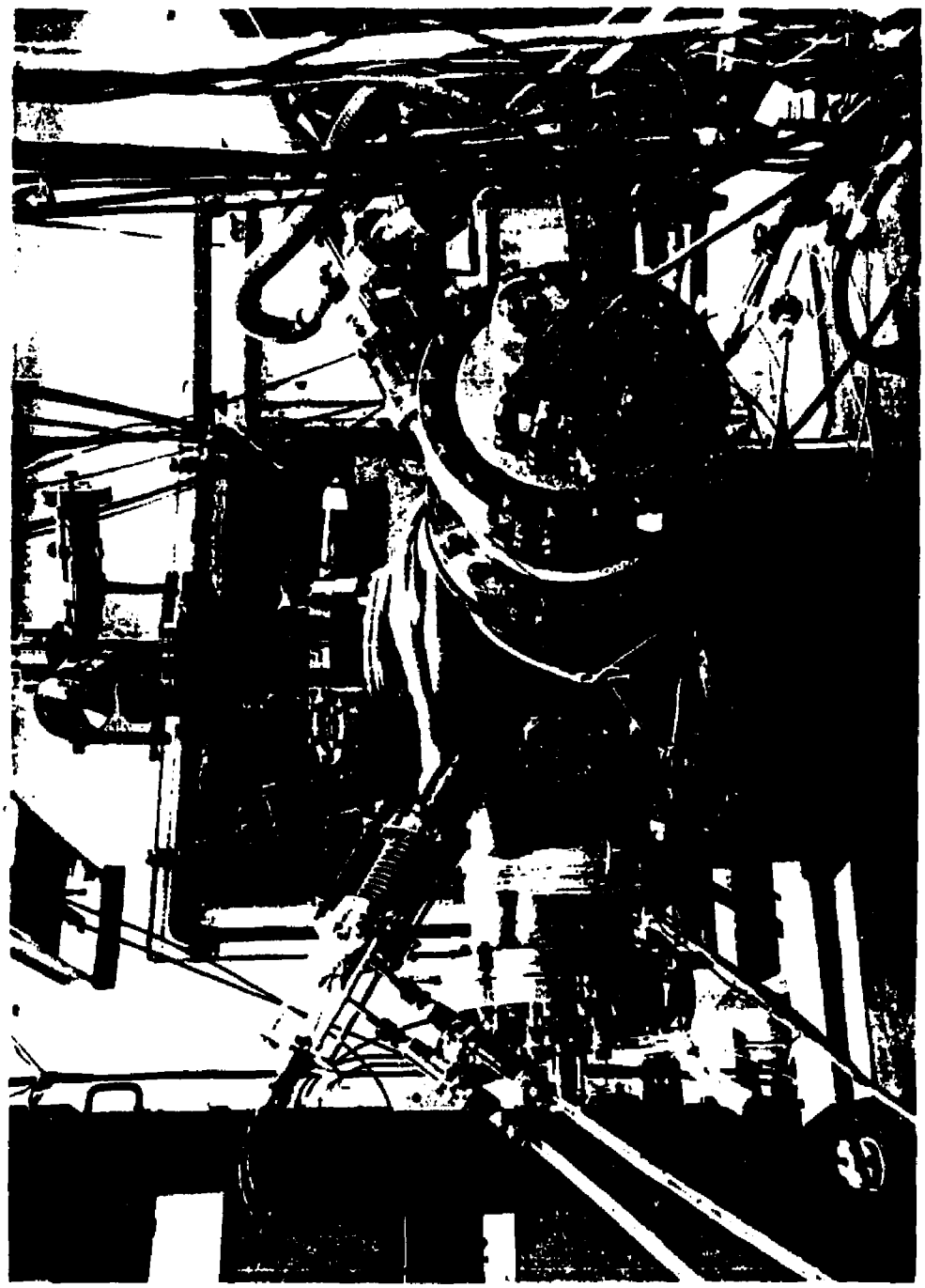

Figure 5: Photograph of the experimental set-up for conventional photoemission study in Surface Physics Laboratory, BNL.

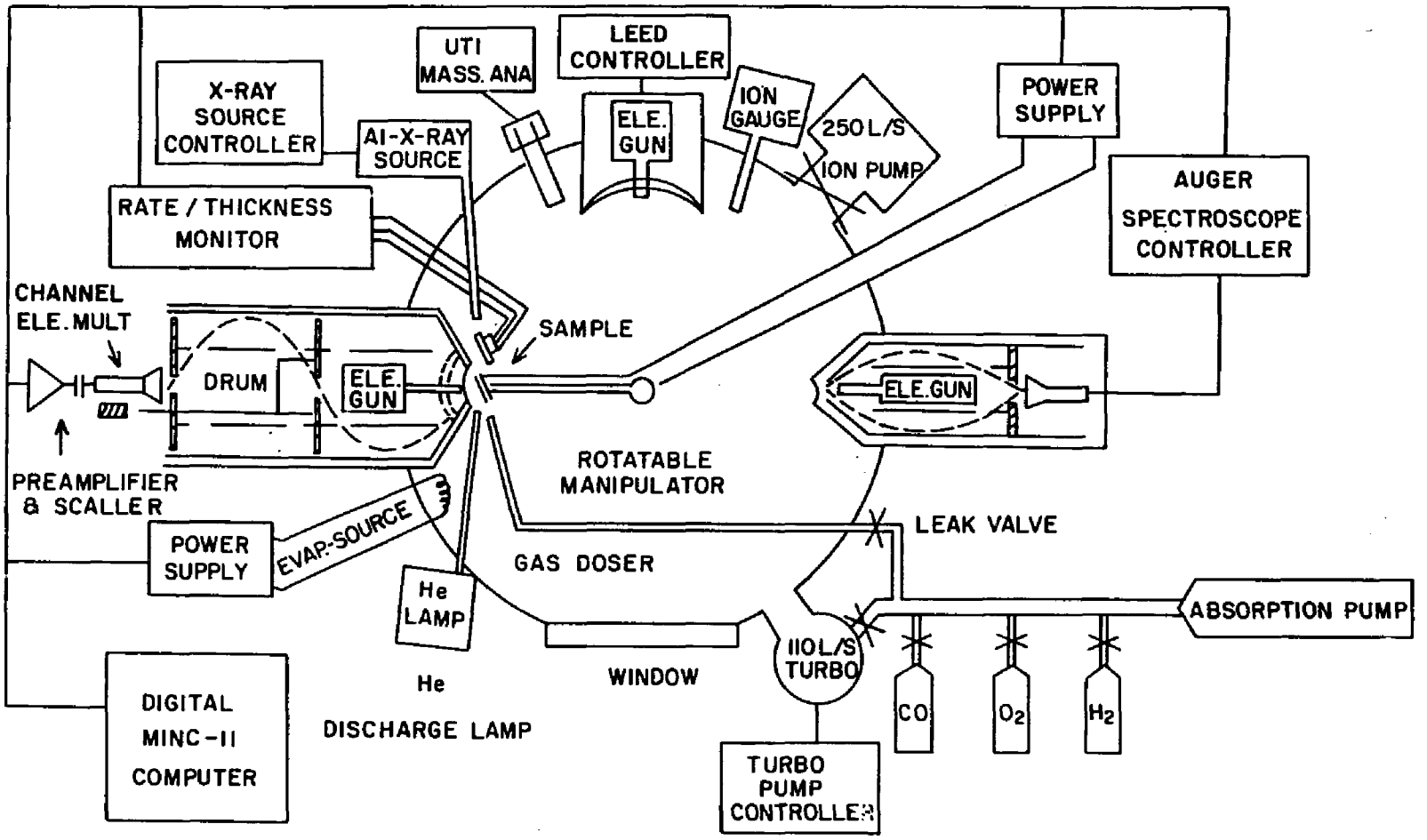

Figure 6: Schematic drawing of experimental set-up for conventional photoemission study in Surface Physics Laboratory, BNL.

2.2. Ultra-high Vacuum System

Vacuum technology provides a practical, impurity-free environment for the systematic study of scientific ideas and the application of these principles. It is the fundamental technique for surface science studies. In this section a brief review is given for the vacuum science and technology. By no means would we be able to cover the whole subject in these few pages. However, detailed descriptions can be found in references [16-17].

2.2.1 The Kinetic Picture of a Gas

For the ideal gases the individual molecules move about and collide with one another. Assuming these random collisions are elastic, Maxwell and Boltzmann calculated the average velocity of the particles as

$$v = \left(\frac{8kT}{\pi m}\right)^{1/2} \tag{2.2.1}$$

with k the Boltzman's constant, T the absolute temperature, and m the mass of the molecule. If one assumes that the gas density is n and the molecular diameter is d_0, then the mean free path can be shown as

$$\lambda = \frac{1}{2^{1/2}\pi d_0^2 n} \tag{2.2.2}$$

In principle the mean free path is pressure P dependent and for air at room temperature it can be written as

$$\lambda\,(mm) = \frac{0.05}{P\,(Torr)} \tag{2.2.3}$$

The pressure on a surface is defined as the rate at which momentum is imparted to a unit surface. A molecule incident on a surface will impart a total impulse or pressure of $2mv\cos\Theta$. By integrating over all possible angles in the half-plane, the pressure on the surface can be given as a function of mean square speed:

$$P = \frac{1}{3}nm\bar{v^2} \tag{2.2.4}$$

The total energy of a molecule is also proportional to its temperature

$$E = \frac{m\bar{v^2}}{2} = \frac{3kT}{2} \tag{2.2.5}$$

So one can obtain the absolute pressure:

$$P = nkT \tag{2.2.6}$$

Dalton discovered that the total pressure of a mixture of gases was equal to the sum of the forces per unit area of each gas taken individually. So from the relation of

$$P_t = n_t kT = n_1 kT + n_2 kT + n_3 kT + \cdots n_i kT \tag{2.2.7}$$

one can derive the following relation:

$$P_t = P_1 + P_2 + P_3 + \cdots P_i \tag{2.2.8}$$

where P_t, n_t are the total pressure and density and P_i, n_i are the partial pressures and densities.

For a classical treatment of such a complex problem such as the flow of gases in pipes, the flow is either viscous or turbulent depending on the Reynolds number R. In the region $R > 2200$ the flow of gas will always be turbulent. An ordered flow of a gas in streamlines occurs in the region bounded by a Reynolds number lower than 1200. When the ordered flow has a maximum velocity in the center of a channel and zero velocity at the wall it is called viscous flow and the character of gas flow is determined by gas-gas collisions. When the gas-wall collisions predominate the gas flow is called molecular flow and is theoretically the best understood of any gas flow.

The intrinsic conductance of the channel at constant temperature can be given as

$$C = \frac{Q}{P_2 - P_1} \tag{2.2.9}$$

where Q is the throughput which measures the volume of gas at a known pressure and temperature that passes a plane in a given time. The simplest and most familiar solution for the viscous flow through long straight tubes is the Poiseuille equation

$$C = \frac{\pi d^4}{128 \eta l} \frac{(P_1 + P_2)}{2} \tag{2.2.10}$$

where d, l is the diameter, the length of the tube, and η the coefficient of viscosity. For molecular flow in a tube of arbitrary length, the total conductance is the sum of the conductances of an aperture and a section of tube of length l,

$$\frac{1}{C_{total}} = \frac{1}{C_{tube}} + \frac{1}{C_{ap}} \tag{2.2.11}$$

where the conductance of an aperture at 22°C has the value

$$C_{ap}\,(L/s) = 11.6A\,(cm^2) \tag{2.2.12}$$

with A the area of orifice, and for a tube the value

$$C_{tube}\,(L/s) = 12.1 \frac{d\,(cm)^3}{l\,(cm)} \tag{2.2.13}$$

2.2.2 Materials in Vacuum

All metals used in an UHV system must have a vapor pressure low enough to prevent vaporization from occurring at the highest temperature encountered. Alloys that contain zinc, lead, cadmium, selenium, and sulfur should not be used in vacuum system construction. Such alloys include the brass which has a certain component of zinc and 303 grades of stainless steel which have sulfur and selenium in them.

Since there is some solubility of gases in metals, the gas may permeate a vacuum chamber wall. Hydrogen is one of the few gases that permeate most metals to a measurable extent because of its high solubility. The permeation rate of hydrogen is proportional to the square root of the pressure difference between the inside and outside of the chamber. Aluminum has the smallest hydrogen permeation, followed by Mo, Cu, Pt, Fe, Ni, and Pd.

The gas load in metals must be reduced to obtain an ultrahigh vacuum. These gases can be either dissolved during the initial melting and casting which consists mainly of hydrogen, oxygen, nitrogen, and carbon oxides, or physi- and chemisorbed from exposure to ambient atmosphere which consists of a large quantity of water vapor, with carbon oxides. These initial concentrations can be substantially reduced by vacuum melting of metal, by pre-outgassing the parts in a vacuum furnace, by *in-situ* bakeout of the completed system, or by sputtering the metal surface with electrons, ions, or photon sources. Chemical treatment is another effective method to clean metal surfaces. It is well known that an oxide barrier to hydrogen diffusion can be formed by an oxygen bake, and hydrogen firing is used to reduce the surface oxide.

A ceramic is a polycrystalline nonmetallic inorganic material formed under heat treatment with or without pressure. Because they are mechanically strong, with high dielectric breakdown strength and low vapor pressures, ceramics have been widely used in UHV as electrical insulators. Alumina (Al_2O_3) is the most commonly used ceramic in applications such as high-vacuum feed-throughs and internal electrical and thermal standoffs. High-density alumina can be easily machined and sealed to the metal with suitable compression, tensile strength, and thermal expansion coefficient.

Glasses are used in the production of vacuum apparatus, ion gauge tubes, view ports, metal-to-glass seals, and internal electrical and thermal insulation. Most glasses used in vacuum technology are made from a silicon oxide base to which other oxides have been added to produce a product with specific characteristics. Glass is brittle, and because of its high thermal expansion and low tensile strength it can shatter if unequally heated.

2.2.3 Pumping Speed

Pumping speed is defined as volumetric rate of the gas throughput across the specified plane.

$$S = \frac{Q}{P} \tag{2.2.14}$$

where S is the pumping speed, Q the throughput across the plane, P the pressure at that plane. Knowledge of the pumping speed is necessary to determine whether the pump is indeed functioning as described by the manufacturer. For an ideal vacuum chamber without any leaks, the pressure as a result of pumping with a speed S can be expressed as

$$P = P_0 e^{-\frac{S}{V}t} \tag{2.2.15}$$

It is obvious that high pumping speed is essential to obtain the ultra-high vacuum. To have some idea of the importance of maintaining the low pressure in the experimental chamber for surface science study, we can calculate approximately how long it takes for residual gases to cover the clean sample surface at low pressure P. According to the kinetic theory the particle flux Γ of an ideal gas striking a unit surface is

$$\Gamma = \frac{nv}{4} \tag{2.2.16}$$

where n is the particle density and v, the average velocity. By substituting the Eq. (2.2.1) and Eq. (2.2.6) we have

$$\Gamma = \frac{\sqrt{2}P}{2\sqrt{\pi kTm}} \tag{2.2.17}$$

Assuming that most particles inside the chamber is air, the incident flux onto the sample surface at room temperature is the function of pressure,

$$\Gamma\,(ML/sec) \approx 3.75 \times 10^5 \times P\,(Torr) \quad . \tag{2.2.18}$$

In other words, at room temperature it takes three seconds for the residual gases to cover the clean sample surface if the chamber pressure is on 10^{-6} Torr region and every molecule sticks to the surface.

2.2.4 Vacuum Chambers

In a vacuum chamber the volume gas is removed first, followed by surface desorption, out-diffusion from the solid, and last, permeation through the solid wall. All these processes except volume gas removal are greatly temperature dependent. At room temperature, it

takes a very long time to reach the permeation limit. High temperature baking is a necessary to obtain a ultrahigh vacuum in a resonable pumping time. So the materials, fabrication techniques, and seals used for construction of chamber walls and internal fixtures must be compatible with this thermal cycling.

The most commonly used materials for ultrahigh vacuum chamber construction are stainless steel and aluminum alloys. O-rings and other high vapor pressure materials are not used anywhere in the ultrahigh vacuum portion of the system. To reduce the outgassing load the components and subassemblies must be first chemically cleaned and go through two initial heat treatments. For example, the stainless steel can be vacuum baked at 800°C to reduce gas load and then baked at 400°C in pure oxygen to keep the hydrogen concentration in the metal as low as possible. But metal-to-glass seals, metal-to-ceramic seals, and sealed copper-gasketed flanges should not be subjected to temperatures higher than 400°C When the system has been completely assembled, it can be baked *in-situ* under vacuum at 150°C to 250°C for 24 hours to remove the surface gas. If the system has been properly cleaned and operated, hydrogen will be the dominant residual gas at the ultimate pressure of a stainless steel system and helium will be the dominant residual gas in a glass system. There are some rules for high vacuum pump baking. An ion pump and liquid cryogenic pump can be baked to 250°C. A turbomolecular pump and gas refrigerator cryogenic pump can be baked at approximately 100°C. A diffusion pump cannot be baked at all.

2.2.5 Total Pressure Measurement

The simplest mechanical gauges are the diaphragm and Bourdon gauges which are operated by a system of gears and levers to transmit the deflection of a solid wall to a pointer. The Bourdon tube is a coiled tube with an elliptical cross section, fixed at one end and connected at the other to the pointer mechanism. Evacuation of the gas in the tube causes rotation of the pointer. The diaphragm gauge contains a pressure-sensitive element from which the gas has been evacuated. By removing gas from the region surrounding the element, the wall is caused to deflect, and in a manner similar to the Bourdon tube the linear deflection of the wall is converted to angular deflection of the pointer. The mechanical gauges are inaccurate and used only as a rough indication of pressure.

The thermocouple gauges are also widely used as a rough indication of pressure which measures pressure-dependent heat flow. Constant current is delivered to the heated wire and a tiny thermocouple, usually iron- or copper-constantan, is carefully spot welded to its midpoint. When the pressure increases heat flows to the walls and the temperature of the

wire decreases. A low-resistance dc microammeter is connected to the thermocouple and its scale is calibrated in pressure units.

It is extremely difficult to measure the pressure in the ultrahigh vacuum region because the particle density is very small. In principle the measurement of pressures lower than 10^{-6} Torr is done by the ionization of gas molecules and the collection of the ions and their subsequent amplification by sensitive and stable circuitry. Each ionization gauge has its own lower pressure limit at which the ionized particle current is equal to a residual or background current. Normally the lower limits of ionization gauge measurement has an order of 10^{-11} to 10^{-12} Torr.

2.2.6 Residual Gas Analysis

Residual gas analysis is a very important vacuum technology which is not only widely used in chemistry, physics, materials and surface science, but it is also a fundamental technique for vacuum trouble-shooting. The residual gas analysis can be done by a mass spectrometer which measures the ratio of mass-to-electric charge of a molecule or atom. The gas molecules are first ionized, then directed through a mass separator, and finally detected.

The positive ions can be produced by electron impact ionization. First, the electrons are drawn across the ionization chamber to the anode from a filament. While crossing this space some of their electrons collide with gas molecules, strip off one or more of their electrons, and create positive ions. These ions are drawn out of the ionization chamber, focused and accelerated toward the mass separation stage. The most popular nonmagnetic mass separator in the modern residual gas analyzers is RF quadrupole mass filter. The filter is constructed by four rods of cylindrical cross section positioned to provide the optimum approximation to the hyperbolic fields. On the rod pair with positive dc potential, the addition of an RF field of magnitude greater than the dc field $(U + V cos\omega t)$ creates a situation in which positive ions are on a potential hill for a small portion of the cycle. Heavy ions have too much inertia to be affected by this short period of instability, but light ions are quickly collected by the rods after a few cycles. This forms a "high-pass" filter. On the other side, for the rod pair with negative dc potential, the addition of an RF field creates a field $-(U + V cos\omega t)$ which allows a potential valley to exist along the axis of the quadrupole for a small portion of the cycle if $V > U$. In this half of the quadrupole, a "low-pass" filter is formed because light ions are conditionally stable and heavy ions drift toward the electrode. Together, a band-pass filter is formed that allows ions of a particular

mass range to go through. The resolution is a function of the ratio of dc to RF potential amplitudes U/V.

Finally, the ions that passed through the mass filter stage are detected by either a Faraday cup or an electron multiplier. At a pressure higher than 10^{-6} Torr, the ion current at the entrance to the detector can reach 10^{-7} Amp. A simple Faraday cup detector will suffice for this high pressure region. Below 10^{-12} Amp an electron multiplier is needed for the high gain. In principle the amplification in an electron multiplier is achieved when positive ions incident on the first dynode generate secondary electrons. The secondary electrons are amplified as they collide with each succeeding dynode. The multipliers are usually operated with a large negative voltage (-1000 to -3000 V) on the first dynode. The typical dynode material is a Cu-2 to -4% Be alloy as suitably heat treated to form a beryllium oxide surface. For a 16-stage multiplier, the overall gain can be 10^6. These multipliers must be stored under vacuum at all times to prevent a continued accumulation of contamination which will cause the gain to decrease.

2.2.7 Interpretation of RGA data.

The interpretation of RGA data taken by mass spectrometer is based on a detailed knowledge of the fragmentation patterns of gases and vapors found in the system. Each gas has its own unique pattern of mass to charge ratio (m/e) peaks due to the molecular fragmentation of cracking that occurs in the ion source. This pattern is determined by the chemical structure of the operating condition of the mass analyzer. In many cases the existence of a particular molecule points the way to fixing a leak or correcting a process step. The UTI company provides a chart of reference spectra which allow the various gas species present in the mass analyzer to be identified. Variations in relative intensities can occur because operating conditions vary from instrument to instrument. In principle, with a similar relative intensity distribution one would be able to determine whether the chamber is leaking or not.

2.3. Sample Preparation

2.3.1 Single Crystal sample

A single crystal sample can be cut from a raw single crystal, then mechanically polished and chemically cleaned. Usually the crystal is spot-welded onto the tungsten wire or foil and then mounted on the sample manipulator. To clean the crystal sample in UHV a repeat Ar gas sputtering and high temperature annealing is widely employed. The high temperature annealing can be done by either resistively heating with massive current through the tungsten wire or an electron bombardment from an adjacent hot filament. After several cycles sputtering and annealing a clean single crystal sample can be obtained. The advantages of using a single crystal sample for surface science study are: (1) it is easy to achieve a well defined large area of single crystal; (2) crystal can be used for a long period of time; and (3) for some cases, there may be no substitute.

In some cases there are many advantages using a single crystal foil for surface science studies. It is much easy to clean the surface, to control the temperature, and to install. However, the precaution must be taken not to melt the sample. Fig. 7 shows the recrystallized Nb(110) foil used in the k-resolved inverse photoemission studies of the Pd overlayers on Nb(110) and the hydrogen chemisorption on Nb(110). The same type of the sample has been used for the photoemission studies. The Nb(110) single crystal substrate used for this thesis work was prepared from 0.002 inch thick polycrystalline niobium foil supplied by the Iowa State University Ames Laboratory. The foil strip was initially outgassed in vacuum and annealed at about 1000°C in a low pressure (10^{-6} Torr) oxygen atmosphere for one hour to remove carbon from the sample. Heating to the temperatures of 2200°C then recrystallized the foil and also depleted the bulk oxygen and carbon impurities which combine with the oxygen and are removed as CO. The cleanliness of the recrystallized foil was determined by Auger and Photoemission spectroscopy (PES). PES was found to be very sensitive to residual traces of contamination (like hydrogen) which are undetectable by the Auger technique. Low Energy Electron Diffraction (LEED) measurements showed that, following the heat treatment, large (110) single-crystal grains (5 -10 mm) had formed in the plane of the foil.

2.3.2 Thin Film Epitaxy

Thin films play a dominant role in modern technology. The advances in thin film techniques have led to the design and fabrication of more sophisticated devices made of

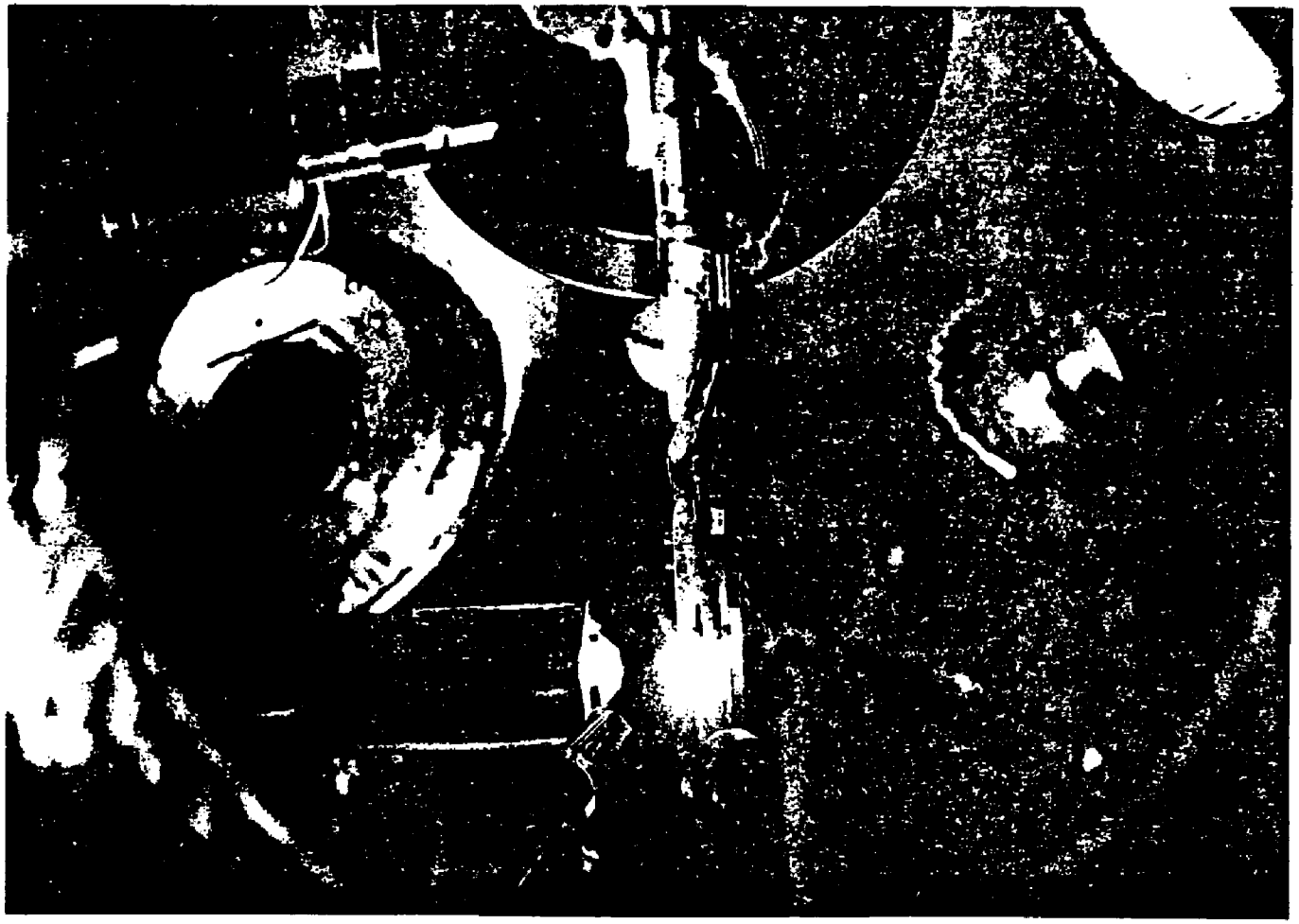

Figure 7: Inside of the inverse photoelectron spectrometor chamber showing the recrystallized Nb(110) sample attatched to the manipulator in front of the k-resolved electron gun.

semiconducting, magnetic, optical, and low-temperature superconducting materials. Epitaxial thin films generally refer to a single-crystal overgrowth on a single-crystal substrate with which a fixed crystallographic relationship exists. As will be discussed, different methods of thin film growth may result in different physical and chemical properties. More information can be found in the references[18].

The techniques which are often used in our group for ultra-thin film epitaxy are thermal evaporations, and sputtering. Solid materials vaporize when heated to sufficiently high temperatures. The condensation of the vapor onto a cooler substrate yields thin solid films. The most commonly used method is resistive heating which consists of heating the materials with a resistively heated filament or boat made of refractory metals such as W or Mo. The choice of the support material is primarily determined by the evaporation temperature and the resistance to alloying or chemical reaction with the evaporant. A comprehensive list of materials, their physical properties of interest for thermal deposition techniques other than by evaporation is given in references [19–20]. The Ni and Pd thin films on Nb(110) or Ta(110) were accomplished by evaporation from resistively heated tungsten baskets which were initially outgassed to ensure that the evaporation pressure would not exceed 3×10^{-10} Torr during evaporation. For some reactive materials with high vapor pressure below melting point, a simple exploding-wire technique can be used. By resistive heating of the evaporant wire to high temperatures before melting, a relatively uniform evaporation rate can be achieved. For the case of Pt thin films on Nb(110) or Ta(110), Pt wires with 0.5mm diameter and 99.998% purity were resistively heated to 1600°C, and typical evaporation rate were about 0.5 ML/min.

These simple resistive evaporation sources have some limitations such as low evaporation rate and difficulty in evaporating high-melting-point materials. Electron-bombardment heating is another technique often used in industries and laboratory which can overcome these drawbacks. The simple electron-bombardment arrangement consists of a heated W filament to supply electrons which are accelerated by applying a negative potential to the W filament and/or bended and focused to the evaporant by suitably designed permanent or wirewound magnets.

Ejected or sputtered atoms due to energetic particles bombardment can also be condensed on a substrate to form a thin film. This technique is best for making films with non-conducting materials, such as carbon *et al.*

For the deposition process the formation of thin films on a substrate is basically a phase change phenomenon involving nucleation and growth with the constraint of the substrate. The factors that will affect thin film formation are vacuum pressure, deposition rate, substrate temperature and substrate structure, and they must be specified in film deposition. The selection of a substrate that allows epitaxial film growth means that the film-substrate interfacial energy has the lowest value at the epitaxial condition and any deviation from this condition tends to increase the interfacial energy and the barrier of nucleation. Whether the epitaxial film forms a three-dimensional nucleus or a two-dimensional uniform layer on the substrate depends on the wetting condition, which is governed by the interfacial energies involved. In principle the deposition of an epitaxial film requires high vacuum, slow deposition rate, high substrate temperature, and single-crystal substrate with a low Miller index surface that has small lattice mismatch with the film. In fact both the lattice match and atomic bonding are important in epitaxy. The theory using minimum interfacial energy principle has correlated epitaxy with lattice match and predicted the occurrence of the Nishiyama-Wassermann and Kurdjumov-Sachs orientations in thick overlayers with astonishing accuracy.

2.3.3 Adsorbate Thickness Measurements

It is always very difficult to measure the amount of adsorbates accurately. At early growth stages, the adsorbate atoms may form three-dimensional clusters on the substrate surface. Even for metal overlayers, the thin film surface may not be perfectly smooth. However, by systematic study and calibration with several surface-sensitive techniques a certain accuracy of adsorbate thickness can be obtained.

A). Photoemission

For a nonreactive thin film without interdiffusion at the interface, the attenuation of substrate valence states can be used to estimate the adsorbate thickness. For transition metal thin films an electronic interface state or adsorbate induced state may appear at submonolayer or intermediate coverage. These states are due to the interaction of adsorbate-substrate and adsorbate-adsorbate, and can be used to determine the changes of structure and monolayer thickness.

B). Auger electron spectroscopy

The Auger electron spectroscopy (AES) is widely used for solid surface analysis. When a thin film grows in a monolayer overgrowth fashion, the AES signal versus film thickness can be calculated by a quantitative method. With the consideration of (1) the attenuation

of a primary beam; (2) the effects of back-scattered and forward-scattered electrons both from thin film and substrate materials; (3) the escape depths of Auger electrons; and (4) the effect of the three-dimensional movements of secondary electrons and Auger electrons in the solid, the curve of Auger electron signal intensity versus film thickness can be estimated for the CMA or LEED optics used for the usual Auger experiment. A detailed discussion of a quantitative Auger electron spectroscopy method are given in references. As a simple example let us consider an adsorbate layer with thickness x and electron mean free path λ_a on the surfaces of substrate with no interdiffusion and reaction. The Auger signal intensity measured by CMA optics will be given by

$$I_A = I_A^\circ \left(1 - e^{-\frac{x}{\lambda_a}\cos\theta}\right) \tag{2.3.1}$$

$$I_S = I_S^\circ e^{-\frac{x}{\lambda_s}\cos\theta} \tag{2.3.2}$$

where I_A° is the Auger signal intensity of pure or very thick adsorbate material, I_S° is that of clean substrate, and θ the CMA detection angle usually is about 42°. By the ratio of Auger signal intensity one would be able to estimate the adsorbate thickness x.

C). Low-energy electron diffraction

Low-energy electron diffraction has been widely employed not only for the study of clean surfaces, chemisorption on these surfaces, and surface reaction, but for the epitaxy of thin film too. When a given species of atoms adsorbs to the surface they congregate into groups of atoms. In this nucleation stage the concentration of adsorbed atoms on the surface may be high enough to be detected by Auger spectroscopy but too small and too scarce to produce noticeable changes in the LEED pattern of the substrate surface. For example, clusters of 3 to 5 atoms randomly scattered on a surface generally are not recognizable by LEED but are noticeable by AES. If the nuclei grow predominantly in lateral dimensions with an order structure, the LEED pattern may reveal a superstructure with periodicity determined by the combination of the nets of the adsorbed layer and the substrate surface. If the atoms are disordered, then LEED may only register a small and uniform increase in background. In the intermediate stages of film growth, LEED may reveal the presence on the substrate surface of three-dimensional crystallites by displaying diffraction patterns of larger crystallite surfaces superimposed on the weakened pattern of the substrate. It turns out that LEED can be most profitably used in the initial and intermediate stages of single-crystalline film growth to distinguish between monolayer formation and three-dimensional growth of nuclei and to determine the structure of the adsorbed layers relative to the substrate.

D). Secondary electron profile

Changes in the secondary electron emission during adsorption of a metal vapor can be used to monitor the surface structure and composition. By measuring the net current i_{cc} flowing into the specimen crystal as a function of deposition time t at a fixed primary beam energy, surface changes can be measured rapidly and precisely. This method is extremely useful when performed in conjunction with AES and IPES. The determination of ultrathin film growth modes from the $i_{cc} - t$ plots has been discussed in detail by Rhead and his co-workers [21]. In principle one would expect to see a very sharp drop in i_{cc} at a monolayer coverage. It has been shown that this marks more accurately the completion of the monolayer than do the variation of the Auger signals. In addition, there are "pre-monolayer breaks" that can be associated with completion of a sub-monolayer structure. The explanation usually put forward is that the changes in emission are due to changes in the work function ϕ which affect especially the escape of secondary electrons with very low energies. Argile and Rhead [22] had suggested that enhancement of emission may also be caused by an enhancement of surface ionization due to surface modes of electron scattering induced by the presence of the adsorbed layer. In other words the surface ionization effect per adatom would be lower for a condensed adlayer island than for dispersed adatoms, and this causes the pre-monolayer breaks. The effect of a second layer, and of disorder, would be to reduce the effects of the scattering at the adsorbate-substrate interface.

E). Quartz crystal vibration measurement

The use of digital period measurement of quartz crystal vibration can reach a ultimate thickness investigation in linearity, accuracy and resolution. The principle is simple. The mass of quartz changes when the film has been deposited onto the quartz crystal, and therefore the oscillation period of quartz changes in a way which is proportional to the change of thickness ΔT. It can be shown that the corresponding equation for frequency measurement is

$$\Delta T = \frac{\rho_q \Delta f}{\rho_d c f^2} \tag{2.3.3}$$

where ρ_q is the density of quartz, ρ_d the density of the deposited material, f the vibration frequency and c a constant related to the addition of or subtraction of a small amount of mass at the surface. The resolution of the thickness monitor can reach ± 0.1 Å after calibration. To estimate the deposited film thickness at the sample surface a geometrical and orientational calibration have to be made.

2.3.4 Sample Temperature manipulation

Sample temperature is a very important factor which affects the physical and chemical properties in surface science study. The special requirements are not easily met by commercial units. Myron Strongin has designed and built a simple manipulator which can vary the temperature of a foil sample from 2500 K to 20 K in ultrahigh vacuum. The sample is resistively heated to warm up and cooled by liquid helium or liquid nitrogen to low temperature. The design uses copper blocks as a mechanical coupling between the cryogenic reservoir and the sample holder, and prevents the heat loss by radiation shielding of a concentric inlet/outlet system which is cooled by liquid nitrogen. All the copper conductors necessary for resistive heating are connected to the sample clamps by a stainless-steel strip which, in turn, is heat sunk to the copper holder by means of a sapphire insulator. The manipulator has been working very well with the following properties: (1) rapid sample cooling to 20 K; (2) capability of annealing the sample up to 2500 K without heating up the cryogenic reservoir; (3) minimum vibration of the sample for photoemission study; (4) full 2 π polar rotation; (5) 10 cm vertical motion; and (6) tiltable for small angles. Chaban and Chabal [23] have also presented a simple design for the sample manipulator operating between 20 and 2000 K in ultrahigh vacuum. Even with a large thermal mass of the sample holder used for stabling the sample temperature, the temperature extremes of their design can be obtained within a few minutes.

2.3.5 Sample Temperature Measurements

Two methods were used to estimate the sample temperature in two regions. For the temperature above 500°C a two color calibrated infrared pyrometer has been used. Below 500°C the temperature was calculated by the sample electrical resistivity. According to Matthiessen's rule any metal resistivity can be divided into two parts, intrinsic resistivity due to the lattice vibration ρ_i and impurity contribution ρ_r. The total resistivity of the sample can be written as

$$\rho = \rho_i + \rho_r \tag{2.3.4}$$

or

$$R = R_i(T) + R_r \tag{2.3.5}$$

It can be deduced that for monovalent metals and some divalent metals the ratio of resistivity at different low temperature is given by [24]

$$\frac{\rho_i}{\rho_\theta} = 4.226\,(T/\theta)^5 \cdot J_5\,(\theta/T) \tag{2.3.6}$$

However, for the transition metals the ratio becomes [24]

$$\frac{\rho_i}{\rho_\theta} = 2.084\,(T/\theta)^5 \cdot J_5\,(\theta/T) \tag{2.3.7}$$

and the tables of J_5 values has been given by MacDonald and Towle (1956) [25-26]. With these assumptions and relations one may estimate the temperature of a purity unknown metallic element from 4 to 300 K by its electrical resistance. The simplest procedure is to measure the electrical resistance R_{295} at room temperature, and measure R_4 by dipping the sample into a dewar of liquid helium. Knowing R_{295} and $R_4 = R_r$, R_i at room temperature can be deduced ($R_i\,(295) = R_{295} - R_4$). Assuming $\rho_i/\rho_\theta = (T/\theta)^5\,J_5\,(\theta/T)\,/J_5\,(1)$ the ratio of resistivity can be written as

$$\frac{\rho_i\,(T)}{\rho_i\,(\theta)} = \frac{\rho_i\,(295)}{\rho_i\,(\theta_D)} \cdot \frac{R_i\,(T)}{R_i\,(295)} \tag{2.3.8}$$

where θ_D is the Debye temperature of metallic element, and for a known value of $T/\theta = 295/\theta_D$ the table in reference [24] gives the value of $\rho_i\,(295)\,/\rho_i\,(\theta_D) = C$. Now to estimate the unknown temperature T at a resistance $R\,(T)$ the following relation can be used to obtain the ratio of resistivity.

$$\frac{\rho_i\,(T)}{\rho_i\,(\theta)} = C \cdot \frac{R\,(T) - R_r}{R\,(295) - R_r} \tag{2.3.9}$$

With this ratio one can estimate T/θ from the reference and finally determine the sample temperature T.

Precautions should be taken if a metallic element is used because it may contain traces of certain impurities. MacDonald and Pearson [27] have shown that the presence of a few atoms per million of certain multivalent elements will produce a marked minimum in the electrical resistance at about 15 K to 25 K. The exact temperature of the minimum electrical resistance depends on the particular impurity elements present and their concentrations.

2.4. Low-Energy Electron Diffraction

In 1927, Davisson and Germer discovered that for an electron beam with energies between 15 to 200 electron-volts (eV) incident on a crystal of nickel, the angular variation of the reflected flux was consistent with electron diffraction theory [28]. Since then, a large amount of work has been done to improve the technique and study the surface structure of crystals [29].

The limited penetration depth and the suitable wavelength make low-energy electron diffraction (LEED) to be a suitable probe of surface geometrical structure.

2.4.1 Diffraction and the Reciprocal Lattice

A plane wave incident on an atom or atoms within a unit cell will be scattered in all directions, but interference between waves scattered from neighbouring unit cells will restrict the net flux to those directions in which the scattered waves from neighbouring cells differs only by an integral number of wavelengths λ . The in-phase condition is met for all integers n which satisfy the Laue condition:

$$a\left(\sin\theta_n - \sin\theta_0\right) = n\lambda \tag{2.4.1}$$

where a is the separation distance between scatterers and λ is the wavelength of incident electrons. θ_0 (θ_n) is the angle of the incident (diffracted) beam with respect to the surface normal. If the incident and diffracted beams are described by unit vectors $\vec{k}_0$ and $\vec{k}'_n$ then the Laue condition can be written in vector form as

$$\vec{a}\left(\vec{k}'_n - \vec{k}_0\right) = n\lambda \tag{2.4.2}$$

or

$$\vec{a}\,\Delta\vec{K}_n = n\lambda \tag{2.4.3}$$

where

$$\Delta\vec{K}_n = \left(\vec{k}'_n - \vec{k}_0\right). \tag{2.4.4}$$

The diffracted beams are determined by $\Delta\vec{K}_n$. In the one-dimensional case, it is clear that they are given by integral multiples of the basic unit ($\lambda/|a|$). This involves the reciprocal of the real space lattice vector $\vec{a}$. We define a reciprocal lattice vector as $\vec{a}^* = (1/\vec{a})$.

2.4.2 Interpretation of diffraction patterns

Let us first consider a clean and unconstructed surface. Assuming $\vec{a}_1$ and $\vec{a}_2$ in real space are separated by an angle α, and $\vec{a}_1^*$ is at $\pi/2$ to $\vec{a}_2$, then the angle between $\vec{a}_1$ and its complementary reciprocal vector $\vec{a}_1^*$ must be $(\pi/2) - \alpha$. so

$$|\vec{a}_1| = \frac{1}{|\vec{a}_1^*| \sin\alpha} \tag{2.4.5}$$

and

$$\sin\alpha^* = \sin\alpha \quad . \tag{2.4.6}$$

For the overlayer with an incommensurate structure, we need to use matrix notations. If a surface structure has lattice vectors $\vec{b}_1$ and $\vec{b}_2$ which differ from the substrate lattice vectors $\vec{a}_1$ and $\vec{a}_2$. then they can be described in terms of substrate lattice vectors,

$$\begin{aligned} \vec{b}_1 &= m_{11}\vec{a}_1 + m_{12}\vec{a}_2 \\ \vec{b}_2 &= m_{21}\vec{a}_1 + m_{22}\vec{a}_2 \end{aligned} \tag{2.4.7}$$

or in matrix notation:

$$\begin{pmatrix} \vec{b}_1 \\ \vec{b}_2 \end{pmatrix} = \begin{pmatrix} m_{11} & m_{12} \\ m_{21} & m_{22} \end{pmatrix} \begin{pmatrix} \vec{a}_1 \\ \vec{a}_2 \end{pmatrix}. \tag{2.4.8}$$

or

$$B = MA \tag{2.4.9}$$

A corresponding relationship between reciprocal lattice vectors will be

$$B^* = M^* A^* \tag{2.4.10}$$

where

$$M^* = \begin{pmatrix} m_{11}^* & m_{12}^* \\ m_{21}^* & m_{22}^* \end{pmatrix} \tag{2.4.11}$$

so finally we have

$$\begin{pmatrix} m_{11} & m_{12} \\ m_{21} & m_{22} \end{pmatrix} = \frac{1}{detM^*} \begin{pmatrix} m_{22}^* & -m_{21}^* \\ -m_{12}^* & m_{11}^* \end{pmatrix} \tag{2.4.12}$$

where

$$detM^* = m_{11}^* m_{22}^* - m_{21}^* m_{12}^* \qquad (2.4.13)$$

This relationship is sufficient to derive the real lattice structure from the observed diffraction pattern if the appropriate reciprocal lattice vectors can be extracted from the LEED pattern.

2.4.3 Diffraction from successive planes of a crystal

The specific atomic positions within the surface unit mesh or in a three-dimensional unit cell including more than one layer at the surface can be determined by LEED crystallography. This is done by comparing the predictions of large-scale computer calculations applied to specific structural models with experimental intensity-voltage (I-V) curves for several diffraction beams. Position coordinates perpendicular to the surface are generally reliable to ± 0.1 Å, those parallel to the surface to ± 0.2 Å unless the atom actually occupies a position of high, two-dimensional symmetry.

2.4.4 Non-planer surface: steps and facets

Thermodynamically, the most stable surface structure is obtained when the total surface free energy is a minimum. A graphical method of determining the equilibrium structure is the Wulff construction or γ-plot [30]. In a γ-plot, the surface free energy is plotted as a function of crystallographic orientation. If a crystal is cut at some inclination to one of the very stable faces, then the surface may divide into a series of facets of "hill and valley" structures, which maintain the macroscopic orientation, but on an atomic scale involve the juxtaposition of planes with low Miller indices and high atomic densities.

2.4.5 Experimental techniques

A). Vacuum system

There are two factors which require low pressure for LEED experiments: (1) to prevent sample contamination during the experiment and; (2) to have sufficient mean free path of electrons for the diffracted electron to reach the detector. Assuming that gas atoms will adsorb with a sticking probability of unity, then at 10^{-6} Torr the surface would become covered with a monolayer of adsorbed gas in 1 second. Therefore a vacuum pressure of 10^{-9} Torr is the maximum acceptable for detailed surface studies.

B). Electron gun

Generally, electrons emitted from the cathode must be accelerated to an anode which is at a positive potential with respect to the cathode.These electrons follow paths which converge towards the central axis, reach a cross-over point where the beam has minimum radius and thereafter begin to diverge. The anode takes the form of a relatively long cylinder with an aperture at the far end. This aperture limits the cone of divergent electrons, and electrons outside this cone are collected by the anode, but the geometry is designed to make it highly probable that any secondary electrons will also be collected. This divergent cone of electrons is then refocused by an electron lens comprising two more elements, a second anode for focusing which is negatively biased with respect to the first anode, and a third anode which is at the same potential as the first anode.

C). Display system

The intensity of the electron beams diffracted from the crystal surface may be measured directly, for example by collecting an electron beam with a channel plate, or indirectly by causing the electrons to impinge on a screen coated with phosphorescent material and then measuring the brightness of the resulting spots of light. Using a channel plate the LEED patterns can be digitized, analyzed and displayed by the computer. The phosphor screen method is easy to construct and use.

2.5. Auger Electron Spectroscopy

2.5.1 Introduction

When a hole is produced in a core subshell by x-ray photoionization or electron-impact ionization, a decay or de-excitation of the system can occur via the emission of x-ray fluorescence or the emission of a secondary electron in a radiationless manner. The secondary electron emitted via the latter process is named after its discoverer, Auger, and can be thought of as an internal x-ray photoeffect.

For a typical distribution of electrons emitted from a solid sample, the spectrum is completely dominated by a broad distribution of inelastic secondary electrons and a rather sharp peak at the primary beam energy. On careful inspection of the secondary-electron distribution, small peaks with the same kinetic energy regardless of the primary energy are evidently superimposed upon the strongly sloping background which are therefore caused by Auger emission. Other small peaks on the secondary-electron background move in tandem with the elastic peak which are due to electron-energy-loss processes [31].

Because of intense and steeply sloping background of secondary electrons emission vs. energy, it can be extremely difficult to observe Auger peak in a normal counting mode. However, electronic differentiation of the signal makes the task easier.

If a perturbing voltage $\Delta E = K\sin\omega t$ is superimposed on the pass energy of an electrostatic analyzer, then the total current collected can be written as a Tayler series:

$$I(E+\Delta E) = I(E) + I'(E)\Delta E + \frac{I''}{2!}(E)\Delta E^2 + \frac{I'''}{3!}(E)\Delta E^3 + \frac{I''''}{4!}(E)\Delta E^4 + \cdots \quad (2.5.1)$$

where the prime denotes differentiation with respect to E. Hence,

$$\begin{aligned} I &= I_0 + \left(I'K + \frac{I'''}{8}K^3 + \cdots\right)\sin\omega t - \left(\frac{I''}{4}K^2 + I''''\right)\cos 2\omega t \\ &\simeq I_0 + I'K\sin\omega t - \frac{I''}{4}K^2\cos 2\omega t. \end{aligned} \quad (2.5.2)$$

If K^3 and higher order terms are neglected, then detection at a frequency ω by use of a phase-sensitive detection system will produce a derivative spectrum (I'). The magnitude of the signal will increase as K, the modulation voltage is increased, but care must be taken not to degrade the instrumental resolution by over modulating the spectrometer.

2.5.2 Calculation of Auger energies

In the relativistic model, atomic transition is assumed to be the transition of one electron from its initial state to the positive energy continuum caused by the interaction of the electron with the electromagnetic radiation emitted by the other electrons when it fills the atomic vacancy. The Auger transition is thereby considered to be one of internal radiation adsorption.

A simplified concept and equation used in calculation of Auger energies is Burhop's empirical methods [32]:

$$E^Z(VXY) = E^Z(V) - E^Z(X) - E^Z(Y') \tag{2.5.3}$$

where $E^Z(VXY)$ is energy of the ejected Auger electrons from an element with atomic number Z; $E^Z(V)$ is the energy of the level in which initial core hole is created; $E^Z(X)$ is the energy of the level from which an electron falls to fill the initial vacancy; and $E^Z(Y')$ is the energy appropriate to an atom already singly ionized in an inner shell (Y is the level from which the Auger electron is excited). $E^Z(V)$ and $E^Z(X)$ can be approximated as the atomic binding energies of electrons in the V and X levels, and $E^Z(Y')$ probably lies between $E^Z(Y)$ and $E^{Z+1}(Y)$. Thus Eq. (2.5.1) can be written as:

$$E^Z(VXY) = E^Z(V) - E^Z(X) - E^Z(Y) - \Delta E^Z(Y) \tag{2.5.4}$$

where $\Delta E^Z(Y) = \Delta Z\,[E^{Z+1}(Y) - E^Z(Y)]$.

The empirically determined quantity ΔZ is called the effective incremental charge and accounts for the change in binding energy of an electron in shell Y of an atom Z ionized in shell X.

2.5.3 The Auger Spectrometer

A). Ionizing Sources

The most common source of ionizing radiation used in AES is electron gun producing an electron beam, which can be focused onto the sample surface. The thermal electrons are produced by heating the W filament at high temperatures. These electrons exhibit Maxwell energy distribution with a FWHM given by

$$\Delta E_K\,(eV) = 2.2 \times 10^{-4}\,T\,(K^{-1}) \tag{2.5.5}$$

In practice the energy resolution for thermal electron gun is about 0.3 - 0.6 eV which is quite satisfactory for AES. The electron coming out from thermionic cathode is then accelerated and focus by the applied electric fields. The production of a core hole can also be initiated by x-ray bombardment, which leads to Auger emission.

B). Electron Energy Analyzers

One of the first types of electron spectroscopy was the retarding-field analyzer which is simply a wire grid placed between the sample and the detector. The potential on the grid is varied from zero volts negatively to the primary energy of the beam. As the potential is scanned, only electrons with sufficient energy can overcome the retarding voltage and reach the detector. The response of an retarding-field analyzer actually yields the current I measured by the electron collector with:

$$I(E_0) = \int_{E_0}^{\infty} N(E)\, dE \tag{2.5.6}$$

To get the standard Auger electron spectrum, the second derivative d^2I/dE^2 is always used by synchronously detecting the collector current at the second harmonic of the modulating frequency. In other words, the first-derivative Auger spectrum $dN(E)/dE$ is obtained by modulating at a frequency ω and detecting at its second harmonic 2ω.

Most common designs for retarding field analyzers use spherical grids to form the concentric hemispheres. The resolution is given by [32]

$$\frac{\Delta E}{E} = 2ab^{-1}\sin^2\theta \tag{2.5.7}$$

where θ is the largest angle the entering beam can make with the symmetry axis of the spheres and still be collected; a and b are the radii of the inner and outer hemispheres.

The most popular analyzer for Auger electron spectroscopy is cylindrical-mirror electron energy analyzer (CMA). A typical CMA consists of two co-axial metal cylinders, the inner one of which is grounded and connected electrically to the sample. A negative potential is applied to the outer cylinder. As this voltage is increased, successive energy windows of the beam are brought into focus at the exit slit. The details on the designs of electron energy analyzer can be found from the references [33].

C). Detection

For the retarding-field analyzers, usually a Faraday cup or the screen is used to record the current arrived. To get better sensitivity, most Auger electron spectrometers use electron multiplier for detection. In principle, after secondary electrons collide with the surface of the electron multiplier more secondary electrons are released, until after about 10^{20} collisions there are enough electrons to produce a measurable current in an amplifier. The electron multiplier can be operated in *dc* or *ac* modes. In the dc mode the dynode multiplier acts as a current amplifier, while in the ac mode the channel electron multiplier provides single-electron counting. The channel electron multiplier is a continuous dynode consisting of a tube of semiconducting glass, the inner surface of which has been processed to give it a high secondary-electron-emission coefficient. The resistance of this multiplier is $\simeq 10^9\Omega$ and the gain $\simeq 10^8$. Generally, above the limit of 150,000 counts per second the channeltron saturates, resulting in peak distortion and resolution loss.

D). The Scanning Auger System

By scanning the electron beam over the specimen surface, the strength of a particular Auger transition can be monitored and displayed as a two-dimension Auger map. If an ion beam is used to etch away the sample, a three-dimensional Auger analysis or depth-profile can be obtained.

2.6. Angle-resolved Photoemission

Angle-resolved photoemission is one of the most powerful technique used to study surface electronic structures as well as geometric structures. The technique not only determines the orientation of the adsorbed molecules, but also their location relative to the substrate crystal lattice [34].

2.6.1 The Photoexcitation Process

An electron excited by electromagnetic radiation may escape from the solid if it has sufficient kinetic energy to overcome the work function barrier. This photoelectric effect was well explained by Einstein in 1905. If the sample is irradiated with monochromatic photon of frequency ν, the energetics of the process are defined by the Einstein relation,

$$K.E. = h\nu - \phi - E_i \tag{2.6.1}$$

where E_i is the initial energy below the Fermi level [35].

Before photoexcited electron reaches the surface, it may suffer various scattering. A quasi-elastic scattering by phonons may influence the direction of outgoing electron and reduce the electron energy by a few meV. With a substantial loss of energy the electron may go through a inelastic scattering by the creation of electron-hole pairs or the generation of a collective electron, or plasmon, oscillation. The mean free path for inelastic scattering of electrons depends strongly on the electron energy. In fact, electrons with kinetic energies in the range 10-1000 eV above the Fermi level are scattered very strongly in solids and those emerged must originate very close to the surfaces [36]. This is why photoemission is a useful probe for studying surfaces of a solid. The high speed of photoemission process is another advantage for simple treatment. Because the typical transition times between electronic states and the escape time of photoelectrons are comparable (about 10^{-15} second), the atoms in a molecule or solid do not have time to rearrange themselves and change the electronic states during the photoemission process [37].

In interpreting the available experimental data the three-step model was widely used because of its simplicity and success [38]. This model divides photoemission complex into three distinct process which are (1) optical excitation; (2) transportation of excited electron to the surfaces; (3) transmission of photoelectron through the surfaces. Despite the successful prediction of the location of some individual photoemission peaks the discrepancies began to appear when the three-steps model is used to predict either the intensity or the shape of the photoemission features.

The most common photoemission technique is the measurement of an energy distribution curves (EDC) of the photoemitted electrons at a particular photon energy. At the region of below 40 eV photon energy, the EDC are dominated by the joint density of initial and final states. Above this energy the EDC reflects more closely the local density of states modified by matrix element effects. The tunability of synchrotron radiation makes two other techniques such as constant final-state (CFS) spectroscopy and constant initial-state (CIS) spectroscopy possible. In CFS mode photoelectron with a fixed kinetic energy are detected while the photon energy is scanned. Hence the transitions between core levels and unfilled states are probed. In CIS mode both the incident photon energy and the spectrometer window energy (kinetic energy) are synchronously scanned to keep the density of initial states for a given occupied level constant. Using CIS technique one is able to obtain information on the density of the unoccupied states above the Fermi level. However the energy dependence and different weighting of the matrix elements will complicate the analysis.

The energy dependence of the photoionization cross section and the electron escape depth make photoemission a surface sensitive technique. The fact that photoelectrons leave a single crystal in preferred directions makes angle-resolved photoelectron spectroscopy a versatile tool for determination of two- and three-dimensional energy-band dispersion for surfaces, adsorbates and bulk solids.

2.6.2 Photoionization Cross-section

The cross section for the photoionization process is the most important factor in determining the emission intensity in the photoemission process.

A). The Golden Rule

According to a first-principles theory of photoemission in a single-step model, the differential cross section for the photoelectron emission is given by so called golden rule expression:

$$\frac{d\sigma}{d\Omega} \propto \sum_i \left[\langle \Psi_f \mid \vec{p}\cdot\vec{A} + \vec{A}\cdot\vec{p} \mid \Psi_i \rangle\right]^2 \delta\left(E_f - E_i - h\nu\right)\delta\left(\vec{k}_f - \vec{k}_i - \vec{G}\right) \qquad (2.6.2)$$

The wave function Ψ_f describes an electron state which contains an outgoing plane wave with the energy E_f and wave vector k_f of the photoelectron, and is often referred to as a time-reversed LEED function. In principle both Ψ_f and Ψ_i can be calculated with the scattering techniques developed for LEED.

B). The Transition Matrix Element

In one-electron approximation the optical transition matrix element for photoemission can be written as

$$M_{fi} = \frac{e}{2mc}\langle \Psi_f \mid \vec{A}\cdot\vec{p} + \vec{p}\cdot\vec{A} \mid \Psi_i\rangle = \frac{e}{mc}\langle \Psi_f \mid \vec{A}\cdot\vec{p} \mid \Psi_i\rangle - \frac{ie\hbar}{2mc}\langle \Psi_f \mid \nabla\cdot\vec{A} \mid \Psi_i\rangle. \quad (2.6.3)$$

The spatial dependence of $\vec{A}$ in the direction perpendicular to the surface may be rapidly changing near the surface. In the dipole approximation the effective potential with a bulk component V_B and a surface component V_S can be introduced to simplify the matrix element.

$$M_{fi} = \frac{-ie}{2\omega mc}[\langle \Psi_f \mid \vec{A}\cdot\nabla V_B \mid \Psi_i\rangle + \langle \Psi_f \mid \vec{A}\cdot\nabla V_S \mid \Psi_i\rangle] - \frac{ie\hbar}{4mc}\langle \Psi_f \mid \frac{\partial A_z}{\partial z} \mid \Psi_i\rangle \quad (2.6.4)$$

where V_S and V_B are surface barrier and bulk potential respectively. It is clear that the intensity and angular dependence of the emission of photoelectrons from a solid is strongly governed by lattice symmetry and electron wavefunction symmetry.

C). Symmetry and Polarization Selection Rules

The angular dependence of the cross section can be used to determine adsorbate geometry. Hermanson [39] has shown that if the detector lies in a mirror plane of the system then only final states which are even under reflection contribute to the photoemission. Because odd states will have no amplitude in the mirror plane. Therefore the product of initial, dipole, and final state in Eq. (2.6.3) must be even under reflection. With a knowledge of the symmetry of the dipole component and the final state, the reflection symmetry of the initial state can be determined.

In the optical transition matrix element the $\vec{A}\cdot\vec{p}$ is the dipole operator. The correct interpretation of angle-resolved photoemission data involves a direct transition between electronic states of distinct symmetries. When a polarized excitation source like synchrotron radiation is used dipole selection rules have to be taken into consideration. The matrix element in general is invariant under all symmetry operations. If the photoelectron is collected in a mirror plane containing the sample surface normal, only the even symmetry final state wavefunction can be detected by the electron energy analyzer [40]. Therefore, for an allowed transition, the direct product of the dipole operator and the initial state must be even. The dipole operator $\vec{A}\cdot\vec{p}$ is even (odd) if the electromagnetic field vector $\vec{A}$ is parallel (perpendicular) to the collection mirror plane. Thus only even (odd) initial states can be detected for $\vec{A}$ parallel (perpendicular) to the collection mirror plane. For the normal

emission angle-resolved photoemission, s-polarized light ($\vec{A}$ lies perpendicular to the plane of incidence) $\vec{A} \cdot \vec{p}$ in the matrix element has odd parity so that optical transitions from odd initial states only are allowed. For the p-polarized light ($\vec{A}$ lies parallel to the plane of incidence) $\vec{A} \cdot \vec{p}$ is even and transitions from even initial states only are allowed.

To demonstrate polarization effects, let us consider the case of CO chemisorbed on late transition-metals. It is well known that at room temperatures CO bonds linearly to the surface with the carbon atom down on the metal substrate. bonding between the molecular 5σ orbital and the unoccupied metallic d orbitals is compensated for by back-donation electrons from the occupied $d-$ orbitals to the unoccupied molecular $2\pi^*$ levels. With the polarized photon source, one will be able to distinguish bonding geometry by making use of symmetry rules. Fig. 8 (a) shows the polar distribution of differential cross section for oriented CO at photon energy 21 eV and 41 eV calculated by Davenport [41]. This suggests that normal emission from the 4σ level of CO on late transition-metals should vanish for *s*-polarized light if the molecule is vertical.

The symmetry of the orbitals and the orientation of the adsorbate molecules can be determined by either polarization-dependent or energy-dependent photoelectron spectroscopy. The transition probability has a maximum when the electric field vector is parallel to the bond between adsorbate and substrate atoms. The SW-Xα calculation was performed by Davenport [42] to describe the qualitative behavior of the photoionization cross section as a function of incident photon energy. It is shown that, for diatomic molecules, the 4σ level exhibits a characteristic molecular "shape resonance" in the photoionization cross section at about 35 eV photon energy. Fig. 8 (b) illustrates this technique for *p*- polarized incident light with a normal orientation of CO on the surface and a CO molecule oriented parallel to the surface. Furthermore, these symmetry properties of electronic excitation from σ and π initial states to the σ "shape resonance" have been exploited, just as in the ARUPS, in the near-edge x-ray-absorption fine-structure (NEXAFS) spectra to determine the molecular orientation on the surface. Such NEXAFS spectra exhibits a strong polarization dependence because the resonance peak intensities are governed by $\sigma \rightarrow \pi$ or $\sigma \rightarrow \sigma$ dipole transitions. Stohr and Jaeger [43] have studied the NEXAFS for CO, NO, and N_2 on Ni(100) using a synchrotron radiation light source. They showed that the $K-$edge fine structure is dominated by intramolecular resonances which arise from a sharp bound-state transition to an unoccupied $2\pi^*$ orbital and a broader σ shape resonance in the continuum. Since the final-state molecular orbitals are of pure symmetry and the resonance peak ride

(a).

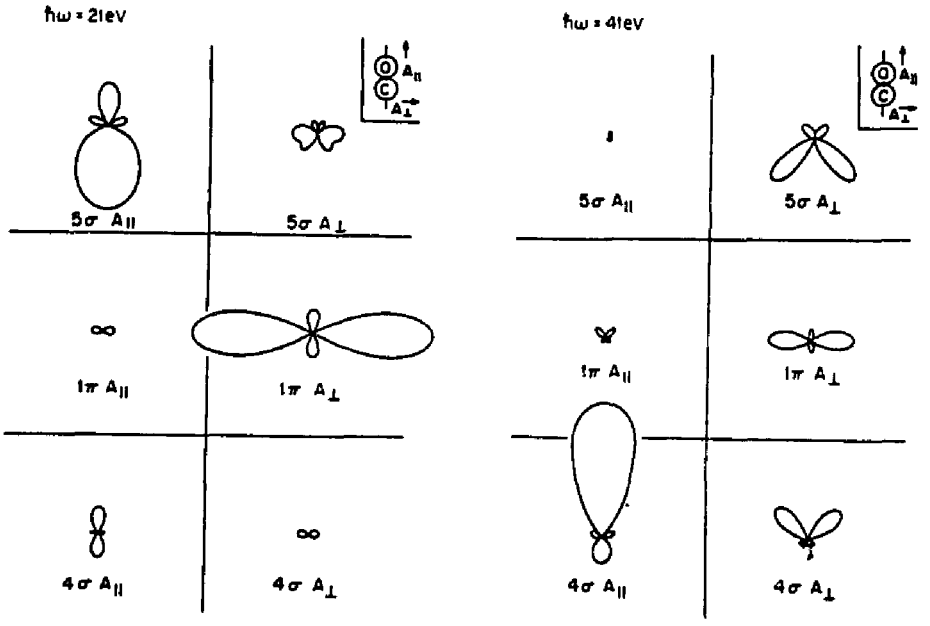

(b).

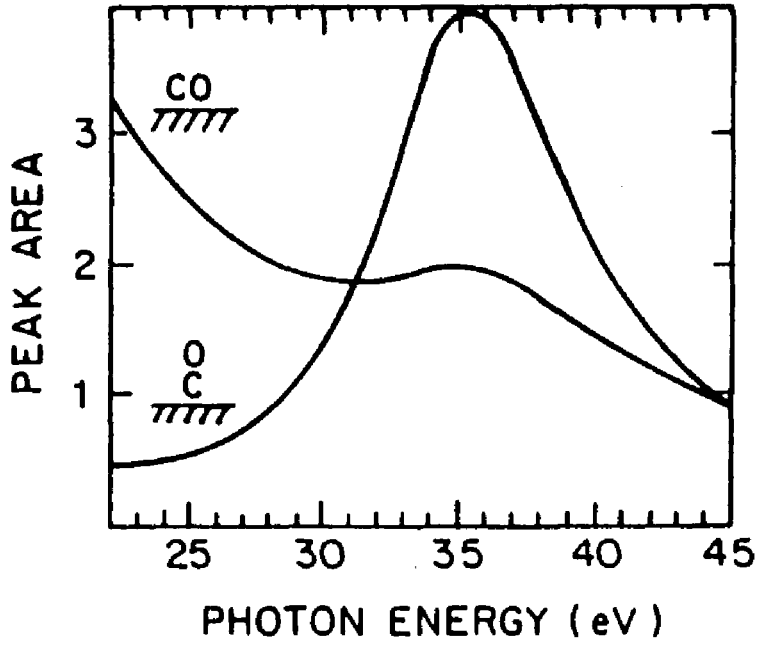

Figure 8: (a) Polar distribution of differential cross section for oriented CO with photon energy 21 eV and 41 eV. (b) calculated curves of the 4σ cross section for different orientation of CO molecule on metal surfaces.

on a structureless background, the intensity variation of the absorption peak as a function of the electric field vector orientation is a sensitive measure of the molecular orientation on the surfaces.

2.6.3 Energy Band Structure

From the Golden rule expression there are two conservation laws for the photoemission process. The energy conservation law requires that the optical transitions be confined to a surface in $\vec{k}$ space,

$$E_f\left(\vec{k}\right) = E_i\left(\vec{k}\right) + h\nu \tag{2.6.5}$$

The momentum conservation law requires a direct or phonon-assisted transitions in reduced-zone scheme,

$$\vec{k}_f = \vec{k}_i + \vec{G} \tag{2.6.6}$$

Let wavevector $\vec{K}$ be outside the solid and $\vec{k}$ be inside the solid. The Einsten relation can be written as more explicit form.

$$K.E. = h\nu - \Phi - E_i = \frac{\hbar^2}{2m}\left(K^{\parallel 2} + K^{\perp 2}\right) \tag{2.6.7}$$

Since the wavevector parallel to the surface of emission is conserved, with an assumption of infinitely long periodic surface $K^{\parallel}$ is given by

$$K^{\parallel} = k^{\parallel} + G^{\parallel} \tag{2.6.8}$$

However, $K^{\perp} = k^{\perp} + G^{\perp}$ is indetermined because of the breaking down of periodicity in vertical direction. This uncertainty in $K^{\perp}$ will bring in a momentum broadening effect in photoemission.

The photoemission process involves creation of electron-hole pairs due to the coupling of the photon field with the solid. The photoelectron also undergo various scattering process such as electron-electron, electron-phonon and electron-impurity scatterings. These scattering processes limit the lifetimes of electron and hole states. Both the electron and hole lifetime effects broaden structure in the energy distribution of the photoemission.

A). Energy band angular dispersion

The energy band angular dispersion $E_i\left(k^{\parallel}\right)$ relation can be converted from kinetic energies E_{kin} and the angle of emission for the states in a straightforward manner using the conservation of energy and momentum equations. Assuming $g^{\parallel} = 0$ the momentum is given by a simple projection:

$$k^{\parallel} = \sin\theta \frac{\sqrt{2m_e E_{kin}}}{\hbar} \tag{2.6.9}$$

From theoretical study and the symmetric behavior of the energy band dispersion relation the character of electronic states can be determined.

B). Adsorbate states

For a physisorbed overlayer the adsorbate-substrate interaction via Van der Waals force is very weak. Examples of such studies are noble gas condensation and some reactive gas condensation at low temperature.

For stronger interacting chemisorption the adsorbate molecule may even break down and dissociate on the substrate surface. In this case the adsorbate bands can lose their two-dimensional character at $k^{\parallel}$ points where coincide in energy with three-dimensional substrate bands. The dissociated chemisorption lead to an atomic adsorption and can be characterized by photoemission spectra with no resemblance to that of the gas phase spectrum. CO and H_2 chemisorption on early transition-metals at room temperature are good examples.

When the adsorbate-substrate interaction is not strong enough to break down the adsorbate molecule, a molecular chemisorption can occur. The characteristic of the photoemission shows only a slight perturbation from that of gas phase spectrum.

C). Surface states

Near the surface the remain periodicity is only towards infinity inside the crystal which results in a modification of bulk state. The surface resonance states can be formed by combining the periodic wave function with the decaying functions. These surface resonances and surface states can be distinguished experimentally from the bulk states for their uncertainty on the momentum perpendicular to the surface, and no interest with bulk Block functions of same E, $k^{\parallel}$ and same symmetry. Following three tests are often used to determine the surface states:

1). The surface state energy $E(k^{\parallel})$ must fall in a gap in the projected band structure.

2). No dispersion on the surface state energy with variable excitation source incident energy.

3). The surface states must be drastically affected by vacuum contamination.

It should be pointed out that the surface resonance state may localized outside the bulk band gaps. The characteristic of surface states depends on their localization near the surface and the strength of the crystal potential. The *d*-like surface states in transition-metals have atomic-like wave functions localized essentially on surface atoms. On the other hand, *sp*-like surface states are determined by the boundary conditions at the surface where Bloch-like decaying functions containing a real and imaginary part of $k^{\perp}$ are matched.

D). Bulk energy bands

The lack of simple conservation law for the third momentum quantum number $k^{\perp}$ complicates the data analysis of three-dimensional bulk energy band. However, with a tunable excitational source it is possible to estimate the full band dispersion $E\left(k^{\perp}\right)$ from the angle-resolved photoemission and k-resolved inverse photoemission data.

The simplest approximation for a direct determination of three-dimensional energy bands is assuming that the final state is a parabolic free-electron-like band in a constant inner potential V_0:

$$E_f\left(\vec{k}_f\right) = \frac{\hbar^2 \vec{k}_f^2}{2m} - V_0 \ . \tag{2.6.10}$$

If one knows the final state band dispersion $E_f\left(k_f^{\perp}\right)$ from photoemission data to some degree, the initial state band dispersion $E_i\left(k_i^{\perp}\right)$ can be derived. By inverting the relation $E_f\left(k_f^{\perp}\right)$, one obtains $k_f^{\perp}$ and $k_i^{\perp}$ from the energy E_{kin} measured in detector:

$$\begin{aligned} k_i^{\perp} &= k_f^{\perp} \\ &= \hbar^{-1}\sqrt{2m\left(E_{kin}+V_0\right) - \hbar^2 k^{\parallel 2}} \\ &= 0.51\text{Å}^{-1}\sqrt{\left(E_{kin}+V_0\right)/eV - 3.81\text{Å}^2 k^{\parallel 2}} \ . \end{aligned} \tag{2.6.11}$$

This equation essentially describes the refraction of the outgoing photoelectron when it crosses the potential step V_0 at the surface.

2.6.4 Experimental Set-up

A fundamental experimental set-up for the angle-resolved photoemission includes a photon source for photoelectrons excitation, angle-resolved electron energy detector and a UHV chamber for accommodation.

A). Photon Sources

As a conventional photoemission investigation, one may employ either VUV radiation produced by an electrical discharge in a gas, or soft x-ray generated by electron bombardment of various materials. For the photoemission near the threshold of most materials, xenon or deuterium lamp with quartz windows, monochromator, polarizers should suffice. For the photon energies at 6.5-11.0 eV region hydrogen discharge lamps with a vacuum monochromator and lithium fluoride windows will be satisfactory. For the photon energies between 12.0 eV to the soft x-ray region conventional window materials have been substituted by a differentially pumping technique. This technique combines a small orifice, through which the light enters the working chamber, and differential pumping enables a

pressure of several Torr to be maintained in the lamp whilst the photoelectron spectrometer is maintained in ultra-high vacuum. These gas discharge lamps give rise to strong emission at fixed wavelengths. For example, the helium discharge lamp have HeI and HeII spectral line at photon energies 21.2 eV and 40.8 eV respectively. The HeI spectral line is due to the $2p$ to $1s$ transition of excited helium atoms and is always stronger than HeII. Besides using a suitable monochromator to separate the two lines, reducing the helium gas pressure in discharge chamber can effectively increasing the HeII spectral line intensity. A high intensity discharge lamp for monochromatized UV angle-resolved photoemission spectroscopy has been designed by Shevchik [44]. It has been estimated that the intensity of the line at 26.9 eV can reach a light intensity of $10^{10} - 10^{11}$ photon/second striking the sample.

The most commonly used x-ray in photoemission are the Al $K\alpha$ ($h\nu = 1487$ eV) and Mg $K\alpha$ ($h\nu = 1254$ eV) lines emitted by aluminium or magnesium when the metals are bombarded with high energy electrons. Since no gas has been used in x-ray tube the whole instrument can be installed in ultra-high vacuum.

The most powerful photon source covering the whole range from the visible to the x-ray region is the synchrotron radiation light source. It will be described in detail in the next section.

B). Angle-resolved Electron Energy Detector

A standard electron spectrometer usually is mounted on a goniometer to detect escape directions covering a solid angle of up to 2π and restrict their angular acceptance to 2° to 10° full angle by introducing extra apertures. The most commonly used angle-resolved spectrometer is the hemispherical deflection analyzer in which two-dimensional, point-to-point focusing occurs after 180° deflection in the field between two concentric hemispheres. Electrons enter near the center of the gap defined by a slit, an aperture or an electron optical image from a lens and exit after 180° deflection. With the analyzer set up to pass energy E_{pass} along a circular path of radius $R_p = (R_{in} + R_{out})/2$, the potential on the outer hemisphere is $V_{out} = E_{pass}[3 - 2(R_p/R_{in})]$ while that on the inner hemisphere is $V_{in} = E_{pass}[3 - 2(R_p/R_{out})]$. Like most of other types of spectrometer, it is necessary to terminate the field at the entrance and exit by appropriate electrodes. In contrast to the traditional designs, Liouville suggested that the source size can be increased by decreasing the the angular acceptance since the product of cross section, angular divergence and kinetic energy remains constant over an electron beam trajectory. In principle one can gain energy resolution with smaller angular acceptance by a retarding 1:1 lens. In other words, because

the resolving power $E_{pass}/\Delta E$ is a constant determined by the geometry of the spectrometer a smaller energy resolution interval ΔE can be achieved with a lower pass energy E_{pass}.

Simultaneous detection for a large solid angle of emission direction on to a position-sensitive detector provide a virtually direct picture of angular distribution of photoelectron and greatly improves the speed of measurement. Eastman and his co-workers [45] have designed and constructed a very sophisticated elliptical-mirror-display-analyzer. A relatively simple design of parallel-detection system using vidicon-camera for angle-resolved electron spectroscopy was presented by Weeks *et al.* [46]. This detector can obtain energy spectra over a $70° \times 70°$ collection geometry with $\pm 1.5°$ resolution in 30-40 min, or collect the intensities of all visible LEED beams in a few seconds.

C). Data Acquisition and Analysis

For the CMA or hemispherical electron energy analyzer, a pulse signal can be detected at the end of channeltron during photoemission process. Filtered by a band-pass electronic discriminator to reduce the noise the pulse signal then is sent to the electronic counter for pulse counting. The counting rate at fixed photon energy can either be sent to the plotter as analog output or store in computer as digital output. The data analyses, such as spectra stacking, normalizing, fitting, smoothing, subtracting, background subtracting, peak height or peak area counting, can be carried out by either the personal computer or VAX cluster at Applied Mathematics Department, Brookhaven National Laboratory.

2.7. Synchrotron Radiation Photoemission

2.7.1 Introduction

Synchrotron radiation is electromagnetic radiation emitted by charged particles moving on circular orbits with highly relativistic velocities. The mechanism of synchrotron radiation is comparable to that of an oscillating dipole which one obtained when projecting the circular orbit sideways. However the radiation intensity is not confined to the fundamental frequency of revolution but due to the $\delta-$ function such as concentration of charge at the particle and due to the relativistic velocities harmonics contribute up to very high order. The individual harmonic lines are smeared out thus leading to a continuous spectrum ranging from the visible through the vacuum-ultraviolet, soft x-ray and far into the x-ray region. The outstanding properties of synchrotron radiation includes [47]:

a) Continuous spectrum from the infrared to the x-ray region.

b) High intensity of photon flux.

c) Collimation of the emitted radiation in the instantaneous direction of flight of the emitting particles.

d) Linear polarization with the electric vector parallel to the plane of the orbits.

e) Circular polarization above and below the plane of the orbit.

f) Time structure with pulse lengths down to 100 ps.

g) High-vacuum environment.

2.7.2 Storage Rings

The basic element of the synchrotron radiation source is an electron storage ring which consists of an array of bending magnets that make the electron travel in circular arcs producing synchrotron radiation [48]. In fact there are many other elements required to make an operational storage ring, such as quadrupole magnets to provide focusing forces that keep the electron-beam transverse dimensions small, sextuple magnets that compensate for certain effects due to the energy spread in the electron beam, beam position monitors and steering coils used to correct deviations from the design orbit, and a computer control system. In order to store the electron beam for a longer time, the average pressure must be in the 10^{-9} Torr to minimize encounters between stored electrons and the residual gas. It is quite straightforward to achieve a base pressure in the $10^{-9} - 10^{-10}$ Torr range even in such large system as storage rings. However, in the presence of 100 kW or more of synchrotron radiation the gas desorption is large, and determines the average pressure and

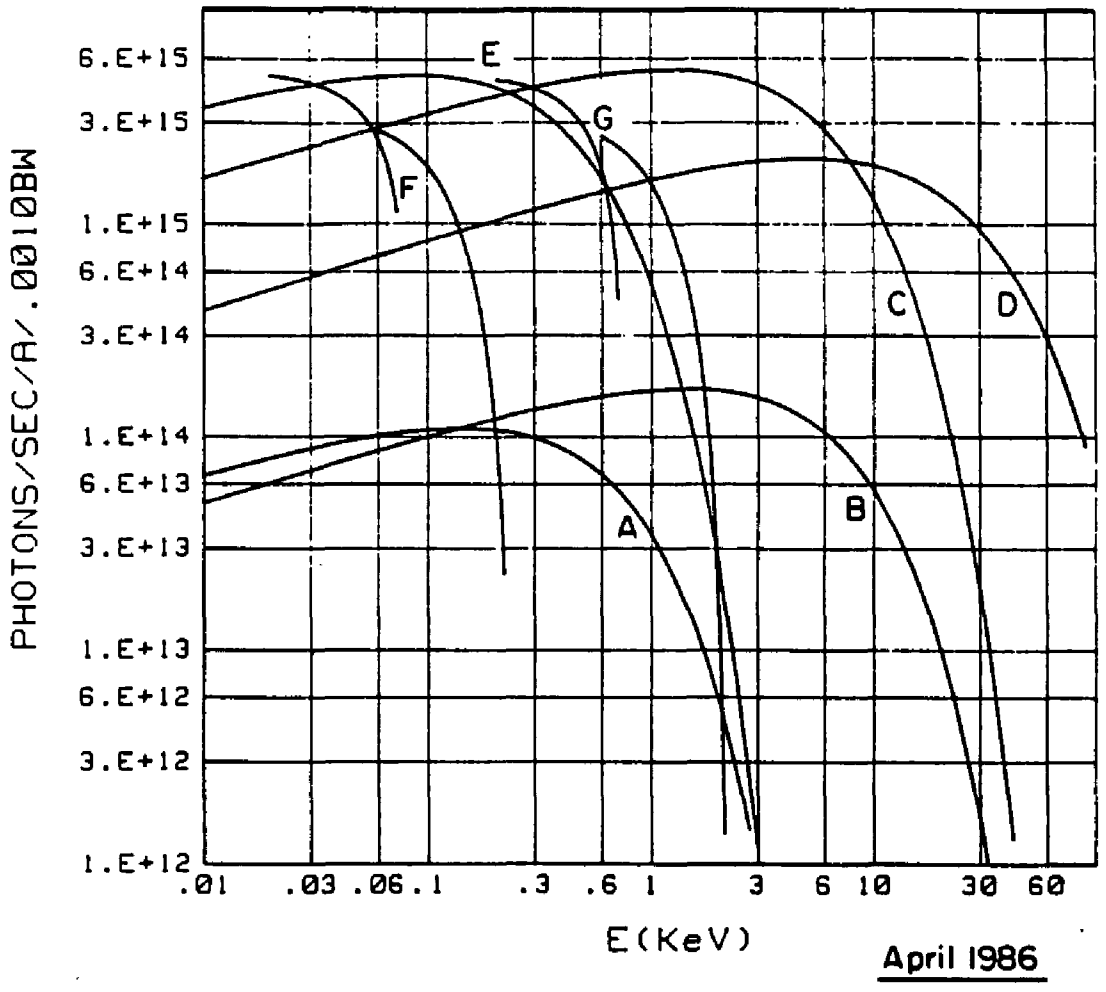

A	VUV Bend	65 horizontal milliradians
B	X-ray Bend	3 horizontal milliradians
C	X25	3 horizontal milliradians (= 1.2 K/γ)
D	X17	5 horizontal milliradians
E	U13TOK	65 horizontal milliradians (= 1.2 K/γ)
F	U5U	Undulator 1st, 3rd harmonics K = 0.5 - 2.5
G	X1	Undulator 1st, 3rd harmonics K = 0.3 - 2.3

Figure 9: Synchrotron radiation spectrum region from NSLS VUV ring.

VUV Storage Ring Parameters (as of April 1986)

Parameters	VUV Storage Ring
Normal Operating Energy	0.750 GeV
Design Current (multibunch operation)	1.0 A (1.1×10^{12} e^-)
Circumference	51.0 meters
Number of Beam Ports on Dipoles	17
Number of Insertion Devices	2
Maximum Length of Insertion Devices	< 3.26 meters
$\lambda_c(E_c)$	25.3 Å (486 eV)
$B(\rho)$	1.28 Tesla (1.91 meters)
Electron Orbital Period	170.2 nanoseconds
Damping Times	$\tau_x \approx \tau_y \approx 17$ msec; $\tau_\varepsilon \approx 9$ msec
Touschek lifetime dependent on current/bunch and vertical emittance	
Lattice Structure (Chasman-Green)	Separated Function, Quad, Doublets
Number of Superperiods	4
Magnet Complement	8 Bending (1.5 meters each) 24 Quadrupole (0.3 meters each) 12 Sextupole (0.2 meters each)
Nominal Tunes ν_x, ν_y	3.12, 1.17
Momentum Compaction	0.023
R.F. Frequency	52.88 MHz
Radiated Power	14.7 kW/Amp. of Beam
R.F. Peak Voltage	100 kV
Design R.F. Power	50 kW
ν_s (synchrotron tune)	0.0022
Natural Energy Spread, (σ_ε/E)	4.5×10^{-4}
Natural Bunch Length (2σ)	7.6 cm (I < 20 mA)
Horizontal Damped Emittance, ε_x	1.5×10^{-7} meter-radian
Vertical Damped Emittance, ε_y	$\geq 2.8 \times 10^{-10}$ meter-radian (adjust.)
Power per Horizontal milliradian, 1A	2.3 watts
Source Size: σ_h, σ_v	0.5 mm, > 0.06 mm

Source of Data: NSLS Parameters, January 1983, compiled by A. van Steenbergen; updated values provided by NSLS staff members.

Table 1: Parameters of VUV storage ring at NSLS.

lifetime of a stored beam. To minimize gas loads due to photon desorption, special care must be taken in the fabrication, assembly, cleaning, baking, and installation of storage ring vacuum components. In the National Synchrotron Light Source, the electron currents in the 700 MeV electron storage ring can reach to 1 Amp within several minutes and with a typical electron beam life times of several hours. Table 1 lists the parameters for VUV storage ring at NSLS. The spectrum region for synchrotron radiation is shown in Fig. 9.

2.7.3 Monochromators

Most experiments with synchrotron radiation select a particular wavelength from the continuum and often scan over a range of wavelengths. A tunable monochromator becomes very important. For the hard x-ray regions a crystal monochromator is used. In VUV regions three main classes of photon energy band-pass filter are the constant deviation Rowland circle types, the plane grating types (PGM) and the toroidal grating monochromator (TGM). In below 50 eV VUV region, a normal incident Rowland circle type grating is suitable for its good resolution. This type of monochromator is widely used in inverse photoemission experiment which will be described in detail in k-resolved inverse photoemission section. As a monochromator for synchrotron radiation work, the Rowland designs are unsatisfactory in various ways, such as fixed in and out directions and rejection of higher diffracted orders, and their good resolution properties can be matched by PGM operating in a grazing incident scheme with modern dedicated storage ring light source.

The general information and theoretical basis of the plane grating monochromator (PGM) for use with synchrotron radiation has been well reviewed and discussed by Howells [49]. A standard PGM requires three reflections and the source is effectively the entrance slit so that its size and distance from the instrument determine its resolution. The wavelength range of PGM can be about 10−1000 Å and its scan can be achieved by a simple mechanism.

The monochromator installed in U7 beamline is a grazing incidence plane grating monochromator (PGM) which consists of two 600 groove/mm ion etched gratings, four focusing mirrors and one parabolic collimating mirror. The vacuum vessel and internal components are designed to operate in the 10^{-10} Torr pressure range. The resolution of PGM is limited by its efficiency or throughput. Concave gratings have the great advantage that collimation, dispersion and focussing are all effectively carried out by one device with only one reflection. This important quantity can be compromised by the toroidal grating monochromator (TGM). A toroidal grating relies on approximate focussing and is perhaps the simplest form of grazing incidence monochromator. A typical TGM have the advantages

of high flux, mechanical simplicity, and low cost. The detail information on the design and the alignment of TGM can be found from the reference [50].

2.8. K-resolved Inverse Photoemission

2.8.1 Introduction

K-resolved ultraviolet inverse photoemission spectroscopy is a newly developed technique for the study of the unoccupied electronic states above the Fermi level. Inverse photoemission consists of transferring an electron from an initial state above the vacuum level into a final empty state above the Fermi level via an optical transition. Fig. 10 compares the process of inverse photoemission with that of photoemission on Cu(001) case. From Fig. 10 part (a), we found that the inverse photoemission is not really the time reversed process of photoemission. The initial state of photoemission is a neutral atom and a photon while the final state of inverse photoemission is a negative ion and a photon; the final state of photoemission is a positive ion and a electron while the initial state of inverse photoemission is a neutral atom and an electron. The net effects can be reflected by the difference in excitation cross sections. Using the same arguments from which the cross section for photoemission transition is derived, we can write the cross section for inverse photoemission as

$$\frac{d\sigma}{d\Omega} \propto \sum_i \left[\langle \Psi_f \mid \vec{p}\cdot\vec{A} + \vec{A}\cdot\vec{p} \mid \Psi_i \rangle\right]^2 \delta\left(E_f - E_i - h\nu\right)\delta\left(\vec{k}_f - \vec{k}_i\right) \qquad (2.8.1)$$

with both the initial and final state above the Fermi level. Johnson and Davenport have applied the quantum-theoretical treatment to calculate the cross section for emission of photons produced in inverse photoemission from an adsorbed molecule [51]. With some approximation, such as the neglect of the difference in the matrix elements of two processes, a simple formula can be derived to relate the cross section for photoemission and inverse photoemission. They showed that the ratio of the inverse photoemission cross section to the photoemission cross section in the UV energy range can be simplified as

$$\frac{(\partial\sigma/\partial\Omega)_{IPE}}{(\partial\sigma/\partial\Omega)_{UPS}} \approx \frac{\omega^2}{c^2\,\vec{k}^2} = \frac{\vec{q}^2}{\vec{k}^2} = \left(\frac{\lambda_e}{\lambda_\gamma}\right)^2 \approx 10^{-5} \qquad (2.8.2)$$

where $\vec{q}$ is photon wave vector and $\vec{k}$ is the electron wave vector. This suggests a much smaller count rate for inverse photoemission which makes the experiment much more difficult than regular photoemission.

K-resolved inverse photoemission can be performed in several modes just as the angle-resolved synchrotron radiation photoemission. One can study the unoccupied electronic states by the energy-dependence and k-dependence excitations. Measurement of the radiated photon energy gives the energy separation of the initial and final states and can be

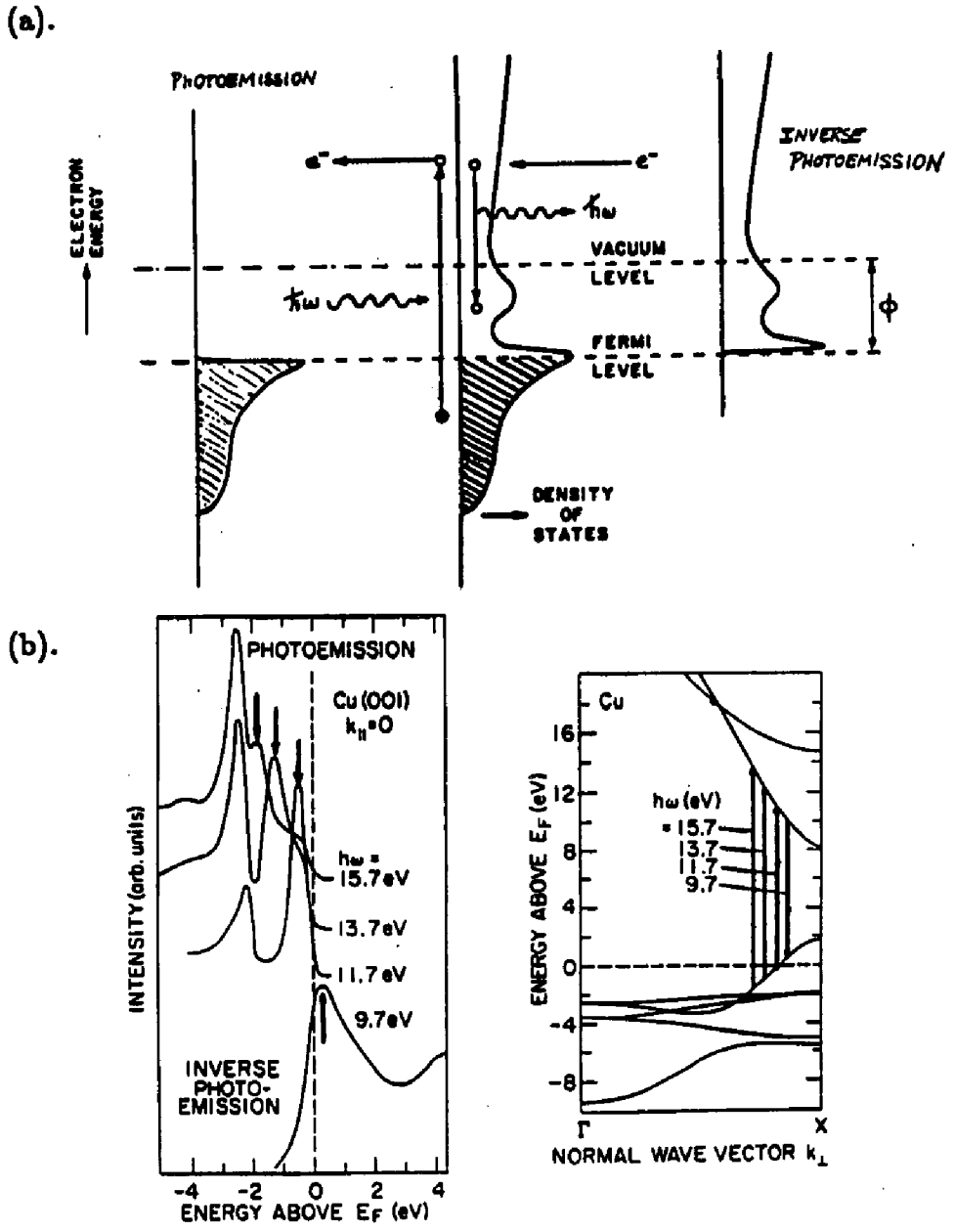

Figure 10: (a) A schematic representation of the relationship between the photoemission and inverse photoemission process. (b) The local electronic density of states and band structure of Cu(001) obtained by photoemission and inverse photoemission studies.

used to determine the unoccupied density of states. The experiment therefore requires the special electron gun and some forms of photon detector [52].

There are two kinds of photon detectors to date used for the inverse photoemission: the Geiger Muller counter with a fixed detected photon energy and tunable photon detectors. The use of Geiger Muller counter for inverse photoemission originated in the group of V. Dose, they combined a calcium fluoride (CaF_2) window backed by iodine vapor to detect a photon at energy of 9.7 eV with resolution of 0.7 eV. To improve the resolution, a strontium fluoride window can be used which alters the photon energy of detection from 9.7 eV to 9.5 eV and reduces the bandwidth to 0.4 eV. The other refinement to get a bandwidth to about 0.1 eV has been to replace the iodine by carbon disulfide while retaining the CaF_2 window. Their photon detection energy is 10.1 eV. The electron gun for these Geiger Muller counter type detector can be operated with a rather poorly focused electron beam. For k-resolved inverse photoemission a tunable photon detector must be used with a special electron gun which can operate at low energy and a high current output with a narrow transverse momentum spread.

2.8.2 Electron Gun

A low-energy high-brightness electron gun for k-resolved inverse photoemission was designed by Stoffel and Johnson [53]. The gun design consists of a diode extraction source and a three-element refocusing lens. The electron source is a 3 mm diameter planar BaO dispenser cathode placed at 1 mm behind the copper anode which contains a 0.2 mm radius aperture. The cathode is heated by an internal filament and produces a divergent beam at an energy equal to the anode potential V_a which is then decelerated to energy V_0 in the lens. The parameter which determine the maximum current I_{max} before space charge effects limiting the current increases is the maximum achievable perveance of an electron gun P_{max}, and

$$P_{max} = I_{max}/V_0^{3/2} \tag{2.8.3}$$

with a unit of $\mu perv$:

$$1\mu perv = 1\mu A/V^{3/2} \tag{2.8.4}$$

It can be shown that the perveance P_{max} is depends only on the geometry of electron gun and not the final beam energy V_0. The upper limit of perveance for a beam with full angular width θ is given by

$$P_{max}\,(\mu perv) = 38\,tan^2\,(\theta/2) \qquad (2.8.5)$$

2.8.3 Photon Detector

The simplest tunable photon detector is the refracting LiF-lens monochromator. The chromatic aberration in the lens will produce strong focusing of different wavelengths near the LiF transmission cutoff. Such devices have a tunable photon energy range of 8.0 eV to 11.5 eV with energy resolution about 0.3 eV to 0.4 eV.

The photon detector used for this thesis work is a normal incidence grating spectrometer to operate efficiently in the range of 10-30 eV with a bandwidth of the order of 150 meV at the longer wavelengths of detection. The schematic of the apparatus is shown in Fig. 4 The photon emitted from the sample surface are collected with a photon flux approximately 0.1 steradians by a holographically ruled diffraction grating which is blazed at 1000 Å with a ruling density of 1200 lines/mm. The diffracted photon is then focused onto a commercially available double chevron channel plate backed by a resistive anode encoder. To improve the efficiency in the energy range of interest the CsI has been coated onto the front surface of the chevron. For the present application only one dimension of the detector is used as the signals are integrated perpendicular to the plane of incidence. Signals from the two ends of the encoder pass through pre-amplifiers to a configuration of NIM modules which produce a ratio or position signal subsequently analysed by a LeCroy 3500 data acquisition system. The schematic drawing of the position sensitive detector is shown in Fig. 11. The spatial resolution of the encoder is approximately 0.4 mm which corresponds to a typical wavelength resolution of order of 5.0 Å in the present application. The local electric field has been provided to prevent both ions and stray ultraviolet light from entering the spectrometer chamber in order to minimize the background count rate and maintain spatial uniformity across the detector. Linearity of the detector is checked by sweeping the specularly reflected beam from the diffraction grating across the front surface of the chevron. Deviations of the order of 2% were found and corrected for near the end of the encoder. Photon detection efficiency as a function of energy was measured by monitoring the bremsstrahlung signal from the sample resulting from higher energy electron beams (40 to 80 eV). These were averaged for a number of different conditions to remove any crystallographic or band structure effects. Measured efficiency curves were then used to normalize the data.

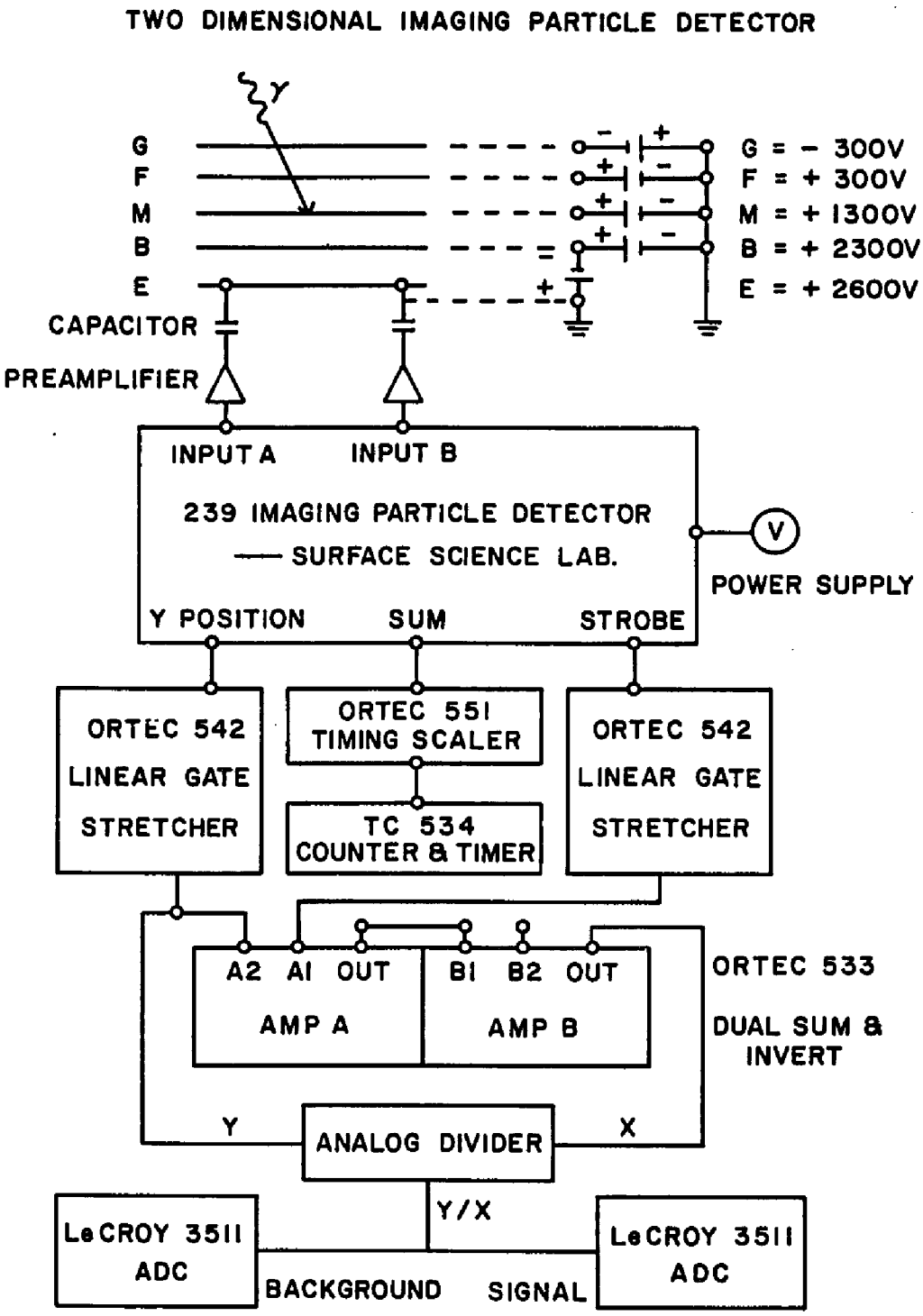

Figure 11: Schematic drawing of the electronic system for data acquisition from k-resolved inverse photoemission spectrometer in the Surface Physics Group, BNL.

2.9. Summary

The study of metal-film growth on crystalline substrates is a field undergoing rapid expansion. The interest is partly due to the recent availability of newly developed surface-sensitive techniques, such as the molecular-beam epitaxy, synchrotron radiation light source, and k-resolved inverse photoemission. Applications of the chemical and physical properties of modified metal surfaces and interfaces to electronic devices have a great impact in the semiconductor industries.

It is difficult to review and discuss in detailed all the techniques and principles used in this thesis work. Generally, synchrotron radiation angle-resolved photoemission has been used to study the occupied electronic state and chemical reactivity of transition metal overlayers. Its unique characters, such as energy-dependence, polarization-dependence, and angular-dependence electron spectroscopy, are best suited to the studies of the electronic structures, crystal structures, and adsorbate structures at the surfaces and the interfacial phenomena. K-resolved inverse photoemission, a synchrotron radiation photoemission type inverse photoelectron spectroscopy, has been used to investigate the unoccupied electronic states of transition metal overlayers and to map the energy-band of solids. Low energy electron diffraction (LEED) and Auger electron spectroscopy (AES) have been used to study the trend and epitaxy of transition-metal thin-film growth. With a combination of these newly developed surface-sensitive techniques, it is possible to obtain a better understanding of the physical and chemical properties of modified metal surfaces.

Chapter 3.
Electronic Structure and Chemical Activity of Selected Transition-Metals

3.1. Introduction

The electronic structure and chemical properties of transition-metals have been the subject of considerable interest during recent years. There is a large literature on the subjects of transition-metals and their compounds. Transition-metals and their compounds are very important because of their unique properties in magnetism, catalytic activity, metal-nonmetal transitions and superconductivity. To understand these macroscopic physical and chemical properties a knowledge of the electronic structure of this class of materials is a basic requirement. Since the transition-metals have an unfilled shells, such as the $3d$-, $4d$-, and $5d$- shells, the d- electronic states play a dominant role in its macroscopic properties.

In this chapter we present and discuss some of the electronic structure and chemical properties of the early and late transition-metals, such as Nb, Ta, Ni, Pd, and Pt. We will review the bulk geometric structure, and their relationship to reciprocal lattice space; we will discuss the electronic structure of the occupied and unoccupied states, the core level spectroscopy, and the energy-bands of Nb; and we will investigate CO and H_2 chemisorption on these metals.

It should be pointed out that studies of metal overlayers are built on the base of a good understanding of the electronic structures and chemical properties of these individual transition-metals. Some of the background work we present here will not only benefit the reader on what significant results we obtained but also be a good checking on our experimental techniques to make sure the consistent results can be obtained.

3.2. The Physical Properties of Transition-Metals

Physical Properties \ Materials	Nb	Ta	Ni	Pd	Pt
Outer Shell Electrons Configulations	$4d^4 5S$	$5d^3 6S^2$	$3d^9 4S^2$	$4d^{10}$	$5d^9 6S$
Most Close-packed Structures	b.c.c. (110)			f.c.c. (111)	
Lattice Constant (Å)	3.30	3.30	3.52	3.89	3.92
Interplane Distance (Å)	2.33	2.33	2.03	2.25	2.26
Monolayer Density (10^{15} atoms/cm^2)	1.3	1.3	1.9	1.5	1.5
Melting Point Temperature (^{0}C)	2415	2996	1455	1554	1769
Cohesive Energy (eV/atom)	7.57	8.10	4.44	3.89	5.84
Electronegativity (Pauling's)	1.6	1.5	1.8	2.2	2.2
Work Function (eV)	4.87	4.80	5.35	5.60	5.70
Conductivity (10^5/ohm-cm)	0.69	0.76	1.43	0.95	0.96
Superconductivity Transition Temp. (K)	9.50	4.50			

Table 2: The major physical properties of selected early and late transition-metals.

In Table 2, we list the major physical properties of Nb, Ta, Ni, Pd, and Pt transition-metals. Nb and Ta, so called early transition-metals or refractory metals, have very similar physical properties to each other. Their lattice constants, atomic radii, cohesive energies, electronegativities, conductivities, and work functions are almost the same. They are both bcc metals with a most close packed (110) surface structure. Nb and Ta are superconducting materials with high transition temperatures. The melting-point temperature of Nb and Ta are 2740°C and 3287°C, respectively, which makes it easy to clean recrystallized foil by resistive heating the sample to near the melting-point temperature. Ni, Pd, Pt are another group of metals which we often call the late transition-metals. They are all fcc metals with a (111) most close packed surface structures. Their melting-point temperatures and vaporization temperatures are much lower than the Nb and Ta melting-point temperatures. For the overlayer experiments of these metals on Nb or Ta substrate, one can simply flash

the sample to achieve a clean Nb(110) or Ta(110) surface for the next experiment. Thin films of these late transition-metals can be obtained by the thermo- evaporation. The trends from Ni to Pt are larger lattice constant and atomic radius, increasing melting-point temperatures and cohesive energies, and slightly increasing the work functions. Ni, Pd, and Pt are very important in industry for their unique properties on magnetism and catalytic activity.

3.3. Electronic Properties of Transition-Metals

Fig. 12 shows the orientation of the bulk fcc and bcc Brillouin zones with respect to the (100), (110), and (111) surface Brillouin zones. The Nb and Ta substrates used in this thesis work always have the bcc close-packed structure with a (110) surface orientation. The bcc (110) surface is the most close-packed and most stable bcc surface and is achieved by partially melting the polycrystalline foil to form a lowest surface energy state. Once the stable single crystal surface is formed the substrate can be annealed to high temperatures to clean the sample without changing the surface structure. The (110) face of a bcc crystal has C_{2v} symmetry. The two-dimensional band structure of Nb(110) and Ta(110) along the normal direction should be along ΓN. The *d*- electronic states in the ΓN direction can be classified as Σ_i states with $i = 1, 2, 3, 4$. It is noted that the Σ_1 state contains s, d_{z^2}, and $d_{x^2-y^2}$, Σ_2 contains d_{xy}, Σ_3 and Σ_4 states include the d_{yz} and d_{xz}. Σ_1 and Σ_4 can mix, and so can Σ_2 and Σ_3, because of the vertical reflection symmetry along ΓN. The Fermi level of Nb and Ta goes through the middle of the *d*- band, and a large manifold of occupied and unoccupied *d*- states will therefore exist. The Ni, Pd, and Pt metal adsorbates have the fcc bulk structure and most stable (111) surface orientation. The band structure of Ni, Pd, and Pt along normal direction should be along ΓL direction. The *d*- states on ΓL direction are called Λ states.

Early in 1970, Mattheiss used the augmented-plane-wave (APW) method with muffin-tin potentials derived from superposed atomic charge densities to calculate the Nb and Ta band structure and the density-of-states [54]. The pioneering work of Mattheiss with full Slater exchange has proven very accurate for the Nb energy-bands below the Fermi level. The energy-band results for Nb are shown in Fig. 13 (a) where $E_n\left(\vec{k}\right)$ curves are plotted along symmetry directions of the bcc Brillouin zone. The corresponding density-of-states curve is shown in histogram form to the right. The dotted line corresponds to the integrated density of states. The Fermi energy is indicated by the dashed horizontal line for each calculation. The energy scale is relative to the constant portion of the muffin-tin potential outside the APW spheres. The theoretical calculation of Mattheiss [54] showed that Nb has a very similar band structure and density-of-states to Ta. The outer shell electronic configuration of Nb is $4d^45s^1$ and Ta $5d^36s^2$, which means almost half of the *d*- states is unoccupied. As shown in the calculated density-of-states the Fermi level is located at about the center of *d*- bands. It is noted that there is a local minimum in the Σ_1 band where it

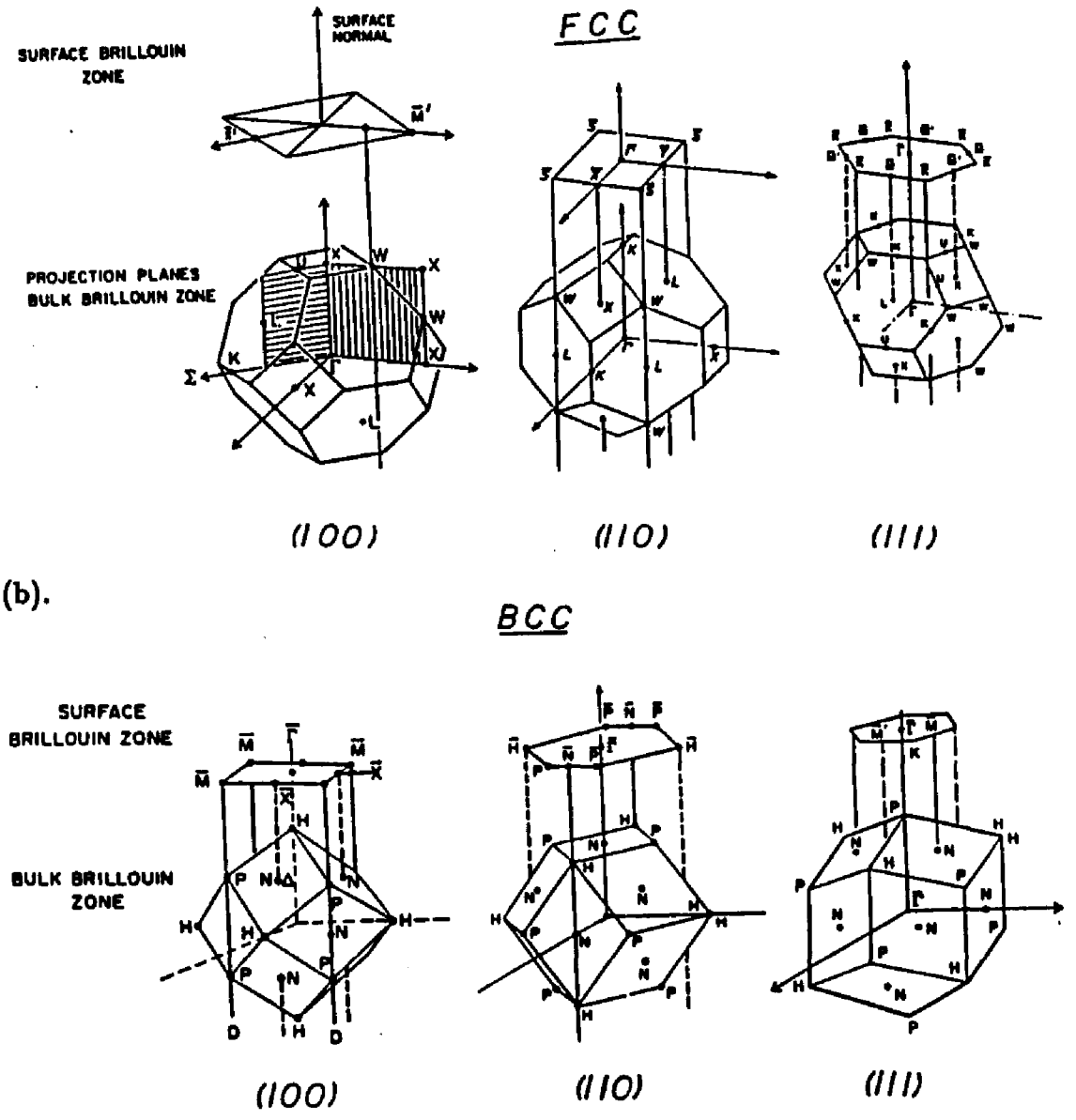

Figure 12: The orientation of the bulk fcc and bcc Brillouin zone with respect to the (100), (110), and (111) surface Brillouin zones. The lines which project into the surface symmetry points are shown.

(a).

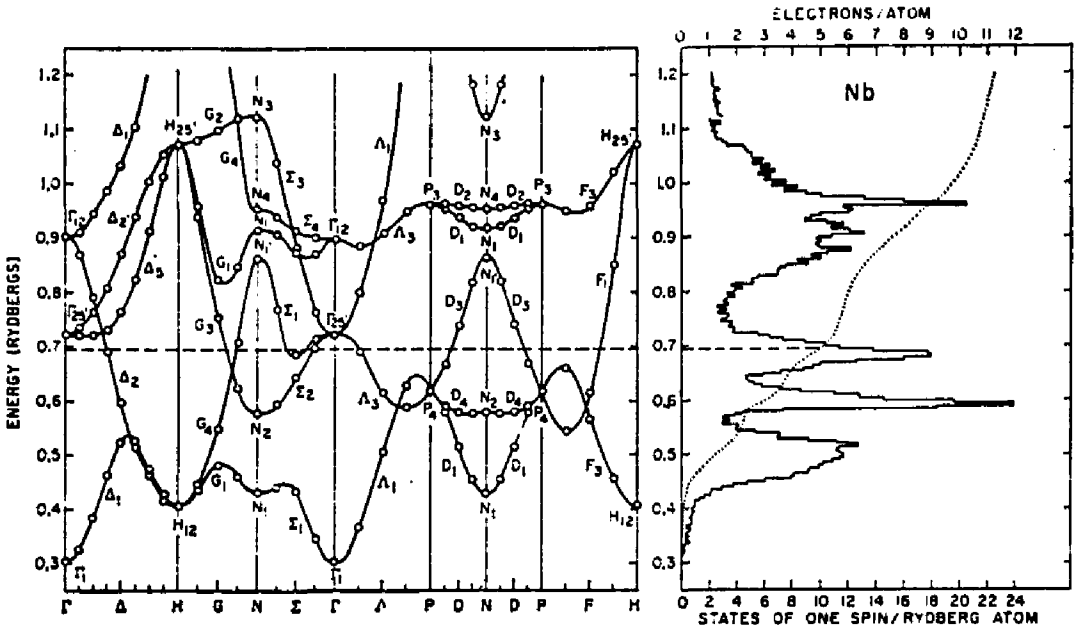

(b).

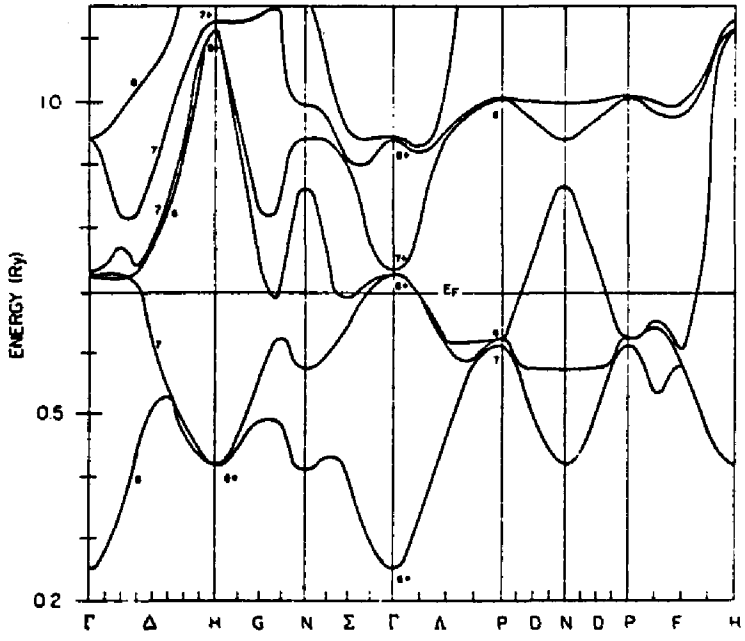

Figure 13: (a) Energy-band and density-of-states curves for the Nb calculated by L. F. Mattheiss (1970). The zero of energy is at the Fermi energy E_F. (b) Energy-band for the Nb calculated by Elyashar and Koelling (1977).

crosses below the Fermi level midway along the Σ direction. This implies a high density-of-states at the Fermi level. Later on, Anderson *et al.* [55] applied the self-consistent augmented-plane-wave method to calculate the Nb energy band for the full Slater ($\alpha = 1$) exchange and $\alpha = 2/3$ exchange. General quantitative agreement is found between their self-consistent $\alpha = 2/3$ results and the non-self-consistent $\alpha = 1$ energy band calculated by Mattheiss. Ho *et al.*[56] have presented a self-consistent calculation of the electronic structure of bulk Nb using the pseudo-potential method. In contrast to the previous calculations on the Nb Σ direction, they show the local minimum in the third band (Σ_1) located above the Fermi level. In other words, the Fermi surface in the pseudopotential calculation does not cut across the Σ symmetry line ($\Gamma - N$). In 1977, Elyashar and Koelling [57] reported the results of a self-consistent relativistic augmented-plane-wave calculation of the electronic structure of Nb. Unlike any of previous work which using muffin-tin approximations of spherical shape inside the muffin-tin spheres and constant in the interstitial region, their calculation was performed using potential and charge density of general shape. Fig. 13 (b) shows the Nb energy-band structure presented by Elyashar and Koelling [57] which gives results differing significantly from any other Nb band structure calculation. Comparing with the results of Mattheiss's calculation along Σ direction of the Nb Brillouin zone, we found that all the symmetry points above the Fermi level shift up to higher energy. However, the first Σ_1 band still dips below the Fermi level and then back above E_F as it disperses from Γ to N. The Σ_3 band hybridizes with Σ_1 and Σ_4 bands. A band gap is created between the Σ_3 and Σ_1 along the normal direction of Nb(110). In principle, this scheme should be the most precise transition-metal band-structure calculation to date. The valence band photoemission studies of Nb for photon energies up to 12 eV were performed by Lindau and Spicer [58] early in 1974. Their results both concerning *d*- band width and structure in the valence band are in favor of the theoretical band structure calculation by Mattheiss. Smith [59] has studied the electronic structure of the Nb(110) surface using angle-resolved photoemission. The results are in good agreement with the relativistic self-consistent calculation by Elyashar and Koelling [57] using no muffin-tin shape approximations. Smith *et al.* [60] also studied the final states along Σ direction of the Nb Brillouin zone using synchrotron radiation as a source. Their constant initial-energy spectra (CIS) obtained using synchrotron radiation show the energy position of the Σ_1 band crossing at the Fermi level.

To compare with the previous work on the Nb density-of-states, we show the AIUPS EDC's with photon energy 21.2 eV and 40.8 eV on Nb(110) at 300 K on Fig. 14 (a).

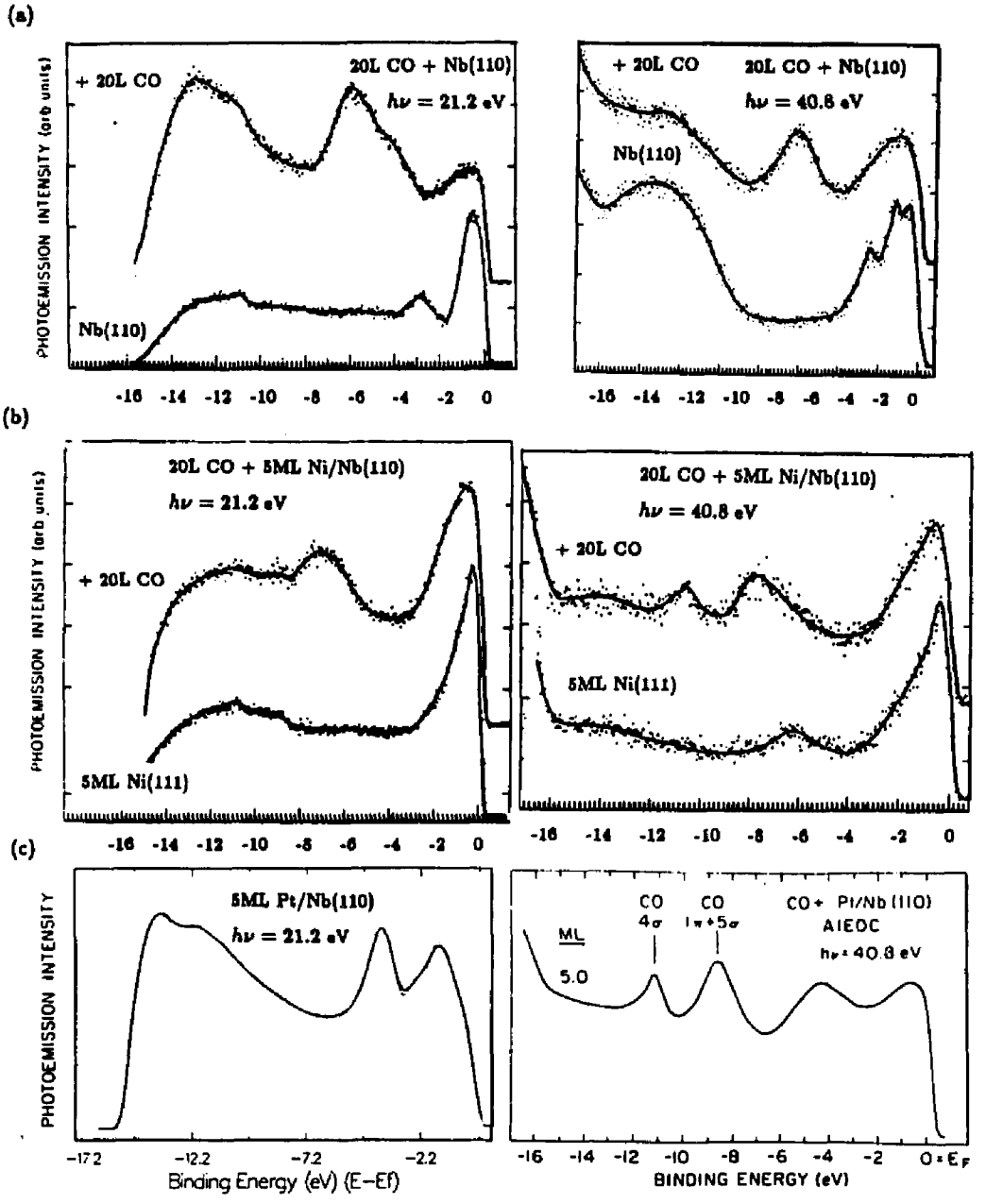

Figure 14: AIUPS EDC's taken at photon energies of 21.2 eV and 40.8 eV for (a) Nb(110) and 20 L CO on Nb(110), for 5 ML Ni(111) (b) and 5 ML Pt (c) on Nb(110) and the same surfaces after exposure to 20 L CO.

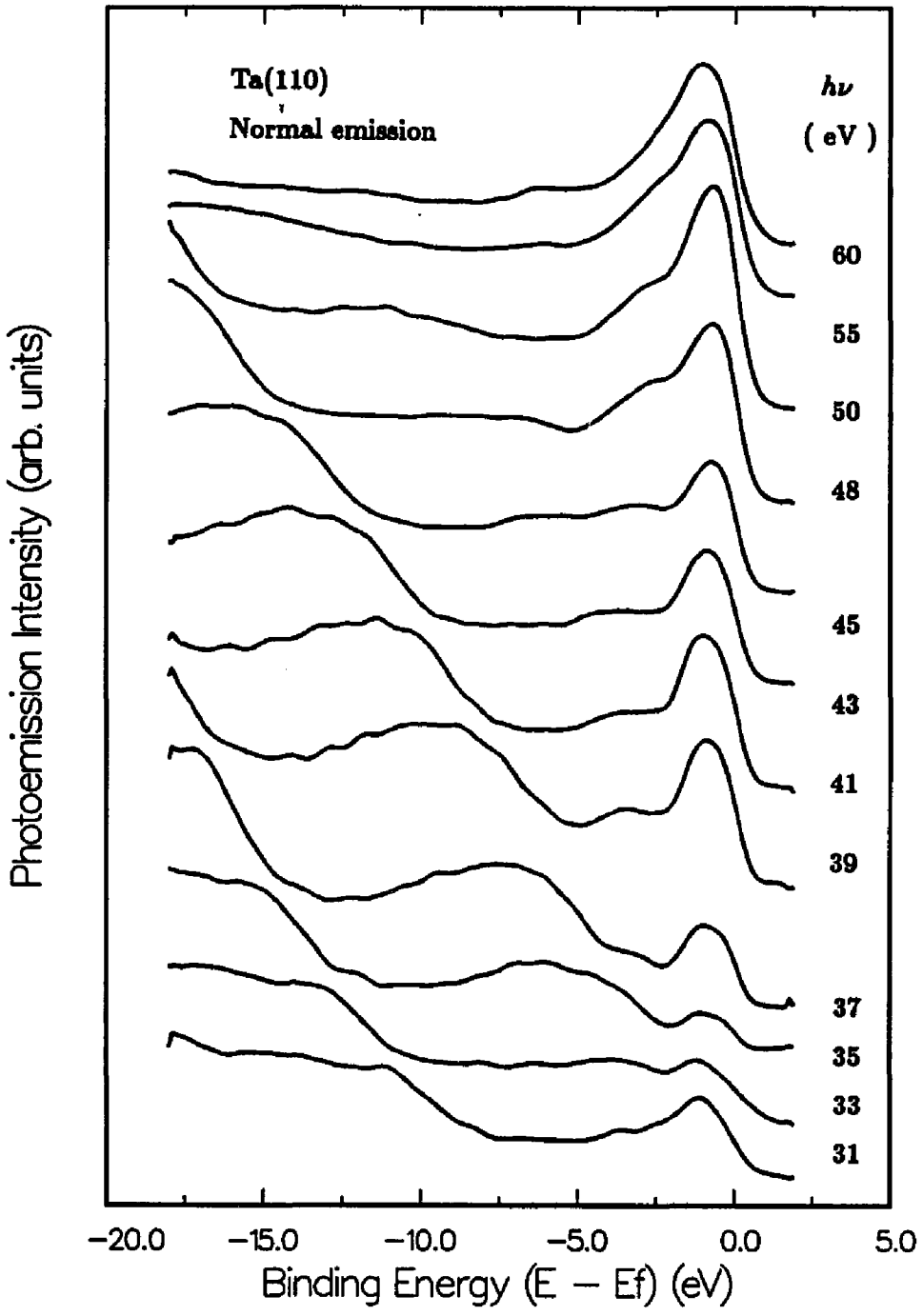

Figure 15: ARUPS normal emission EDC's with photon energy range from 31 eV to 60 eV on Ta(110) at 300 K.

The intense peak at 0.4 eV below the Fermi level E_F is due to a direct photoexcitation transition from a local minimum in the Σ_1 band where it crosses below E_F midway along the Σ direction. A weaker peak at -3.1 eV can be attributed to the bulk transition from the lowest Σ_1 valence band. The minimum at -1.8 eV results from a band gap between Σ_1 and Σ_2 which turns out to be very sensitive to both disorder and surface contamination. Additional photoemission states located between -0.4 eV to -1.8 eV are sometimes observed in polycrystalline samples and can be attributed to photoemission from other Nb surface planes. In the 40.8 eV photon energy EDC's, a broad feature located at -13.0 eV is due to the Nb $N_{2,3}VV$ Auger transition which originates from the decay of valence electron to fill the Nb 4*p*- holes at the binding energies of 30.8 eV and 32.5 eV. The way to distinguish the Auger transition states from the initial states on the EDC's is to vary the incident photon energy. The initial states will have a fixed energy position on EDC's, while the Auger states will shift to higher binding energy on the same scale as the photon energy is increased or shift to lower binding energy on the scale as the photon energy is reduced. This is illustrated in Fig. 15 which shows the angle-resolved synchrotron radiation photoemission normal emission EDC's on Ta(110) at 300 K. The photon energy has been varied from 31 eV to 60 eV with a fixed 45° incidence. Three Ta Auger transitions were observed which shift to higher binding energy on the same scale as the incident photon energy is increased. The Auger feature in the EDC's of 31 eV photon energy are Ta $N_{6,7}VV$ Auger transitions which are due to the filling of 4*f*- core holes at 21.6 eV and 23.5 eV binding energies. The second and the third one, which appear in the EDC's of 33 eV and 43 eV photon energies, are Ta O_3VV and O_2VV Auger transition. They originate from the decay of valence electrons to the 5*p*- core holes at the binding energies of 32.7 eV and 42.2 eV, respectively. It should be mentioned here that for some monochromators with poor optical elements, second order light may appear. In this case the features caused by the second order light will shift to a higher binding energy twice that of the photon energy change or shift to a lower binding energy twice that of the photon energy change.

Fig. 16 shows the KRIPES spectra obtained from the clean Nb(110) surface with normal incident geometry as a function of incident electron beam energy with respect to the Fermi level. Above E_F, the spectra are dominated by three distinct features. The one right above E_F is identified as Σ_1 state which shows a strong dispersion as a function of incident electron energy. The one located at about 3.0 eV from E_F is the split off Σ_1 state and the one at about 3.5 eV is the Σ_4 state. They both have a very localized character with

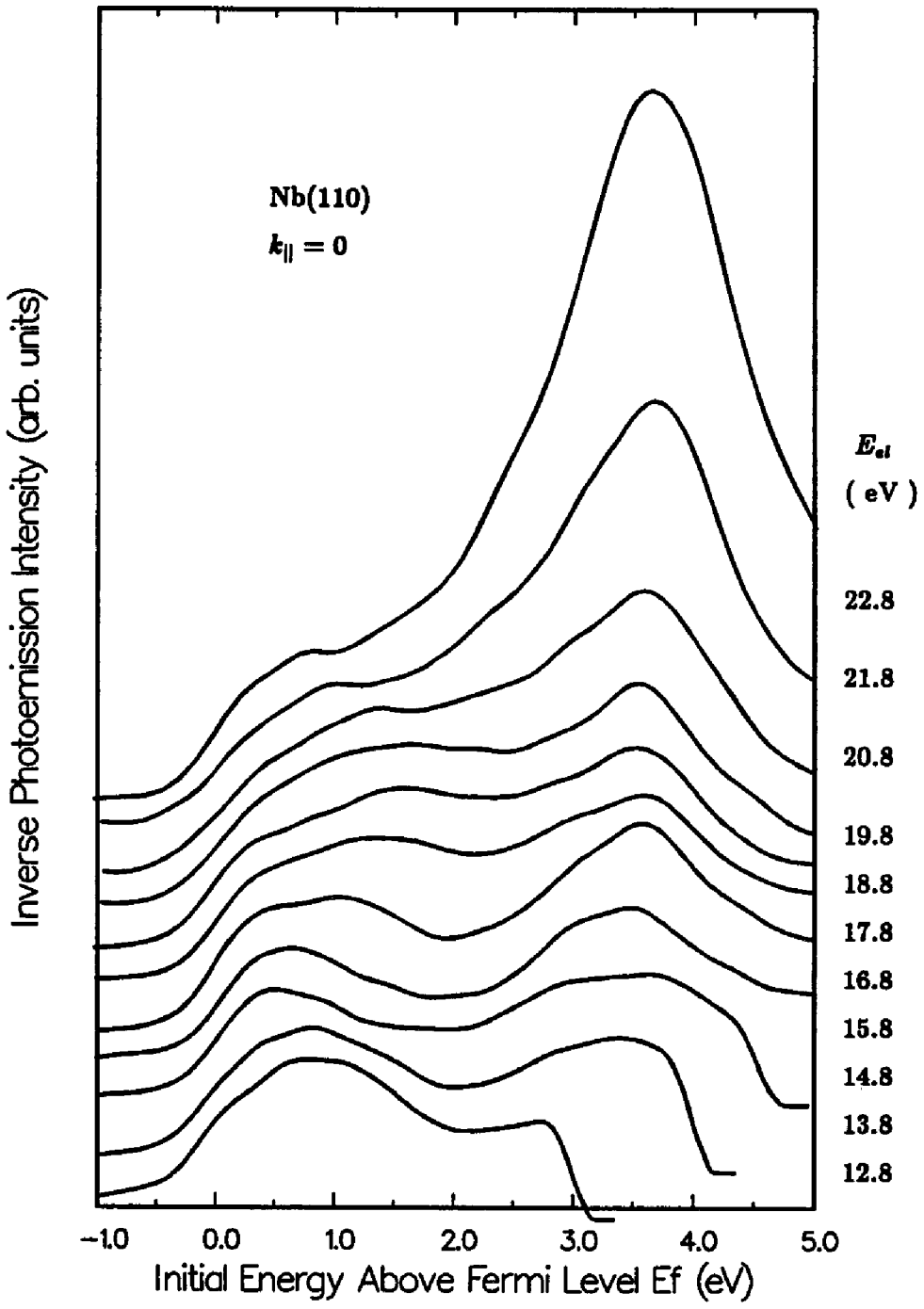

Figure 16: Inverse photoemission spectra for Nb(110) at $\bar{\Gamma}$ point ($k_{||} = 0$) taken as a function of initial-state electron energy E_{el} relative to the Fermi energy E_F.

(a) with the calculation of Mattheiss. (b) with the calculation of Elyashar.

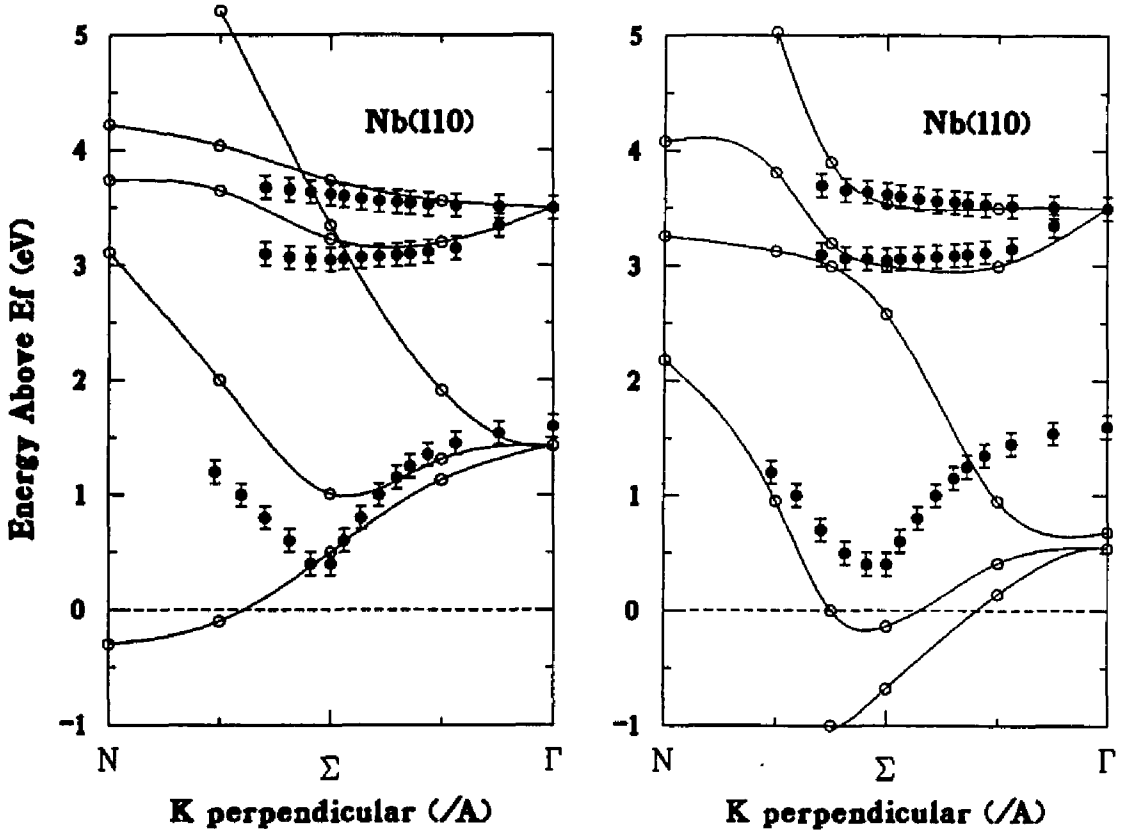

Figure 17: Experimental dispersion curves (solid circles) along the Σ direction of Nb(110) Brillouin zone compared with the band structure calculations of (a) Mattheiss and (b) Elyashar.

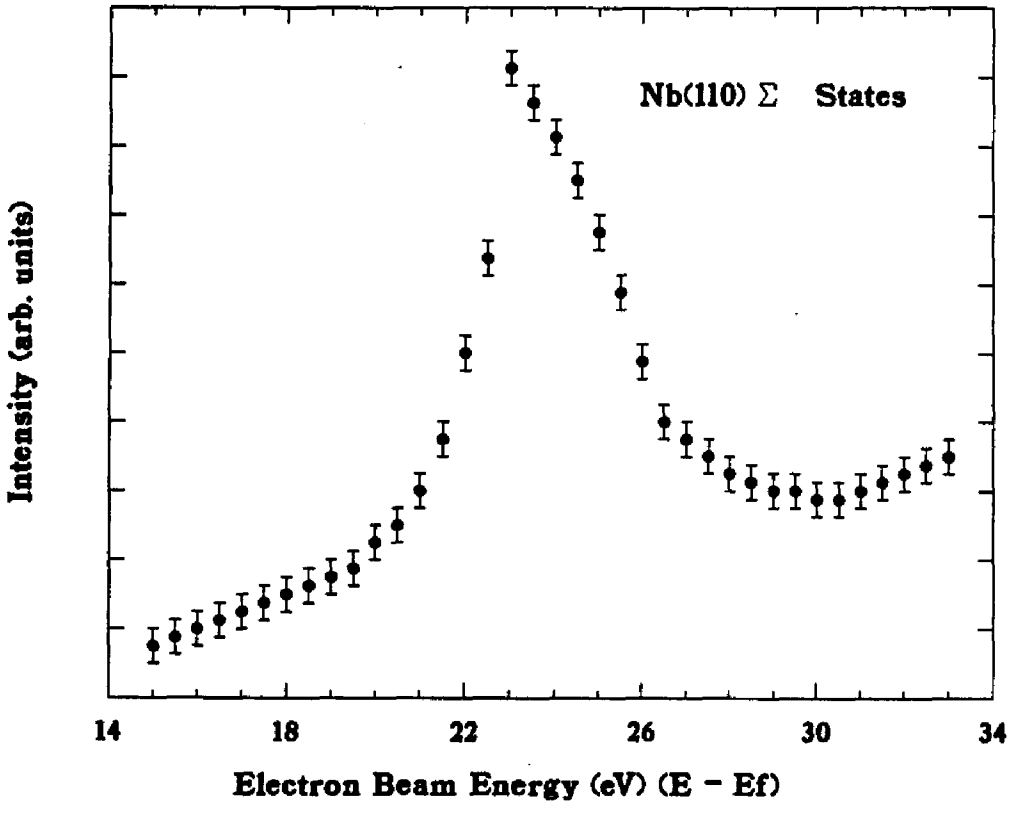

Figure 18: Variation of the intensity of Nb Σ_1 to $\Sigma_{1,4}$ direct transitions as a function of incident electron beam energy.

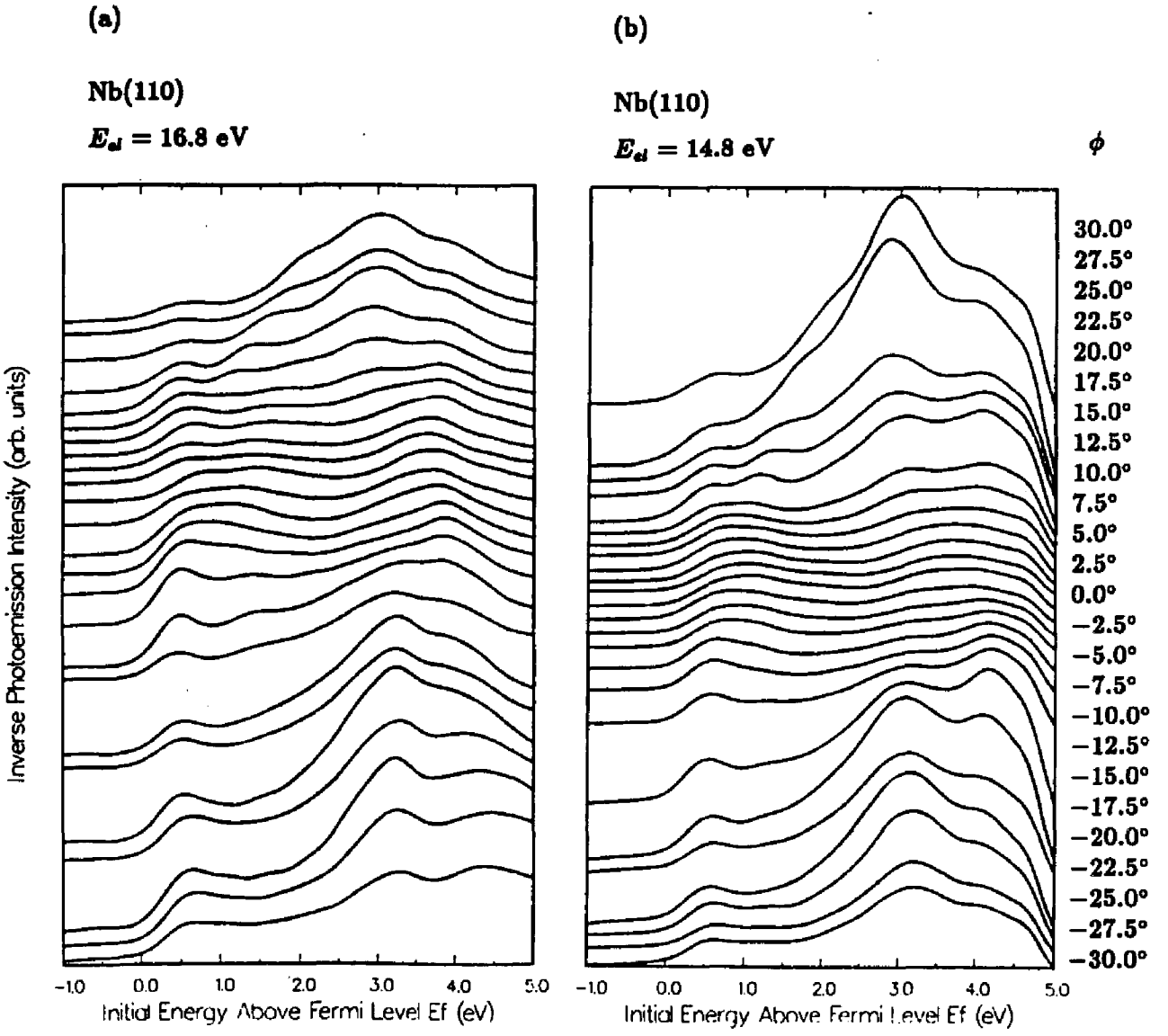

Figure 19: Inverse photoemission spectra for Nb(110) taken at 14.8 eV and 16.8 eV initial-state electron energies with respect to E_F as a function of incident angle away from the surface normal along the $\bar{\Gamma}\bar{P}$ direction.

respect to $k_\perp$, as expected for *d*- derived states. The characteristics of these assignments are consistent with the theoretical band structure calculations [54]. However, to compare in detail the Nb bulk band structure with the theoretical calculations, one needs to calculate $k_\perp$ from the electron beam energy E_{el} in order to plot the experimental band structure along Σ direction. The simplest approximation to obtain $k_\perp$ from the experiment is to choose the normal incident geometry and assume that the initial state of the incident electron is a parabolic free-electron-like band in a constant inner potential V_0. Therefore energy and momentum conservation will give

$$E_i(k_i) = \frac{\hbar^2 k_i^2}{2m} - V_0 \; ; \quad (V_0 > 0) \; . \tag{3.3.1}$$

By inverting Eq. (3.3.1), one obtains

$$k_\perp = 0.51 \left[E_{el} - 3.81 \left(k_\parallel + g_\parallel \right)^2 + V_0 \right]^{1/2} \quad . \tag{3.3.2}$$

Where E_{el} is the incident electron energy with respect to the Fermi level and $g_\parallel$ can be any reciprocal-lattice vector parallel to the Nb(110) surface. Generally $g_\parallel$ is set equal to zero to simplify Eq. (3.3.2). V_0 is the inner potential, for which the free-electron-like value is best fit for 7.8 eV. However, the result obtained from the free-electron-like model is inconsistent with the theoretical calculations. This is because the model of free-electron-like initial state ignores the interaction of incident electron with the real crystal potential of Nb. By turning on the real potential, band gaps open up at the boundary of the Brillouin zone. The interaction of electron with crystal potential becomes very strong for the low energy incident electrons like those used for the inverse photoemission. To achieve a better approximation, we adopt a semiempirical method to plot the dispersion of Nb *d*- states as a function of $k_\perp$. We can identify the direct transition between different bands. The first step is to obtain the dispersion of initial Σ_1 state of incident electron before decayed into final states. As mentioned before, this initial Σ_1 state should not be free-electronlike due to the interaction with crystal potential. From the KRIPES experiments, we are able to identify the $\Gamma_{25'}$ symmetry point by varying the incident electron beam energy E_{el}. The electron energy corresponding to the Γ point is determined as 20 eV above the Fermi level. The other symmetry point N_1 is taken from Smith and Williams' CIS experiment [60] which give approximately 12 eV initial energy above the E_F. Mo is one column to the right of Nb in the periodic table and crystallizes in the bcc structure. It is assumed that Mo has a similar Σ_1 band structure as Nb because they are adjacent in the periodic table. In fact, the results

of a Slater-Koster parameterization of the energy bands of Nb calculated by Mattheiss [54] are nearly identical to the Mo bands of Petroff and Viswanathan [61] except that the Fermi level is lowered by 1.6 eV. Therefore, we can interpolate the initial Σ_1 band between the symmetrical points of N_1 and Γ_{25} from the calculated Mo band structure of Zunger and Cohen [62]. With this initial state incident electron, one can determine the final state from the KRIPES normal incident spectra as a function of electron beam energy and plot the Nb Σ band structure above E_F. In Fig. 17 we compare our semiempirical calculation of Nb Σ band structure with the augmented-plane-wave calculation of Mattheiss [54] (a) and the relativistic self-consistent calculation with no muffin-tin shape approximations [57] (b). The Σ band structure from the APW calculation of Mattheiss has been rigidly shifted up 1.0 eV to fit the critical point Γ_{12} with the experimental data. The dispersion of the *d*- states is in good agreement with the calculation of Mattheiss. The energy scale difference can be caused by the nonself-consistent approximation which may require a further alignment of the Fermi level to the experimental results. Comparing with the self-consistent relativistic APW calculation of Elyashar and Koelling's (Fig. 17 (b)), we found a better agreement with experimental data except the initial state energy of the symmetry point $\Gamma_{25'}$ is about one eV different. The discrepancy on the energy scale of the $\Gamma_{25'}$ point suggests a further theoretical study on the electronic structure of Nb could be attempted. In the Fig. 17, the reason that we could not identify a Σ_3 band is possibly due to its *sp*- character which would have a much weaker intensity. For a bcc crystal the electronic dipole selection rules forbid the transition from Σ_1 to Σ_2 [89] and therefore, the Σ_2 state will not be seen. Our results show that the lowest unoccupied Σ_1 band disperses down to E_F midway on the $\Gamma - N$ line where photoemission spectra show a peak in intensity at the Fermi level [60]. Therefore, we conclude that the Σ_1 band crosses the Fermi level E_F midway on the $\Gamma - N$ symmetry line.

As evidenced by the large density of states of the two bands involved, the transition from Σ_1 to Σ_1 and Σ_4 are very strong. Our experiments indicate that the intensity of the state located at 3.5 eV initial energy has a maximum at about 23.0 eV incident electron energy. Fig. 18 shows the intensity variation of the Nb Σ_1 to $\Sigma_{1,4}$ direct transitions as a function of normal incident electron beam energy. We could not determine whether this maximum is due to the transition of $\Sigma_1 \rightarrow \Sigma_1$ or $\Sigma_1 \rightarrow \Sigma_4$ with the present instrumental resolution. However, this intensity peak up can be attributed to the enhancement of the cross section at 23.0 eV electron energy. El-Batanouny and Strongin [63] have performed the constant initial state (CIS) mode photoemission with a normal emission geometry on Nb(110) to measure

directly the photon-energy dependent cross section $\sigma^{Nb}(h\nu)$. The CIS result shows that the $\sigma^{Nb}(h\nu)$ exhibits a distinct maximum at 23 eV photon energy. Johnson and Davenport [51] have applied a quantum-theoretical treatment to the cross section of photons produced in inverse photoemission. They show that the relation of matrix element for photoemission $M\left(\vec{k}\right)$ and inverse photoemission $M'\left(\vec{k'}\right)$ can be expressed as

$$M\left(\vec{k}\right) = -M'\left(\vec{k'}\right). \tag{3.3.3}$$

In other wards, the photoemission matrix elements may be used for inverse photoemission provided the direction is taken from sample to electron source.

We also measured the Nb(110) *d*- state dispersion with $k_{||}$ to identify their band characters. Fig. 19 shows the KRIPES of Nb(110) as a function of the angle of electron incidence away from surface normal along $\bar{\Gamma}\bar{P}$ direction. As the incident angle tilts away from the $\bar{\Gamma}$ point the Σ_1 state shifts towards E_F suggesting antibonding character for these states. The Σ_4 state splits into two features when the angle of the incident electron tilts along $\bar{\Gamma}\bar{P}$ direction. The intensity of Σ_4 states reaches their minimum at the $\bar{\Gamma}$ point. No dispersion were observed for Nb(110) Σ_4 states. These results should be useful for improving theoretical descriptions of Nb and the related adsorbate-Nb substrate complexes.

Fluorescence from core hole recombination in metals have been used to study the many-body effects, core hole lifetime, and spin-orbit partner processes [64-65]. So far the studies have been mostly the alkali metals because of their simple electron configuration. During inverse photoemission studies of Nb(110), we also investigated the fluorescence processes due to the decay of valence electron into the empty $4p_{1/2}$ and $4p_{3/2}$ states created by the incident electron beam. The spectral profiles for Nb(110) are shown in Fig. 20. The main fluorescence state is observed at about 30 eV photon energy and its threshold is approximately at an electron beam energy of 35.85 eV respect to the Fermi level.

Now let us take a look at the electronic structure of late transition-metals that we used as the overlayers. The electronic structure and chemical activity of Ni, Pd and Pt have been well studied and reasonably understood. All Ni, Pd and Pt have their *d*- bands almost filled. The solid state or the metallic electronic configuration of Ni, Pd, and Pt is well described by $d^9\ (sp)^1$. This indicates that the band structure effects due to the electronic configuration changes between the metallic and atomic structures is very small for Pt. Later on this argument is used to prove that the reduced electronic density of states at E_F is not due to the atomic configuration of ultra-thin films. The occupied *d*- band width

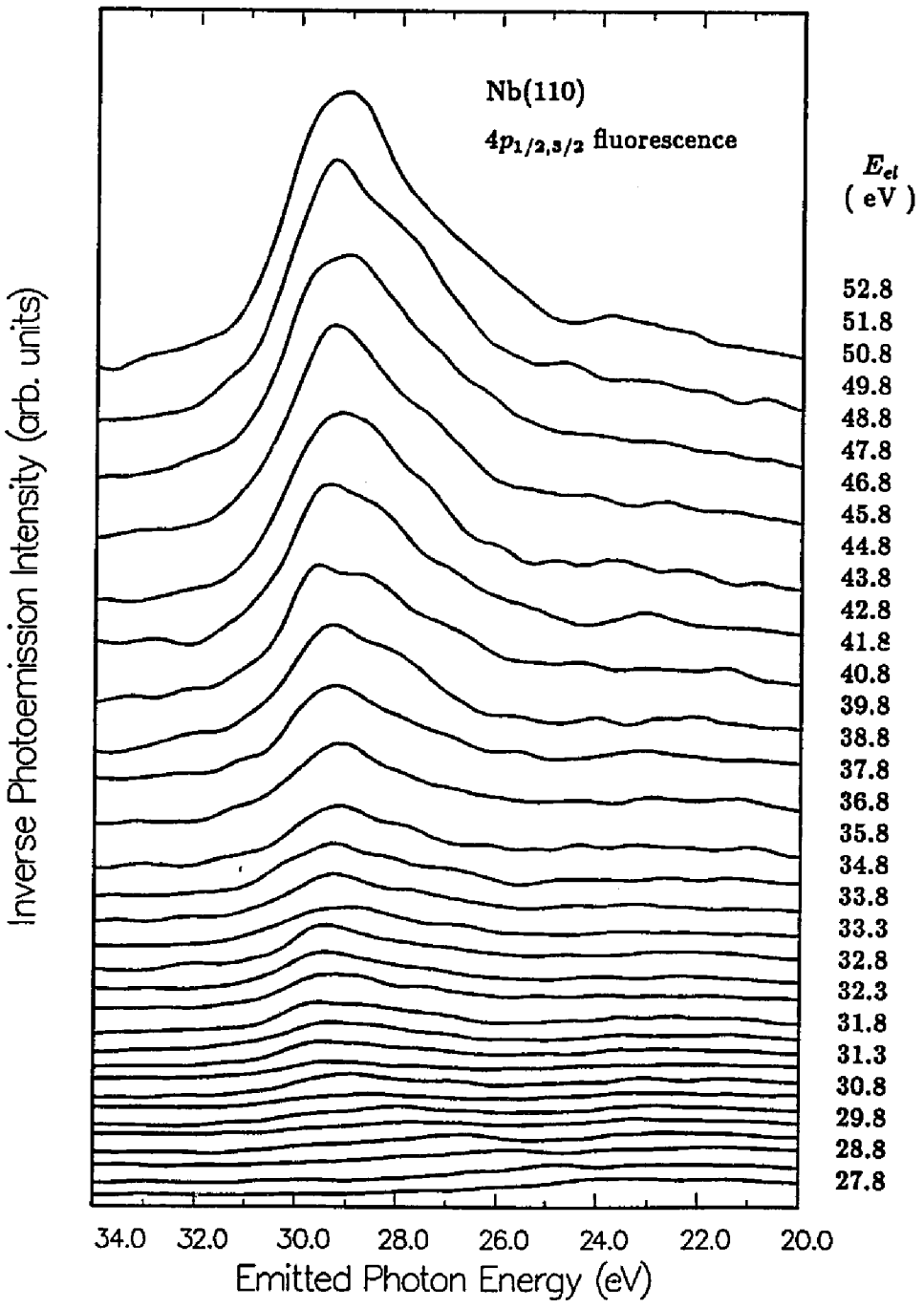

Figure 20: Nb fluorescence spectra, due to the decay of valence electron into the empty $4p_{1/2}$ and $4p_{3/2}$ states created by inverse photoemission electron beam, as a function of electron beam energy.

of these late transition-metals predicted by theoretical calculation is of the order 4 to 5 eV. Fig. 14 (b) and (c) show the valence band of Ni(111) and Pt(111) measured by AIUPS. The experimental values for the occupied *d*- band width of Ni(111) are observed to be much smaller than those obtained by band calculation. Smith and his co-worker have reported angle-resolved UPS results for Ni(001) which show a *d*- like band width of 4.3 eV in good agreement with the band calculation [66]. They showed the deep *d*- band peak moves from 3.0 to 4.3 eV binding energy with respect to the Fermi level as the azimuthal angle changes from the ⟨100⟩ to the ⟨110⟩ azimuth. The continuous movement of the relatively constant amplitude peak with ϕ suggests that an angle-integrated experiment would integrate the peak position so that no peak would be seen.

For the EDC's of Ni(111) taken at photon energy 40.8 eV, we find a deep feature at about 6 eV below the Fermi level. This feature has been the subject of some controversy since an O_{2p} state is also observed at this initial energy on Ni. However it has been shown by Smith [66] that for the normal emission angle-resolved photoemission, the 6 eV peak has an apparent excitation threshold near a photon energy 24 eV, and that this peak shifts $2 \sim 3$ eV to higher binding energy as photon energy increased from 23 eV to 40 eV. In a later chapter, we will present the experimental evidence to show that this 6 eV feature is due to an intrinsic one-electron excitation.

It is noted from photoemission studies that the (111) surface of all the noble-metals support a Shockley type surface state at the bottom of the *s-p* band gap. These surface states have binding energies close to the Fermi level and they disperse towards the vacuum level near the center of the zone. Recent theoretical and experimental studies have shown that a Shockley-type surface state also exists on (111) surface of transition-metals. Unlike the (111) surface of the noble metals, these Shockley-type surface state would be unoccupied at the center of the zone of transition-metal (111) surface. For Pd(111) surface, an unoccupied Shockley-type surface state has been predicted in a first principles calculation by Louie [67]. Indeed, a recent inverse photoemission studies of the Pd(111) surface by Johnson *et al* [68], using the same apparatus as the one we used for present work, have clearly demonstrated that the transition-metal Pd(111) surface supports a Shockley-type surface state. Fig. 21 shows the inverse photoemission spectra recorded as a function of angle of incidence defined with respect to the surface normal. The surface state at about 1.5 eV initial energy disperses upwards away from the Fermi level. Their results indicated that the

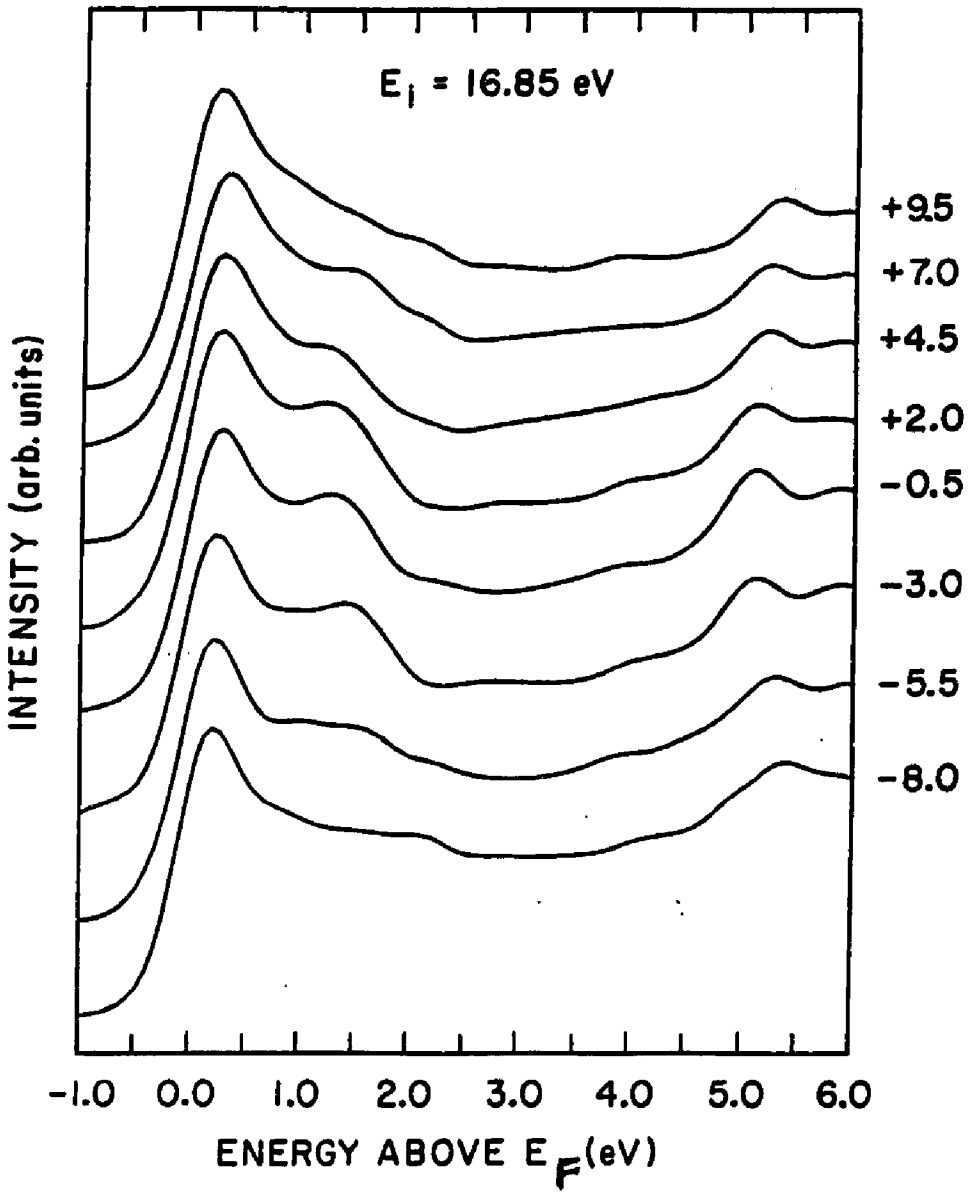

Figure 21: Inverse photoemission spectra from Pd(111) recorded as a function of angle of incidence defined with respect to the surface normal. The incident electron beam energy is 16.85 eV with respect to the Fermi level.

effective mass may be influenced by interaction with the bulk band edge that lies 1.0 eV above E_F at the center of the zone and disperses upwards away from the center of the zone.

3.4. Chemical Activity of Transition-Metal Surfaces

3.4.1 CO Chemisorption on Transition-Metal Surfaces

CO chemisorption on transition-metal surfaces has been studied extensively over the past few decades. These studies have shown that on the left side of the first-row transition-metals, up to Fe, the adsorption at room temperatures is likely to be dissociative, and on the right side from Co, it is molecular adsorption [69]. The variation of dissociation behavior with the surface of a given metal is significant only for the metals on the borderline of CO dissociative and molecular adsorption. In general close-packed surfaces tend to be the least active in dissociation. There is also evidence that surfaces with steps and kinks may be extra active, as in the anomalous dissociation of CO by a high Miller index Pt surface [70]. The variation of dissociation behavior with different transition-metals has been referred to the occupation of electronic *d*- states and their relation to the CO molecules 5σ and $2\pi^*$ states [71]. Presumably when the bond is sufficiently weakened by population of the CO antibonding orbital $2\pi^*$, at some point with the help of thermal vibration, CO molecules may be titled or even lie parallel to the transition-metal surface with splitting of CO, and coordination of separate C and O to the surface. Saha and Khanra [72] have extended Doyen-Ertl Scheme [73] to study the preferential orientation and dissociation of the CO molecule on transition-metal surfaces. Their calculation shows a barrier of 0.87 eV for changing the orientation of the CO molecule from the normal to the parallel position on the Ni(110) surface. The study also showed that the CO molecule, once stretched 20% in the parallel position would lead to a total energy of the system lower than the total energy of the system with CO normal to the surface.

Fig. 14 (a) shows photoemission spectra from saturated CO chemisorption on Nb(110) surface at 300 K as a function of different photon energy. The dissociation of CO results in C 2*p*- and O 2*p*- states located at about 4.0 eV and 6.0 eV binding energy from the E_F, respectively. Fig. 14 (b) and (c) show the CO molecular adsorption on late transition-metal surfaces at 300 K. The distinct CO molecular states 4σ, 1π and 5σ are observed. For this strong molecular chemisorption case, it is found that on transition-metals CO bonds linearly to the surface with the carbon atom down on the metal substrate. Bonding between the molecular 5σ orbital and the unoccupied metallic d_{z^2}- orbitals is compensated for by back bonding from the occupied $d_{xz,yz}$- orbitals into the unoccupied molecular $2\pi^*$ level [74–75]. Exploiting the polarization properties of light in an allowed and a forbidden geometry, we

found that for CO chemisorption on thick Ni and Pt films supported by Ta(110), the CO molecule is more or less bonded linearly to the surface with the carbon atom down on the metal films.

When the temperatures is reduced to 80 K, a significant difference is observed for CO chemisorption. Fig. 22 shows the valence band spectra at 80 K for increasing CO exposures up to saturation. It is found that there is first emission from dissociated C and O and then the 4σ emission at -11.65 eV due to molecular CO is observed. For the exposure series in Fig. 22, 0.9 L is the lower bound on the exposure prior to the onset of 4σ emission. The average lower bound from four exposure series is 0.7 L. The average upper bound is 20 L. If it is assumed that there is a molecular precursor to dissociation and that its sticking coefficient is unity, and that the dissociation products remain in the surface, then the C and O fractional coverage prior to the onset of 4σ emission has a lower bound of 2 times 0.2 and an upper bound of 2 times 0.3 defined with respect to the Ta(110) surface atomic density. This is, of course, only a crude estimate, since there are experimental uncertainties including the calibration of the pressure gauges.

The molecular CO adsorbed at 80 K is a metastable species which converts to C and O after the surface is heated to 160 K, as also shown in Fig. 23 (a). As the surface was heated stepwise up to about 160 K, the valence band spectra were continuously monitored for changes and no CO dissociation was apparent until 158 to 164 K was reached. Fig. 23 (a), curve 2, was taken after the surface was maintained at this temperature for about 90 seconds and then cooled again.

It should be mentioned at this point that a surface which contains (more) residual oxygen prior to CO exposure has a greater tendency to dissociate CO molecules. This is indicated in Fig. 23 (b). It is noted that the O_2p cross section for normal incidence and 45° emission is much stronger than that for 45° incidence and normal emission. This may be expected of p orbitals lying parallel to the surface, although a separate polarization-dependent angle-resolved photoemission experiment would be required to clarify the situation. As far as whether the initial CO dissociation at 80 K on the clean Ta(110) surface is due to small amounts of oxygen which either modifies the surface electronic structure or creates surface defects is concerned, we think it is likely that the dissociative adsorption of CO at 80 K is an intrinsic surface property even if oxygen facilitates the dissociation.

Angle-resolved photoemission coupled with a synchrotron radiation light source provides several methods for qualitatively or quantitatively determining the orientation of

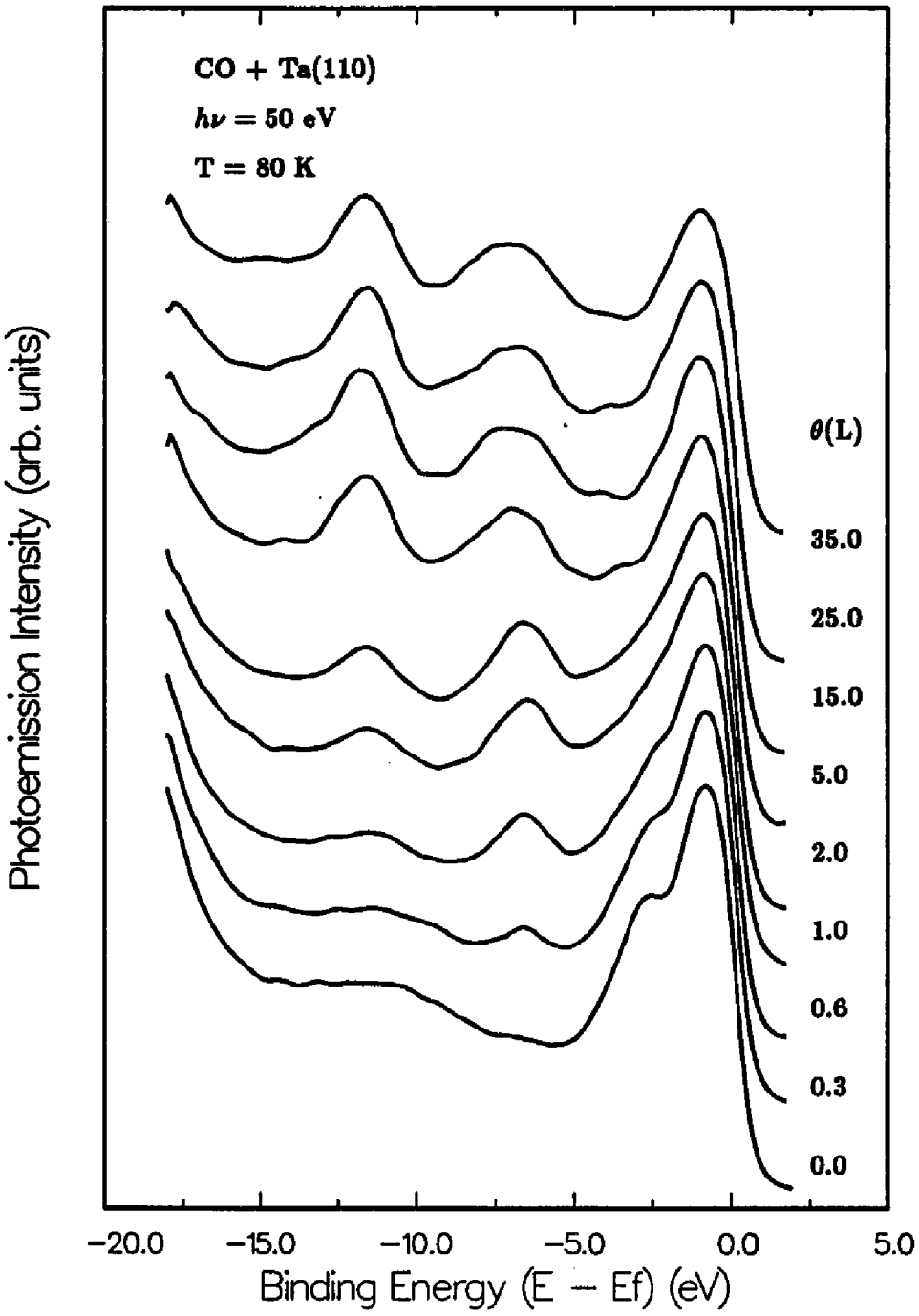

Figure 22: ARUPS normal emission EDC's on Ta(110) with a increasing CO exposure to the saturation at 80 K. The incident photon energy is 50 eV with incidence angle 45° away from the surface normal.

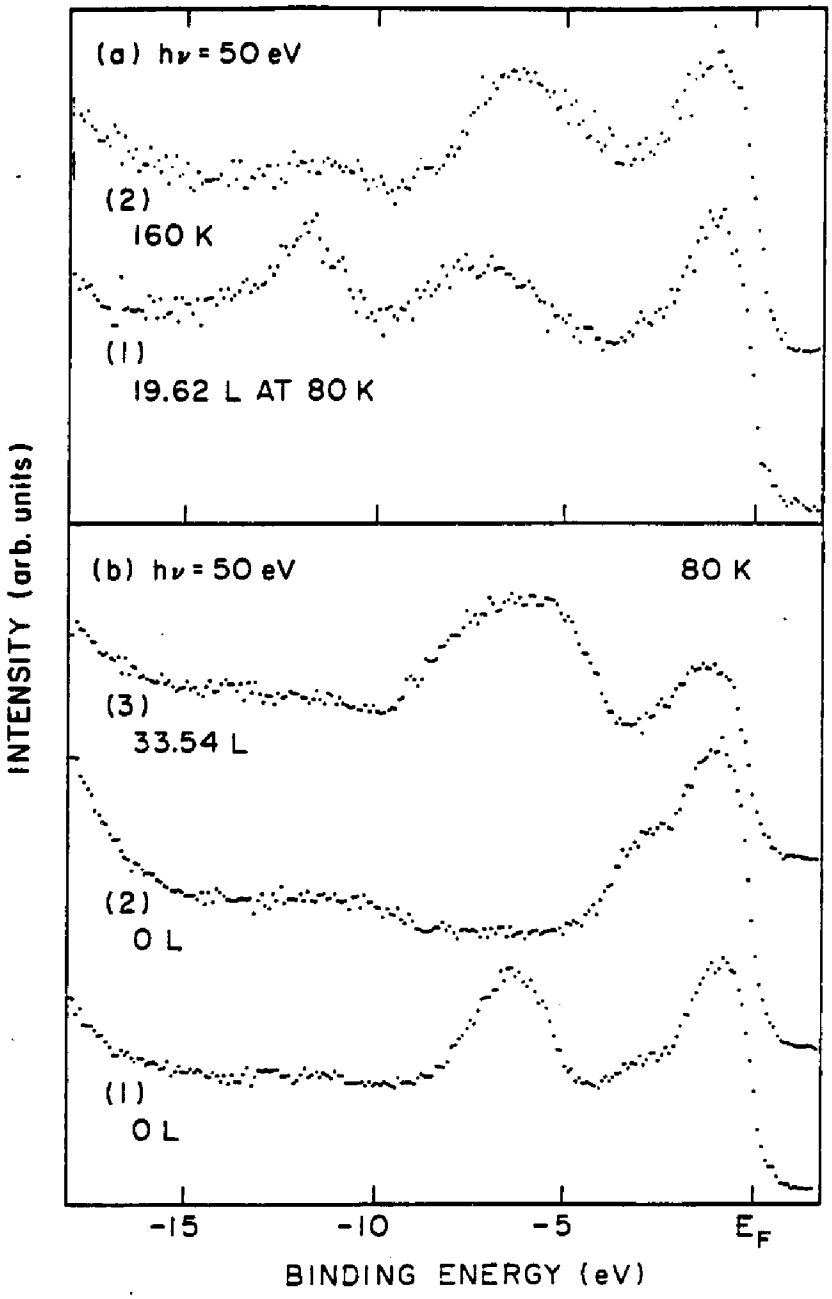

Figure 23: Valence band spectra showing: (a) The dissociation of CO molecularly adsorbed on Ta(110) at 80 K after heating to about 160 K. The geometry is 45° incidence and normal emission. (b) The dissociative adsorption of CO at 80 K on an oxygen-contaminated Ta(110) surface. (1) surface before CO exposure, normal incidence and 45° emission; and (2) surface before CO exposure, 45° emission; and (3) after 34 L CO, 45° incidence and normal emission.

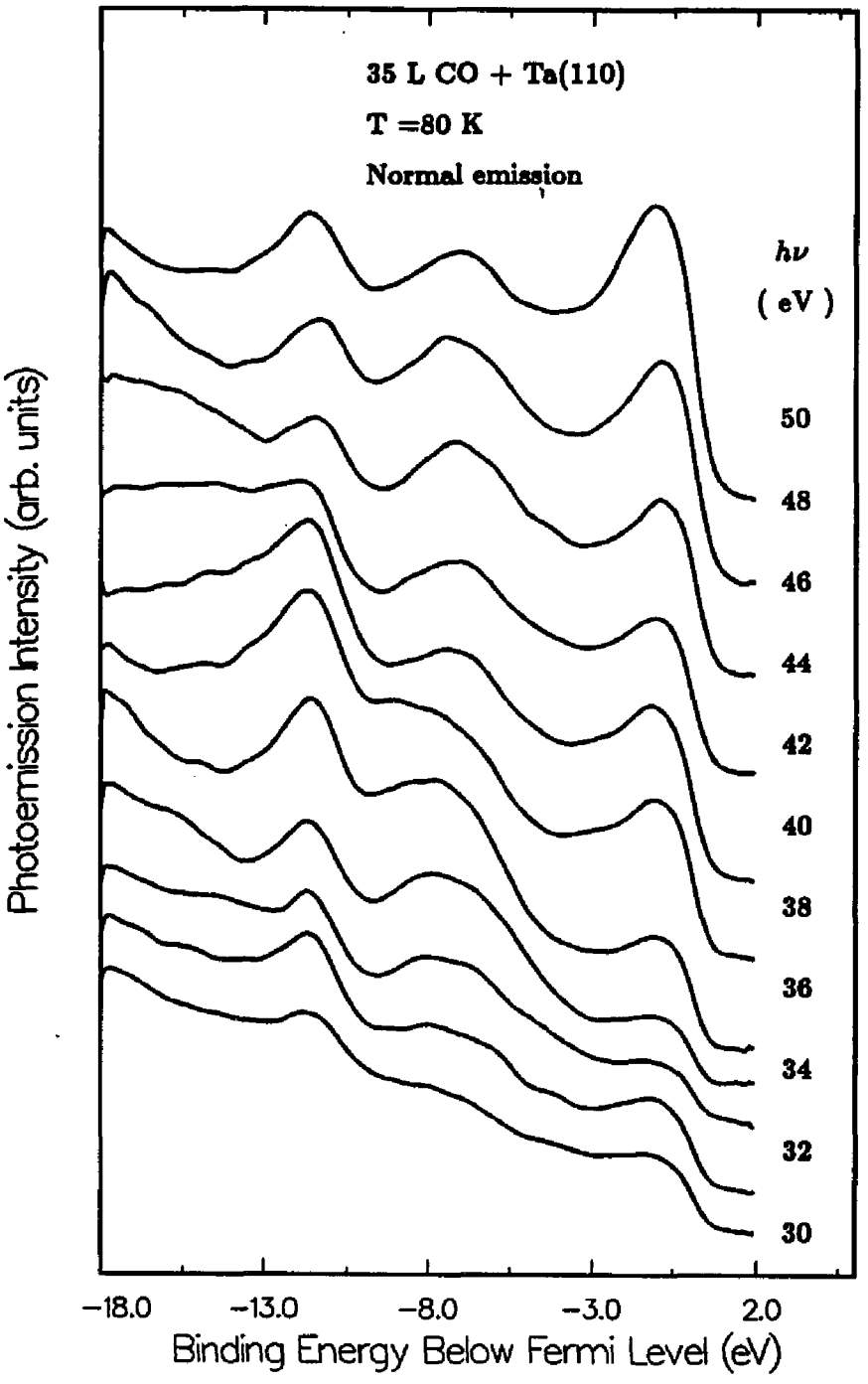

Figure 24: ARUPS normal emission EDC's on Ta(110) after a saturated exposure of CO at 80 K with the photon energy ranging from 30 eV to 50 eV. The angle of incidence is 45° away from the surface normal.

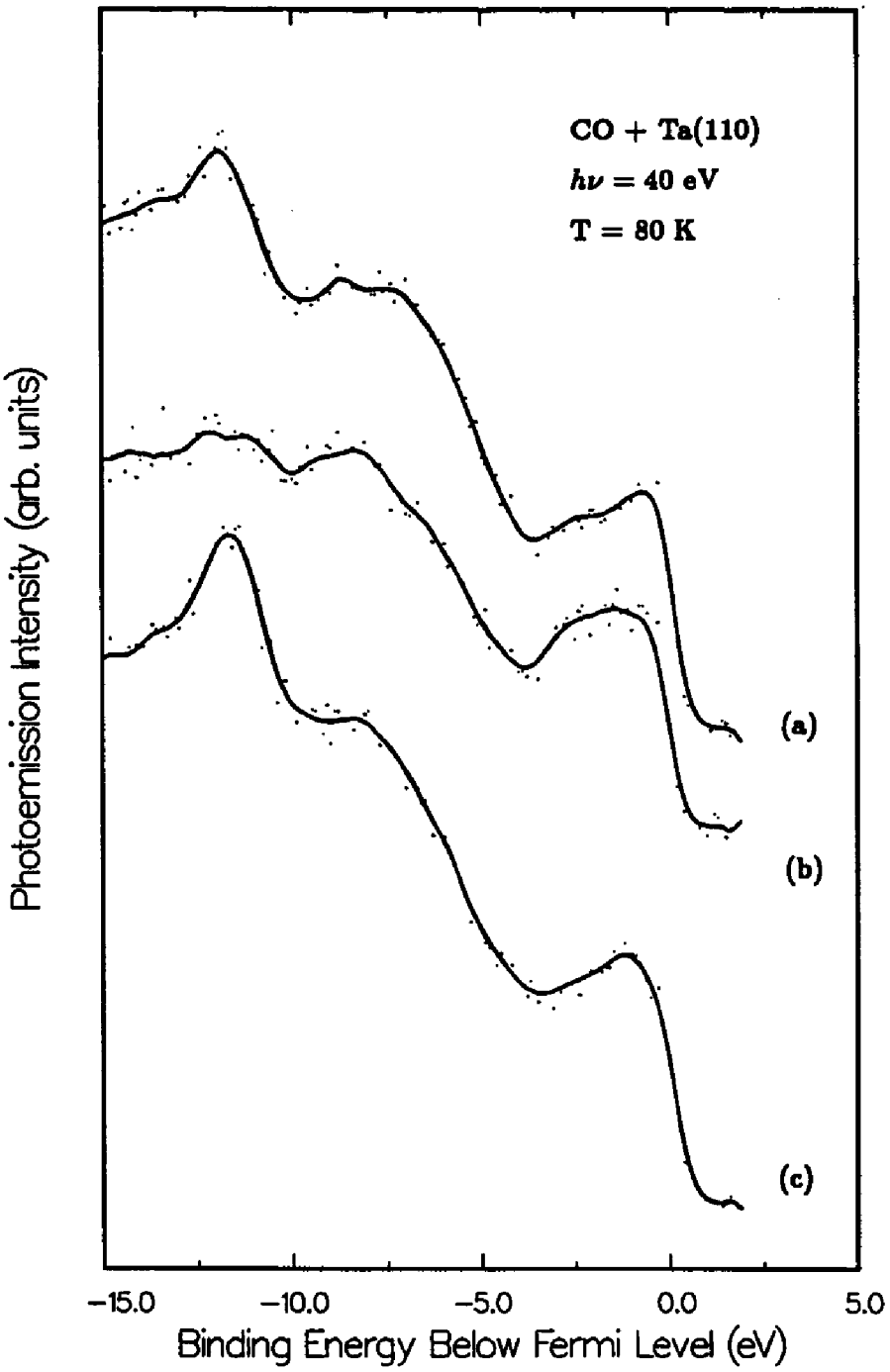

Figure 25: ARUPS EDC's with a photon energy 40 eV on Ta(110) after a saturation exposure of CO at 80 K. The geometries of measurement are (a) 45° angle of incidence and normal emission, (b) normal incidence and almost normal emission ($\Delta\theta < \pm 5°$), and (c) normal incidence and 45° emission.

molecules such as CO with respect to the metal surface. A simple way to probe the bonding symmetry between the adsorbate and metal atoms is using the polarized nature of synchrotron source and dipole selection rules. Assuming the CO molecular orientation is along the sample normal, for pure *p*-polarized light, which has the electromagnetic field vector $\vec{A}$ lying parallel to the plane of incidence, only emission from the even orbitals (such as σ levels) can be detected in the plane containing the incident light and its $\vec{A}$ vector. We call this configuration the "σ-allowed" geometry. In the "σ-forbidden" geometry the detector is positioned perpendicular to this incident plane, and only the odd orbitals (such as π levels) are detected.

CO chemisorption on Ta(110) at 80 K shows photoemission features typical of weakly bonded CO molecules. However, we still found that the CO first dissociated onto Ta(110) surface before molecular adsorption occurred. It is possible that dissociated carbon and oxygen atoms block the active sites such as surface defects, steps, or edges. Fig. 24 shows the ARUPS normal emission EDC's on Ta(110) after a saturated exposure of CO gas at 80 K with photon energy ranging from 30 eV to 50 eV. No obvious shape resonance is observed. Fig. 25 shows the special selected geometry for employing the $\vec{A}$ of polarized light coupled with angle-resolved detector. Curve (a) is taken with *p*- polarized light and the detector in the surface normal. Curve (b) is taken with *s*- polarized light and the detector 5° away from the surface normal, and the projection of the detector direction onto the surface is perpendicular to the polarization vector (the "σ-forbidden" geometry). Curve (c) is also taken with *s*- polarized light but the detector is in the plane of the polarization vector and the surface normal and 45° away from surface normal (the "σ-allowed" geometry). If the molecule is standing upright on a flat surface, curve (a) should show greatly enhanced 4σ and 5σ states whereas the 4σ intensity should be zero in curve (b) because of simple selection rules. In Fig. 25 curve (a), the 4σ state is enhanced, and we see a shake-up satellite peak appears at 2.1 eV below the 4σ state indicating a weak CO interaction with Ta(110) surface as in adsorption on noble metals. This shake-up satellite peak is a screened state due to charge transfer from the metal *d*- orbitals to the previously unoccupied CO $2\pi^*$ orbital. The $2\pi^*$ orbital may be pulled down by the presence of the *d*- hole. In a traditional picture of the molecular orbitals of CO, the 2π and 5σ orbitals are mainly located on the carbon end, the 4σ and 1π orbitals on the oxygen end. When chemisorbed on the transition-metals, CO bonds linearly to the surface with the carbon atom down on the metal substrate. The primary interactions are the hybridization of CO 5σ with metal d_{z^2}- and *s*- states, and that

of CO 2π with metal $d_{zx,yz}$- states. The 4σ and 1π orbitals are not involved in the bonding interaction. Since they are located away from the metal surface (oxygen atom end), the screening effects are expected to be important.

The CO species at 80 K may not have its molecular axis normal to the surface. This is shown in Fig. 25, curve (b), for normal incidence and electron near-normal emission. In this geometry, forbidden for σ symmetry, we still observe emission in the 4σ region. The emission may not totally result from impure polarization or deviation from the ideal geometry if one compares with the CO chemisorption on a thick Ni(111) film at the same geometry, where there is little doubt on the perpendicular orientation of the molecular axis. Furthermore, the molecular species is only weakly adsorbed on the surface, as deduced from the observation of a satellite structure 2.1 to 2.2 eV below the 4σ emission in Fig. 25, curve (c).

3.4.2 H_2 Chemisorption on Nb(110)

The interaction of hydrogen with transition-metals has been studied for many years. An excellent review of electronic structure, crystal structure, and mechanical properties of metal hydrides can be found in references [76-77] It is believed that at room temperature hydrogen is not only adsorbed on transition-metal surfaces, but is also absorbed into the near surface region or even into the bulk [60,78-80]. For hydrogen on Ni, Pd, and Pt single crystal surfaces no hydrogen bonding orbital is seen in photoemission at room temperature, except for some slight changes in the *d*- band. However, measurements at low temperatures on these late transition-metals showed the existence of two-dimensional H-metal split-off states. Generally, at room temperature hydrogen strongly chemisorbs on the transition-metals and the adsorbate bands lose their two-dimensional character at $k^{\|}$ points where the adsorbate bands coincide in energy with the substrate bands. This strong interaction alters the bulk wave function near the surface and thereby changes the excitation probability and transmission of excited bulk electrons through the surface.

The hydrides of the group-VB metals, such as Nb and Ta, are particularly important because of their unique property of high mobility of hydrogen. Peterman *et al.* [81] have studied the NbH_x and TaH_x ($0.6 \leq x \leq 1.0$) using photoemission spectroscopy and compared with their self-consistent energy band structure calculations. Their experiments showed that two hydrogen-induced features appear below the Nb *d*- band. However, their band structure

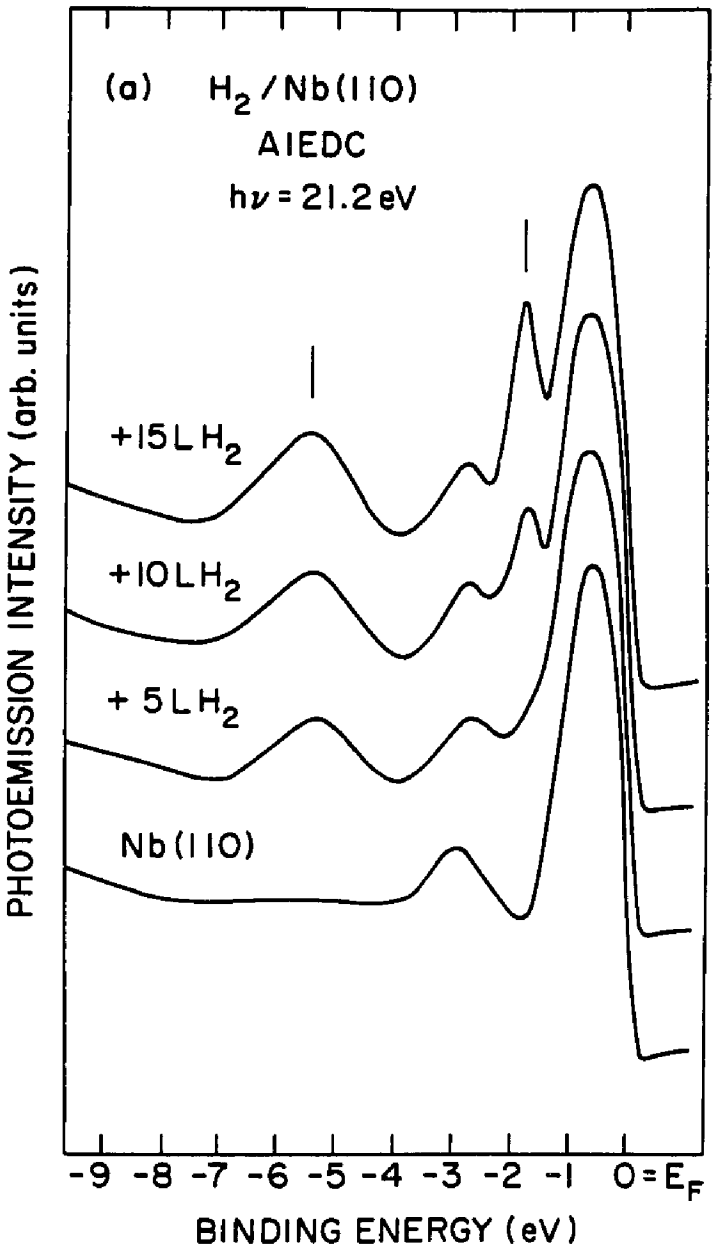

Figure 26: AIUPS EDC's from Nb(110) after various exposrue of H_2 at 300 K. The incident photon energy is 21.2 eV.

calculation predicts only one hydrogen-induced feature. The cause of the discrepancy between the previous calculated density of states and photoemission data has been discussed by Ho *et al.* [82] Their first-principles total-energy calculations give a better description of the metal-hydrogen interactions in the metal hydrides. However, no energy-band structure was shown which makes it difficult to compare with the angle-resolved photoemission experiments. The study of hydrogen chemisorption of W(100) by Feuerbacher and Williams [83] suggested that the strong overlap of hydrogen 1*s*- with specific metal-group *d*- orbitals which are strongly localized at the surface may lead to four levels of hydrogen-induced states. In that case three of them below the Fermi level.

Fig. 26 shows the AIUPS EDC's for hydrogen chemisorbed on Nb(110) at room temperature. Two hydrogen induced features were observed at the initial state energy -6.0 eV and -1.8 eV. The -6.0 eV feature is much broader and probably can be assigned to the hydrogen bonding state [59]. The feature at -1.8 eV is very sharp and can be attributed to the hydrogen modified Nb state. Similar hydrogen induced states have been seen in photoemission spectra at different photon energy from hydrogen adsorbed on Nb(110) [78] and Ta(110) [84] surfaces. However, some differences in interpretation exist. Smith [78] found that the initial-state energy of this dominant feature at -1.8 eV is photon-energy dependent in the normal emission geometry. Together with a 1×1 LEED pattern after a saturation hydrogen exposure, it is believed that a three-dimensional complex of metal and hydrogen is formed in the near-surface. The non-linear growth of hydrogen induced states as a function of hydrogen exposure suggests some mechanism which is related to dissociation, diffusion, or limited surface chemisorption sites. Murgai *et al.* [84], who performed the analogous experiment for hydrogen on Ta with synchrotron radiation, showed that at normal emission the initial-energy of the hydrogen induced states on Ta(110) does not disperse with photon energy and therefore suggested a two-dimensional nature of hydrogen on Ta(110). Because of final-state effect, the cross section of the hydrogen induced Σ_2 excitation become large below 16 eV photon energy. For the EDC's of hydrogen on Nb(110), the separation of the Σ_2 excitation and the dominant hydrogen induced state is about 0.6 eV, which may not be well resolved in the study of Smith [78]. It is possible that the evidence of dispersion behavior on hydrogen modified Nb(110) has been mistaken from the Nb Σ_2 excitation.

To obtain a better insight into the hydrogen interaction with transition-metals, we have also conducted a k-resolved inverse photoemission study of hydrogen on Nb(110) at room temperature. With a saturation exposure of 20 L hydrogen on Nb(110), Fig. 27 shows the

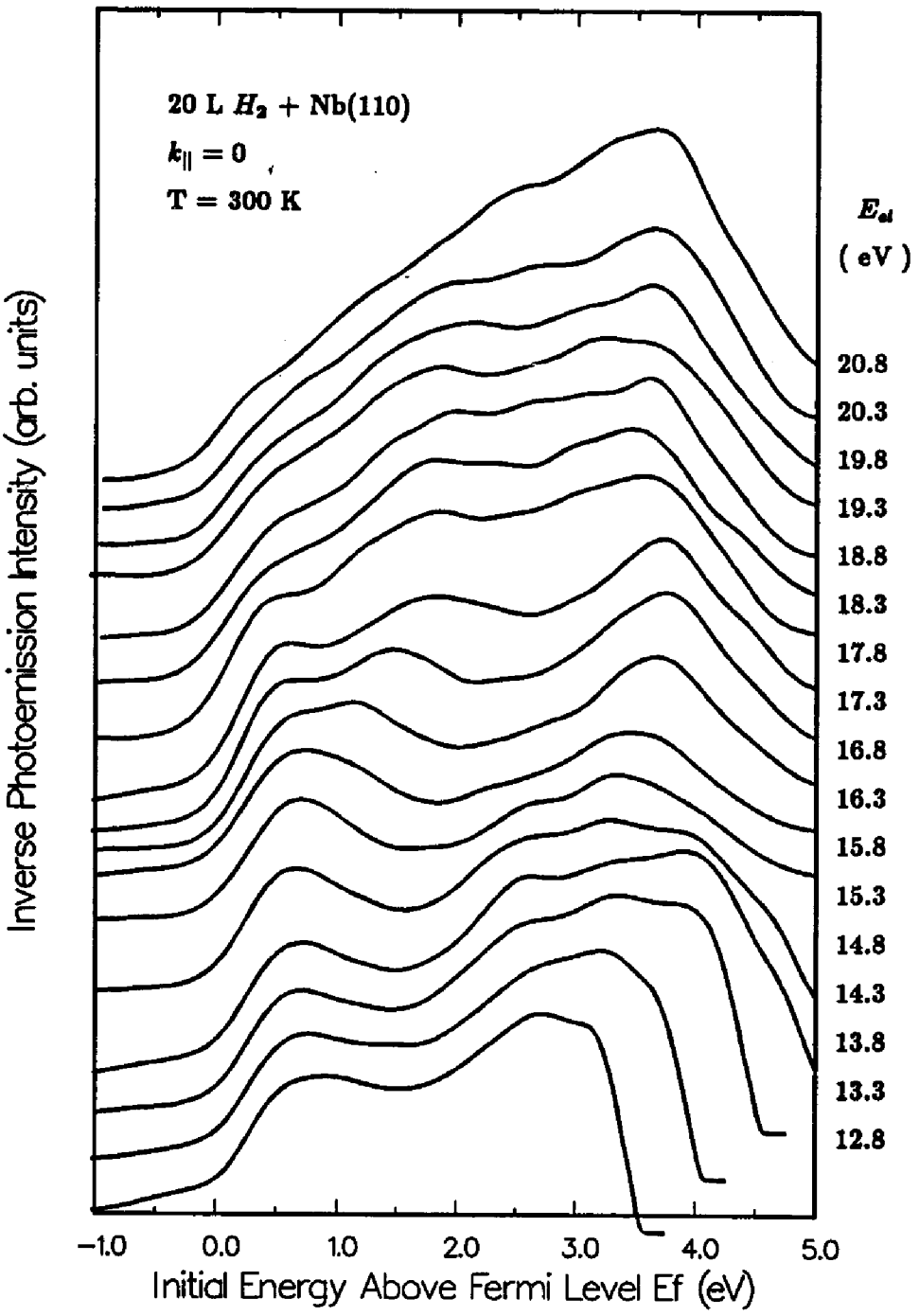

Figure 27: KRIPES spectra of Nb(110) saturated with 20 L hydrogen obtained in normal incident geometry as a function of incident electron energy with respect to the Fermi level.

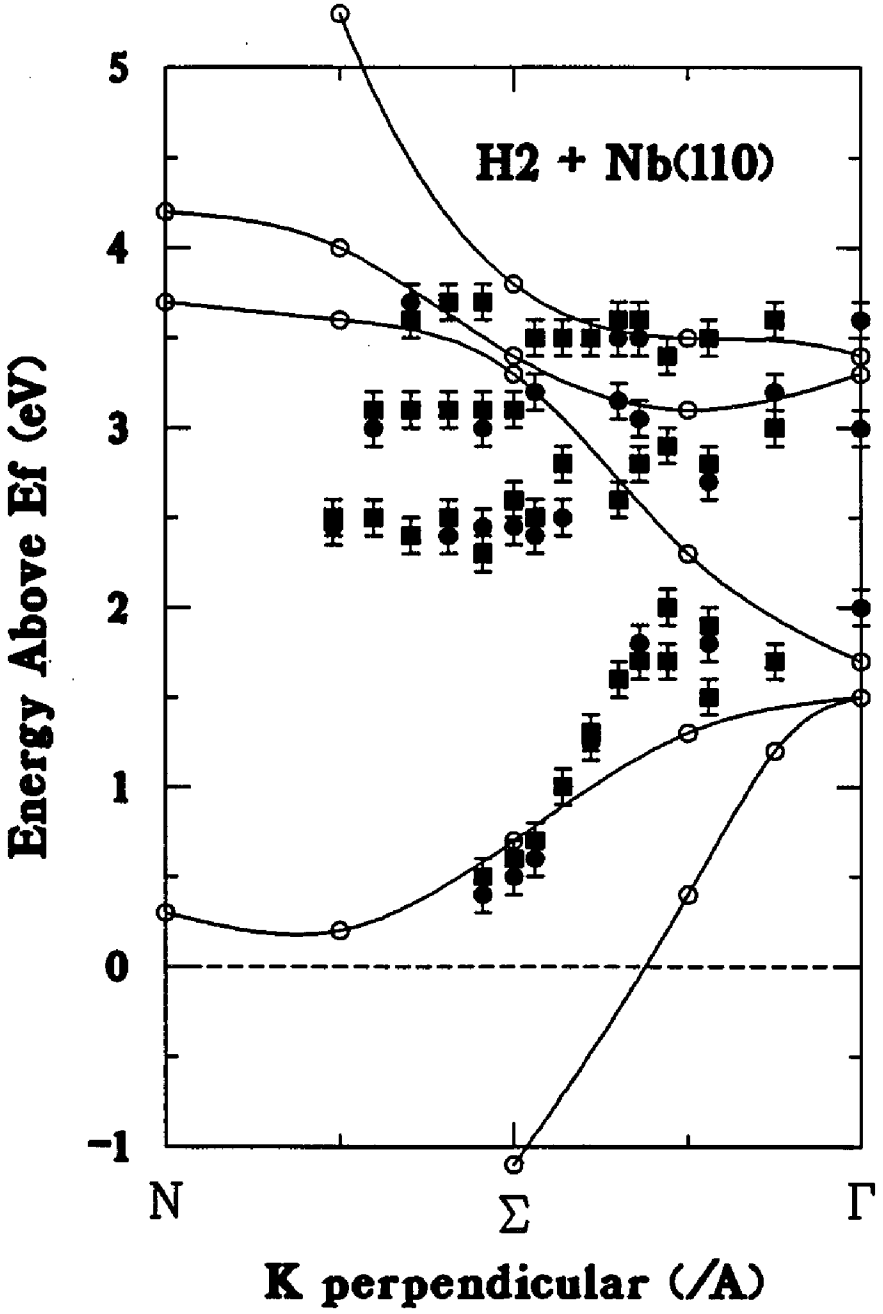

Figure 28: Experimental data of hydrogen chemisorption on Nb(110) compared with the theoretical calculation of Peterman on γ-NbH.

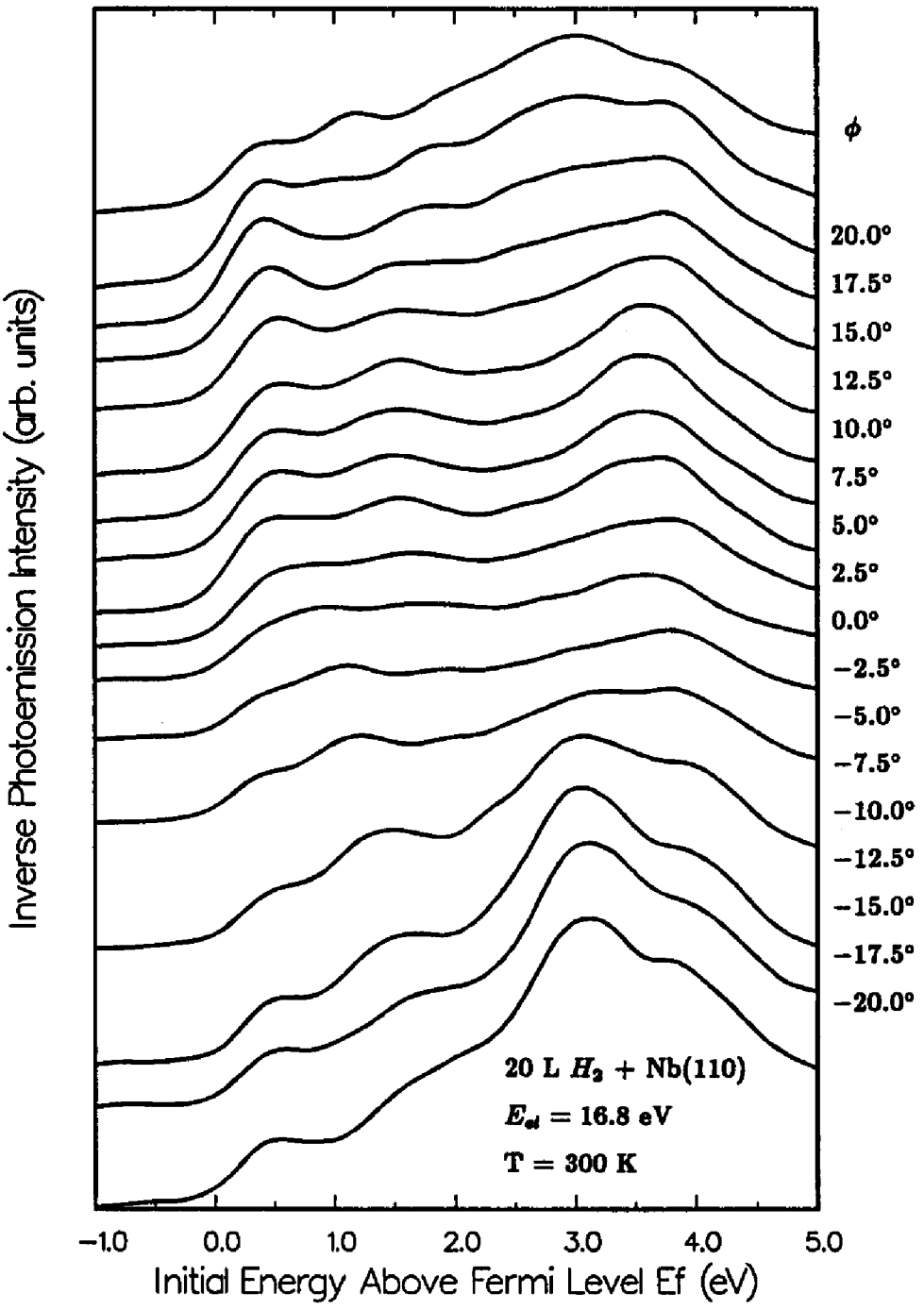

Figure 29: KRIPES spectra of Nb(110) saturated with 20 L hydrogen obtained as a function of incident angles tilted along the $\bar{\Gamma}\bar{P}$ direction. The incident electron energy is -16.8 eV with respect to the Fermi level.

empty state energy-distribution curves obtained in normal incident geometry from Nb(110) as a function of incident electron beam energy with respect to the Fermi level. Two hydrogen induced states can be extracted. The state located at 2.6 eV initial energy above the Fermi level is very localized and possibly split off from the Nb *d*- state in the surface region. The intensity of this split off state goes through a minimum near the Γ point along the surface normal direction. The other hydrogen-induced state located near the Fermi level has a similar dispersion as the first Σ_1 above E_F. However, at the Γ point of the Brillouin zone the initial energy of this hydrogen-induced state is 0.5 eV higher than that of Nb $\Gamma_{25'}$ point. It is noted that this hydrogen-induced state only appears above 17 eV electron beam energy. To compare with the theoretical energy-band calculation of Peterman's [81] on γ-NbH, we plot the data of our hydrogen chemisorption on Nb(110) along the Σ direction in Fig. 28. As a first-order approximation, we use the same initial-state band of Nb obtained from previous section to extract the final state data. Even with a rigid shift of 1.8 eV on the theoretical calculated energy-band, we found almost no agreement on the hydrogen-induced states, since the most of theoretical calculations the primary effect of adding hydrogen into the lattice is just a lowering and hybridization of the metal states.

To our knowledge, this is the first time that a k-resolved inverse photoemission study of hydrogen chemisorption has been made on the transition-metals. Lack of theoretical support from energy-band calculation makes the interpretation of our k-resolved inverse photoemission data difficult. The hydrogen-induced feature near the Fermi level can be due to either the hydrogen modification of the first Σ_1 band above E_F or the Σ_2 band, as Murgai and Strongin [84] have shown that the presence of the hydrogen alters the matrix element of bulk transition in Ta(110) to allow the excitation of Σ_2 state. Previous normal photoemission spectra have indicated that the Σ_1 band is modified by adsorbed hydrogen and pulled down to below the Fermi level. The fact that this structure becomes significant only below 18 eV photon energy in the photoemission experiment[84] and above 16 eV electron beam energy in the inverse photoemission suggest that this may be a hydrogen-modified Σ_2 state. The hydrogen-induced state in 2.6 eV initial-energy has a flat character as a function of incident electron energy or along the Σ direction of the Nb Brillouin zone. It is possible that this state is due to the interaction of hydrogen 1*s*- state with Nb *d*- state at the surface region. Fig. 29 shows the KRIPES obtained as a function incident angles tilted along $\bar{\Gamma}\bar{P}$ direction from Nb(110) surface saturated with 20 L hydrogen. The incident

electron beam energy is at 16.8 eV from the Fermi level, where the intensity of the hydrogen-induced state at 2.6 eV has a minimum. Careful examination of the hydrogen-induced state near the Fermi level reveals that the dispersion of this state actually has a opposite curvature (positive curvature) to the Nb Σ_1 band near E_F. This state disperses away from the Fermi level when the angle of incident electron tilts away from the surface normal. This kind of dispersion character can be related to bonding of adsorbate to the substrate. At this point, it is possible that these two new states originate from the interaction of hydrogen 1*s*- with the unoccupied Nb *d*- states.

In summary, we have studied the CO chemisorption on Nb(110) and Ta(110) at 300 K and 80 K using angle-resolved synchrotron radiation photoemission. At 300 K, CO molecule dissociates on the metal surface to form carbon and oxygen species. However, CO molecularly adsorbs on the surface of Nb(110) and Ta(110) at 80 K which may be due to the low activation energy for CO dissociating at low temperatures. Hydrogen chemisorption on Nb(110) has been studied by the photoemission and k-resolved inverse photoemission. The two states below the Fermi level can be assigned to hydrogen-induced bonding and antibonding orbitals. The nature of the two states above the Fermi level are not clear and requires further study.

3.5. Summary

In this section, we have presented and discussed the correlation between the electronic structure and chemical properties of transition-metals. The fcc transition-metal, such as Ni, Pd, and Pt, have a (111) most close packed surface and a more than half filled *d*- band. CO molecule chemisorbs strongly on these late transition-metal surfaces. CO bonds linearly to the surface with the carbon atom down on the metal substrate. The primary bonding arises from the CO 5σ orbital interaction with the unoccupied metallic *d*- orbitals and the interaction between the occupied *d*- orbitals and the unoccupied molecular $2\pi^*$ level. Adsorption of hydrogen onto these surface at low temperatures produces a bonding hydrogen level split off from the substrate *d*- bands. At room temperature hydrogen dissociates and adsorbs into subsurface site where the split-off state is not visible. The bcc transition-metal, such as Nb and Ta, have a (110) most close packed surface and a less than half filled *d*-band. At room temperature CO dissociates on Nb(110) or Ta(110) surface, but molecularly chemisorbs at 80 K due to the lower activation energy at the low temperatures. The adsorption followed by absorption of hydrogen into the Nb subsurface has been confirmed by the photoemission and inverse photoemission studies. However, a further study on the inverse photoemission data is required for a complete understanding of the electronic structure of hydrogen chemisorbed on Nb(110) and the hydrides of Nb. These fundamental physical and chemical properties will provide a solid background for the further understanding the nature of a modified metal surfaces and the metal-metal interfaces.

Chapter 4.
Electronic Structure and Chemical Activity of Pt Overlayers

4.1. Introduction

Angle-resolved synchrotron radiation photoemission, low-energy electron diffraction and Auger electron spectroscopy have been used to study the growth of Pt overlayers on Nb(110) and Ta(110) at different temperatures to determine the effect of electronic structure and overlayer morphology on surface chemical activity. Previous investigations have shown that the chemical activity of the metal overlayers can be varied by interactions with the substrate and can be different from the bulk material of either the overlayer or substrate. For example, CO does not chemisorb at room temperature on Ta(110), W(110), or Au(111) surfaces covered by a monolayer of Pd [4,6,85]. The novel chemical behavior of the Pd monolayer can be traced to the apparent low electronic density of states at the Fermi level (E_F). We believe that both the electronic and geometric structure of the overlayer play a very important role in modified surface chemical activity, but as will be demonstrated we attribute the novel chemical activity of Pt overlayers to substrate-induced modification of the surface layer's valence band electronic structure which superficially resembles that of a noble metal with a fully occupied *d*- electronic density of states. We define as interface states the new Pt states localized in atomic layers immediately adjacent to the interface. These electronic interface states which appear shifted below the Fermi level due to the rehybridization of the *d*- orbitals of the thin-film overlayers with the metal substrate may prevent electron donation from CO 5σ states to the Pt overlayer and reduce *d*- electron back donation to the CO $2\pi^*$ unoccupied states. In the previous experiment of Pd/Ta(110) [4] the Pd monolayer surface, with an atomic structure identical to the Pd(111) surface, had a drastically reduced CO sticking coefficient at room temperature. When the temperature was reduced to liquid nitrogen temperature to induce CO adsorption, modification of the CO molecular orbitals showed that the CO-metal chemical bond was weaker, as evidenced by the transposition of the $1\pi - 5\sigma$ levels and the strengthening of the 4σ shake-up peak due to the readjustment of the valence electrons of the system to screen the photoinduced 4σ hole.

In this chapter the results for Pt overlayers on Nb(110) at room temperature and on Ta(110) at low temperature will be presented to demonstrate that the Pt monolayer undergoes the structural phase transition from a commensurate to an incommensurate structure below a monolayer coverage, and the combined effect on the sticking of CO is very similar to that of Pd overlayers on refractory metals. Pt was chosen for this experiment because of its chemical and catalytic properties, which differ significantly from the Nb(110) and Ta(110) substrate, and because its *d*- band structure and relative Pauling electronegativity suggest a strong interaction between the Pt and Nb or Ta. Another important reason to study the Pt overlayers on Nb(110) or Ta(110) is that, unlike Ni and Pd, the band structure effects due to the electronic configuration changes between the metallic and atomic structures are expected to be very small. This is because the ground solid state electronic configuration for Ni, Pd, and Pt is approximately $d^9\,(sp)^1$ which happens to be the Pt atomic configuration. Hence the lower *d*- band cannot be attributed to intrinsic effect that the electronic structure of monolayer metal going into the atomic configuration. By studying this unique system, a better understanding of the correlation of the *d*- band surface structure with the chemical and catalytic properties is expected.

It should be mentioned that for the Pt overlayers on Nb(110) or Ta(110) the monolayer density is divided into commensurate and incommensurate regions. For the submonolayer Pt coverage, a commensurate $Pt^*(110)$ structure is formed on top of the Nb(110) or Ta(110). The monolayer density at submonolayer coverage of Pt will be $1.3 \times 10^{15} atoms/cm^2$. Above one monolayer coverage, Pt atoms form a close-packed fcc(111) structure with a monolayer density of $1.5 \times 10^{15} atoms/cm^2$. However, the interplane distance (thickness) of a Pt monolayer is always fixed to 2.26 Å.

Finally, the variation of CO photoemission features with photon energy, polarization and experimental geometry have been carefully studied at different Pt coverages and low temperatures. Comparison of these results with the theoretical models and predictions can provide insight into the nature of the metal-CO bonds on the overlayer surfaces.

4.2. Atomic Structure of Pt Overlayers

Pt coverage of $0.1 < \theta < 10.0$ monolayers were examined on a Nb(110) substrate kept at room temperature. Fig. 30 shows the normalized attenuation curves $I(\theta)/I(0)$ for the Nb 167 eV MNN Auger transition for $\theta < 5ML$ (ML = monolayers) based on the AES taken at 2 KeV electron energy. In the same figure, computed curves for three theoretical models of metal epitaxy are presented under the assumption that no reaction occurs at the Pt-Nb interface. They are Frank-van der Merwe mode (Fig. 30 (a)) with a layer-by-layer growth formation, Volmer-Weber mode (Fig. 30 (b)) with island formation, and Stranski-Krastanov mode (Fig. 30 (c)) with island growth on top of an initial continuous layer. Assuming a resonable escape depth of 7.1 Å for an Nb Auger electron with kinetic energy 167 eV, we found that experimental data could be fit quite well assuming layer-by-layer growth of Pt on Nb.

The LEED patterns shown in Fig. 31 (a) at low Pt coverage are identical to that of clean Nb(110) substrate but with increased background intensity. We believe that as in the case of Pd, commensurate Pt islands have formed on the surface of Nb(110) which we label as Pt*(110). At Pt coverage of about one monolayer, a set of ordered satellite spots appear in the LEED pattern (Fig. 31 (b)) which are assumed to be due to multiple scattering between an incommensurate Pt layer and the Nb(110) substrate. We believe this indicates that the Pt layer has undergone a first order structural phase transition from the commensurate to incommensurate structure. This might occur when the Pt islands exceed a critical size, and this might correspond to an island where the interior atoms become a clear majority. An alternative explanation might be that just before the completion coverage of the Nb(110) surface, some Pt is statistically deposited in a second layer which forces Pt islands to go incommensurate. At higher coverage, the LEED pictures shows that the ordered beat structure becomes fainter and the pattern characteristic of Pt(111) emerges.

These AES and LEED results consistently suggest that before the structural phase transition occurs at one monolayer of Pt on Nb(110), deposited Pt atoms form a commensurate Pt*(110) structure on top of Nb(110). With further deposition the Pt atoms form an incommensurate Pt(111) structure, and the epitaxy is in a layer-by-layer growth mode.

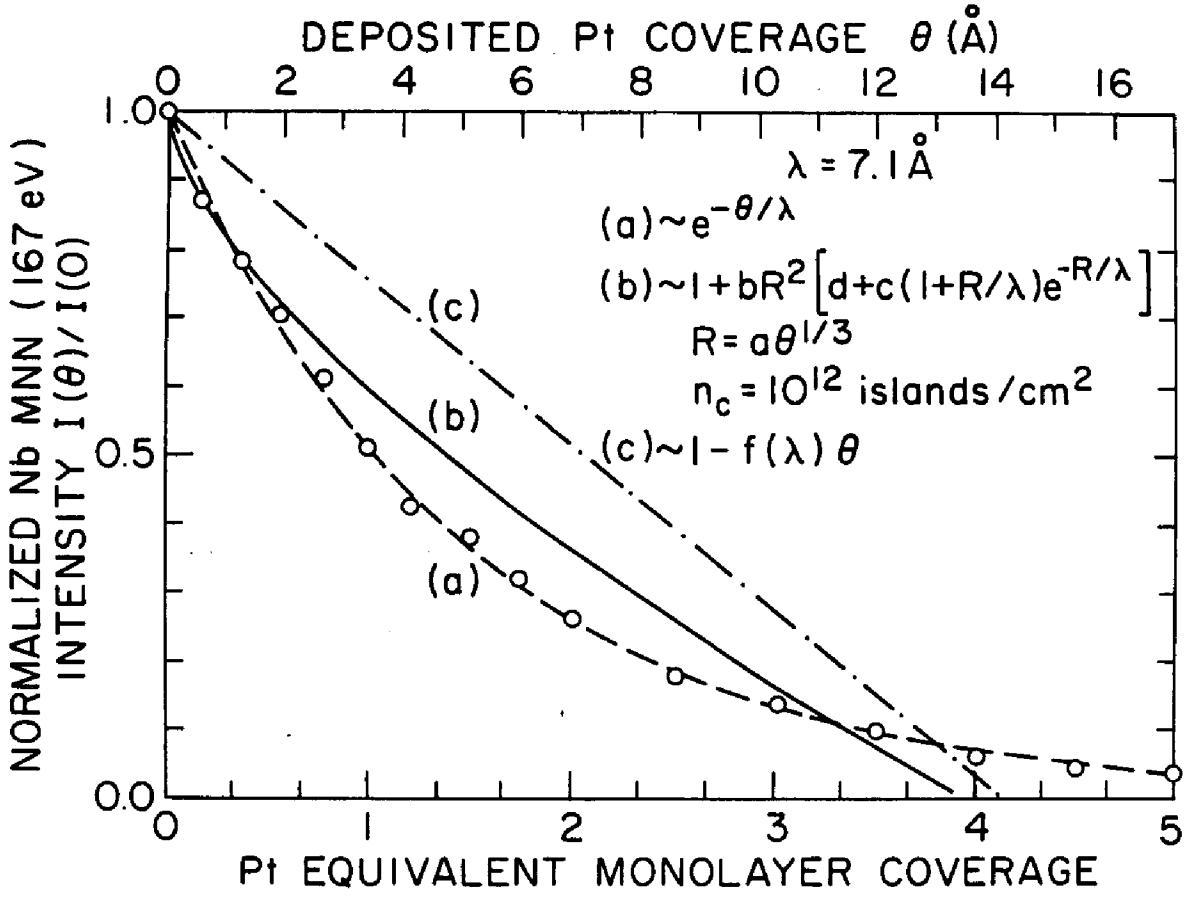

Figure 30: Normalized attenuation curves $I(\theta)/I(0)$ for the Nb 167 eV MNN Auger transition for Pt coverage $\theta < 5$ ML.

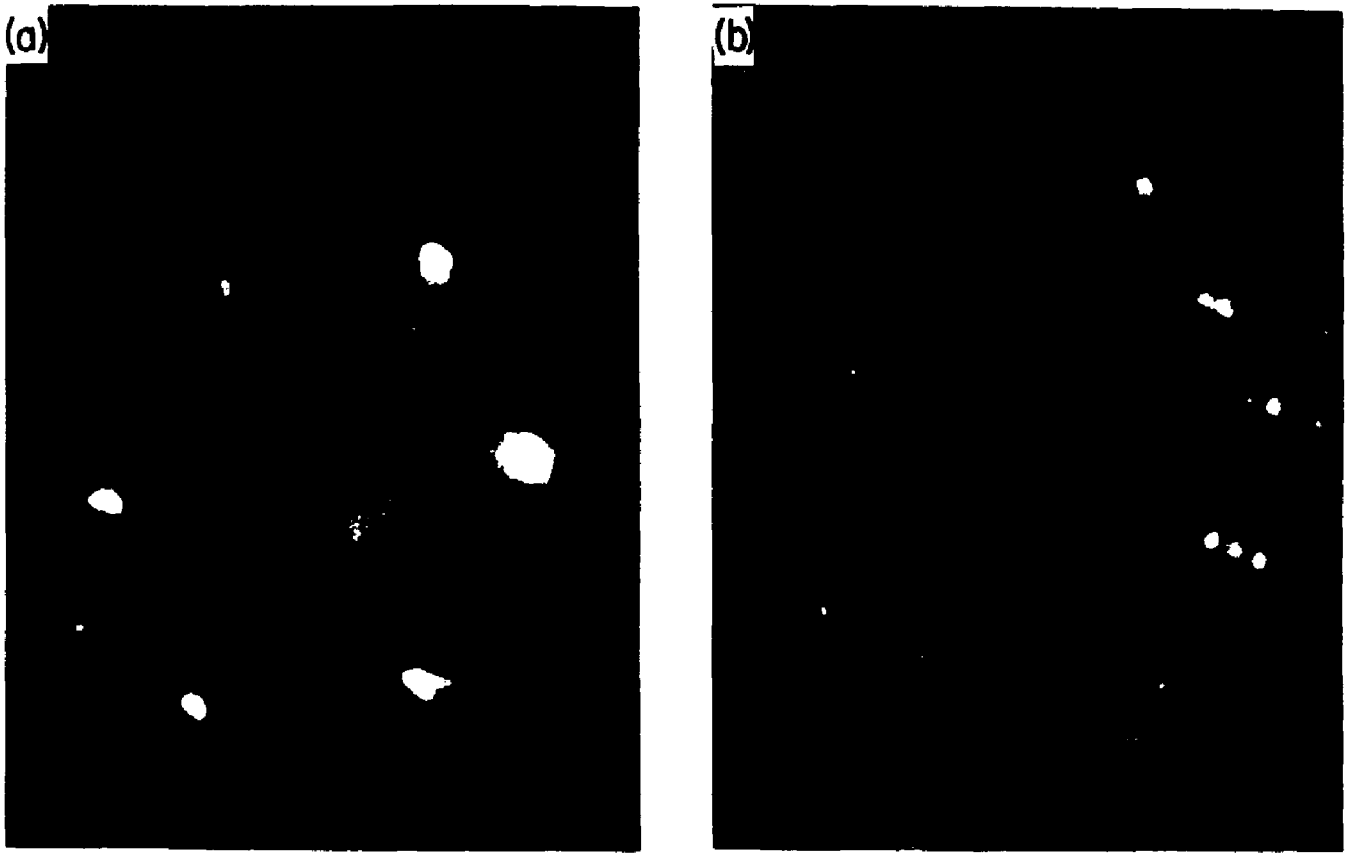

Figure 31: LEED patterns of (a) a commensurate Pt*(110) and (b) an incommensurate monolayer of Pt(111) on the surface of Nb(110).

4.3. Electronic Structure of Pt Overlayers

Angle-integrated photoemission spectra for increasing coverage of Pt, obtained at photon energies of 21.2 eV and 40.8 eV at an angle of incidence of about 45° are shown in Fig. 32. Photoemission from clean Nb(110) is characterized by a large peak 0.4 eV below the Fermi level (E_F). This peak is due to a direct photoexcitation transition from a local minimum in the Σ_1 band where it crosses below E_F midway along the Σ direction. A weaker peak at -3.1 eV can be attributed to the bulk transition from the lowest Σ_1 band [60,86]. The minimum at -1.8 eV results from a band gap between Σ_1 and Σ_2 which turns out to be very sensitive to both disorder and surface contamination [4,79] Additional photoemission states located between -0.4 eV and -1.8 eV are sometimes observed in polycrystalline samples and can be attributed to photoemission from other Nb surface planes. For submonolayer Pt coverage, the valence band spectra show four derived peaks located at -1.6 eV, -2.3 eV, -2.7 eV and -4.5 eV below the Fermi level. The -2.3 eV and -2.7 eV peaks develop rapidly with Pt coverage and reach a maximum value at one monolayer. The -2.3 eV and -4.5 eV peaks are relatively weaker at low Pt coverage and shift about 0.7 eV to lower binding energy as Pt coverage approaches and exceeds a monolayer.

At higher coverage the Pt valence band undergoes further evolution. The -1.7 eV peak grows faster and shifts to lower binding energy. At coverage greater than monolayer coverage, the -2.3 eV and -2.7 eV peaks start to disappear. Beyond a coverage of a few monolayers, the -3.8 eV peak begins to grow rapidly and finally reaches the same intensity as the -1.5 eV peak, and the valence band photoemission spectra appear similar to those reported for single crystal Pt(111).

Correlation of the variation of valence band electronic states with Pt coverage suggests that -1.5 eV and -3.7 eV peaks which only grow to significant intensities above two monolayers coverage come mainly from the bulk Pt 5d- electron density of states and indicates that significant amounts of Pt metal appear on the surface. The peaks at energy -2.3 eV and -2.7 eV only appear at low coverage of Pt on Nb(110). We suggest these are Pt-Nb electronic interface states formed from hybridization of the *d*- bands between Pt and the underlying Nb substrate. For Pd overlayers on Nb(110), resonable agreement was found between theoretical calculations and experimental results for Pd^*-Nb(110), and a Pd-Nb(110) resonance state was observed at about -3.0 eV energy below E_F for commensurate Pd on Nb(110) [10]. Angle-resolved photoemission identified the Pd-Nb interaction states, *i.e.* d_{zz}- and d_{yz}- like initial states were detected [62] which are involved in the bonding between the Pd adlayer

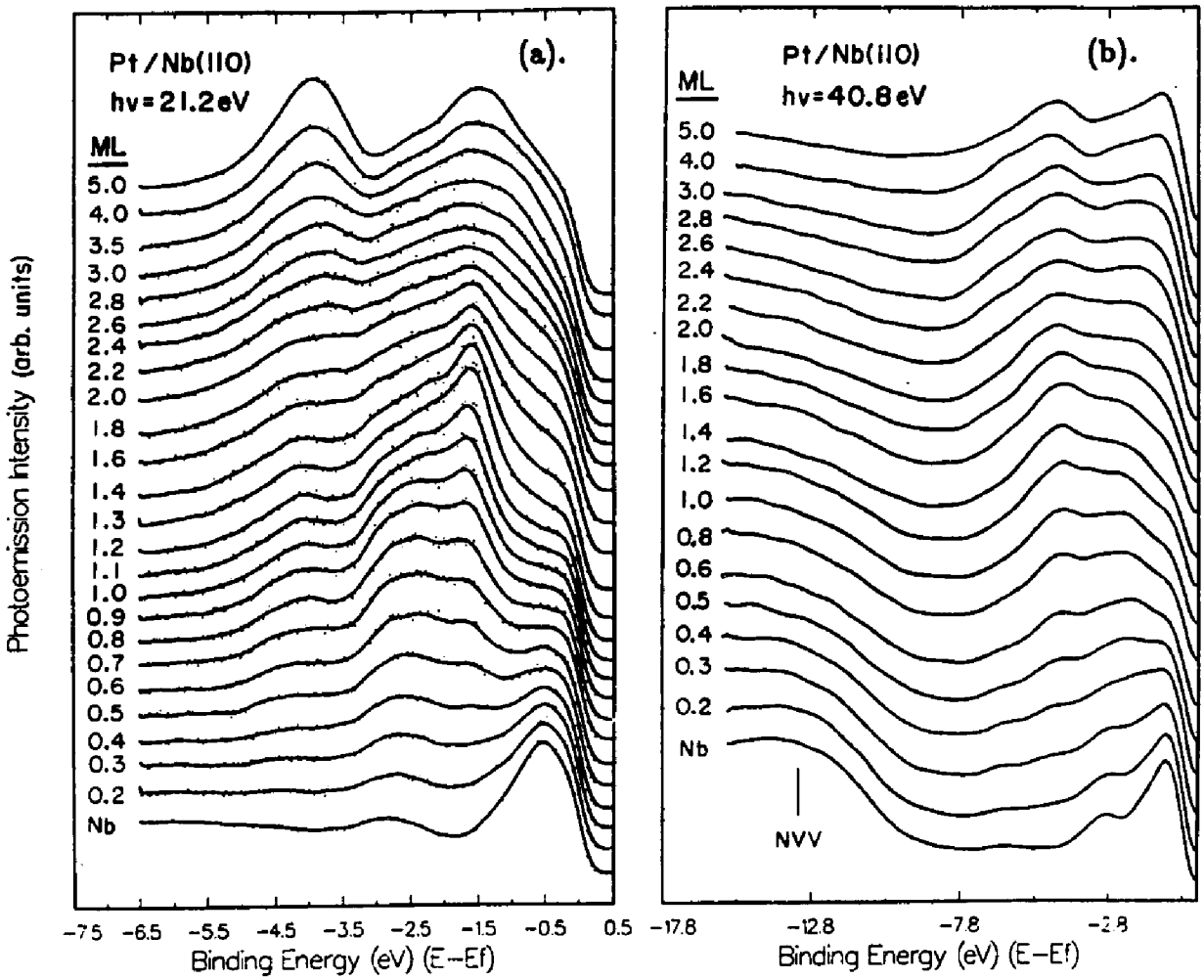

Figure 32: Angle-integrated photoemission spectra obtained from a Nb(110) surface for various coverage of Pt with photon energies of 21.2 eV (a) and 40.8 eV (b).

and the Nb(110) substrate. The energy difference between the d_{xz}- and d_{yz}- like initial states was found to be close to the calculated value of 0.3 eV. Similar results are expected for Pt. At low Pt coverage, a commensurate Pt*(110) was formed on the surface of Nb(110). Thus the overlayer has the same C_2 point-group symmetry as the Nb(110) substrate. This two-fold symmetry of the Pt*-Nb(110) system gives rise to an energy splitting of the Pt d_{xz}- and d_{yz}- like initial states which produces the -2.3 eV and -2.7 eV photoemission peaks.

In comparing Pt-Nb(110) to Pd- and Cu-Nb(110), it should be noted that the nearest-neighbor distance for Pt(111) planes is 2.77 Å, about 3% smaller than that for Nb(110) planes. The cohesive energy of Pt is 5.84 eV/atom and is much larger than that of Pd, Ni, Au, Ag and Cu. This indicates stronger interactions between the Pt atoms. The fact that the commensurate Pt structure persists up to monolayer coverage on Nb(110) indicates that there are strong interactions between the adsorbate and substrate atoms which tightly bond the adsorbate atoms to the substrate and force the Pt overlayer into the Pt*(110) structure. For the photoemission spectra at this stage, overlayer formation is dominated by strong electronic interface states located at 2.3 eV and 2.7 eV below the Fermi level as discussed earlier. After the structural phase transition the -2.3 eV and -2.7 eV peaks are quickly overwhelmed by the Pt bulk states and finally disappear at about two monolayers coverage where they are replaced by Pt bulk *d*- states at -1.5 eV and -3.7 eV binding energy. This indicates that the Pt-Nb(110) interface is covered by Pt metal. It should be mentioned that the photoemission spectra in Fig. 32 have been normalized. The actual photoemission intensity of five monolayer Pt is five times larger than the one shown in Fig. 32. The significant difference of photoemission intensity for various Pt coverage may arise from the difference in photoionization cross section of Pt and Nb substrate and also due to the superposition of photoemission from various parts of the Pt overlayers.

4.4. Work Function of Pt Overlayers

It is well known that the electronic work function of a clean single crystal surface depends on the crystallographic orientation of the surface. Closely packed surface planes exhibit a higher work function than planes with a more open lattice structure because every surface protrusion on an atomic scale associated with the surface roughness has a positive dipole moment when compared to the smoothest atomically perfect surface, such as the most-close-packed (110) surface in a bcc crystal or (111) surface in an fcc crystal. Adsorption of atoms and molecules may also change the sample work function. Usually, electronegative adsorbates give rise to an increase in the work function and electropositive adsorbates reduce the work function. Generally the work function of the adsorbed layer is influenced not only by the surface atomic structure but also by the electronic structure. In a simple model, changes in the work function due to adsorption can be described in terms of the dipole moment p and the density of the adsorbed species n, *i.e.*

$$\Delta\phi = -4\pi enp \tag{4.4.1}$$

However the occurrence of large initial charge transfer and strong depolarization with increasing coverage of adsorbate may complicate this picture. Bauer [87] has studied the dipole moments of transition metal atoms adsorbed on a W(110) surface by combining field ion microscopy (FIM) and probe hole field electron emission current measurements (FEM). For the Pd and Ni which have higher electronegativity and work function than W(110) substrate, their adsorption reduce the work function at submonolayer coverage. This work function decrease is attributed to the atomic- roughness dipole effect and the effects of shift and broadening on valence and affinity levels of the atom upon adsorption [88].

During the photoemission experiments, we applied a 6 V battery to measure the work function ϕ of Pt overlayers from the energy difference between the incident photon energy and the width of the angle-integrated photoelectron energy distribution curves (AIEDC's). The dependence of the Pt overlayer work function as a function of Pt coverage is shown in Fig. 33. Up to 0.5 monolayer Pt coverage, the work function increase slightly. A break point is observed at about 0.5 monolayer coverage. From 0.5 to 1.0 monolayer coverage, the work function increase almost linearly. Above one monolayer Pt thickness, rate of the increase slows down and finally the work function saturates at about two monolayers Pt coverage. The lack of a minimum in the work function at submonolayer coverage of Pt may be explained by the strong interaction of Pt adsorbate with an atomically more open

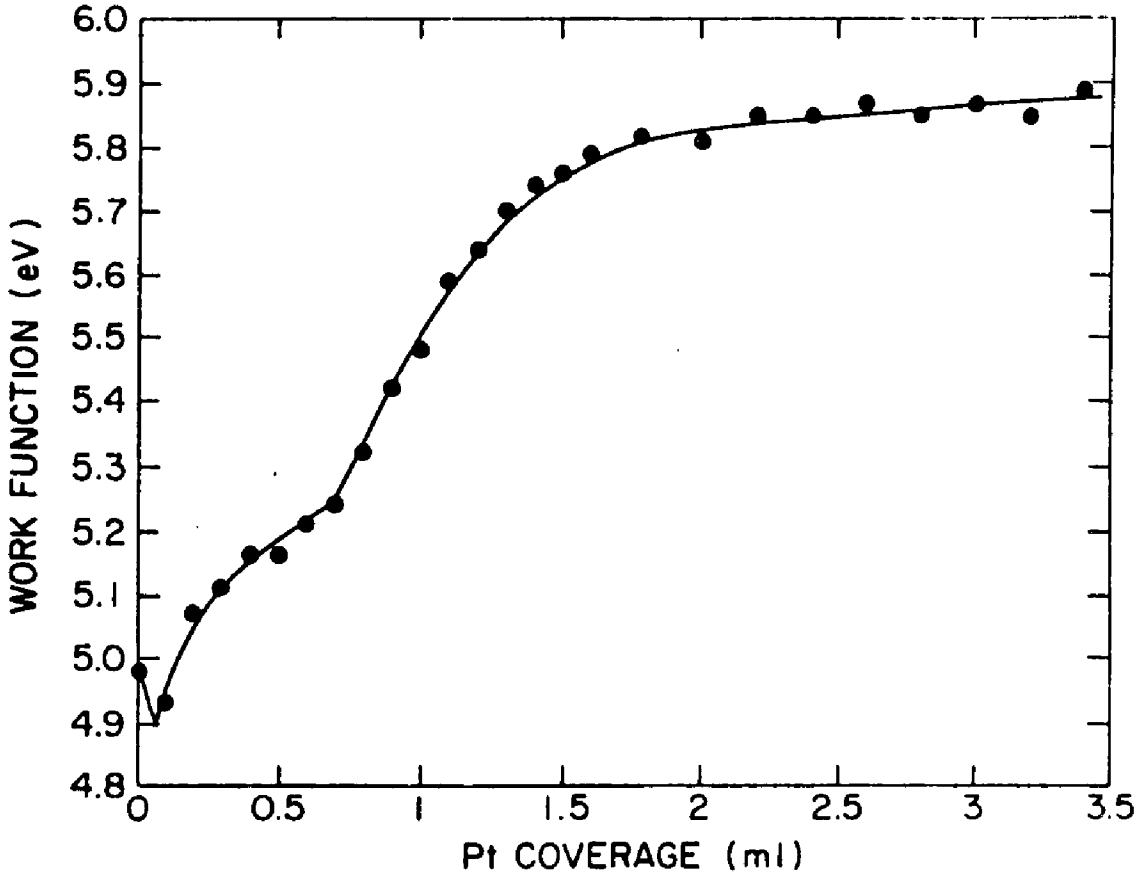

Figure 33: The dependence of work function of Pt overlayers upon the deposited Pt coverage on Nb(110).

substrate Nb(110) and epitaxial smoothing of the surface. Obviously, the work function here is a very sensitive indication of the surface structure of the adsorbate system.

4.5. CO Chemisorption on Pt Overlayers at 300 K

Fig. 34 shows the effects of the exposure of 20 L (one Langmuir = 1×10^{-6} Torr-second) CO on Nb(110) and selected Pt overlayers at 21.2 eV and 40.8 eV photon energy. The exposure of 20 L CO is sufficient to saturate the surface. The spectrum of CO chemisorbed on a Nb(110) surface shows that CO dissociates into individual C and O atoms producing C_{2p} and O_{2p} bonding states at about -4.0 eV and -6.0 eV binding energy, respectively. According to previously published work, CO dissociates on the Nb surface because the Nb valence *d*- band contains partially filled *d*- states to which electrons can be donated from CO 5σ orbitals and occupied *d*- states from which electrons can be back donated to the unoccupied molecular $2\pi^*$ levels [74,89-90] The resulting partial occupancy of the antibonding level weakens the CO bonds, leading to dissociation at room temperature. It is possible that at room temperature upon CO interactions with the Nb surface there initially exists a precursor adsorption state with the CO molecular axis considerably tilted towards or even parallel to the Nb surface. This state would enhance charge transfer from metal *d*-orbitals to the CO $2\pi^*$ and result in a strong interaction between the Nb substrate and the CO molecular oxygen end, and thus break the CO bonds to form a dissociative CO chemisorption on Nb surface. We have studied the influence of this precursor adsorption state on CO dissociative chemisorption on Ta(110) at low temperatures. More detailed results will be discussed in the next section. Fig. 35 shows the CO saturation coverage as determined from the height of C, O or CO photoemission peaks as a function of Pt coverage after an exposure of 20 L CO. The CO saturation peak height was obtained from the UPS spectra after the overlayer background has been subtracted. The error in CO coverage is estimated to be within 10%. It is possible that some Pt atoms reside in the second layer at Pt coverage approaching a monolayer. However, there are not enough Pt atoms in the second layer to show significant CO chemisorption which would be reflected in the photoemission spectra. At submonolayer coverage of Pt, a reduction in the amount of dissociative CO chemisorption was observed. The lack of molecular chemisorption on the Pt islands suggests that the presence of the Pt monolayer passivates the surface. We attribute the passive nature of the Pt to its unique electronic structure. The hybridization of the Pt 5*d*- states with substrate Nb makes the *d*- states of the Pt overlayer narrower and shifts them to higher binding energy, which reduces the electronic density of states at the Fermi level. We argue that the fully occupied Pt overlayer *d*- band prevents the charge transfer between the CO and the hybridized Pt layer and virtually eliminates the

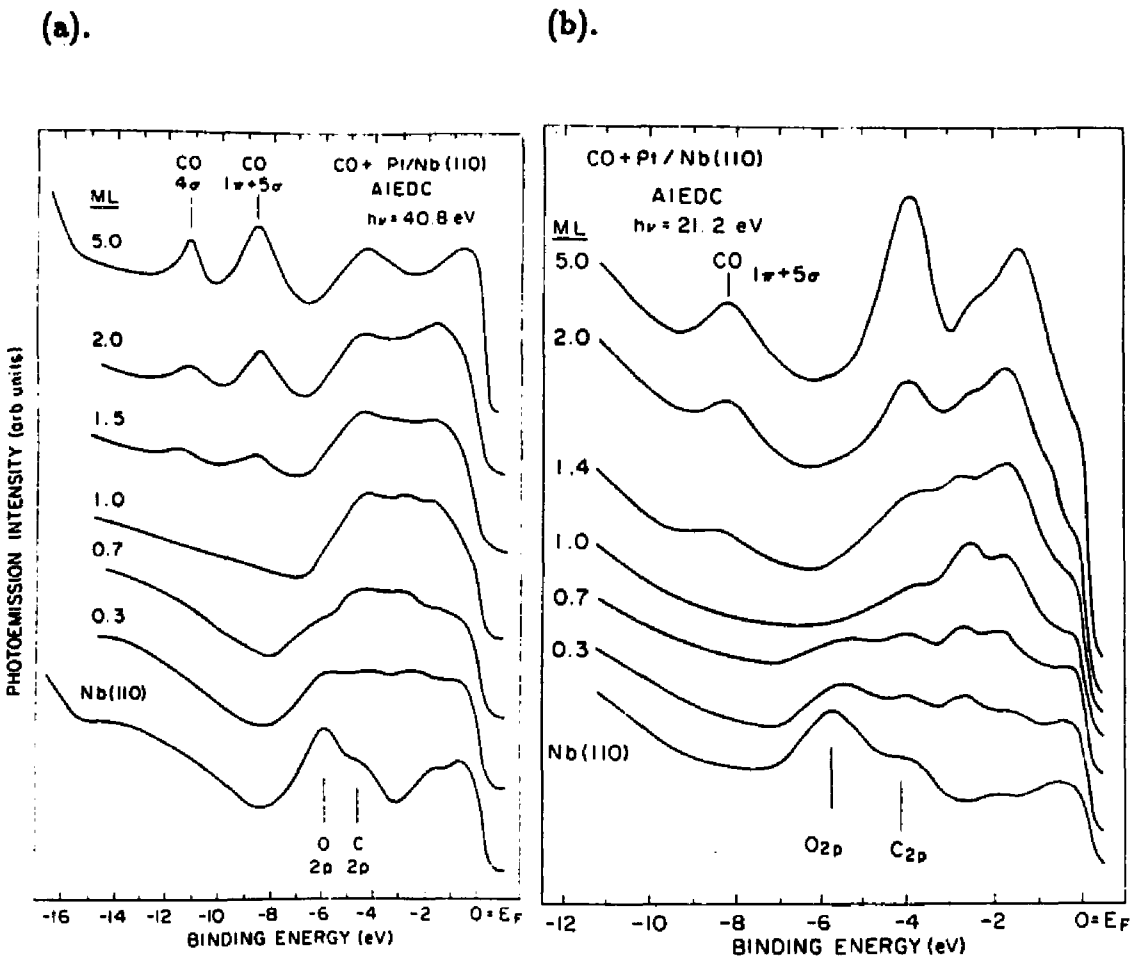

Figure 34: Angle-integrated photoemission spectra with 21.2 eV and 40.8 eV photon energies at 300 K for the selected Pt coverage on Nb(110) after exposure to 20 L CO.

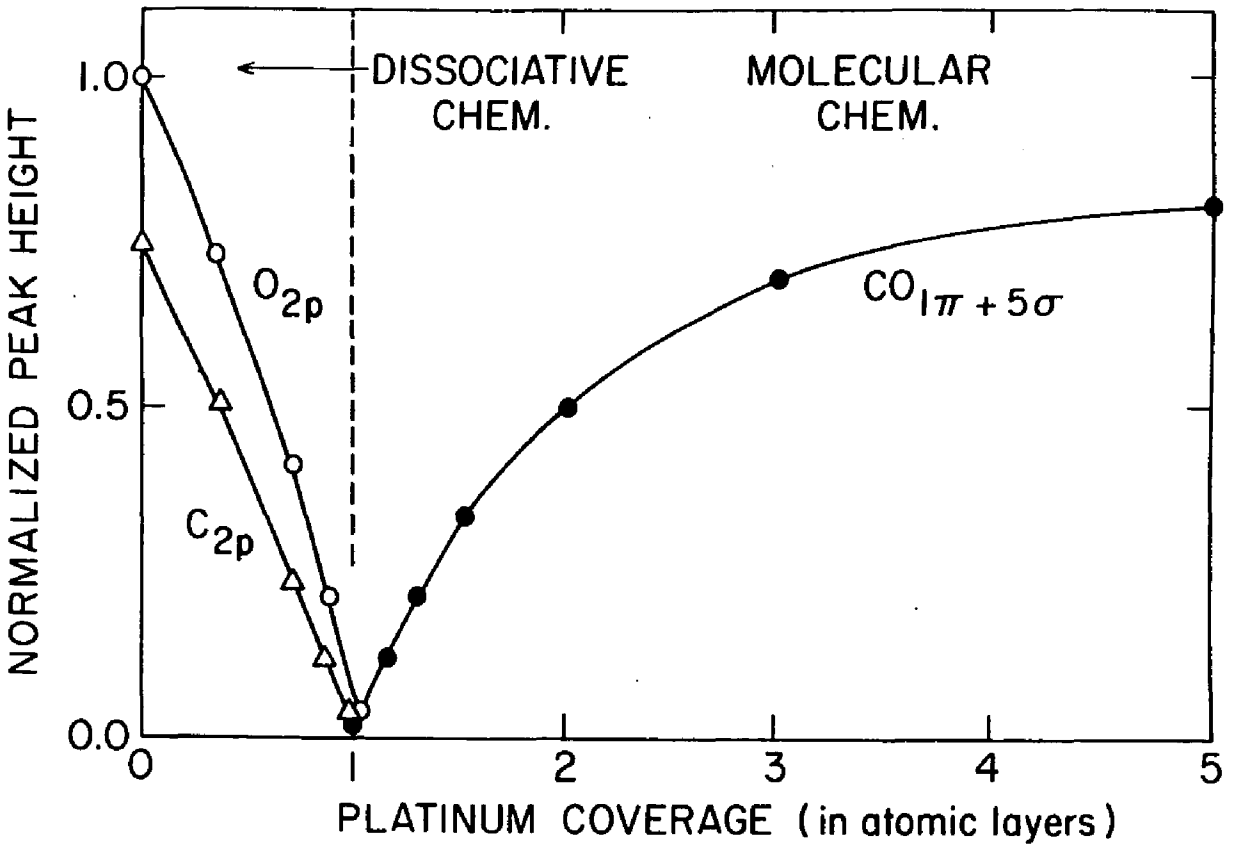

Figure 35: Coverage of CO on Pt overlayers on Nb(110) substrate after exposure to 20 L CO.

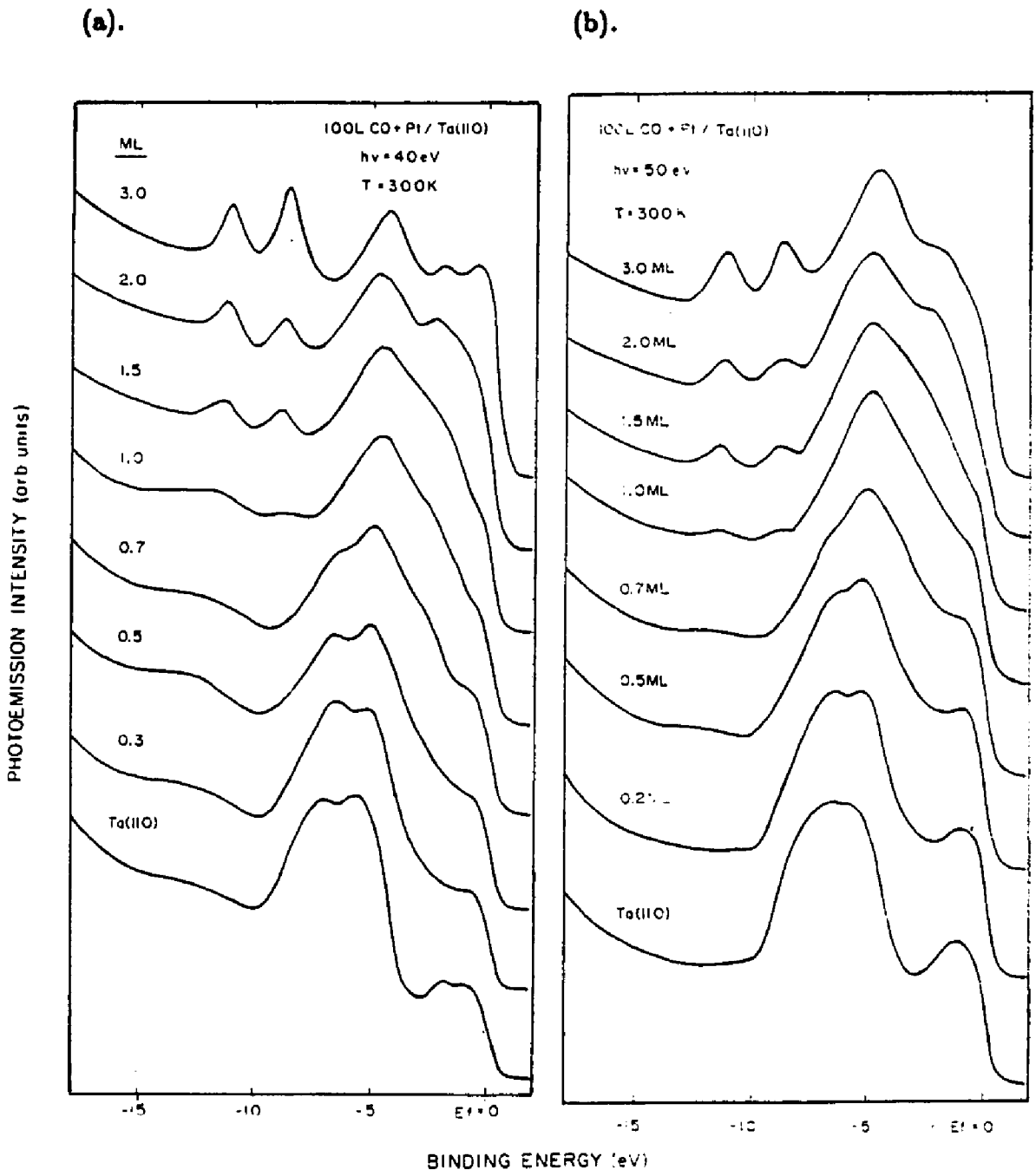

Figure 36: Normal emission ARUPS EDC's with 40 eV and 50 eV photon energies at 300 K for selected Pt overlayers on Ta(110) after exposure to 100 L CO.

CO adsorption. At one monolayer coverage when a Pt layer covers the surface, the electronic interface resonance reaches its maximum and no CO chemisorption was observed. Beyond a monolayer Pt coverage, the Pt bulk features start to appear and molecular CO adsorption begins. At five monolayers coverage, the overlayer shows the Pt(111) bulk character and molecular CO features. It should be mentioned here that it is inappropriate to attribute this chemical property to Pt atoms blocking the Nb(110) substrate active sites because the Pt surface itself readily chemisorbs CO molecules at room temperature. The key point is that the Pt monolayer undergoes changes in electronic structure which reduces its ability to form bonds with CO molecules.

Synchrotron radiation photoemission has been used to study the CO chemisorption on Pt overlayers supported by Ta(110) at 300 K. Fig. 36 shows the ARUPS EDC's taken at 40 eV and 50 eV photon energies after 100 L CO exposure to the Pt overlayers on Ta(110). It is noted that the results are very similar to that of Pt overlayers on Nb(110). No CO molecules adsorb on a monolayer of Pt surface. This result will be used to compare with the CO chemisorption on the same surface at 80 K in the next section.

Previous work has shown that CO chemisorbs on transition-metal surfaces by bonding linearly with the carbon atom down on the metal surface. Ligand to metal unoccupied *d*-orbital σ donation from CO 5σ orbital is balanced by metal occupied *d*- orbital to ligand π back donation into the CO $2\pi^*$ orbital. The large shift of the CO 5σ resonance state to higher binding energy is primarily determined by the σ interaction with metal atoms but has small π contributions. By using the molecular-orbital cluster models, Bagus [91] suggests that the bonding of CO to a metal arises primarily from the metal π to CO $2\pi^*$ interaction, and σ interaction actually produces a repulsion. This interpretation of the *s-p* metal CO interaction as σ repulsion and π bonding has been extended to the transition metal-CO interaction.

4.6. CO Chemisorption on Pt Overlayers at 80 K

To gain insight into the modified metal surface a low temperature experiment was performed at 80 K to induce CO chemisorption on the non-reactive surface modified Pt monolayer and to minimize CO bond breakage on the Ta(110) surface. CO chemisorption on Pt overlayers at 80 K has been carefully studied on the Ta(110) surface by angle-resolved synchrotron radiation photoemission. We show that the strength of the CO-metal bonds is significantly modified by thin film substrate interactions and cooling a Pt monolayer on Ta(110) to 80 K induces CO molecular adsorption. In addition, polarized synchrotron radiation was used to deduce the bonding geometry of CO on the modified metal film surfaces and this showed that the geometry of the CO-metal bond does not change for the surface studied.

From LEED, AES, and photoemission experiments, we found that the trends of electronic structure and morphology of Pt overlayers on Ta(110) are very close to that on Nb(110) substrate. This is because that the Ta has a very similar valence band and an identical lattice constant to Nb. The reason we chose Ta as the substrate is due to its low binding energy of the sharp core levels ($4f_{7/2} \sim 21.5eV, 4f_{5/2} \sim 23.5eV$). The splitting of these 4f states is perfect for our monochromator when using synchrotron radiation as light source. LEED and AES results show that deposited Pt atoms grow layer-by-layer. At submonolayer Pt coverage, a commensurate 1×1 structure is observed which is reflected by the multiple scattering of low energy electron beam between the Pt and the underlying Ta substrate. Above a monolayer of Pt thickness, a structural phase transition occurs, just like the Pt overlayers on Nb(110) case, and Pt atoms form a (111) incommensurate adlayer on Ta(110) surface. Photoemission studies show that addition of Pt to Ta(110) induces intense new states centered at 3-4 eV below the Fermi level. For the Pt overlayers on Nb(110), these states have been identified as interface bonding resonances. The interaction between the Pt adlayer and Ta(110) substrate reduces the density of states near E_F and increases the binding energy of the modified *d*- states. Similar valence band modification has been seen for Pt and Pd on other refractory metal surfaces [92-93]. Calculations for Pd overlayers on Nb(110) [10] suggest, by analogy, little net charge is transferred into the Pt *d*- band states but the significant Nb *d*- components are added to the wave function at Pt atomic sites and at the surface. Pt *d*- states are presumably localized on Nb sites adjacent to the interface. This implies that a strong chemical bond has formed between Pt and the substrate of Nb(110) or Ta(110).

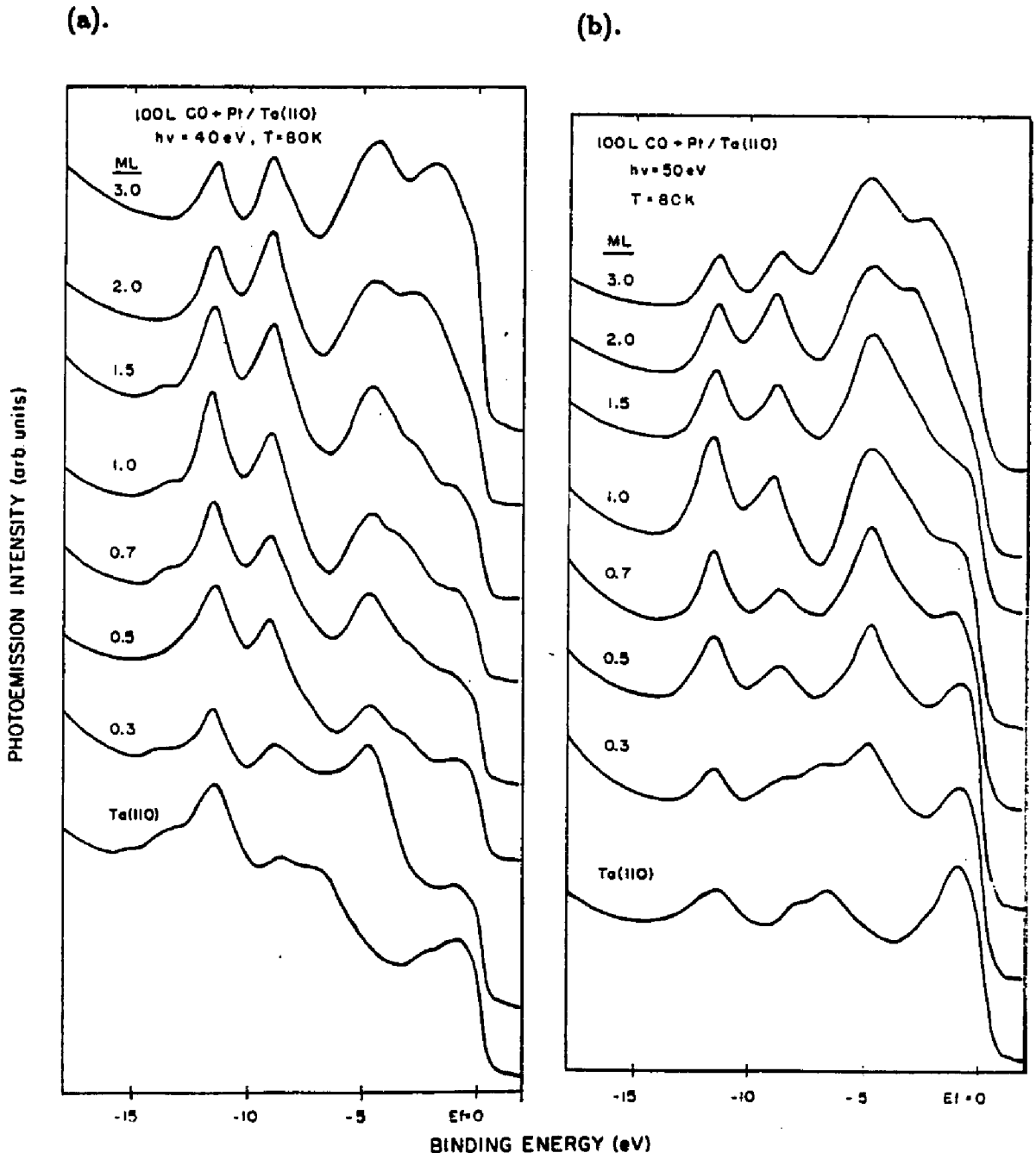

Figure 37: Angle-resolved photoemission normal emission spectra taken at 40 eV and 50 eV photon energies for the selected coverage of Pt on Ta(110) after a saturation exposure of CO at 80 K.

At room temperature, three distinct CO adsorption regimes are observed. For Ta(110) and submonolayer coverage of Pt, dissociative chemisorption occurs. Above monolayer coverage photoemission features attributable to molecular CO chemisorption appear. Increasing amounts of CO stick to the surface when the number of surface Pt atoms is increased beyond a monolayer coverage. The third regime of CO chemisorption is not readily apparent in room temperature photoemission spectra but is visible when the surface is cooled to 80 K. The adsorption of CO on Pt/Ta(110) at 80 K is illustrated by the photoemission spectra in Fig. 37. It is noted that after CO molecules adsorb onto a monolayer Pt surface, a new state appears at about 2 eV higher binding energy from the 4σ level. This state is enhanced at 40 eV photon energy and shows very little CO coverage dependence. A similar feature has been reported for the chemisorption of CO on Cu(100) at room temperature [94], where this state has been assigned to multi-electron excitation or shake-up process from the main peak 4σ state. Satellite features, similar to those reported by Plummer [74,94,95] and others for CO on Cu and attributed by Schonhammer and Gunnarson [96-97] to screening during photoemission from the 4σ by the 2π CO orbital, indicate that the involvement of the CO 2π level in bonding to the metal d_π (d_{xz}, d_{yz}) and d_σ (d_{z^2}) states is reduced. The fact that CO is not retained at room temperature on Pt monolayers supported on Ta also shows that the $5\sigma - d_\sigma$ (d_{z^2}) bond is weakened and suggests that there are fewer Pt metal surface states available to accept electrons from the CO 5σ level. These results are consistent with the trends noted in density of states calculations by Sung and Hoffmann [98] performed for close-packed surface layers of 3*d*- transition metals going from Ti(0001) to Ni(111). Sung and Hoffmann [98] found that the metal Fermi level decreases in energy and the overall width of the valence band decreases, as one goes through this series. The net effect is a reduction of overlap of the projected metal *d*- states and the 2π orbitals. Our photoemission results show that the Pt 5*d*- states do indeed move to greater binding energy. The interaction of CO molecules with modified surface electronic structures is characterized by the weak chemisorption of CO on noble metal surfaces.

Fig. 38 shows the ARUPS EDC's taken at 40 eV photon energy on Pt overlayers after a saturation exposure of CO gas at 80 K. If the CO molecule is standing upright on a flat surface, the 4σ intensity should be zero in the geometry of curve (b) because of the simple dipole selection rules. Only the odd orbitals (such as 1π level) can be seen in the geometry of curve (b) if the incident light is purely polarized. In the geometry of curve (a) and (c), the even orbitals (such as 4σ and 5σ levels) should be enhanced. These symmetry rules are

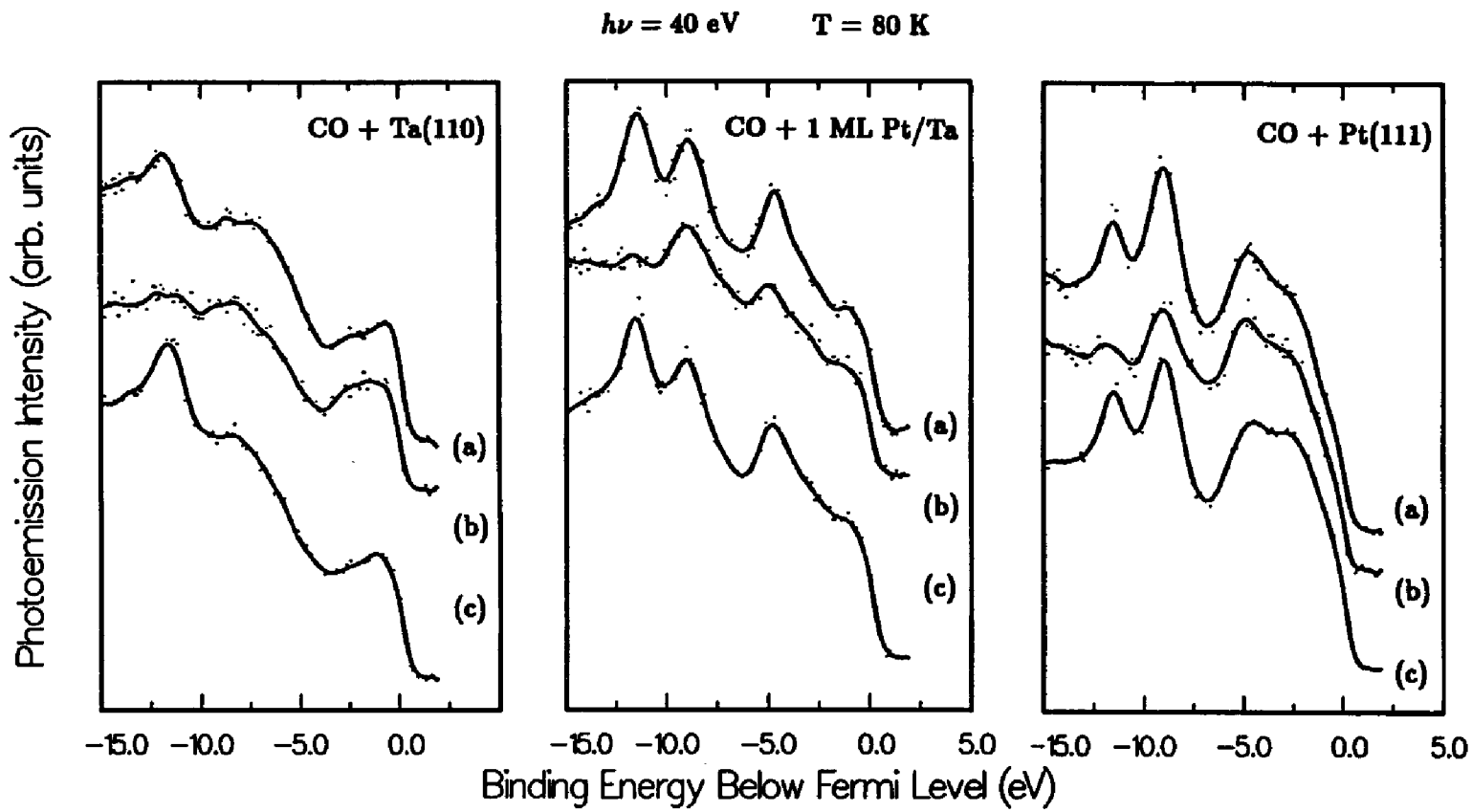

Figure 38: ARUPS EDC's of Ta(110), a monolayer of Pt, and a thick Pt(111) layer on Ta(110) taken at a photon energy 40 eV after a saturation exposure of CO at 80 K. The geometries of measurement are (a) 45° angle of incidence and normal emission, (b) normal incidence and almost normal emission ($\Delta\theta < \pm 5°$), and (c) normal incidence and a 45° emission.

clearly observed for CO adsorbed on Pt(111) surfaces. On curve (b) the 1π level dominates the CO induced states. The remaining of 4σ and 5σ states in this "forbidden geometry" is due to the incomplete polarization of the incident radiation. For the chemisorption of CO on a monolayer Pt surface at 80 K, the shape-up satellite is enhanced at the geometry of curve (a) and (c) where only the σ states should be enhanced. This is another evidence that the shake-up satellite is derived from the 4σ main peak and caused by the readjustment of the valence electrons of the system to screen the photoinduced 4σ hole. The screening effect on the 4σ hole reduces the electron occupation on $2\pi^*$ and thus indicates a weaker bond of CO molecule to the surface of a monolayer Pt [99]. It is still plausible that the intensity of CO induced states change as a function of Pt coverage. It might be partially due to the background changes upon the Pt overlayer growth on the Ta(110) substrate.

4.7. Summary

To summarize, we believe that a electronic hybridized Pt monolayer on the substrate of Nb(110) or Ta(110), as evidenced by the formation of electronic interface resonances at higher *d*- band binding energy, is responsible for the modified surface chemical activity. The strong Pt-Nb interface interaction makes the Pt *d*- band appear to be occupied and behave noble-metal-like. The substrate induced Pt valence band states at monolayer coverage are interface states which have a reduced density of states at the Fermi level. The decreased chemical activity of Pt when the coverage approaches a monolayer can be accounted for by an inert Pt overlayer blocking the active Nb(110) substrate. No CO chemisorption was observed at one monolayer coverage of Pt on Nb(110) and Ta(110) at room temperature, confirming that the modified Pt-Nb(110) and Pt-Ta(110) produces a chemically inert surface. When significant amounts of unmodified Pt appear at the surface, the chemical activity of the Pt overlayers resembles that of a Pt(111) surface.

Angle-resolved synchrotron photoemission spectra for CO on Pt overlayers of varying thickness on Ta(110) show that the strength of the CO-metal bond can be changed by varying the surface electronic structure. The temperature dependence of CO chemisorption on a modified Pt monolayer indicates a weak chemisorption at 80 K. By using the synchrotron radiation polarization vector $\vec{A}$ in the allowed and forbidden geometries we found that CO on Ta(110) at 80 K may not have its molecular axis normal to the surface. However, with the increase of Pt coverage on Ta(110) the CO molecules eventually became oriented nearly normal to the surface at 80 K.

Chapter 5.
Electronic Structure and Chemical Activity of Ni Overlayers

5.1. Introduction

Our previous work has been focused on studies of Pt and Pd overlayers on Nb(110). For Pt on Nb(110), a structural phase transition from a commensurate epitaxial overlayer to an incommensurate overlayer was found at about one monolayer coverage. Photoemission results show modification of the Pt-derived states attributable to Pt-Nb bonding. To compare with the results of Pt and Pd overlayers we chose Ni, which has a d^8- electronic configuration and a larger difference in lattice constant with with respect to the Nb or Ta substrate, as adsorbate to investigate the modified electronic structures and chemical properties. Using the same surface-sensitive techniques as mentioned before for studying Pt overlayers, we present here a study of the electronic structure and chemical activity of Ni overlayers on Nb(110) and Ta(110) at different temperatures.

Ni overlayers on Nb(110) and Ta(110) are another examples of an fcc late transition-metal on a bcc early transition-metal surface with (111) aligned fcc layers growing epitaxially on the (110) bcc metal substrate. Ni and Cu have very similar metallic radii. The growth of Cu overlayers on Nb(110) is quite different from that of Pt and Pd overlayers[9,11,60,100-104]. In the early stages of growth, less than 1.5 monolayers of Cu grow in an incommensurate structure resembling a strained fcc (100) Cu surface. Above that coverage the overlayer transforms to a fcc Cu(111) surface-like structure. The photoemission results indicated that the interaction between the *d*- band complexes of the Cu overlayer and the Nb substrate is weak. Our results show another interesting example which differ from those obtained with Cu, Pt and Pd overlayers on refractory metal substrates. The cohesive energy of Ni is about 21% larger than that of Cu and 12% larger than that of Pd. This implies the Ni-Ni atoms may have a stronger bonding. The lattice mismatch is another important factor affecting metal overlayer growth. The lattice mismatch of Ni on Nb(110) or Ta(110) is much larger than that of Cu, Pt and Pd which makes it a good system for studying the effect of increasing interfacial misfit on the formation of an fcc(111)/bcc(110) interface.

Since the deposited Ni atoms agglomerate on top of Nb(110) or Ta(110) to form the strained fcc (111) islands, we assume that a monolayer of Ni atoms corresponds to 1.9 ×

$10^{15} atoms/cm^2$, and the interplane distance of Ni overlayers, *i.e.* a monolayer thickness, is 2.03 Å. As in the Pt overlayer studies, this is a simplified picture, however, the error caused by this approximation should affect the estimate of Ni overlayer thickness by less than 10%.

5.2. Atomic Structure of Ni Overlayers

Deposited Ni overlayers with coverage from 0.1 to 10 ML were obtained on a Nb(110) substrate at room temperature. Systematic AES studies as a function of Ni coverage were performed in 10^{-11} Torr region. Fig. 39 shows the normalized attenuation curves $I(\theta)/I(0)$ for the Nb 167 eV MNN Auger transition for $\theta < 3ML$ based on the Auger spectra taken with a primary beam energy of 2 KeV. For Ni coverage less than 0.5 ML, the attenuation rate of Nb MNN Auger intensity is almost linear. A second linear region occurs above about two equivalent monolayer coverage. Three theoretical models describing the mechanism of metal overlayer epitaxy are presented under the assumption that no reaction occurs at the Ni-Nb interface. They are Frank-van der Merwe model (Fig. 39 (a)) with a layer-by-layer growth formation, the Volmer-Weber model (Fig. 39 (b)) with a islands formation, and the Stranski-Krastanov model (Fig. 39 (c)) with island growth on top of an intermediate continuous layer formation. Assuming a reasonable escape depth of $\lambda = 7.1$ Å for Auger electrons with a kinetic energy 167 eV, we found that none of these three calculated behaviors of growth modes can fit all of our experimental data well. Instead, if we combine features of two models and assume that two layer thick islands grow in a layer-by-layer mode at early stages, and that the growth mechanism of Volmer-Weber mode can explain subsequent growth. In Fig. 39 (c) it is assumed that three dimensional island growth occurs on top of the substrate and that these islands are hemispherical with an average radius R and concentration $N_c = 10^{12}\, islands/cm^2$ in the early stages of nucleation. For the coverage less than 2.5 ML, the calculated curve fits the experimental data quite well. Generally speaking, the attenuation of the Nb substrate is slower than would be expected for the layer-by-layer growth of a uniform Ni films and is consistent with the formation of Ni clusters beyond 0.2 ML coverage on Nb(110).

Fig. 40 shows the LEED patterns for ordered layers produced by different coverage of Ni on Nb(110). For $\theta < 0.2$ ML, the pattern of Fig. 40 (a) is observed. This LEED pattern is identical to that of clean Nb(110) but with an increased background intensity which implies that the Ni atoms are not ordered and randomly occupy Nb(110)-equivalent sites on the crystal surface. Fig. 40 (b) and (c) display patterns typically observed for the coverage of $0.2 < \theta < 1.0$ ML. Fig. 40 (b) indicates the formation of a distinct Ni structure which we label as Ni*(111) and is manifested in the set of extra spots displayed in the figure. These ordered satellite spots may be due to the multiple scattering between the Ni*(111) islands and the underlying Nb(110) surface or between Ni*(111) structure on top of islands

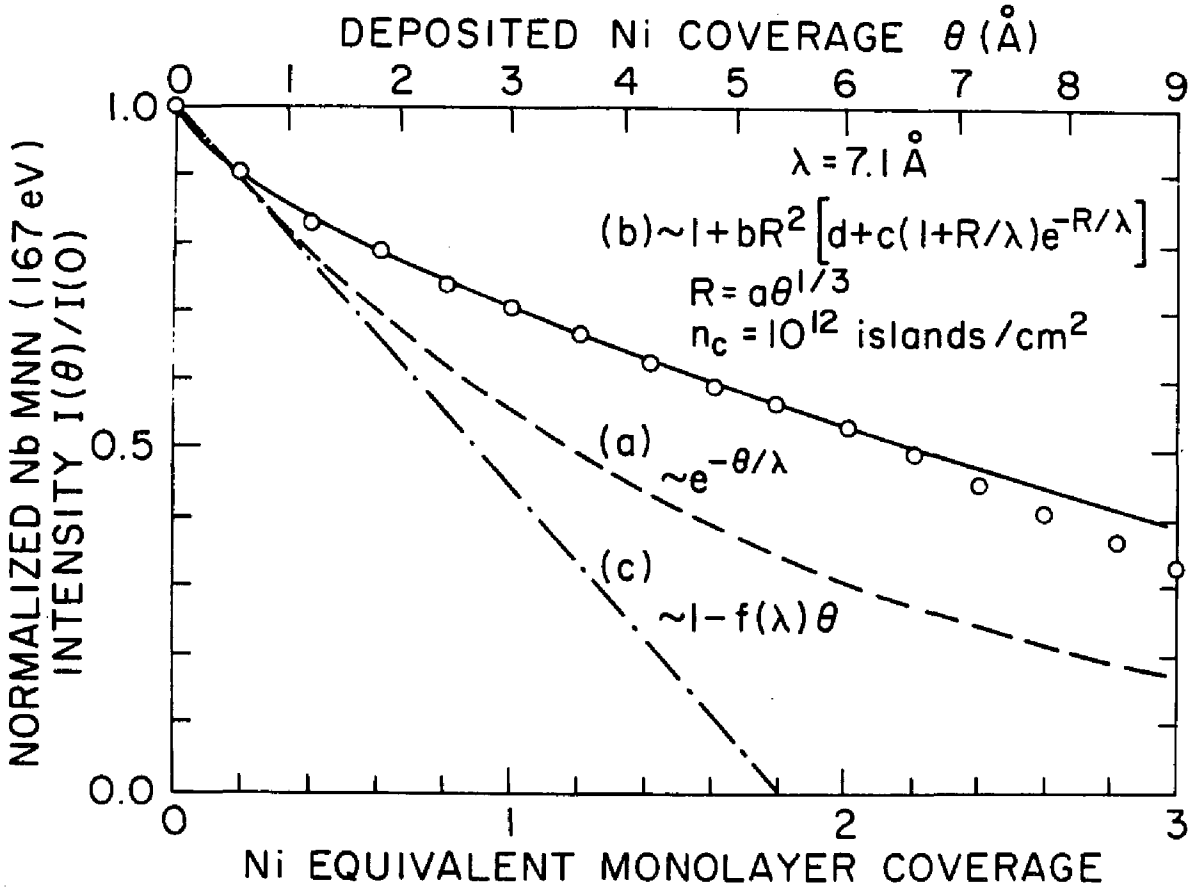

Figure 39: Attenuation curves of normalized Nb MNN Auger signal (kinetic energy 167 eV) intensity versus deposited Ni atom coverage. Experimental data is plotted as circles. Three main growth mechanisms for unreacted Ni overlayers on Nb(110) substrate are presented: (a) layer-by-layer growth; (b) 3-D island growth; and (c) island growth on top of an intermediate continuous layer of thickness d. The escape depth of Nb MNN Auger electron is taken to be 7.1 Å and the density of Ni islands on top of Nb(110) is assumed to be $10^{12}/cm^2$.

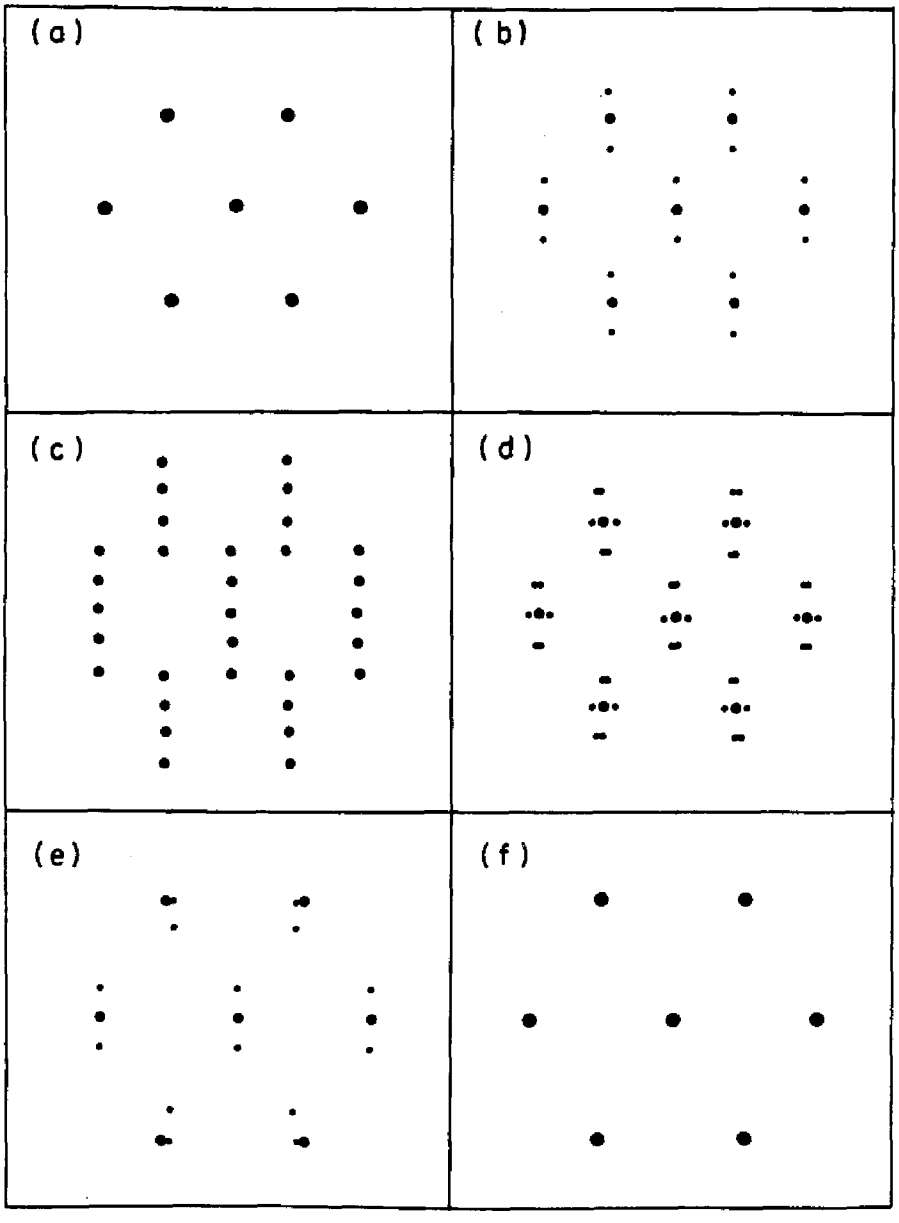

Figure 40: LEED patterns observed during the growth of Ni overlayers on Nb(110) surface: (a) less than 0.2 ML coverage; (b) $0.2 < \theta < 1.0$ ML; (c) $1.0 < \theta < 2.0$ ML; (d) $2.0 < \theta < 2.5$ ML; (e) $2.5 < \theta < 3.0$ ML; (f) $3.0 < \theta < 5.0$ ML.

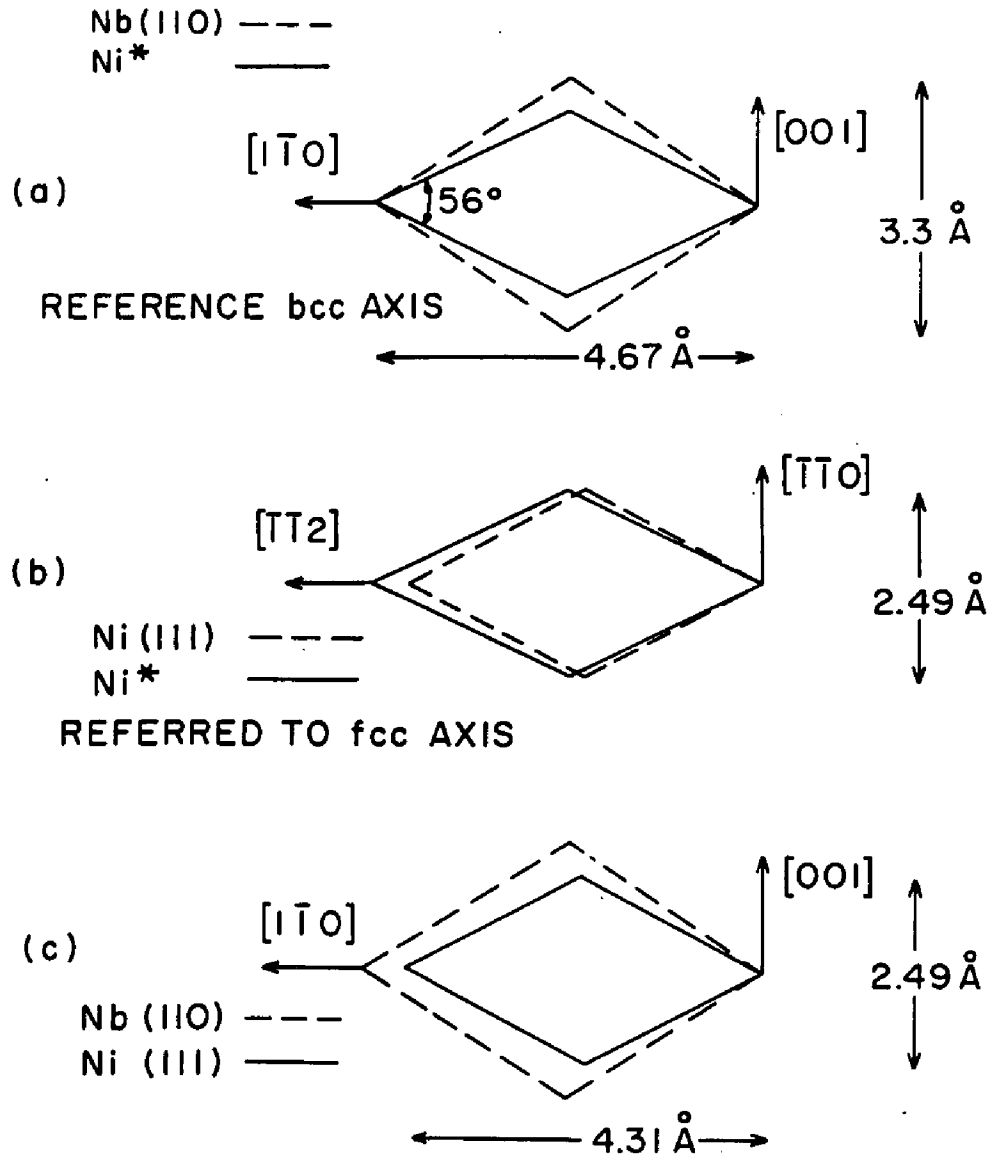

Figure 41: Real-unit meshes of Ni overlayers on Nb(110) surface: (a) Ni*(111) (solid) on Nb(110) surface (dashed); (b) Ni*(111) (solid) compared with Ni(111) (dashed); (c) Ni(111) (solid) compared with Nb(110) (dashed).

and the commensurate Ni structure at the bottom. The additional spots thus correspond to superlattice with a unit cell four times larger than that of the clean Nb(110) surface in the [001] direction (*i.e.* 4×2.49 Å $\approx 3 \times 3.3$ Å). No change in the basic pattern was observed with increasing coverage in this region, and the spot spacing was found to remain constant. However, the intensities of the satellites were found to increase with increasing coverage, implying the formation of two- dimensional growth of islands. In Fig. 40 (c), the definition and uniform intensity of the Ni*(111) and satellite beams suggests that there are large areas covered by Ni*(111). This is consistent with the AES measurements which suggests two-layer thick island growth in a layer-by-layer formation. Deposition above two monolayers of Ni atoms led to the appearance of another new set of spots having about 1/12 of the repeat spacing in the $[1\bar{1}0]$ direction of Nb(110) (shown in Fig. 40 (d) and (f)), and LEED spots associated with Ni*(111), Ni(111), and satellites which coexist in the initial stages of formation of the Ni(111) phase. No evidence of multiple scattering satellites between Ni*(111) and Ni(111) has been observed at any time. The new set of spots in Fig. 40 (d) can be understood as multiple scattering between Ni(111) islands with Nb(110) surface or with the commensurate Ni first layer on top of Nb(110) since Ni(111) unit cell has a 8% mismatch with that of Nb(110) in $[1\bar{1}0]$ direction. The increased coverage leads to a decrease in the intensities of satellite spots and the disappearance of Ni*(111) spots, leaving behind both Ni(111) and the satellite spots. Finally at coverage greater than three monolayers of Ni only the Ni(111) spots are visible. These observations strongly indicate that a structural transition from Ni*(111) to Ni(111) occurs in preference to the growth of a Ni(111) third layer over the rigid Ni*(111) second layers. This transition is more likely to be a first-order structural phase transition. Furthermore, the propagation of the structural transition seems to occur through the formation of Ni(111) islands. The real spacing unit meshes of Ni*(111) and Ni(111) are shown in Fig. 41. Fig. 41 (a) shows the Ni*(111) unit mesh which is a rhombus with 56° and 124° angles and two diagonals which are about 2.49 Å and 4.67 Å, respectively. The former is equal to the Ni lattice constant along the $[\bar{1}10]$ direction of Ni(111) and has a 25% mismatch with Nb(110) in [001] direction. The latter is equal to the Nb lattice constant in the direction of $[1\bar{1}0]$ of Nb(110) and has an 8% mismatch with Ni(111) in $[\bar{1}\bar{1}2]$ direction. Thus Ni*(111) is commensurate with Nb(110) substrate along the $[1\bar{1}0]$ direction and incommensurate along the [001] direction. In fact, the Ni*(111) unit mesh may well be obtained from Ni(111) by stretching the latter by about 8% along the $[\bar{1}\bar{1}2]$ direction. Fig. 41 (c) shows the real unit mesh of Ni(111) referred to

the Nb(110) axis. The alignment of the Ni(111) planes relative to the Nb(110) follows the Nishiyama-Wassermann relationship, in other words, the direction of $[1\bar{1}0]$ of fcc overlayer is in parallel to that of $[\bar{1}\bar{1}2]$ of bcc substrate.

5.3. Electronic Structure of Ni Overlayers

Fig. 42 (a) shows the angle-integrated ultra-violet photoemission energy distribution curves (AIEDC) for increasing coverage of Ni overlayers taken at 21.2 eV photon energy. Unpolarized light from a helium discharge lamp was used with a 45° angle of incidence. The spectra show the energy distribution of photoelectrons as a function of the initial states below the Fermi level for normal emission. Nb has a less than half filled *d*- electron shell. Nb(110) *d*- band structure is dominated by two peaks located at 0.4 eV and 3.1 eV below the Fermi level. The minimum at -1.8 eV is due to the *s-d* hybridization gap which is very sensitive to both surface disorder structure and surface contamination. This gap can be used to monitor sample quality during sample preparation. As Ni atoms are deposited onto Nb(110) surface, a new feature appears at 1.5 eV below the Fermi level. This feature grows into a shoulder on the Nb(110) *d*- states as the Ni coverage increased, and saturates at about two equivalent monolayer coverage. We attribute this new feature to an electronic interface bonding state due to the *d*- electron hybridization of Ni adsorbate and Nb substrate. This interface state seems relatively weak and is located much closer to the Fermi level than is observed with Pt and Pd overlayers on Nb(110). This might be attributed in part to the larger misfit at the interface between the Ni islands and the Nb substrate, and may mean that fewer Ni atoms are in the more highly coordinated Nb(110) hollow sites. The three-dimensional nature of the Ni islands also reduces Ni-Nb contact because the stacking of Ni atoms prevents them from having a significant number of Nb nearest neighbors. Fig. 42 (b) shows the AIEDC's with photon energy 40.8 eV for Ni coverage less than three equivalent monolayers. In the clean Nb(110) spectrum, a broad feature at -13 eV is due to the Nb NVV Auger transition. As Ni coverage increased, this broad Auger feature attenuated in a way which can be described by the Volmer-Weber island growth mechanism. It should be noted that above 0.4 equivalent monolayer Ni coverage a weak feature appears at 6 eV below the Fermi level. This feature is observed continuously to the multilayers characteristic of bulk Ni. The peak does not shift, and broadens only slightly with increasing coverage indicating that the excitation is substantially the same as in bulk Ni. The assignment of this -6 eV satellite has been controversial for many years [105–107]. Hufner and Wertheim [108] found that similar satellite peaks are observed in conjunction with the Ni 2*p*, 3*s*, and 3*p* core level X-ray photoemission peaks. They attributed this satellite to photoionization with the simultaneous promotion of a 3*d*- electron to a higher-energy state. Smith and co-workers [109] attributed this feature to direct interband transitions. Kemeny and Shevchik [110] carried

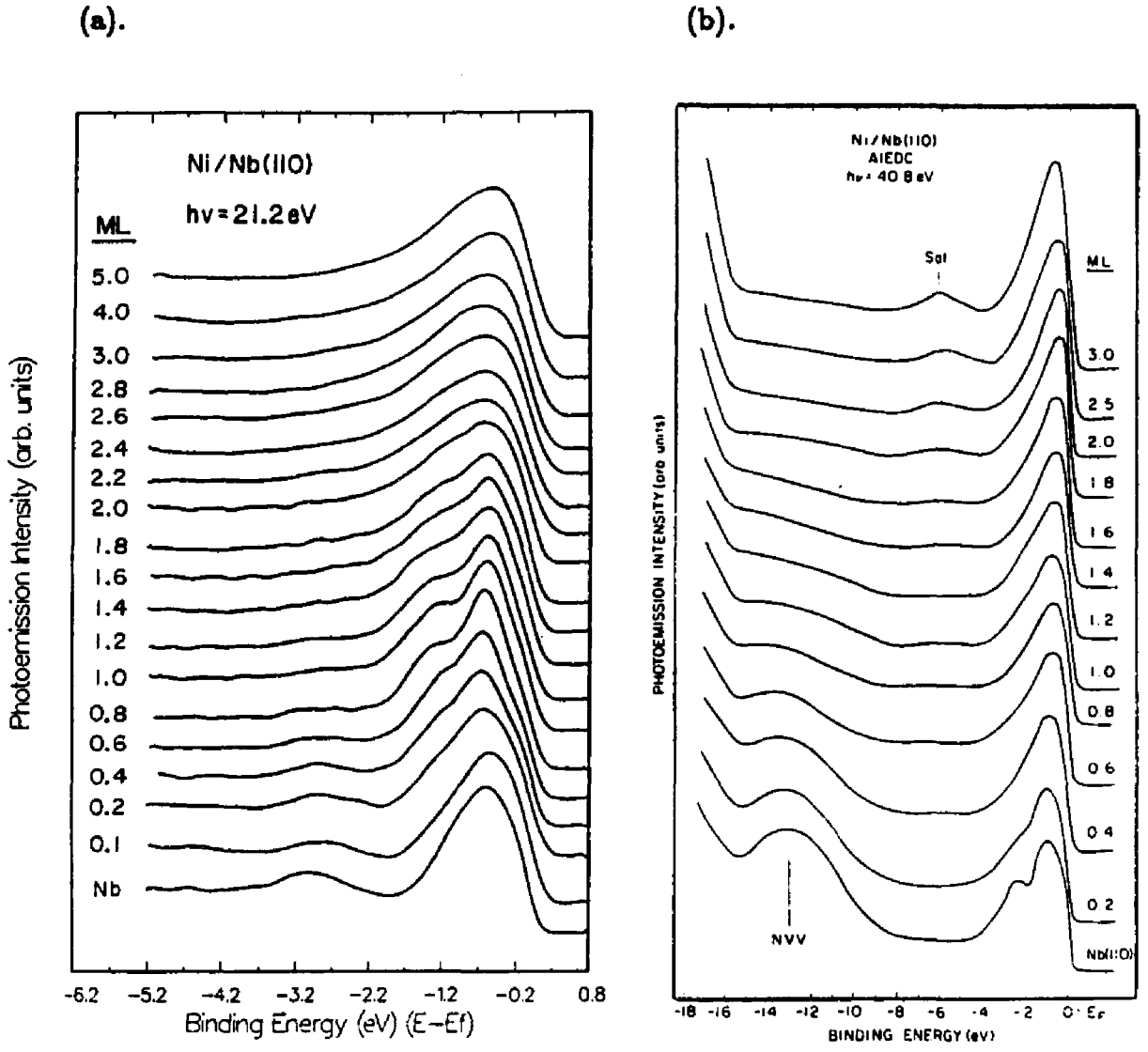

Figure 42: AIUPS EDC's of Ni overlayers on Nb(110) with 21.2 eV and 40.8 eV photon energies at 300 K. Ni equivalent monolayer coverage θ is indicated at the right-hand side of each curve.

out an experiment on the alloy Ni_9Zn to show that the peak at -6 eV for bulk Ni is not an extrinsic loss feature exhibited by all photoelectrons traversing a Ni medium. Instead, it is an intrinsic excitation which occurs with high probability when a Ni level is photoionized. Further work conducted by Tibbetts and Egelhoff [111] provided an important insight into the origin of this -6 eV feature. In a photoemission experiment conducted on Ni vapor deposited on an amorphous carbon substrate, they showed the structure at 6 eV binding energy is observed for dispersed Ni adatoms as well as for bulk Ni, and thus concluded that the -6 eV feature is a quasiatomic $3d^84s$ to $3d^74s4p$ excitation in bulk Ni. In other words, assuming the solid ground-state configuration of $3d^94s$ for Ni, two d- electrons are simultaneously excited, one of them into the continuum which is detected spectroscopically, and the other one into the empty $4p$- state above the Fermi level. The remaining excited atomic state of $3d^74s4p$ can be estimated by Moore's tables [112] as having an energy of about 6 eV above the ground state of Ni^+. The excitation threshold of the -6 eV feature near photon energy 24 eV can be attributed to the final state band structure effect.

5.4. Work Function Changes of Ni Overlayers

In order to gain further insight into the growth mechanism of Ni overlayers on Nb(110), we have also measured the work function, ϕ, from the width of AIEDC's. The dependence of the work function upon the deposited Ni coverage is shown in Fig. 43. Contrary to the case of Pt overlayers, the work function of Ni overlayers actually decreases at early growth stages. The minimum work function is obtained at Ni coverage equivalent to one monolayer. Above this coverage the work function increases sharply, and finally saturates at about three equivalent monolayer coverage. Similar trends of work function have been observed for Pd overlayers on Nb(110) except that the inflection points occur at different coverage. The work function of Ni(111) is about half an eV larger than that of Nb(110). It is expected that the work function will increase and eventually saturate at the value of Ni(111). The reason for the initial decrease in work function of Ni and Pd overlayers on Nb(110) and Ta(110) is not clear. However, several explanations are presented here to achieve a better approach. A simple way of describing the decrease in work function upon Ni submonolayer coverage is to assume that the Ni agglomerates rapidly after deposition. In principle, the photoelectrons escape more readily from the edges of the islands and formation of islands may make the surface rougher and reduce the work function. However, this model fails in explaining the decrease of work function in early stages of Ni overlayer growth. It was pointed out by Gurney [113] that the work function variations in metallic atom chemisorption on metals can also be caused by the shift of the valence and electronic affinity levels of adatoms caused by the presence of the metal surface. When the metal atom approaches the substrate, the valence level shifts towards the Fermi level by $e^2/4r$ and broadens. Conversely, the affinity level moves down towards the Fermi level. The modification of the valence level reduces the ionization potential of Ni atoms. The adsorbed individual Ni atoms may form positive adions, thus reducing the work function at submonolayer coverage. Although the decrease in work function can be qualitatively explained by the atomic roughness of the islands growth and the shift and broadening of valence and affinity levels of the atom upon adsorption, the inflection point of the work function at one equivalent monolayer of Ni coverage requires further theoretical study.

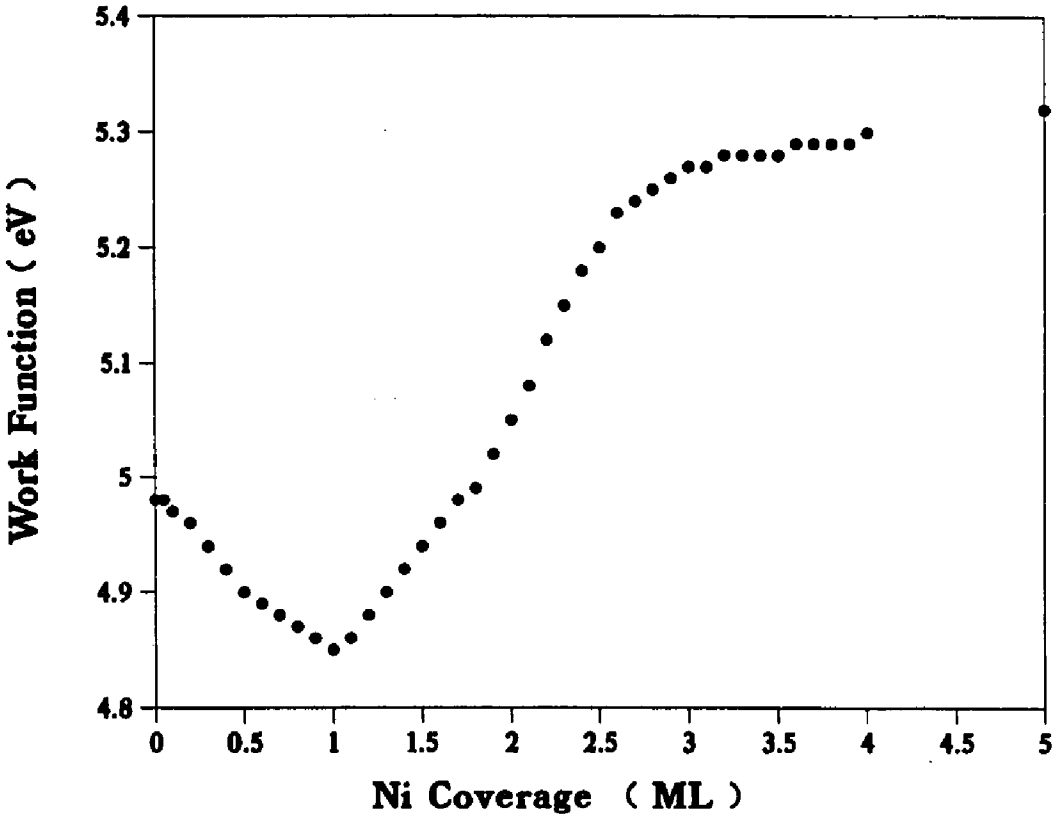

Figure 43: The dependence of work function of Ni overlayers on Nb(110) upon the deposited Ni equivalent monolayer coverage.

5.5. Hydrogen Chemisorption on Ni Overlayers

The behavior of hydrogen adsorption and absorption on Pd overlayers has attracted considerable attention in recent years. Strongin and co-workers [9] have reported that a few layers of Pd dramatically increase the rate of hydrogen uptake into bulk Nb. They estimated that in the modified system every hydrogen molecule that hits the surface dissociates and is absorbed into the Nb bulk. They further showed [114] that Pd atoms grow in a commensurate 1×1 structure on Nb(110) up to one monolayer coverage and that no increase in hydrogen uptake rate was observed for this structure. The passive chemical activity of a monolayer of Pd on Nb(110) was attributed to the modified surface electronic structures which behaves like a noble metal. The striking increase in hydrogen uptake rate after the transition to the incommensurate Pd(111) phase was attributed to the Pd 4*d* bands which broaden and cross the Fermi level resulting in an increase in the density of states near E_F [115]. Motivated by these significant results, we have studied hydrogen adsorption on Ni overlayers on Nb(110) at room temperature.

At 300 K H_2 strongly chemisorbs on the early transition-metals such as Nb, Ta and W, but very weakly on the late transition-metals like Ni, Pd and Pt. There is a rapid intial dissociative adsorption of H_2 molecules on the Nb surface. The incorporation of hydrogen atoms into the bulk of Nb is slowed down by the relatively strongly chemisorbed hydrogen atoms present on the surface which impede the further dissociation of incoming H_2 molecules. For the Pd overlayers on Nb(110), the H-surface bond is broken at the interface region and results in a large increase in hydrogen uptake. Fig. 44 shows AIEDC's for different hydrogen doses and Ni coverage on Nb(110). When H_2 chemisorbs on Nb(110) (see Fig. 26) two hydrogen-induced states were observed at the valence level. A broad feature near -5.4 eV binding energy is attributed to the bonding state between the hydrogen 1*s* and the metal *d*- orbitals. A sharp peak which grows in the Nb *s-p* gap at -1.8 eV is attributed to the antibonding state.

At Ni coverage of one equivalent monolayer on Nb(110) (Fig. 44 (a)), the hydrogen induced bonding and antibonding states are dramatically reduced in intensity. The existence of these hydrogen-induced states suggest that the Nb(110) surface may not be fully covered by Ni atoms which is consistent with the LEED and AES results which indicated that deposited Ni atoms grow by the formation of three-dimensional islands. We could not estimate the hydrogen uptake rate although it is expected that even at submonolayer Ni

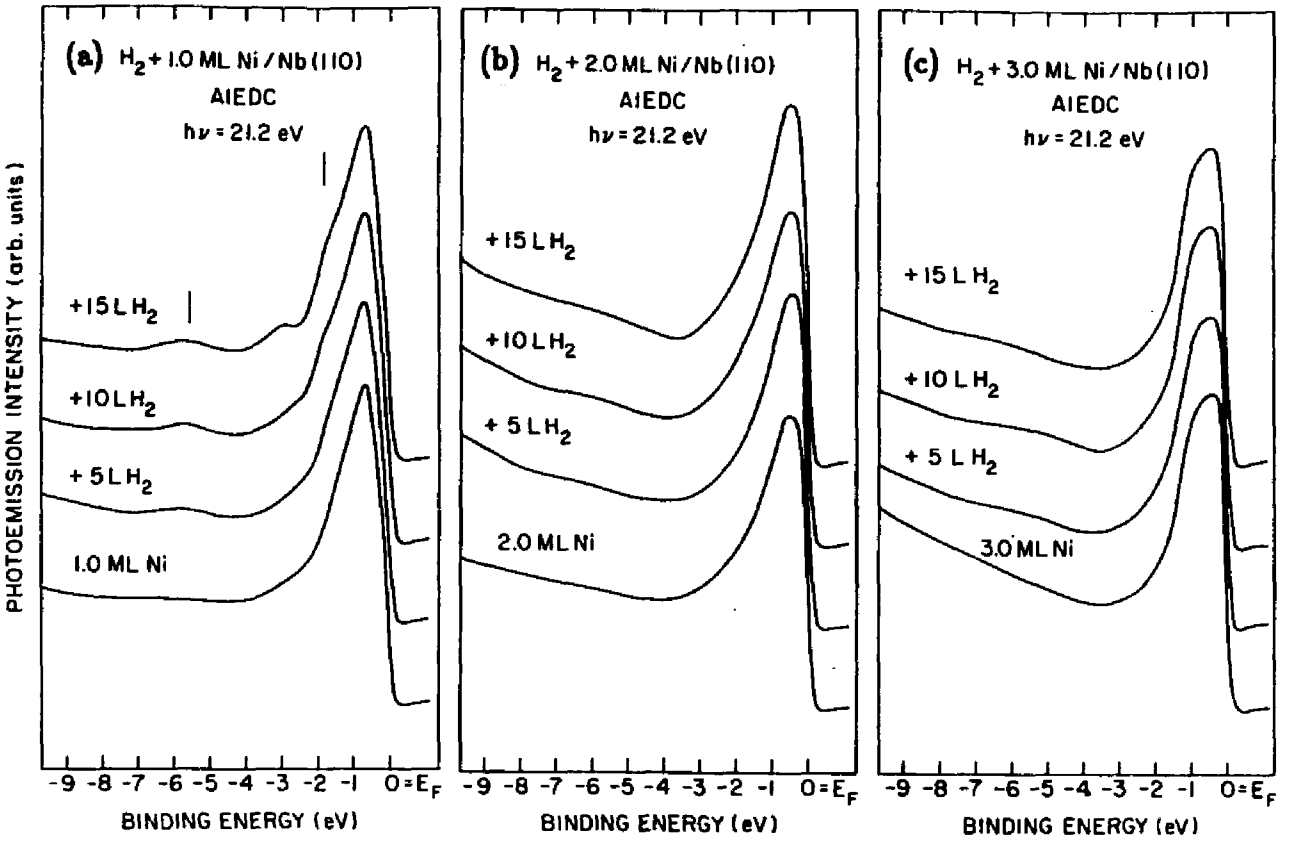

Figure 44: Angle-integrated photoemission spectra with 21.2 eV photon energy for Ni overlayers on Nb(110) after exposure to H_2 at 300 K. 5 L, 10 L, and 15 L of H_2 have been dosed to (a) 1 ML Ni; (b) 2 ML Ni; and (c) 3 ML Ni on Nb(110).

coverage, the hydrogen uptake rate will be increased, since Ni agglomerates to form three-dimensional islands which have a strained fcc (111) structure. At about two equivalent monolayer Ni coverage (Fig. 44 (b)), H_2 chemisorption produces very small effects. A broad feature appears at -5.8 eV which may be attributed to a hydrogen enhanced direct transition from the bulk *s-p* band of Ni. Himpsel *et al.* [34] suggested that a new type of chemisorption bond on the transition-metal occurs where the bonding is predominantly with the free-electron-like *s-p* bonds. To explain the invisibility of H_2 chemisorbs on Ni(111), Plummer and Eberhardt [116-117] suggested that hydrogen 1*s* split-off band shifts up toward the Fermi level (E_F) as the hydrogen concentration is decreased. At a concentration of half monolayer of hydrogen on Ni(111), this band merges into the bulk bands and loses its identity.

Hydrogen can be used as a marker with Pd or Pt overlayers on Nb(110) since a commensurate (110) configuration on the Nb surface results in a composite substrate which is unable to dissociate the incoming H_2 molecules. The interpretation of hydrogen adsorption on Ni overlayers supported by Nb(110) is complicated by the fact that deposited Ni atoms agglomerate to form three-dimensional fcc (111) clusters. Obviously, more work is required to fully understand the nature of hydrogen adsorption on Ni overlayers supported by Nb(110).

5.6. CO Chemisorption on Ni Overlayers at 300 K

CO chemisorption on transition-metals can be used as a surface marker since the CO chemisorption features change depending on the specifics of the CO-metal interaction. At 300 K, CO dissociates into individual carbon and oxygen atoms on refractory metal (such as Nb and Ta) surfaces but retains its molecular character on the late transition-metals like Ni, Pd, and Pt. Fig. 45 (a) shows the AIEDC's taken with a photon energy of 21.2 eV for 20 L of CO chemisorbed on Ni overlayer with various coverage. Features observed on Nb(110) at -4.8 eV and -5.8 eV correspond to C_{2p} and O_{2p} respectively. As Ni atoms are deposited on the Nb(110) surface, the CO dissociation rate is reduced. Up to 0.4 equivalent monolayer of Ni, the dissociation rate of CO decreases linearly. At 0.6 equivalent monolayer coverage of Ni atoms, a shoulder appears on the O_{2p} peak. As more Ni atoms were evaporated onto the Nb(110) surface, the shoulder on the O_{2p} feature becomes a broad peak around -7.4 eV. This is attributed to the excitation of 1π and 5σ orbitals in molecular CO chemisorbed on the surface. At one equivalent monolayer coverage of Ni atoms, dissociative CO chemisorption is reduced dramatically and a molecular CO chemisorption is observed. To get a better picture of the interaction of CO with Ni overlayers, AIEDC's with a 40.8 eV photon energy for 20 L of CO chemisorbed on various coverage of Ni are shown in Fig. 45 (b). The molecular CO 4σ orbital at -10.8 eV is observed as early as 0.6 equivalent monolayer Ni coverage. As more Ni atoms are deposited on the Nb(110) surface, molecular CO features like 4σ, 1π and 5σ peaks gain intensity. The 4σ peak shifts about 0.5 eV to the lower binding energy, while 1π and 5σ peaks remain almost fixed in energy. Above three equivalent monolayer Ni coverage, CO chemisorption typical of that observed on Ni(111) occurs. The coverage of dissociated and molecular CO species on the surface of Ni overlayers as a function of Ni coverage is summarized in Fig. 46.

The primary interactions between CO and transition-metals are the expected forward and back donations, the mixing of CO 5σ with surface d_{z^2}- and s- states, and the mixing of CO $2\pi^*$ with metal $d_{xz,yz}$- states. The bonding arise mostly from the metal $d_{xz,yz}$- to CO $2\pi^*$ electron donation. Also, the d- bands of the Ni adsorbate occur at lower energy than those of the Nb substrates. The interaction between d_σ and 5σ of CO increases, but their interaction with $2\pi^*$ gets smaller since the $2\pi^*$ orbitals are further away from the Ni d_σ- orbitals. The bonding between the CO and the transition-metals is dominated by the interaction of the CO $2\pi^*$ with the metal $d_{xz,yz}$- orbitals. Therefore, it is expected that the CO will dissociate on Nb or Ta surfaces and molecularly adsorb on Ni, Pd, and Pt surfaces.

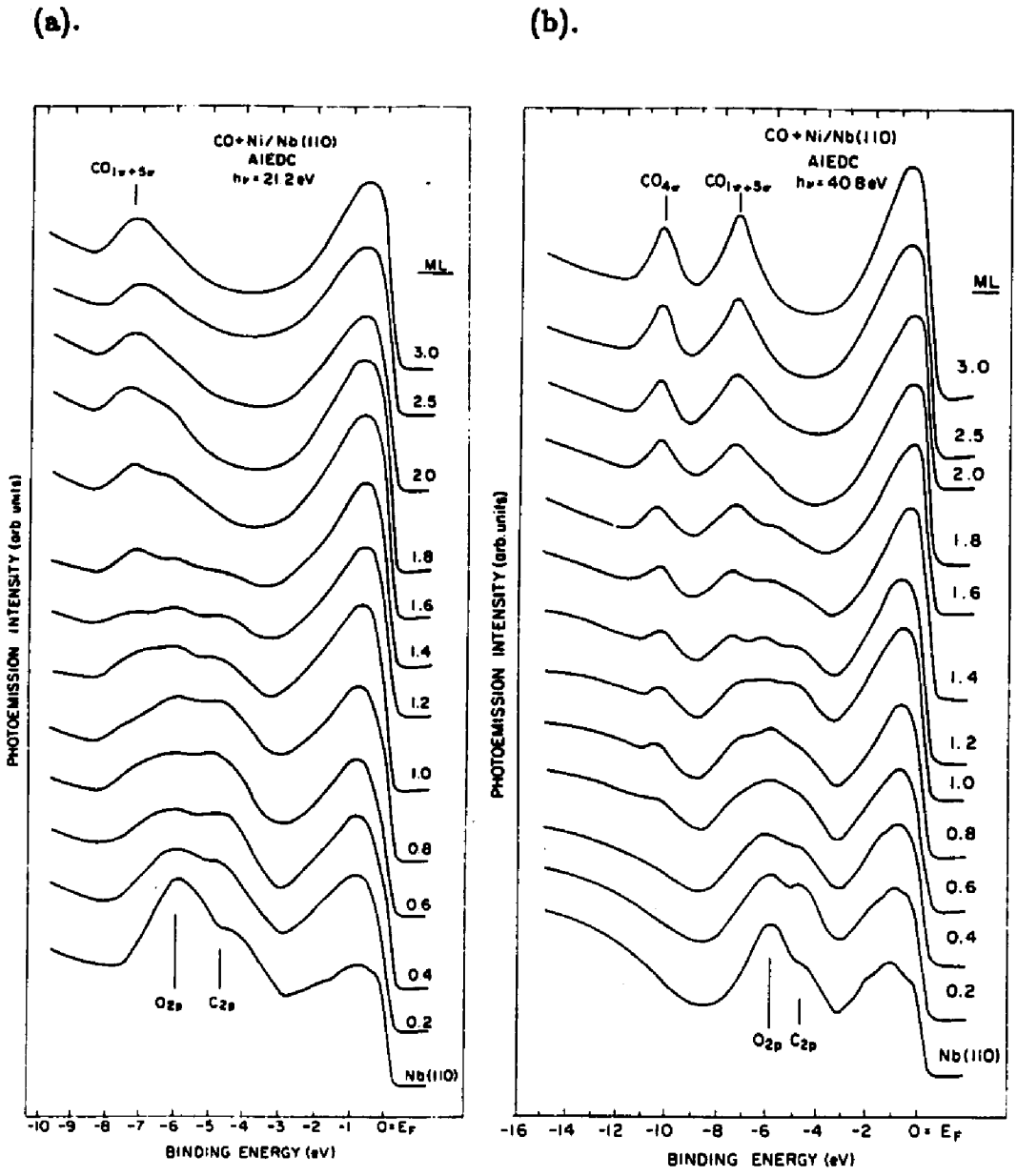

Figure 45: Angle-integrated photoemission spectra with 21.2 eV and 40.8 eV photon energies for Ni overlayers on Nb(110) after 20 L CO exposure at 300 K. Ni equivalent monolayer coverage θ is indicated at the right-hand side of each curve.

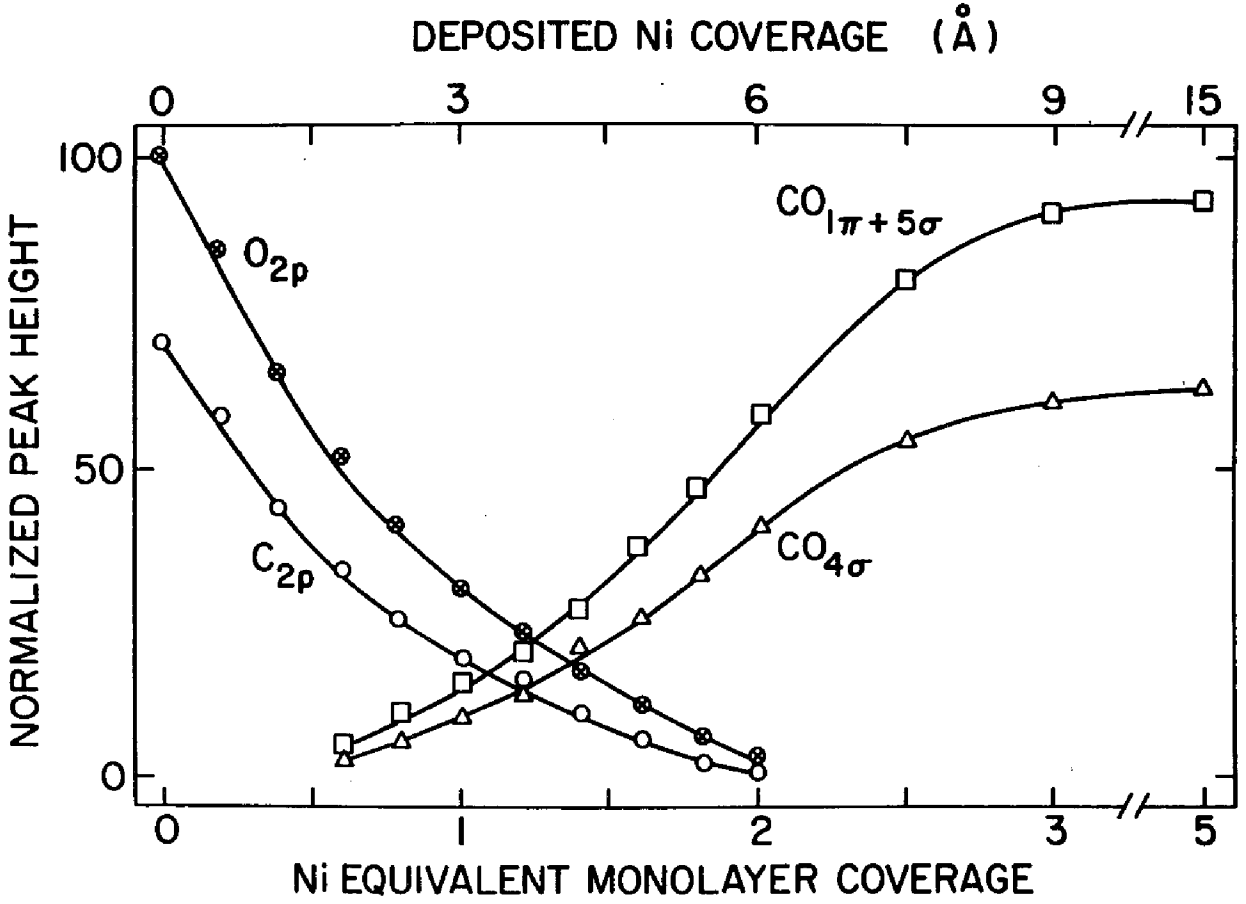

Figure 46: Coverage of CO on Ni overlayers on Nb(110) substrate after exposure to 20 L of CO.

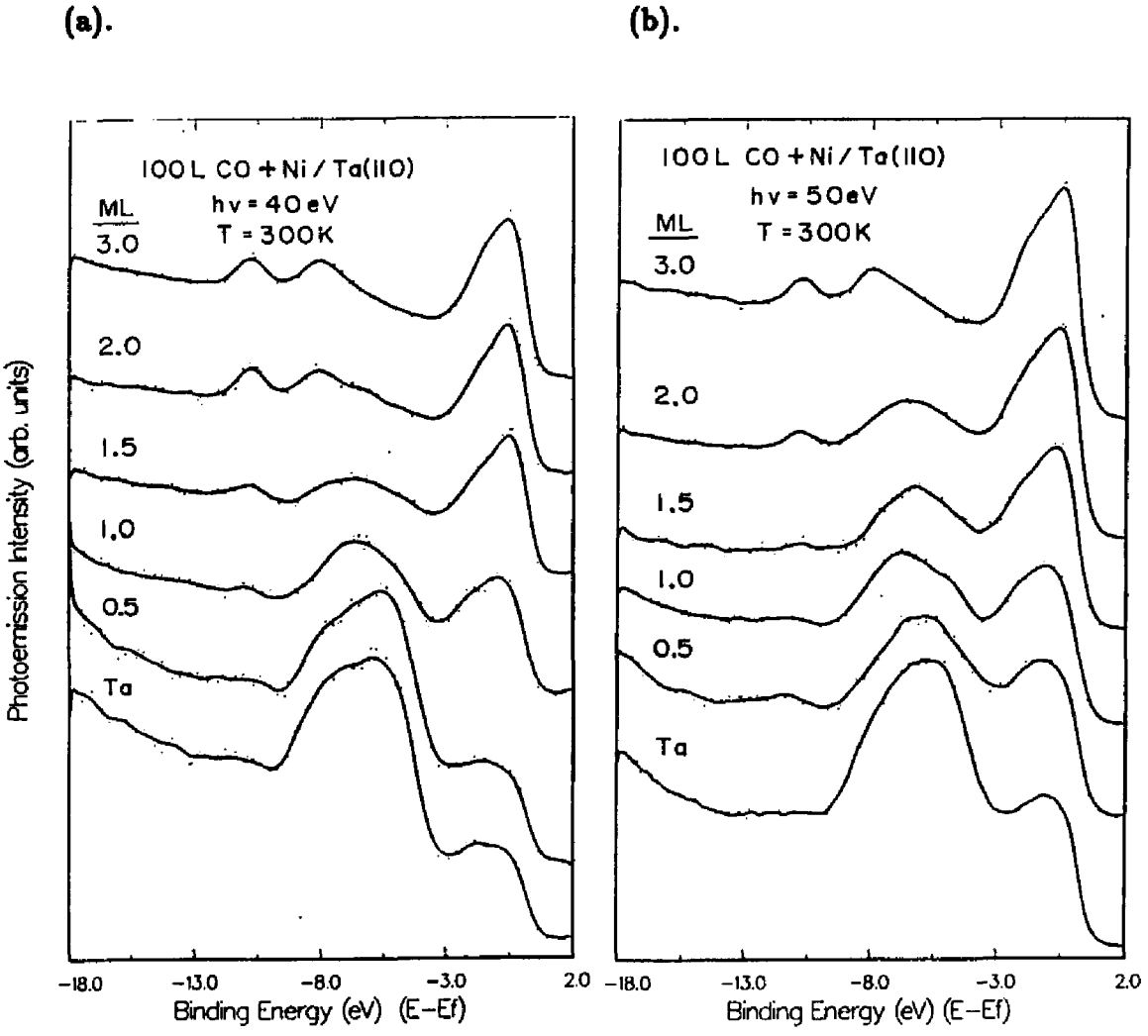

Figure 47: ARUPS EDC's taken at 40 eV and 50 eV photon energies for Ni overlayers on Ta(110) after 100 L CO exposure at 300 K.

In the previous section, we showed that there is little modification or hybridization of the *d* bands on the interface between the Ni adlayer and the Nb substrate. This is due to the large mismatch between the Ni adsorbate and Nb substrate unit cells which prevents the Ni atoms from laying flat as occurs with Pd and Pt. Ni metal can be seen at submonolayer coverage, hence CO molecules either dissociate on the Nb substrate surface or adsorb molecularly on the surface of Ni clusters.

Similar results have been also obtained for Ni overlayers on Ta(110). LEED and AES studies indicate that at submonolayer coverage, Ni agglomerates on top of Ta(110) to form three-dimensional islands which have strained fcc (111) structures and are aligned in the Nishayama-Wasserman orientation. Above two monolayer Ni coverage, the three-dimensional islands undergo a structural transformation to assume the Ni(111) close-packed structure and cover the Ta(110) substrate surface. Photoemission spectra from the strained Ni phase show very little modification of the *d*- bands. Fig. 47 shows the chemisorption of CO on Ni overlayers supported by Ta(110). As the Ni atoms are deposited onto the Ta(110) surface, the dissociation rate of CO is reduced. At an equivalent monolayer Ni coverage, the coexistence of dissociated and molecular CO species is observed on the metal surface. This phenomena can be explained by the growth of Ni in three-dimensional islands on top of Ta(110), the same situation as in the case of CO chemisorption on a monolayer Ni on Nb(110).

5.7. CO Chemisorption on Ni Overlayers at 80 K

Angle-resolved synchrotron radiation photoemission at 40 eV and 50 eV photon energies has been used to study CO chemisorption on Ni overlayers on Ta(110) at 80 K. Fig. 48 shows EDC's taken with 40 eV and 50 eV photon energies at 45° incidence and normal emission angle as a function of Ni overlayers after 100 L CO exposure at 80 K. Molecular CO 4σ, 1π and 5σ states were observed through various Ni coverage at 80 K. As deposited Ni coverage increased, we found that the 4σ state shifts to lower binding energy toward E_F while 1π and 5σ states remain almost fixed. As we discussed in Chapter 3, CO weakly bonds to the Ta(110) surface at 80 K with the molecular axis either tilted or randomly oriented as in physisorption. When Ni atoms are deposited on Ta(110), CO chemisorbs molecularly to the Ni islands. The shift of 4σ state reduces the energy difference between the 4σ and 1π states which implies a greater charge transfer from the metal *d*- states to CO $2\pi^*$ states and a stronger interaction. Further, the shape of 4σ state becomes narrower as the Ni coverage is increases. This may be attributed to a gradual transformation from a disordered molecular orientation on Ta(110) to an ordered vertical orientation on Ni(111) with the carbon end near the metal surface and oxygen away from it. Another interesting effect is the shape resonance of the 4σ state as function of Ni coverage. At about one equivalent monolayer Ni coverage, the 4σ state reaches its maximum intensity. One possibility is that the three-dimensional island growth produces a rough surface which at early growth stages might trap more CO molecules than would be expected for a smooth surface. The trend from weak to strong CO molecular chemisorption and from a disordered CO molecular orientation to a vertically oriented molecular bond can also be supported by the gradual disappearance of shake-up satellite of CO 4σ states. The spectra acquired at 40 eV and 50 eV photon energies are very similar except that at 50 eV the Auger transition states have shifted away from the CO 4σ, 1π and 5σ regions which leaves the CO state free of spectra interferences.

In Fig. 49, we show the ARUPS EDC's in the "σ-allowed" and "σ-forbbiden" geometry for the chemisorption of CO on one monolayer and five monolayers of Ni supported on Ta(110). The 4σ state in the "σ-allowed" geometry is much more intense than in the "σ-forbbiden" geometry. If we assume that the remaining 4σ peak in the "σ-forbbiden" geometry is due to the incomplete polarization of incident light, the adsorbed CO molecules are more or less standing up vertically with respect to the metal surface at 80 K. Upon closer inspection, one can see that the intensity of the remaining 4σ level on the one monolayer Ni surface is higher and the 1π level is broader than on the 5 ML Ni(111) surface. This may

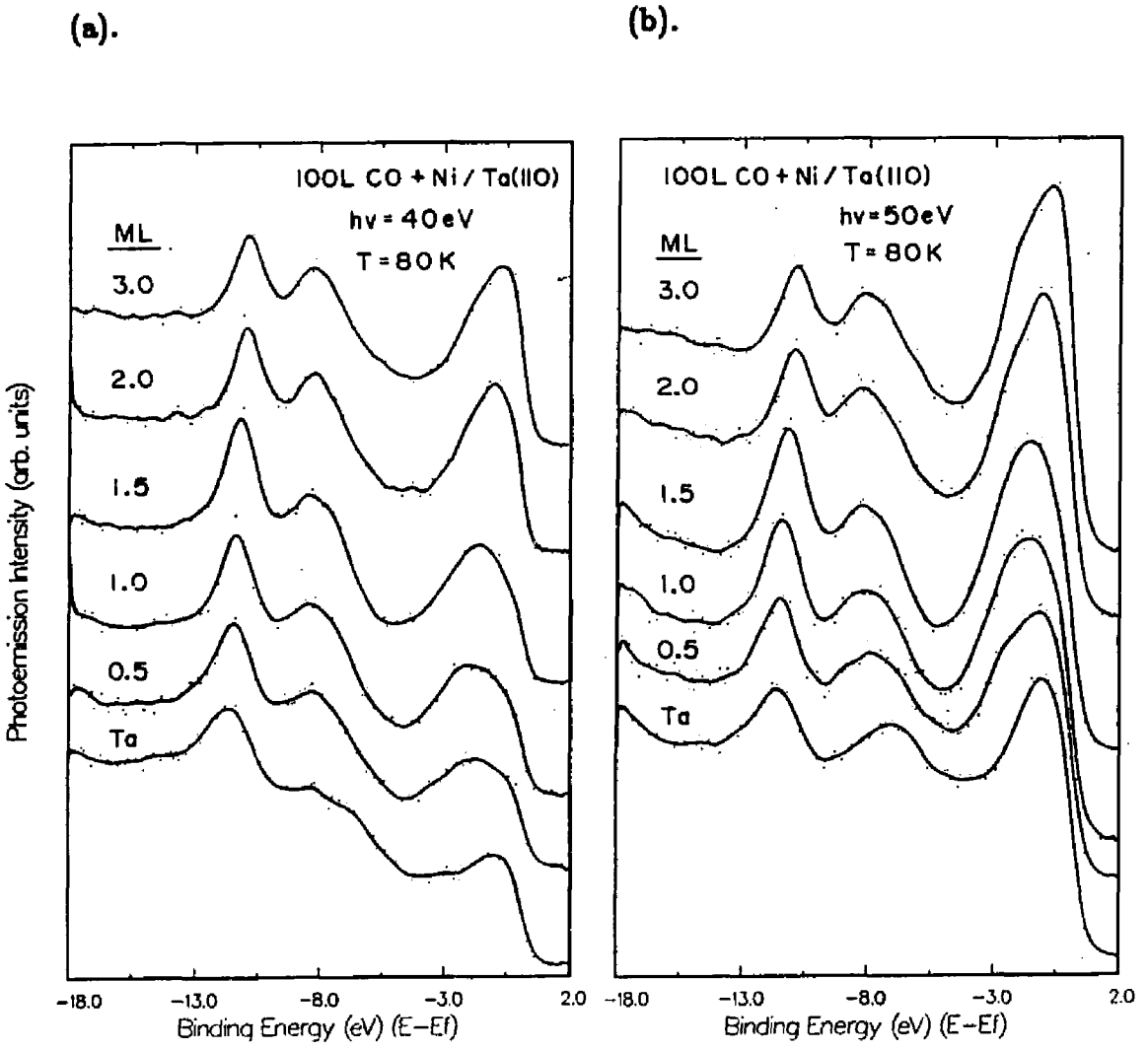

Figure 48: ARUPS EDC's taken with 40 eV and 50 eV photon energies at 45° incidence and normal emission are shown as function of Ni coverage after 100 L CO exposure at 80 K.

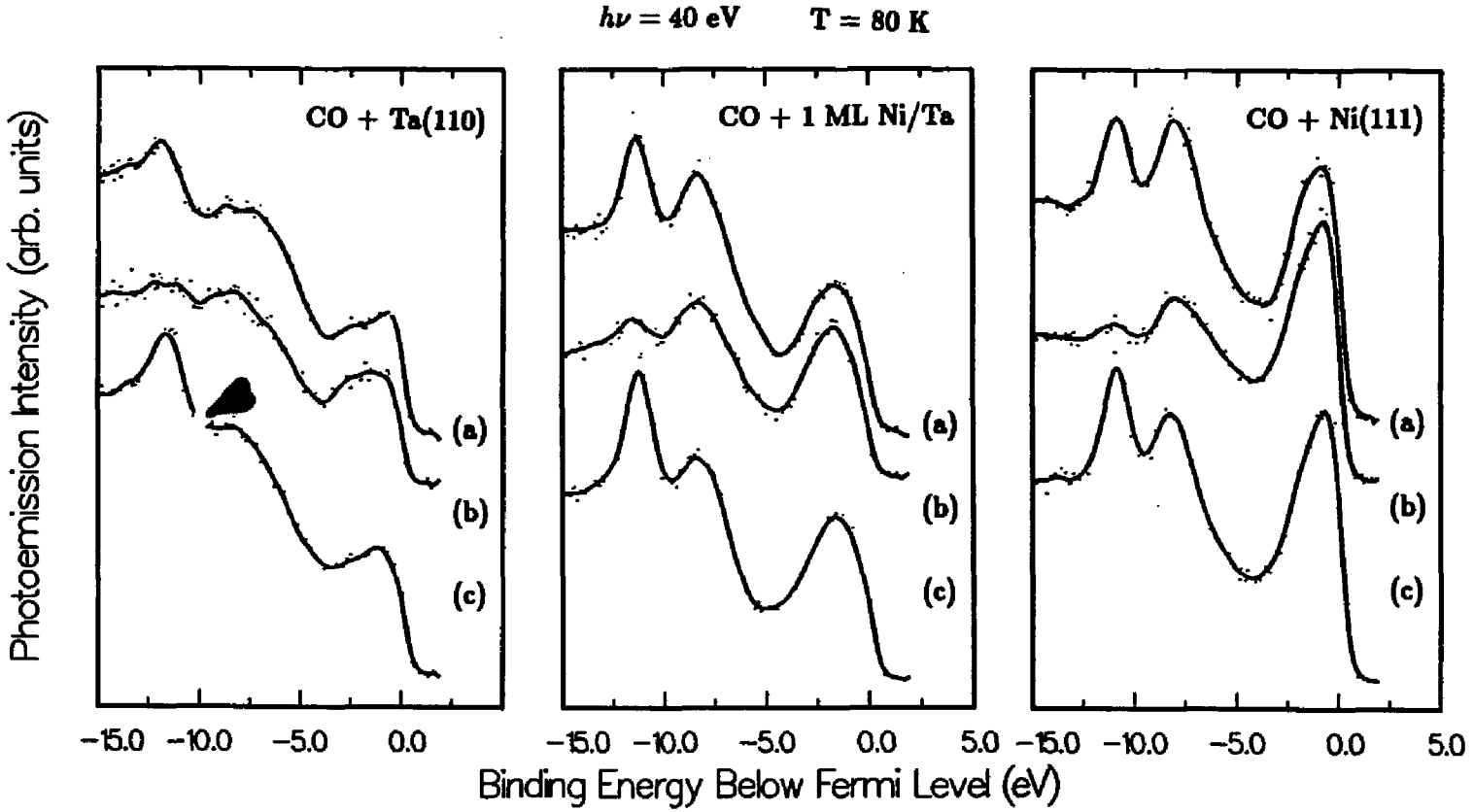

Figure 49: ARUPS EDC's taken at a photon energy 40 eV on Ta(110), 1 ML Ni and 5 ML Ni supported by Ta(110) after a saturation exposure of CO at 80 K. The geometry of measurements are (a) 45° angle of incidence and normal emission, (b) normal incidence and almost normal emission ($\Delta\theta < \pm 5°$), and (c) normal incidence and a 45° emission.

be explained by the fact that some of CO molecules are oriented randomly at the edge of Ni islands. The lack of multi-electron excitation from shake-up processes (4σ satellite) for the chemisorbed CO on Ni overlayers suggests a stronger interaction between the adsorbed CO molecule and the modified Ni/Ta(110) surface at 80 K than is observed for Pt overlayers.

5.8. Summary

Utilizing same techniques described in the previous chapter a systematic investigation has been conducted to understand the nature of Ni overlayers on Nb(110) and Ta(110) substrates at different temperatures. The results indicate that, unlike Pt and Pd, Ni randomly enters into equivalent surface sites at very low coverage ($\theta < 0.5ML$) but agglomerates on Nb(110) and Ta(110) to form three-dimensional islands which have a strained fcc (111) structure and are aligned in the Nishayama-Wasserman orientation. These islands can be produced from a close-packed Ni atomic plane by introducing an 8% strain along the $[1\bar{1}2]$ direction of Ni(111). At two equivalent monolayers Ni coverage, the three-dimensional Ni islands undergo a structural transformation and assume the Ni close-packed (111) structure. Photoemission spectra for the strained Ni phase are characterized by the appearance of a Ni-derived interface state at -1.5 eV binding energy, which is due to *d*- states hybridization between the Ni adlayers and the Nb substrate. At 300 K, exposure of an ultra-thin ($0 < \theta < 2ML$) Ni/Ta(110) film to the CO gas causes partial dissociation of the adsorbed CO, leading to the coexistence of CO, C and O on the surface. The coexistence of these two distinct CO chemisorption phases is attributed to the three-dimensional growth habit of Ni on Nb(110). When the surface is cooled to 80 K only molecular CO adsorption is observed. The absence of CO 4σ shake-up satellite indicates a relatively stronger chemisorption on Ni monolayers at 80 K than for similar Pt or Pd overlayers on Nb(110).

Chapter 6.
Surface Compounds Produced by Heat Treatments

6.1. Introduction

There are many other ways to modify the metal surfaces besides thin film epitaxy. One of the simplest ways is to increase the sample temperature after certain amounts of metal films have been deposited onto the substrate surface. By carefully controlling the rate of interdiffusion, reaction and segregation of adsorbate-substrate one may successfully modify the electronic structure, morphology and composition of the metal film to form a unique surface compound with different physical and chemical properties [118]. In this chapter, we describe the modification of Pt and Ni thin films on Nb(110) and Ta(110) substrates using PES and AES to investigate changes in the electronic and chemical properties and using LEED to detect the morphology of these modified metal surfaces after annealing.

We found that deposited Pt atoms undergo interdiffusion and reaction at elevated temperatures. In the temperature region spanning 300°C to 2000°C, no evidence for a ordered surface phase was found. For the Ni thin films on Nb(110), unique surface compound was identified when Ni layers on Nb(110) or Ta(110) were heated to certain temperatures. Vapor deposited Ni films on Nb(110) and Ta(110) originally have the close-packed Ni structure. Introduction of Nb or Ta into the overlayer by heating produced a compound which had the approximate stoichiometry expected for Ni_3Nb or Ni_3Ta. This surface phase appears to be related to the bulk Ni_3Al structure, however, there are some modifications of the geometrical structure of the surface compound as well as the electronic properties, and this is discussed in the following sections. Additional synchrotron results for the Ta core levels of Ni/Ta(110) are also presented to give some idea of the interface morphology.

The study of Ni_3Nb or Ni_3Ta surface compounds is of particular interest since bulk A_3B metal system such as Ni_3Al are high-strength alloys and the fact that there is some evidence that compounds of this structure can be formed by surface reactions is of great interest. The high-strength properties of some of these alloys is related to their interfacial properties [119–120], and it is possible that studies of surface layers of these materials will give insight into the structure of these interfaces.

6.2. Surface Composition Changes of Pt Overlayers

Based on the idea that there could be a significant range of temperatures for which atoms in excess of one monolayer would be driven from the surface and for which one monolayer commensurate Pd would be stable, Strongin and Sagurton [101] have performed thermal treatments of thick Pd overlayers on Nb(110). They found that a commensurate Pd monolayer on Nb(110) could be formed by heating to remove Pd from thicker layers. Furthermore, it is shown that no unusual or dramatic changes in the photoemission spectra between a deposited Pd(111) monolayer and a annealed Pd^*(110) monolayer. Hence the increase in the hydrogen uptake rate with coverage beyond one monolayer of Pd is attributed to the shift toward higher energies of the local density of states at the surface, instead of structural phase transition. To gain the further information on adsorbate-substrate interaction, reaction and interdiffusion at high temperatures, we also annealed 20 ML Pt films supported on Nb(110) at temperatures ranging from 300°C to 2000°C. Fig. 50 shows the valence band photoemission spectra at 21.2 eV photon energy at various annealing temperatures. It is clear that thermal treatments cause the hybridized *d*- bands to shift to higher binding energy and the Pt states form a composite structure similar to that of a deposited Pt(111) monolayer on Nb(110). LEED pictures taken after the first heat treatments show only diffuse Pt(111)-like patterns. After several thermal treatments, neither the stable ordered Pt surface monolayer nor the stable ordered surface compound was identified by LEED, AES, and photoemission investigations. Our results suggest that, unlike Pd films supported on Nb(110), Pt atoms continually undergo interdiffusion and reaction at elevated temperatures. By controlling the annealing times at temperatures ranging from 500°C to 700°C, an equivalent monolayer composition could be achieved. The annealed Pt/Nb surfaces show a reduction of CO chemisorption. This decreased chemical activity may be due to alloy effects when the Pt atoms intermix with the Nb(110) substrate after annealing. We think it is more likely due to the special electronic structure of this modified metal surface. This will be discussed in Section 6.4.

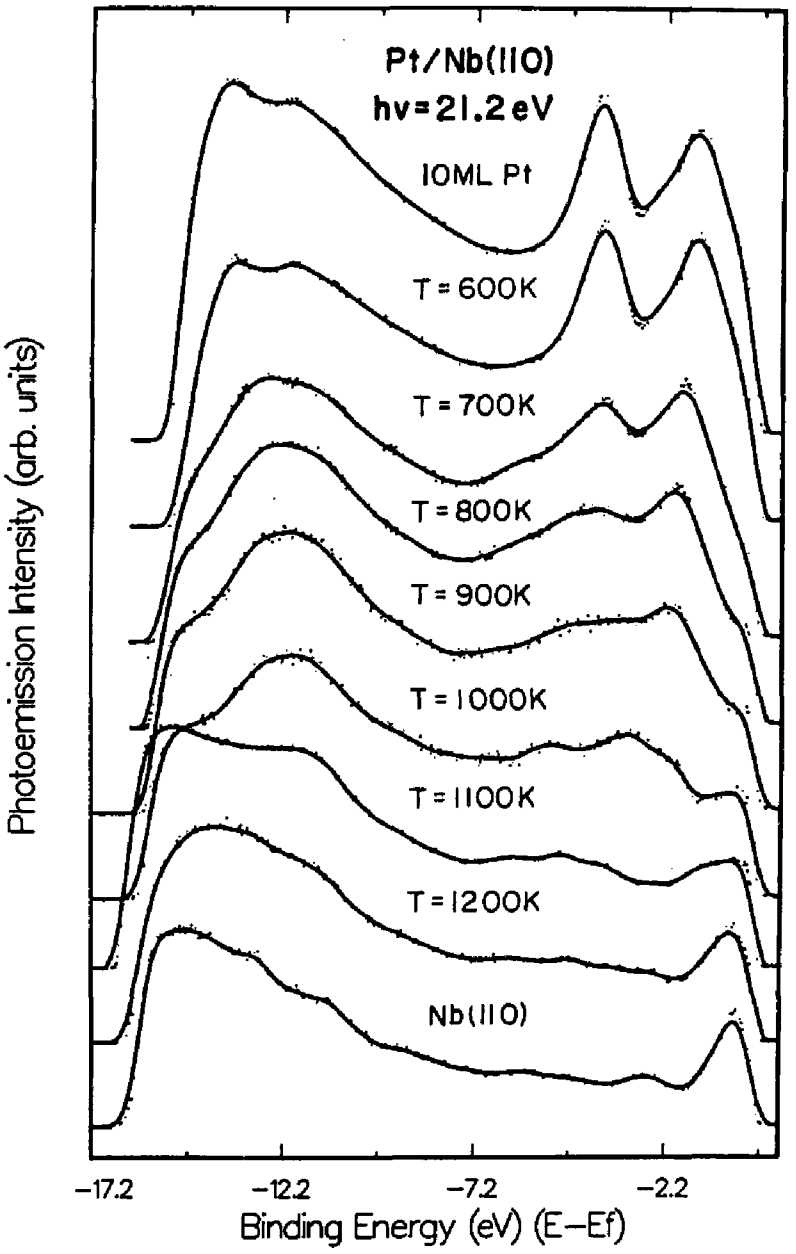

Figure 50: AIUPS EDC's at 21.2 eV photon energy for the 20 ML Pt overlayers on Nb(110) after annealing at temperatures from 600 K to 1200 K.

6.3. Surface Composition Changes of Ni Overlayers

In this study, 20 ML thick Ni films on Nb(110) and Ta(110) were annealed by resistive heating of the foil substrate. In Fig. 51 we show that interdiffusion and reaction between the Ni film and the refractory metal support is triggered by heating the substrate beyond 800°C. Examination of Fig. 51 shows that the near-surface concentration of Ni is reduced. The 61 eV Ni $M_{2,3}M_3M_4$ Auger signal decreases more rapidly at the beginning of heat treatment. This is followed by a relatively flat region where the Ni concentration appears stable. A coincident growth of the Nb core-valence-band Auger lines between 166 and 179 eV and their saturation when the overlayer comes into thermal equilibrium shows that Nb has entered the Ni overlayer. Comparison of the relative intensity of the Ni and Nb Auger features as a function of temperature suggests that the effective Ni concentration decreases at higher temperatures. We believe that the region where the Auger signal changes rapidly is due to rapid diffusion and reaction regime describing the interdiffusion of Ni and Nb, and the flat regime is due to the Ni formation of a stable surface compound. The relative amounts of Ni and Nb (or Ni and Ta) can be varied by changing the annealing temperature. The amount of Ni at thermal equilibrium decreases at all temperatures but tends to cluster around a higher concentration (50% - 75%) for Ni between 800 and 950°C and then changes to a lower Ni concentration (20% - 30%) when the temperature exceeds 990°. We denote the region of variable concentration produced by annealing from 800 to 990°C as the partially reacted region and the region produced by temperatures exceeding 990°C as the fully stabilized region. Similar results were obtained for Ni films on Ta(110). The Ni-Ta surface compound was found to be more stable and persisted over a wider range of temperature (*i.e.* 800 – 1300°C for Ni-Ta, compared to 800 – 1100°C for Ni-Nb).

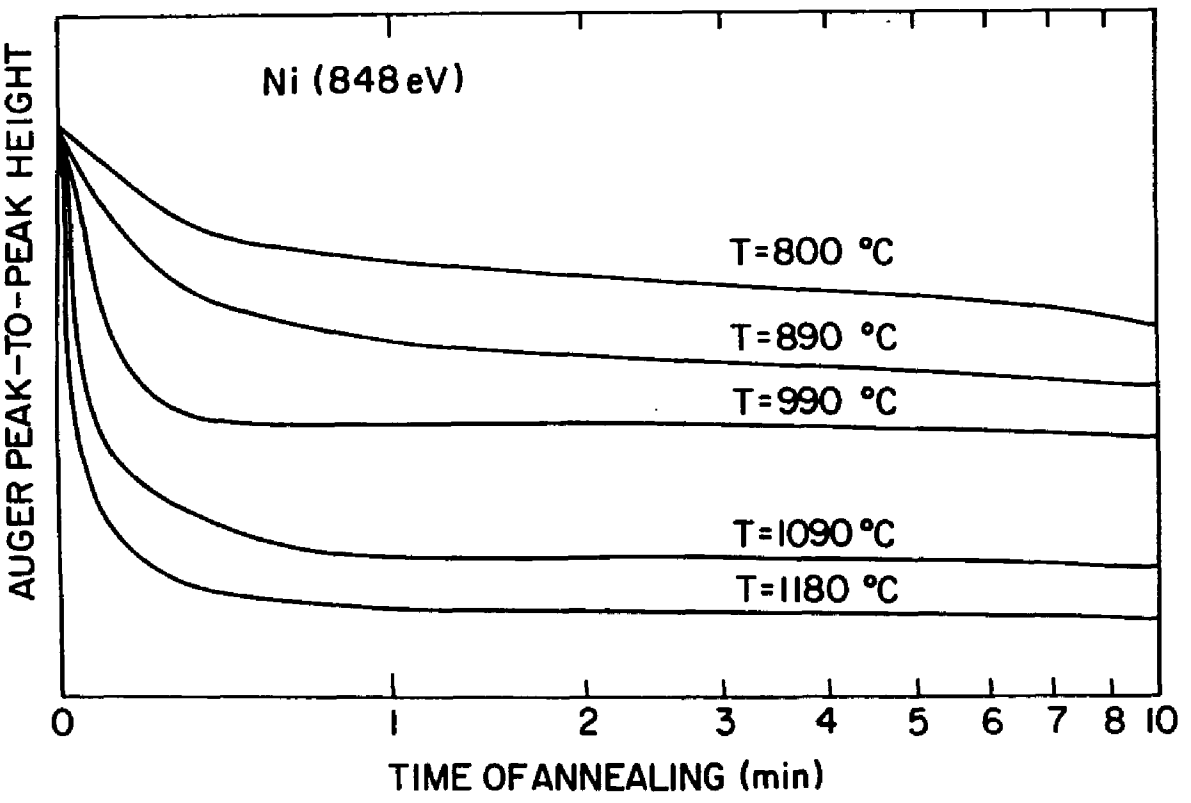

Figure 51: Ni L_3VV (848 eV) Auger electron $dn(E)/dE$ peak-to-peak heights for thermally stabilized Ni overlayers supported on Nb(110). Isothermal heat treatment were performed at the temperature indicated

6.4. Electronic Structure of Ni_3Nb and Ni_3Ta Surface Compounds

The electronic structure of the Ni-Nb and Ni-Ta surface compounds can be inferred from photoemission data. Valence-band spectra are shown for Ni overlayers on both Nb (Fig. 52 (a)) and Ta (Fig. 52 (b)). It is noted that the entry of Nb or Ta into the Ni overlayer drastically modifies the distribution of Ni *d*- states. The most intense Ni 3d component shifts from -0.4 eV to -1.0 eV binding energy (*i.e.* shift about 0.6 eV) for Ni-Nb and from -0.4 eV to -1.1 eV for Ni-Ta. The general shape of the Ni *d*- states is the same for both Ni-Nb and Ni-Ta, analogous *d*- states are marked by vertical tic marks on the spectra taken from both Ni-Nb or Ni-Ta at 1000°C. To the best of our knowledge no calculations of the electronic structure of Ni-Nb or Ni-Ta exist in the open literature. To interpret the electronic structure for Ni-Nb and Ni-Ta we use calculations published for the Ni-Si system [121–128].

The general features of the electronic structure of Ni-Si alloys can also be discerned in Ni-Nb and Ni-Ta spectra. The most intense Ni *d*-states are probably non-bonding states whose configuration is determined by the overlap of the Ni *d*- states. Reduction in Ni coordination drives these states towards a more atomiclike configuration. This reduces the width of the *d*- band because the overlap of *d*- states is reduced and shifts the states to lower binding energy because the *d*- states become more localized. In Ni silicides, little or no transfer of charge takes place because the metal-Si bonds are covalent. The specific features of the Ni-Nb and Ni-Ta bonding due to hybridization of Ni *d*- states and Nb or Ta *s*- or *d*- states is more specific to these systems and cannot be compared to the Ni-Si system. Comparison of our valence states to those published by Franciosi *et al.* [121] for Ni_2Si, NiSi and $NiSi_2$ suggests that our Ni-Nb and Ni-Ta surface compound is Ni metal-rich because our valence bands most strongly resemble those published for Ni_2Si. We also believe that the valence state with the greatest binding energy is a Ni-Nb or Ni-Ta bonding state and is most likely derived from the Nb (Ta) *s*- / Ni *d*- states (*e.g.* is *d*-s hybrid). From structural analysis discussed later we favor a stoichiometry close to Ni_3Nb or Ni_3Ta. This observation is in apparent disagreement with the results presented in Fig. 52 which suggest a low Ni concentration. However, we can account for the apparent reduced Ni concentration by suggesting that some of the Nb Auger signal could have been derived by the underlying Nb(110) substrate. A final valence-band feature that should be noted is the state at, or

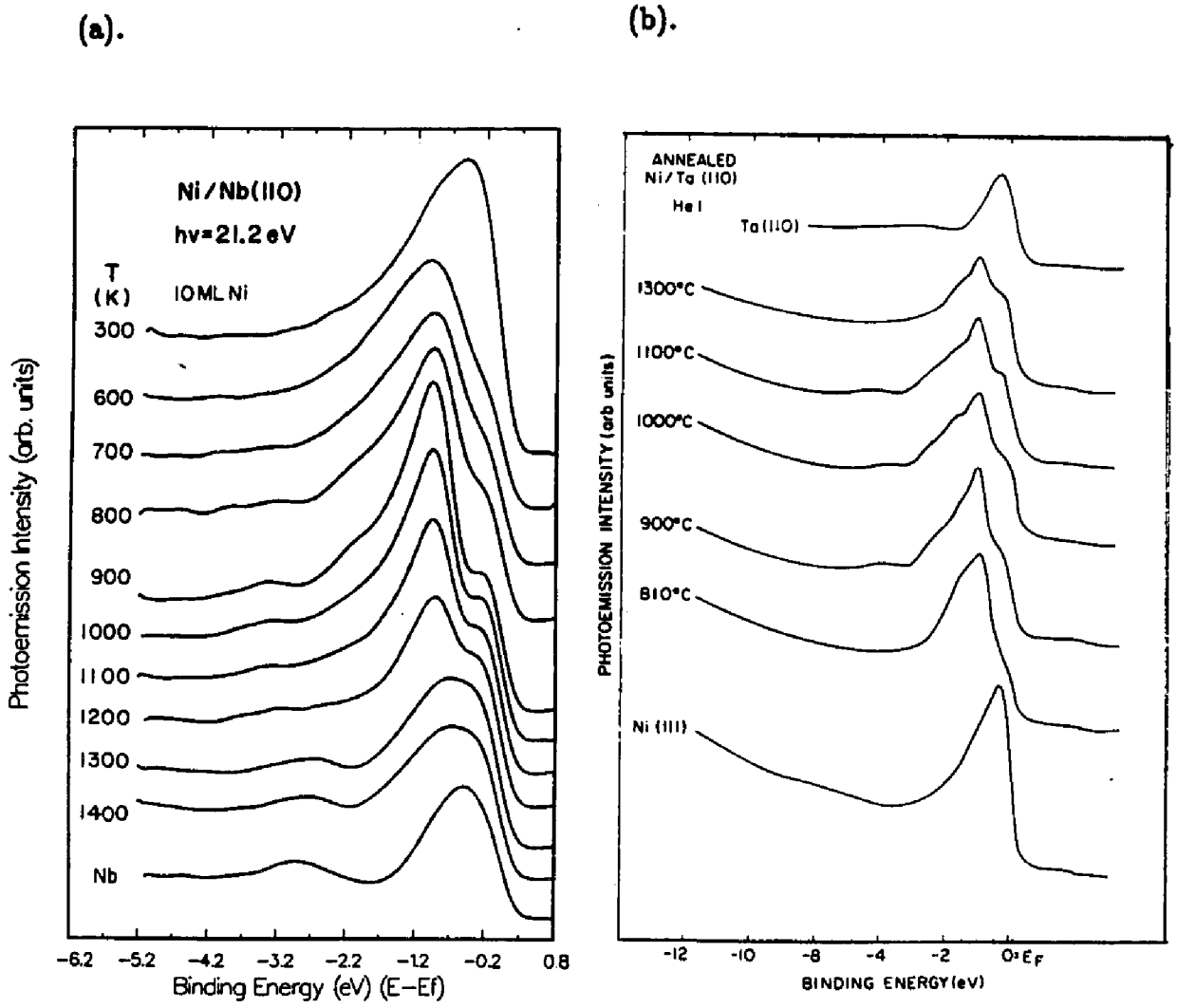

Figure 52: Photoemission energy distribution curves of (a) Ni films supported on Nb(110) at temperatures ranging from 800 to 1100°C and (b) Ni films on Ta(110) at temperatures ranging from 800 to 1300°C. All measurements were done using HeI 21.2 eV photon energy

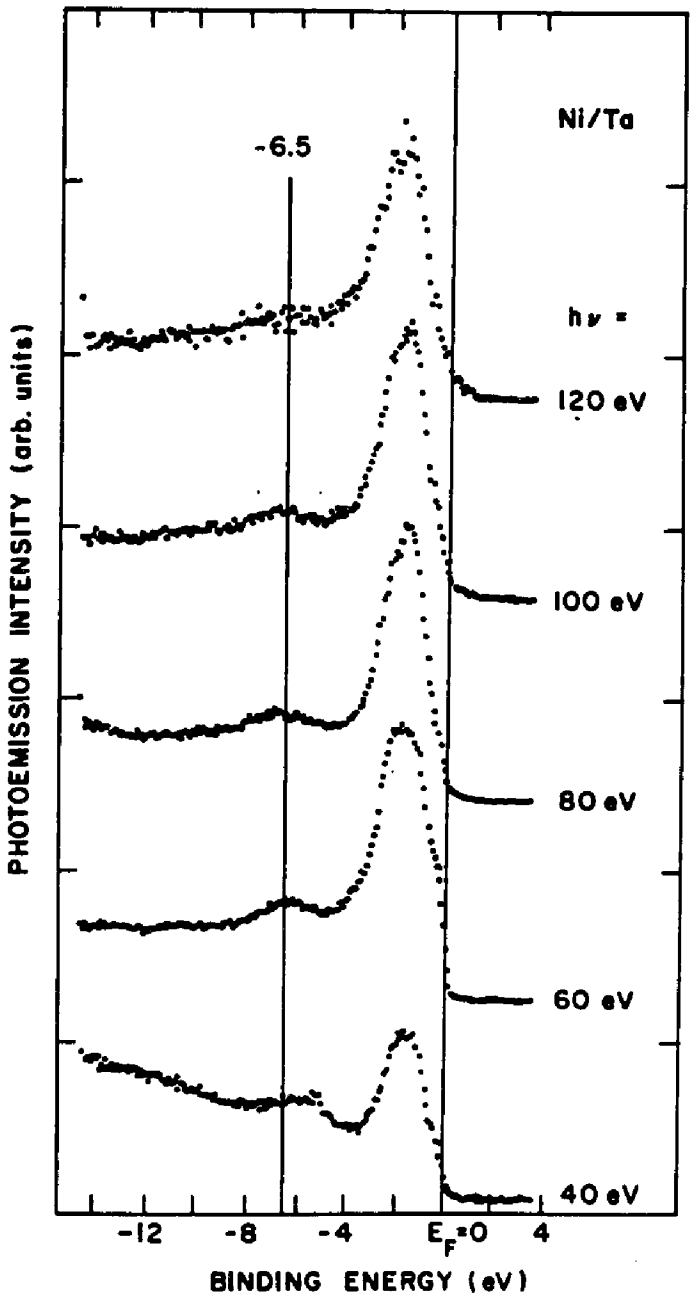

Figure 53: Photoemission spectra at different energies for Ni_3Ta produced by annealing a Ni layer at ≈ 1000°C for several minutes. Note the decrease in the states at E_F as one approaches the minimum in the Ta photoemission cross section at 120 eV

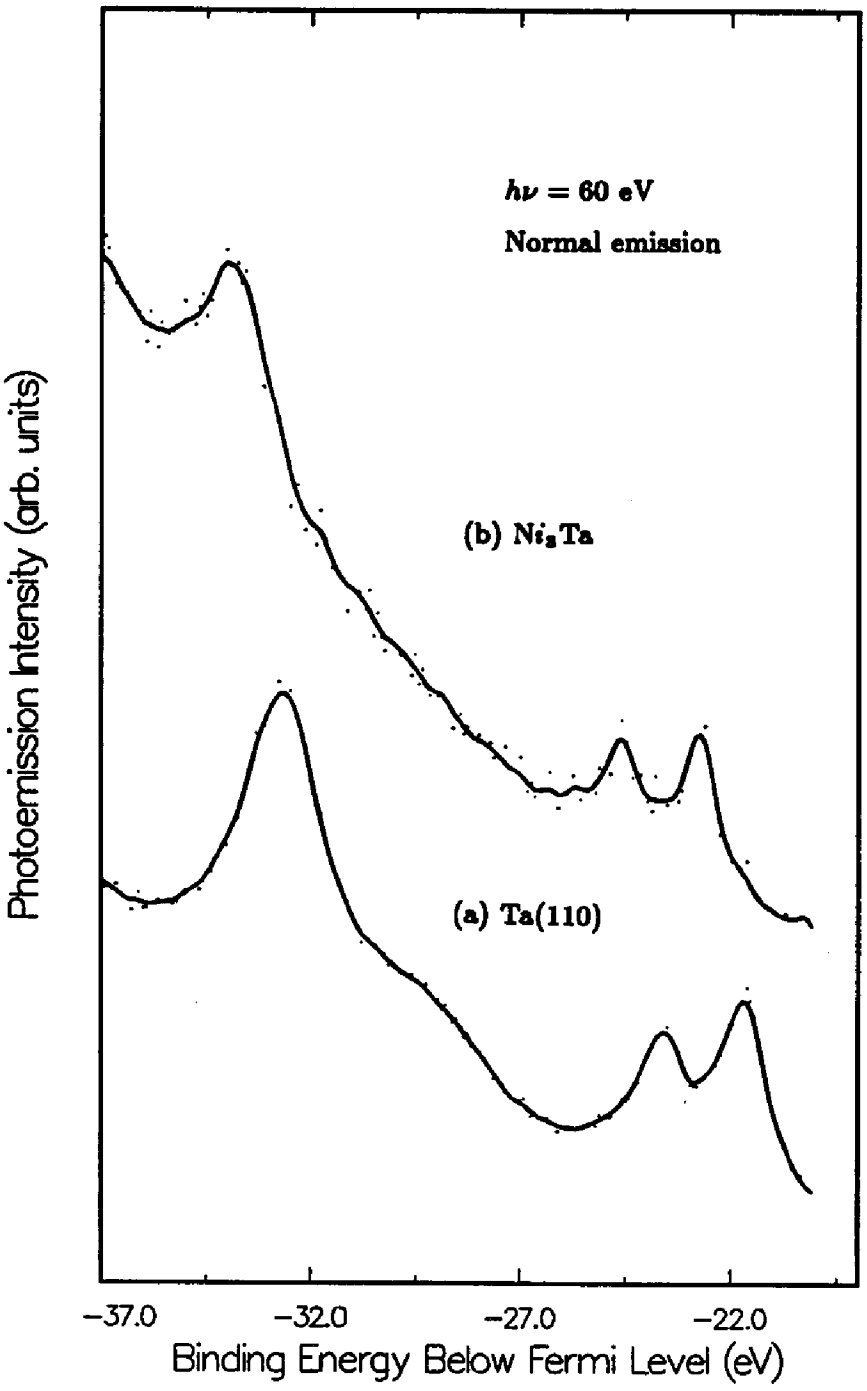

Figure 54: **Photoemission energy distribution curves for the Ta $4f$- core levels of Ta(110) and of the Ni-Ta surface compound taken at 60 eV photon energy. The lack of a substrate derived Ta $4f$- component in the spectrum obtained for Ni-Ta demonstrates that an extended overlayer has been produced by the mixing of Ni and Ta.**

near the Fermi level. This state is absent in the Ni-Si LDOS (local density of states) [122]. We interpret this state as being due to non-bonding Nb or Ta *d*- states.

Variation of the photoemission cross section with photon energy can be used to identify the origin of various elements of the Ni_3Ta *d*- band and can be used to deduce the spatial distribution of the Ni and Nb components. These measurements were done for Ni/Ta as opposed to Ni/Nb because Ta has a low-lying $4f$- core level that can be used for studies of interface morphology [124]. Valence-band photoemission measurement taken using synchrotron radiation for Ni_3Ta are shown in Fig. 53 as a function of photon energy. There appears to be a significant density of states at E_F at low photon energies where Ta has a large photoemission cross section. In our own measurements, the *d*- states observed at E_F are Nb derived and the Ni *d*-states are shifted significantly below E_F. This could be due to the effect of a thin Ni_3Nb or Ni_3Ta layer from the Nb or Ta substrate. This has been found to be the case for Pd layers on Nb(110) [101] or Ta(110) [125] and appears to be the case here for Ni_3Nb on Nb(110) or Ni_3Ta on Ta(110). We have already mentioned that the *d*- states observed at E_F in Fig. 52 may be due to emission coming from the Nb or Ta substrate. In Fig. 53 which is taken from the reference [126], we show a test of this hypothesis for Ni_3Ta by going to a photon energy where there is a photoemission minimum for Ta, such as the Cooper minimum, and reduced photoelectron mean free path. In this case at 80 eV and 100 eV photon energy it can be seen that the states at E_F are greatly decreased and the remaining Ni derived states are below E_F. Although this experiment was not done for Nb, we feel confident that a similar situation occurs; *i.e.* the hybridized *d*- band is filled and the observed states at E_F are from the underlying Nb. In this case we cannot come to a definite conclusion about the morphology of the near surface layer.

Fig. 54 shows the Ta $4f$- core levels for Ta(110) and our Ni_3Ta layer produced by heat treatment. the Ni_3Ta layer shows no bulk Ta $4f$- emission which demonstrates that the Ni_3Ta layer is at least 4λ in thickness where λ is the photoelectron mean free path estimated in this case to be $\approx 6 - 8$ Å.

6.5. Atomic Structure of Ni_3Nb Surface Compounds

	Annealing Time			
Temperature	3 Seconds	5 Seconds	10 Seconds	10 Minutes
800°C	Ni(111)	Diffuse Ni(111)	Diffuse Ni(111)	Disorder
890°C	Diffuse Ni(111)	Diffuse Ni(111)	Diffuse Ni(111)	Diffuse P(2×2)Nb/Ni(111)
990°C	Diffuse P(2×2)Nb/Ni(111)	Diffuse P(2×2)Nb/Ni(111)	P(2×2)Nb/Ni(111)	P(2×2)Nb/Ni(111)
1090°C	P(2×2)Nb/Ni(111)	P(2×2)Nb/Ni(111)	P(2×2)Nb/Ni(111)	P(2×2)Nb/Ni(111) +Nb(110)
1180°C	Nb(110)+ P(2×2)Nb/Ni(111)	Nb(110)+ P(2×2)Nb/Ni(111)	Nb(110)	
1280°C	Nb(110)	Nb(110)	Nb(110)	
1350°C	Nb(110)	Nb(110)		

Table 3: Low-energy electron diffraction patterns obtained for a 10 ML thick Ni overlayers supported on Nb(110) subjected to isothermal anneals of varying duration

The structure of the fully stabilized Ni_3Nb layer was studied using low-energy electron diffraction and Auger electron spectroscopy. Table 3 summarizes the results of a careful LEED study of various Ni/Nb surfaces produced during this study. By using the Ni(111) and Nb(110) LEED pattern shown in Fig. 55 (a) and (d) as a calibration, we have found that the lattice parameter of the Ni_3Nb surface compound is 5.1± 0.1 Å. Bulk Ni_3Nb has an orthorhombic unit cell with an R-type ordered layer in the (010) direction [125–126]. The lattice parameter of Ni_3Nb(010) shown in Fig. 56 is very close to the LEED result obtained here and is very close to the Ni(111) interatomic spacing except a Nb atom has replaced one out of four Ni atoms.

As shown in Table 3, it was found that this region showed a stable $p(2 \times 2)$ structure referenced to Ni(111). Before describing some of the properties of this surface phase we

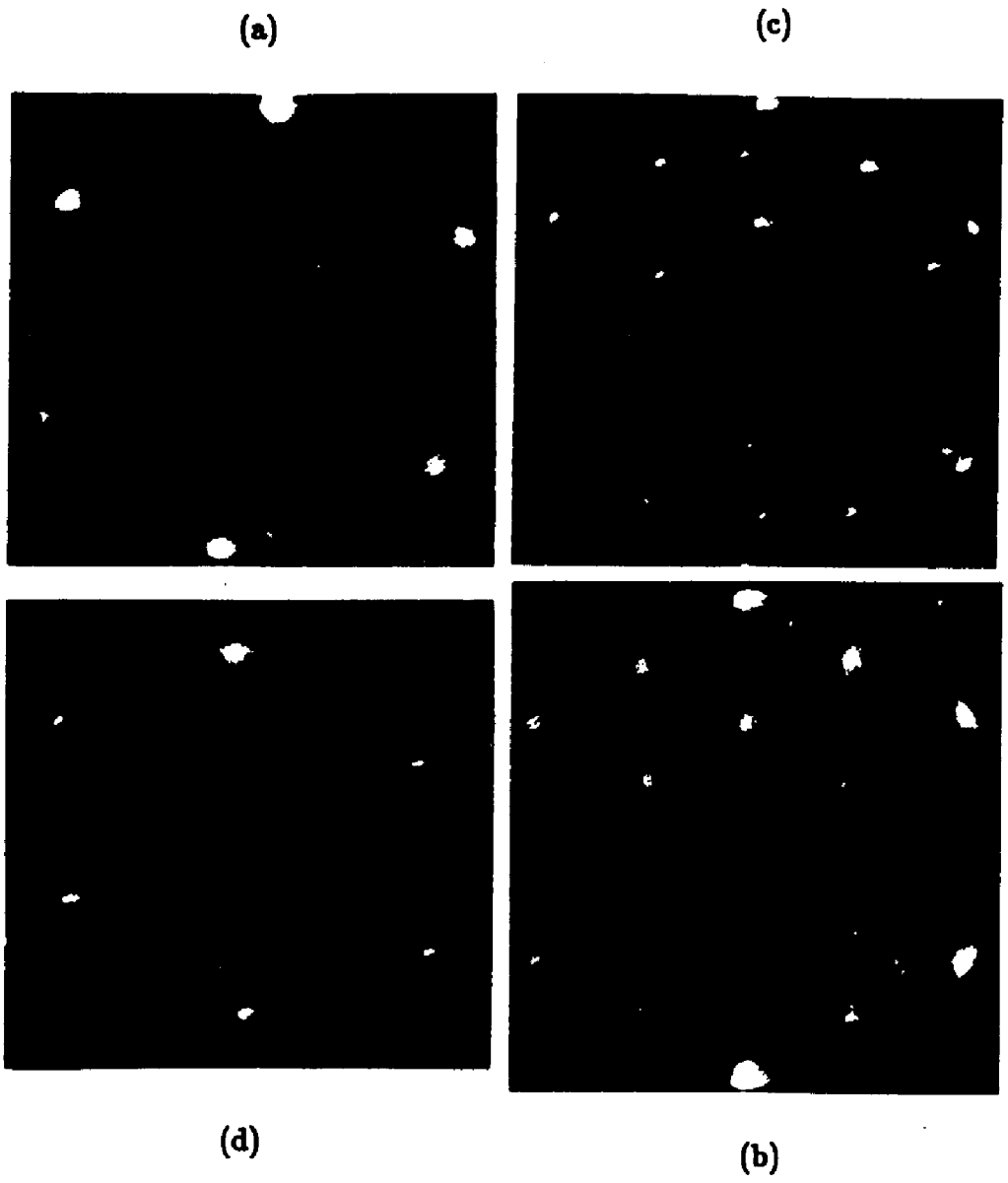

Figure 55: Low-energy electron diffraction patterns for (a) 10 ML Ni film (Ni(111)), (b) thermally stablilized Ni/Nb ($p(2 \times 2)$ Ni(111)), (c) the same surface heated to higher temperatures ($p(2 \times 2)$ Ni(111) + Nb(110)), and (d) Nb(110) substrate.

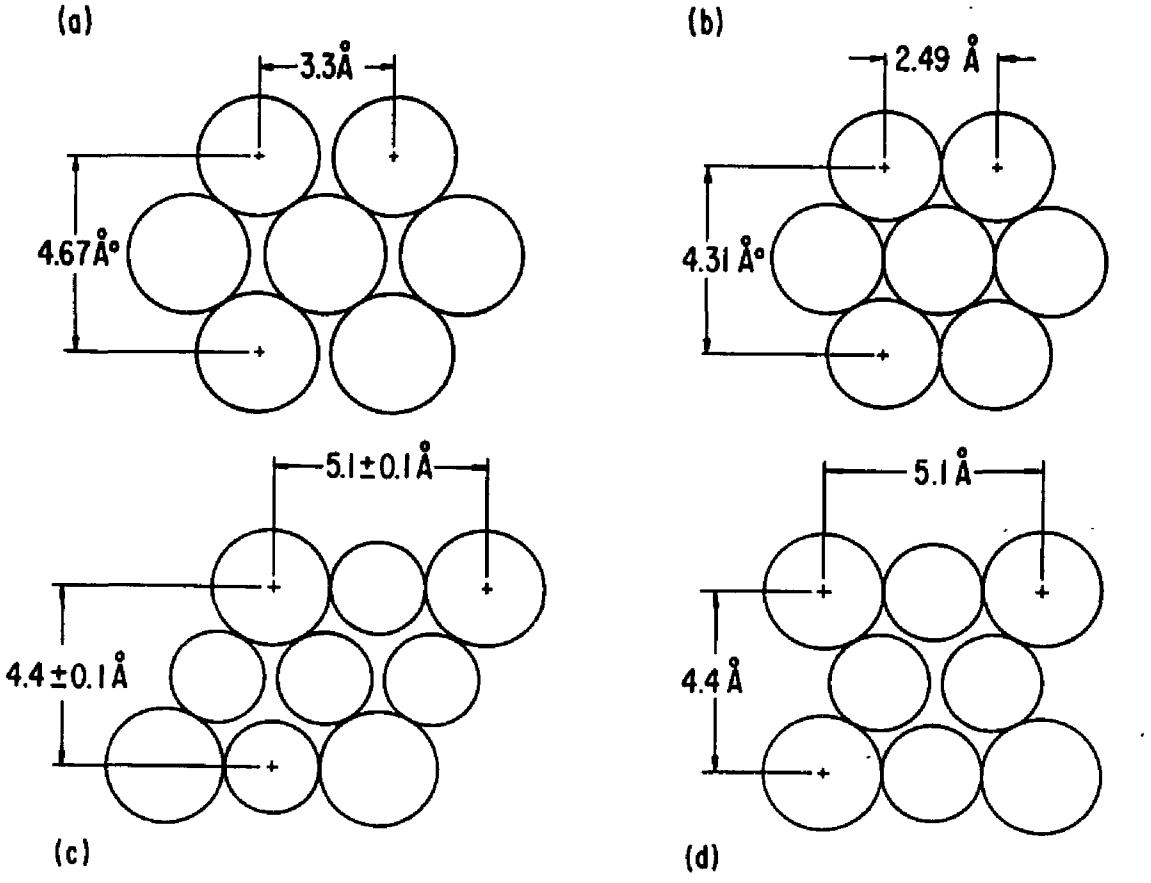

Figure 56: Hard-sphere models for (a) the Nb(110) surface, (b) the Ni(111) surface, (c) Ni_3Nb assuming T-type stacking, and (d) Ni_3Nb assuming R-type stacking. The larger spheres are Nb and the smaller spheres are Ni atoms.

point out the following. The mechanism of forming surface compound at an appropriate temperature is still not clear. It is simple to think of the Nb atoms as diffusing through the Ni film and forming a (2×2) structure on the surface. Even with the fact that Nb is not expected to segregate on Ni [129-130], it would still possible for Nb to segregate to the Ni surface in the present situation of a thin Ni layer on Nb. At this point it seems equally plausible to think of the Ni layer as diffusing into the Nb bulk, with some Nb from the bulk modifying the remaining Ni on the surface.

In general we find the $p(2 \times 2)$/Ni(111) phase shown in Fig. 55 is stable at about 1000°C. The LEED pattern of the ordered surface structure can be produced by the ordered surface structure that has a hexagonal unit cell with a lattice constant of 5.1± 0.1 Å in real space. This spacing is very similar to the Ni(111) hexagonal unit cell and is probably related to why this compound can easily form. This ordered structure has the triangular (T)-type structure [127] found for Ni_3Al and is somewhat different from bulk Ni_3Nb which has a rectangular (R)-type structure. A hard-sphere model of an ideal Ni_3Nb surface structure is shown in Fig. 56 (d). Annealing at 900°C for long times and 1200°C for a short time (several seconds) produces a combination of $p(2 \times 2)$/Ni(111) and a Nb(110) structure. Islands of this compound apparently are left as Ni atoms diffuse into the Nb bulk and not enough Ni atoms are on the surface to form a complete layer of Ni_3Nb. Fig. 55 (d) shows the emergence of Nb(110) spots together with the Ni_3Nb features.

There are two basic types of close-packed ordered structures for A_3B alloys, designated as the triangular (T)-type and the rectangular (R)-type [127], as illustrated in Fig. 56 (c) and (d), respectively. The R-type closed-packed structure occurs in the bulk $Ni_3Nb(010)$ phase and has a very similar lattice constant to the surface T-type close-packed structure observed here. The reasons this alloy forms this different type of surface structure may be correlated with two fundamental alloying variables: geometry and electron concentration (e/a, the average number of valence electrons per atom) difference between the overlayer and the substrate. Fig. 56 shows that the T-type close-packed structure fits the Nb(110) substrate much better than R-type. The minimum total mismatch of T-type unit cell to an underlying Nb(110) layer is 34% smaller than the R-type close-packed structure. It is therefore plausible that the T-type close-packed structure has a lower surface energy on top of the Nb(110) substrate, since the Nb atoms can more easily replace the Ni atoms during the annealing, as compared to the R-type structure.

Systematical studies of close-packed ordered A_3B structures have also revealed that with a decrease in e/a, the ordered structure changes from predominantly hexagonal to predominantly cubic stacking and further decrease in e/a leads to a change in the basic layer structure from R- to T-type [131–133]. Considering the electron concentration, the Nb substrate has a e/a of ≈ 5.00, and the bulk structure of Ni_3Nb has an e/a of ≈ 8.75. Because of this, the average valence electron concentration of the Ni_3Nb surface structure will be decreased because the Nb substrate has a much lower electron concentration. Hence, the reduction of the electron concentration of the surface structure because of Nb substrate's lower e/a can possibly lead to the change of stacking character from the bulk R-type to the T-type surface structure. We also mention that the reduced density of states at the Fermi level E_F is also thought to be an effect of the underlying Nb or Ta substrate which hybridizes with the d-band of the surface layer to leave a relatively inert surface layer with electronic properties that appear to be different from the bulk.

6.6. Chemical Activity of Ni_3Nb Surface Compounds

In previous sections, LEED and AES studies showed that a stable ordered $Ni_3Nb(010)$ surface compound could be produced by thermal treatments on Ni/Nb. The photoemission study of this unique surface compound shows that the hybridized *d*- states shift to higher binding energy and electronic density of states is reduced near E_F. In general, this surface compound exhibits a new atomic structure and surface electronic density of state on the surface which is quite different from either that of Ni adsorbate or that of Nb substrate. In our earlier discussion of Ni and Pt films, we found that changes in the electronic structure modified their chemical properties. We exposed these thermally modified surfaces to H_2 and CO to determine if the chemical properties of these surfaces were also changed.

Fig. 57 (a) and (b) show the angle-integrated photoemission spectra at 21.2 eV photon energy in Ni_3Nb surface compound after various CO and H_2 exposures. We found that CO does not adsorb on the $Ni_3Nb(010)$ surface. In other words, this surface is inert to CO molecules at room temperature. No hydrogen induced features were observed in Fig. 57 (b). In view of the present results, it is unlikely that hydrogen molecules dissociate on the surface and diffuse into the bulk because UPS is sensitive to surface H-Nb bonds. It should be noted that this surface compound has greatly reduced chemical activity as compared to either Ni(111) or Nb(110), and it is tempting to correlate this reduction in chemical activity with the movement of the *d*- bands below E_F and the noble-metal-like character of this layer. Similar results were obtained for Ni_3Ta surface compounds.

This is another example which shows that the chemisorption of simple molecules on bimetallic compound cannot be interpreted by describing the alloy surface as a mere superposition of individual metals.

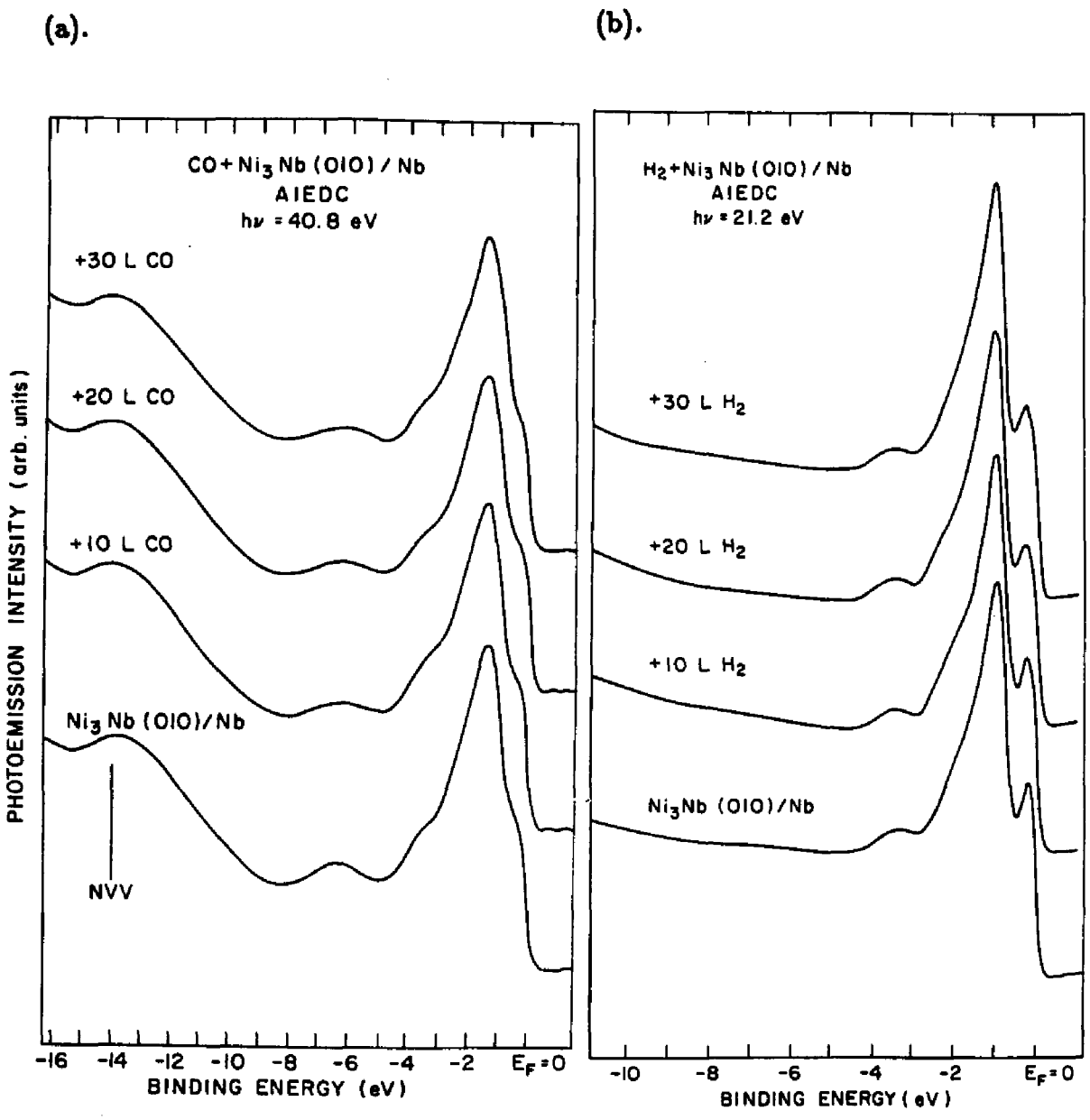

Figure 57: AIUPS EDC's of $Ni_3Nb(010)$ surface compound after various exposure of (a) CO or (b) H_2 at 300 K.

6.7. Summary

In this chapter, we report our studies of surface compounds produced by heat treatments. The attempt was to discover and understand the new surface intermetallic compounds for Pt/Nb and Ni/Nb systems.

It is found that Pt atoms undergo interdiffusion and reaction at elevated temperatures. No stable ordered surface compounds were observed for Pt/Nb system. However, novel Ni/Nb and Ni/Ta surface compounds were made by thermal stabilization of Ni overlayers deposited on clean Nb(110) or Ta(110) substrates. Low-energy electron diffraction studies show that the surface compound is ordered and has a hexagonal structure. Auger and photoemission investigation show that the most stable surface compounds have a stoichiometry at or very near A_3B where A = Ni and B = Nb or Ta. Comparison of our results with bulk data suggests that our surface Ni_3Nb or Ni_3Ta has a structure more like bulk Ni_3Al than bulk Ni_3Nb. Examination of the surface composition at various annealing temperatures further suggests that the near-surface stoichiometry can be controlled by varying the annealing temperature which controls the reaction kinetics and interdiffusion parameters.

It will be of great interest to see if other surface compounds related to the A_3B structure can be formed by heat treatments. These would include, for example, Co_3Ti, Ni_3Al, and Ni_3V. The relationship of these structures to their bulk counterparts promises to give important insight into how the changes of degrees of freedom and surface energies modifies the formation of these alloys. Furthermore the changed chemical properties of these layers may provide a way to passivate the surfaces of certain reactive transition-metals.

Chapter 7.
K-resolved Inverse Photoemission Studies of Pd Overlayers

7.1. Introduction

Interface states, like surface states, play an important role in the characterization of the interface geometrical structure and the interaction of two materials. Photoemission studies of Ni, Pd, and Pt monolayers on Nb(110) in previous chapters have strongly suggested the existence of interface resonance states below the Fermi level. LEED and AES studies on Pd/Nb(110) indicate that a structural phase transition from a commensurate (110) epitaxial overlayer to an incommensurate overlayer occurs at about 1.2 monolayer Pd coverage. However, the electronic structure above the Fermi level is still unknown. As a complementary technique to angle-resolved photoemission, k-resolved inverse photoemission has been demonstrated to be able to map the unoccupied energy-band of solids.

In this chapter we present a k-resolved inverse photoemission study of Pd overlayers on Nb(110) to demonstrate the bonding and antibonding interaction between the transition-metal adsorbate and substrate at the interface. We report the first observation of an antibonding interface state above the Fermi level in a metal-metal system. We further show that upon the formation of the interface the interface state shows two-dimensional dispersion rather than the three-dimensional dispersion characteristic of the Nb bulk band. In other words, we observe a Nb derived state, which only exists as a result of the formation of the interface and has antibonding character. Our results also indicate a modification of the interface state due to changes in the nearest-neighbor coordination and in the thickness of Pd.

In the following sections, I will first briefly review the previous studies of the morphology and electronic structure of Pd overlayers on Nb(110) and their relationship with chemical activity. Then the band structure of Pd monolayers on Nb(110) will be presented to compare with the theoretical predictions. The emphasis will be put on the characterization of the interface state. Finally, the nature of the Pd(111) image state as a function of the growth of Pd overlayers will be discussed.

7.2. Morphology and Chemical Activity of Pd Overlayers

As mentioned before, Pd has similar physical and chemical properties to Ni and Pt. Pd overlayers on Nb(110) is a metal-metal system that has received considerable attention because of its unique chemical properties. Most of the experimental work on Pd overlayers on Nb(110) has been carried out in this Laboratory by other scientists using PES, LEED, AES, and work function measurements. To verify the previous results on the morphology of Pd overlayers on Nb(110), we conducted the LEED and AES experiments at a lower pressure. Together with a new secondary electron emission current measurement, we are able to determine precisely the thickness and geometric structure of Pd overlayers on Nb(110) at room temperature. This enables us to consider the inverse photoemission results systematically with the modified surface structures.

Generally, our results on the morphology of Pd overlayers on Nb(110) are in good agreement with the previous studies [11]. The study shows that, like Pt overlayers, Pd first grows epitaxially on the Nb(110) substrate upon deposition until a coverage of approximately 1.2 monolayers. At this point the Pd undergoes a structural phase transition from a commensurate (110) to an incommensurate Pd(111) structure. This change is marked by the appearance of multiple scattering beats between the Pd(111) overlayer and the Nb(110) substrate in the LEED patterns. Fig. 58 shows the LEED patterns before and after the structural phase transition of Pd overlayers on Nb(110). After the structural phase transition, the intensity of the multiple scattering beats increases with Pd coverage while the spacing between spots remains constant. This implies that the transition takes place via the formation of Pd(111) islands. Sagurton and Strongin [101] have correlated the surface structure of Pd overlayers on Nb(110) with the electronic structure obtained from photoemission studies. They observe no unusual or dramatic changes in the photoemission spectra in the neighborhood of the phase transition. Therefore, they conclude that this phase transition has no substantial effect on the surface electronic structure. Besides the LEED technique, which is based on the manifestation of multiple-scattering events in the final state of the excited-electron wave function reflecting the geometry of the atomic environment, Batanouny and Strongin [68] have employed angle-resolved synchrotron radiation photoemission from valence levels to obtain Pd overlayer site geometry information. By utilizing polarization effects and photoexcitation cross-section effects, they have demonstrated that the bonding-orbital symmetry is d_{zz}- or d_{yz}-, and concluded that the Pd overlayer on Nb(110) has a hollow-site geometry.

(a).

(b).

Figure 58: LEED patterns of (a) Nb(110) substrate and (b) monolayer Pd on Nb(110) showing characteristic multiple scattering beat structures.

(a).

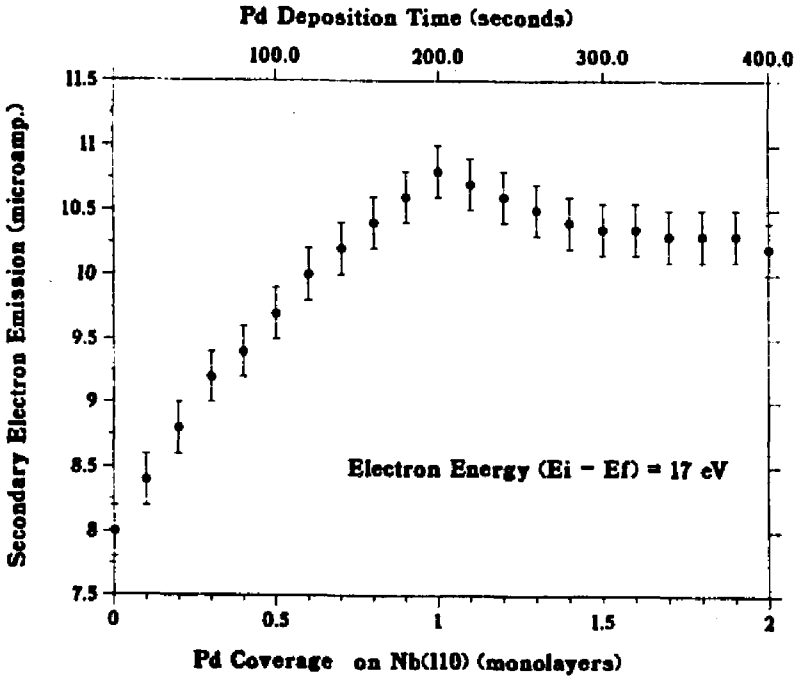

(b).

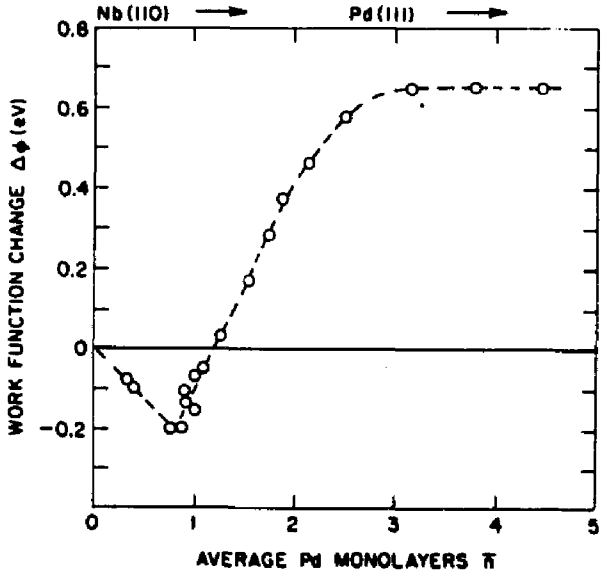

Figure 59: (a) Secondary electron emission measured during constant flux deposition of Pd on Nb(110). (b) Work function change as a function of Pd coverage on Nb(110).

The study of secondary electron emission as a function of changes in surface structure and composition reveals an interesting result on the growth of Pd overlayers on Nb(110). Fig. 59 (a) shows the deposition of Pd on Nb(110) followed by changes in the secondary emission current I_{cc} for the calibrated Pd coverage thickness. Changes in secondary electron emission (SEE) during the inverse photoemission experiment are observed by measuring changes in the net current I_{cc} flowing into the sample. Up to one monolayer coverage of Pd, there is an almost linear rise in I_{cc}, followed by a sharp break with a change in sign of the slope of the plot which indicates very precisely the completion of the Pd monolayer. The crossover points can be obtained with precision and they are stable and reproducible between successive measurements. The usual explanation of this trend and sensitivity is that the changes in emission are due to changes in the work function which affect especially the escape of secondary electrons with very low energies. In Fig. 59 (b), we show the work function changes as a function of Pd coverage on Nb(110). This work function measurement is consistent with that of the secondary electron emission work. When the work function decreases as the Pd coverage approaches one monolayer, the secondary electron current increases; with the work function increase above one monolayer coverage, the secondary electron current decreases. Rhead and Argile [21,22] suggested that this enhancement of secondary electron emission may also be caused by an enhancement of surface ionization due to surface electron scattering modes induced by the presence of the adsorbed layer. This simple scheme can be used to explain the pre-monolayer breaks, the effect of a second layer, and of disorder.

With all this information on surface structure and composition, we now discuss the chemical properties of Pd overlayers on Nb(110). Strongin and co-workers [134] have demonstrated that thin layers (20 $\sim$ 130 Å) of Pd or Pt greatly enhance the uptake rate of hydrogen into bulk Nb with almost every hydrogen atom that hits the surface passing into the bulk. They presented a model to show that large uptake rates are achieved by modification of the surface properties of Pd with the bulk properties of Nb which therefore results in a smaller barrier for hydrogen atom migration into the bulk. Colbert and Strongin [135] have also investigated the interaction of CO with Pd overlayers on Nb(110) using photoemission. They found that at room temperature CO does not adsorb onto a Pd monolayer. Like a Pt monolayer on Nb(110), a monolayer of Pd on Nb(110) is noble-metal-like. As mentioned earlier, these unique chemical properties are attributed to the modified electronic and geometrical structure of the interface. In the commensurate (110) phase, the valence band of

a Pd monolayer is dominated by an interface resonance state caused by the Nb-Pd bonding interaction at about 1.5 eV below the Fermi level. The characteristic of this modified valence band is similar to the valence band of a noble metal. This interpretation on the inert chemical reactivity of a monolayer of Pd on Nb(110) has also been confirmed by Williams and Batanouny [136] using resonant photoemission in the CIS mode. Their studies on the valence photoelectron behavior in the vicinity of core thresholds indicate a decrease in the local density of states near E_F for a monolayer of Pd on Nb(110).

7.3. Electronic Structure of Pd Overlayers

To explain the unique chemical properties of Pd overlayers on Nb(110), a knowledge of the geometrical structure of the surface and interface is not enough. In this section, we will review previous photoemission studies of the electronic structure of Pd overlayers on Nb(110) below Fermi level. Then we report a recent k-resolved inverse photoemission study of the electronic structure of Pd overlayers on Nb(110) above the Fermi level. Finally, a simple interface bonding and antibonding model is presented to describe the interaction of transition-metal adsorbates with the Nb(110) substrate.

The photoemission studies of Pd on Nb(110) were carried out in Strongin's group in the early 1980's [63,135,137]. Fig. 60 shows the angle-integrated photoemission EDC's as a function of Pd coverage on Nb(110) taken at 21.2 eV photon energy by Shang-Lin and Batanouny [137]. Like Pt overlayers on Nb(110), as the Pd coverage approaches to one monolayer, two pronounced energy states were observed which significantly reduced the density of states at the Fermi level. These two states were proposed to be a resonant *d*- state at -3.1 eV initial energy and a surface resonance state at -0.7 eV. We are particularly interested in the so-called resonant *d*- state at -3.1 eV initial energy due to the interaction of Pd *d*- levels with the Nb(110) bulk bands. This state is either attenuated or shifts to -2.4 eV initial energy as the Pd coverage rises above two monolayers. The angle-resolved synchrotron radiation photoemission study of submonolayer Pd on Nb(110) by Batanouny and Strongin shows two localized initial states of mixed Pd-Nb d_{zz}- d_{yz}- character at about -2.0 eV [63]. Using energy-dependent and polarization-dependent techniques, they showed that the bonding-orbital symmetry is d_{zz}- or d_{yz}-, thereby suggesting a hollow-site geometry for the Pd^*(110) overlayer on Nb(110). The energies of the photoemission features identified with bonding between the Pd overlayer and the Nb(110) substrate may be different from previous experiments, but the general conclusion is that the bonding state due to the interaction of Pd *d*- levels with the Nb bulk band is observed at one monolayer Pd coverage. Kumar and Bennemann [10] have used a self-consistent tight-binding scheme to study the local electronic density of states for Pd overlayers on Nb(110). They showed that at low coverage Pd induces a Pd-Nb resonance near the bottom of the Nb *d*- band. They predicted that the resonance state would shift to lower binding energy as the Pd coverage is increased. The modification of the Pd-derived resonance state is attributed to the Pd-Nb bonding and reduced the Pd nearest-neighbor coordination.

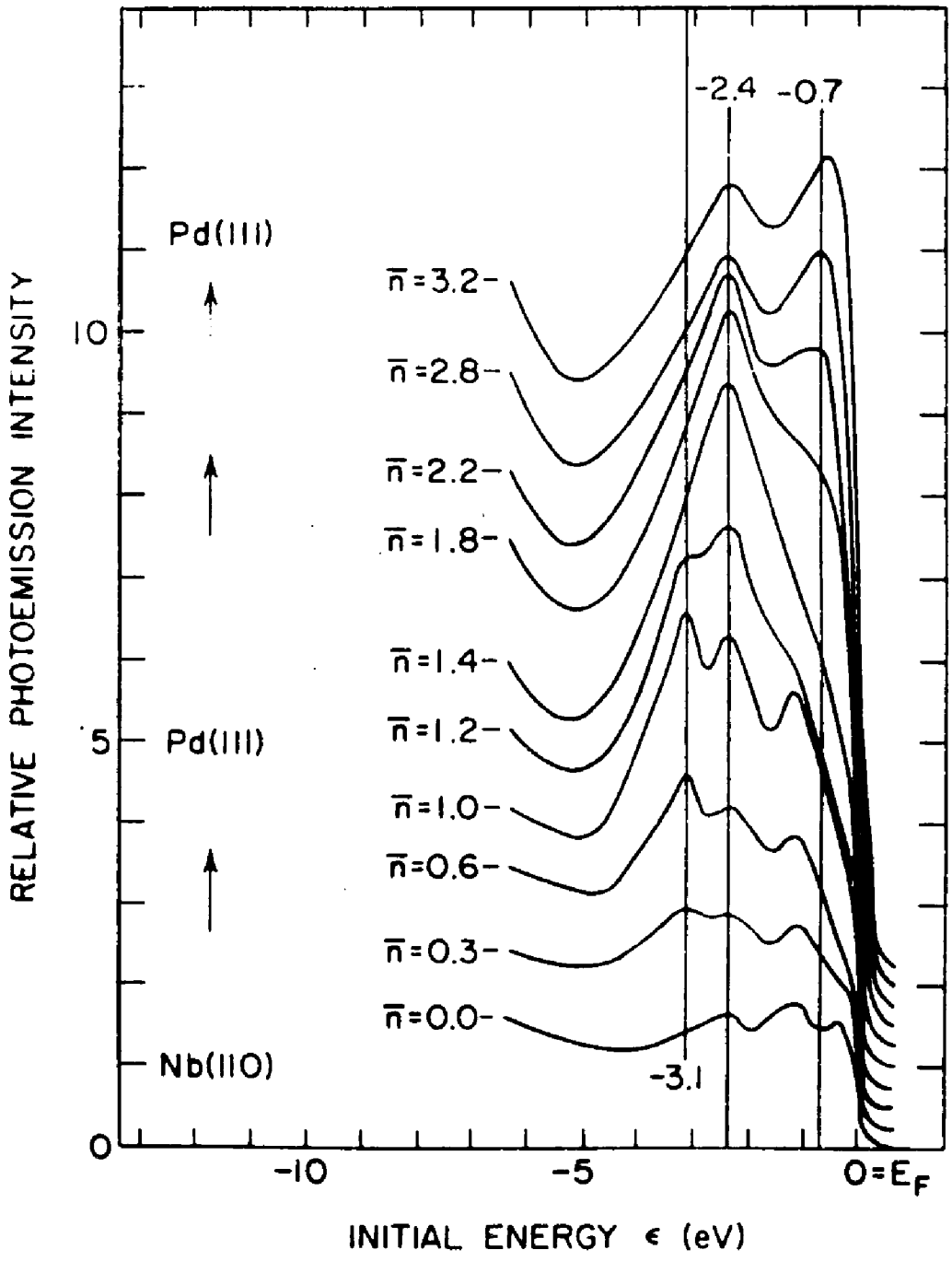

Figure 60: AIUPS EDC's of various coverage of Pd overlayers on Nb(110). $\bar{n}$ is the average number of Pd monolayers.

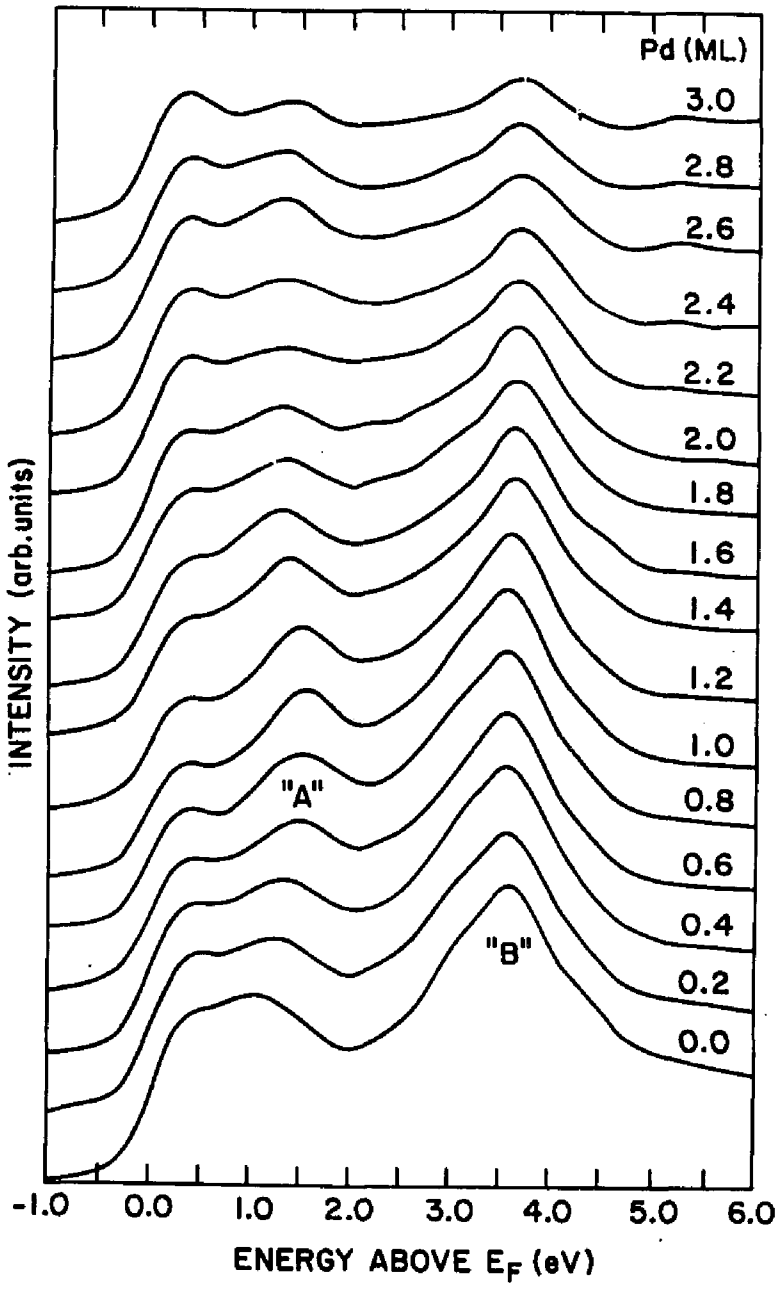

Figure 61: K-resolved inverse photoemission: normal incidence spectra of a clean Nb(110) substrate surface with Pd overlayers of various coverage. Note the strong shift of the Nb-derived features at about one monolayer of Pd coverage.

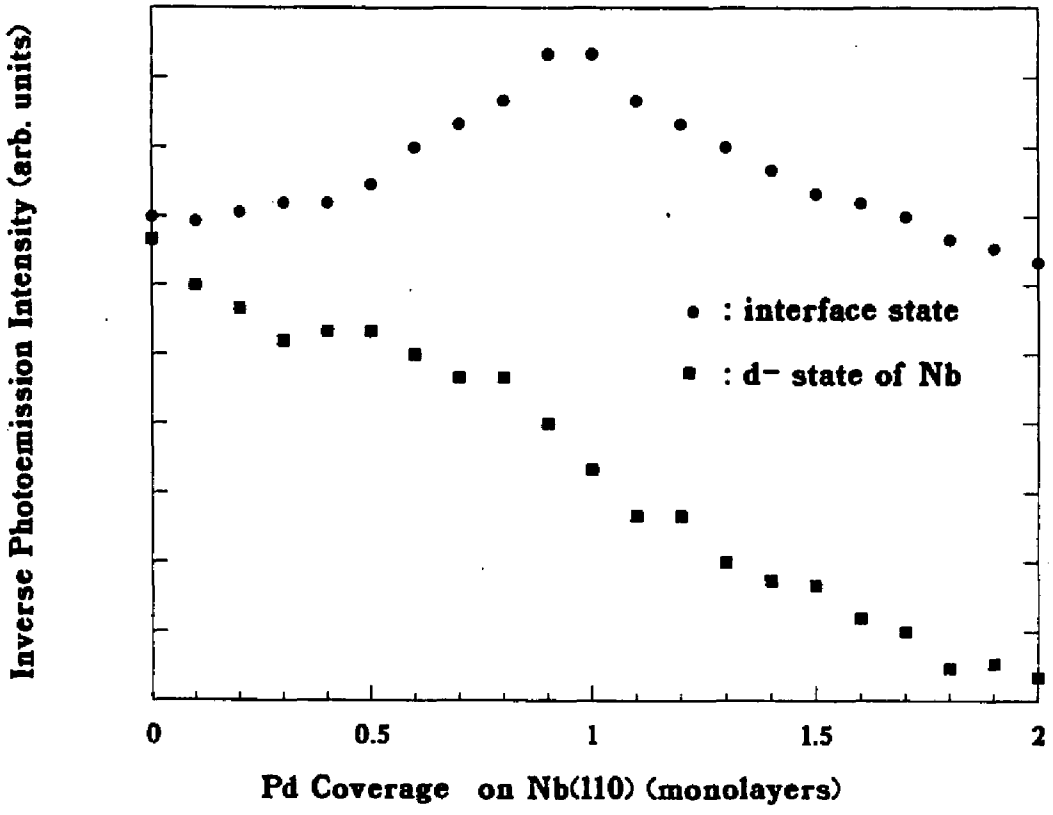

Figure 62: Amplitude dependence of the k-resolved inverse photoemission peaks of the antibonding interface state and the Nb *d*- state as a function of Pd coverage. The normally incident electrons have an energy of 16.8 eV referred to the Fermi level.

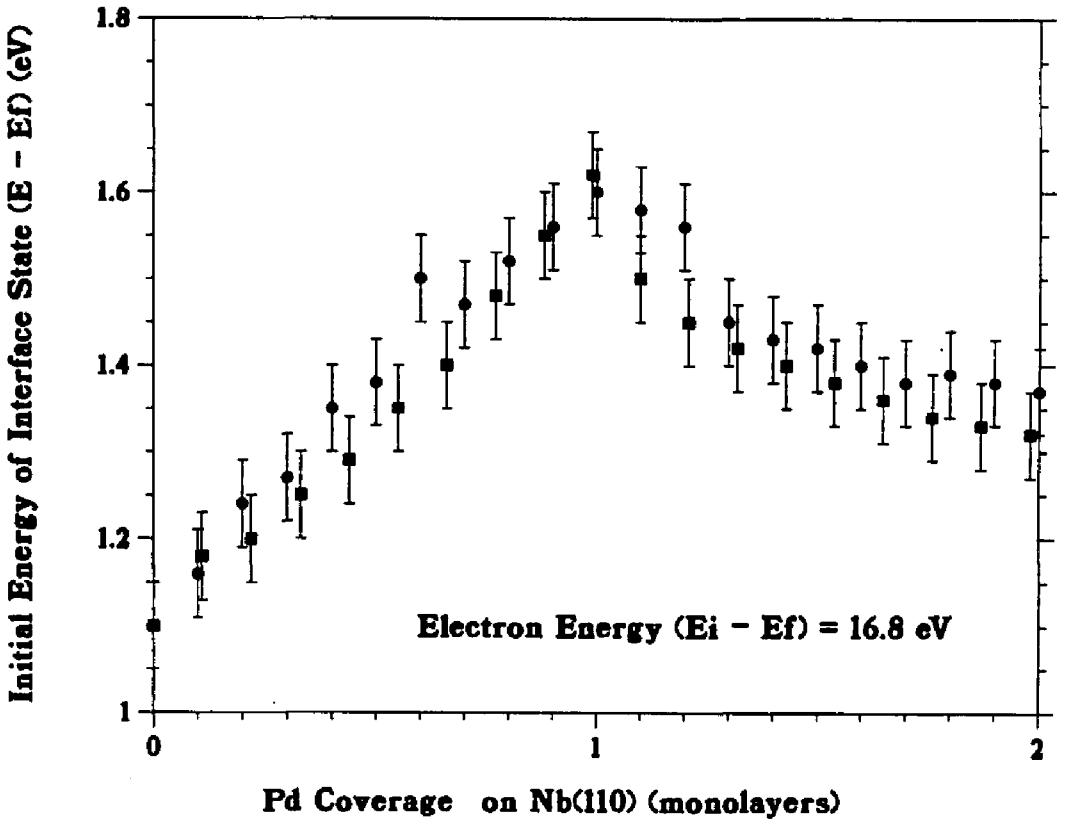

Figure 63: The initial energy of the antibonding interface state referred to the Fermi level as a function a Pd coverage. The normally incident electrons have an energy of 16.8 eV referred to the Fermi level.

Now we present a recent k-resolved inverse photoemission study of Pd overlayers on Nb(110). To our knowledge this is the first time a metal-metal system has been systematically studied by k-resolved inverse photoemission. Our data show unambiguously that an antibonding interface resonance state exists above the Fermi level which is very sensitive to the geometrical structure of the Pd-Nb interface.

The experiment was performed on a 0.005 inch thick recrystallized Nb(110) foil shown in Fig. 7. Ultrathin Pd layers were grown *in situ* by evaporating pure Pd from a W-basket, at a pressure of 2×10^{-10} Torr onto the clean Nb(110) substrate. The surface structure of the Pd overlayers was constantly monitored by LEED. The secondary electron current produced by the inverse photoemission electron beam was used, together with AES and a quartz crystal thin film thickness monitor to determine precisely the Pd overlayer thickness. The k-resolved inverse photoemission apparatus incorporates a BaO-cathode electron gun which has been specially designed by Stoffel and Johnson [53] for low energy and high currents in the space-charge limited electron energy region giving an energy spread of approximately 2.75 eV with a momentum resolution of 0.1 $\AA^{-1}$. Photon detection and analysis were accomplished by a normal incidence grating spectrometer in the energy range 10-30 eV with a resolving power of about 75 [138]. Inverse photoemission spectra were obtained as a function of incident electron beam energy for different angles of incidence.

Fig. 61 shows k-resolved inverse photoemission spectra as a function of Pd coverage on Nb(110) taken at normal incidence with a electron energy of 16.8 eV. As the Pd coverage approaches one monolayer, the Nb *d*- states at the Fermi level and at E_F+3.5 eV are attenuated. The most significant phenomenon is that the Nb state at E_F+1.1 eV shifts to 1.6 eV initial energy. Above a monolayer Pd coverage, where the structural phase transition occurs, the state at E_F+1.6 eV shifts back to E_F+1.3 eV followed by the build up of Pd(111) density of states at the Fermi level. As the Pd coverage increases from two to three monolayers, the Pd(111) surface state and image state appear at E_F+1.2 eV and E_F+5.1 eV respectively. First, it is clear that the state located at E_F+1.6 eV for one monolayer of Pd on Nb(110) is derived from Nb *d*- states via their interaction with the Pd *d*- levels. Fig. 62 shows the intensity dependence of this Nb-derived interface state and of the Nb *d*- state at E_F+3.5 eV as a function of Pd coverage. As the Pd overlayer thickness increases, the Nb(110) *d*- state at E_F+3.5 eV is attenuated linearly, whereas the Nb-derived interface state shows a maximum at one monolayer Pd thickness. The decreasing intensity of the interface state above two monolayers can be attributed either to

changes in the Pd-Nb interaction at the interface or to attenuation by the Pd overlayers. Fig. 63 shows the initial energy of the interface state as a function of Pd coverage. We see that as Pd is deposited onto the Nb(110) surface, the Nb *d*- state at E_F+1.1 eV shifts to higher energy at about E_F+1.6 eV. Above one monolayer Pd coverage, the interface state shifts to lower binding energy. We attribute the binding energy shift of the interface state to the weakening of the Pd-Nb interaction due to the structural phase transition from a commensurate P*d**(110) to an incommensurate Pd(111) structure and the increase in Pd thickness. This inverse photoemission measurement is a direct observation of the surface structural phase transition and of changes in Pd nearest-neighbor coordination. K-resolved inverse photoemission measurements with an electron beam energy of 16.8 eV for both clean Nb(110) and the surface of bulk Pd do not show the feature at E_F+1.6 eV. The binding energy of the feature at E_F+1.6 eV is also very sensitive to the geometrical structure of the Pd-Nb interface. Together with the results of theoretical studies [10] and photoemission data for Pd overlayers on Nb(110), we suggest that this Pd-induced state above the Fermi level is an antibonding interface state which exists due to the junction between the Pd adsorbate and Nb substrate. To test this suggestion, we have carried out a series of k-dependent and energy-dependent inverse photoemission experiments on the monolayer Pd on Nb(110) to map the band structure of the interface state. The results are discussed in detail in the next section.

An interesting phenomenon is that within the resolution of our experiment (about 0.3 eV), no obvious sudden change in the binding energy of the interface state is observed when the monolayer Pd undergoes the structural phase transition from commensurate P*d**(110) to incommensurate Pd(111). This indicates that the growth mechanism of the Pd fcc lattice proceeds in a domain-like fashion rather than by an instantaneous transition from the substrate bcc configuration to the close-packed bcc structure.

Another interesting subject is the character of the image state and the Shockley-type surface state for the modified (111) surface. Do we still expect to see these surface states for ultrathin metal films? Shang-Lin and Batanouny[187] have studied the Pd overlayers on Nb(110) by AIUPS and have shown that the Pd(111) surface state commences with the deposition of the third atomic layer and is completely established at the full fourth layer. In our k-resolved inverse photoemission experiments with much slower Pd deposition rate and a better vacuum (10^{-11} Torr range), we were not only able to observe the appearance of the surface state but also the binding energy shifts of the image state. Our data in Fig. 61

show that the surface state and image state of Pd(111) are observed beginning with the deposition of 2.5 monolayers of Pd and are completely established at about 5 monolayers. It is noted that there is a 0.2 eV shift of the Pd(111) image state to lower binding energy when the thickness of deposited Pd layer increases from 2.5 to 5.0 monolayers. This can be attributed to a 0.2 eV increase in the work function as the Pd coverage grows from 2.5 to 5.0 monolayers on Nb(110) [137].

7.4. Band Structure of Monolayer Pd

There has been considerable interest in interface states or interface resonances for thin films. Batanouny and Davenport [11] have taken angle-resolved photoemission (ARUPS) data and performed a self-consistent linear augmented-plane-wave (LAPW) calculation on the occupied electronic structure of a Pd monolayer adsorbed on Nb(110). They found good overall agreement between theory and experimental results on the occupied band structures. Fig. 64 shows the experimental dispersion of Pd-induced states on Nb(110) and the calculated dispersion for a bcc(110) Nb film with an adsorbed Pd monolayer. It is found that most of the Pd features overlap the Nb bands and are resonances rather than surface states. The Pd *d*- band manifold overlaps mainly *s*- like Nb bands and the interaction between the two metals is weak, which leads to sharp resonances. It is shown directly that the Pd *d*-like states lie below the Fermi level. Therefore the Pd density of states resembles that of a noble metal. With the use of a self-consistent tight-binding scheme, Kumar and Bennemann[10] have calculated the occupied and unoccupied local electronic densities of states (LDOS) for commensurate Pd^* (110) and incommensurate Pd(111) layers on Nb(110). At the coverage less than one monolayer, they noted that Pd induces a Pd-Nb resonance near the bottom of the Nb *d*- band. After calculating the interface energy and comparing with the photoemission data they predicted a commensurate to incommensurate structural transformation for about one monolayer of Pd. They showed that the *d*-electron charge transfer across the interface and the LDOS of Pd at the Fermi level are small. The latter is due to narrowing of the band via reduced Pd coordination and to shifting via hybridization with the substrate.

From the k-resolved inverse photoemission data, we can map the dispersion relation of this new Pd-induced state derived from Nb(110) as a function of $k_\perp$ and $k_\parallel$ to prove that it is a true anti-bonding interface state. First, we will investigate the dispersion with $k_\perp$ to show that the 1.6 eV state is localized in the Pd/Nb interface. Then we will study the dispersion relation along $k_\parallel$ to show that this interface state has antibonding character, *i.e.* the state at E_F+1.6 eV is not only an interface state, it is an antibonding interface state.

The interface states can be distinguished experimentally from the oscillatory bulk states since they lack a well-defined momentum perpendicular to the surface $k_\perp$. One can keep $k_\parallel$ fixed and vary $k_\perp$ by tuning the incident electron beam energy E_{el} at selected angles. Bulk states generally exhibit an energy band dispersion $E(k_\perp)$ as E_{el} is varied while interface states, like surface states, remain stationary in their binding energy and change only in

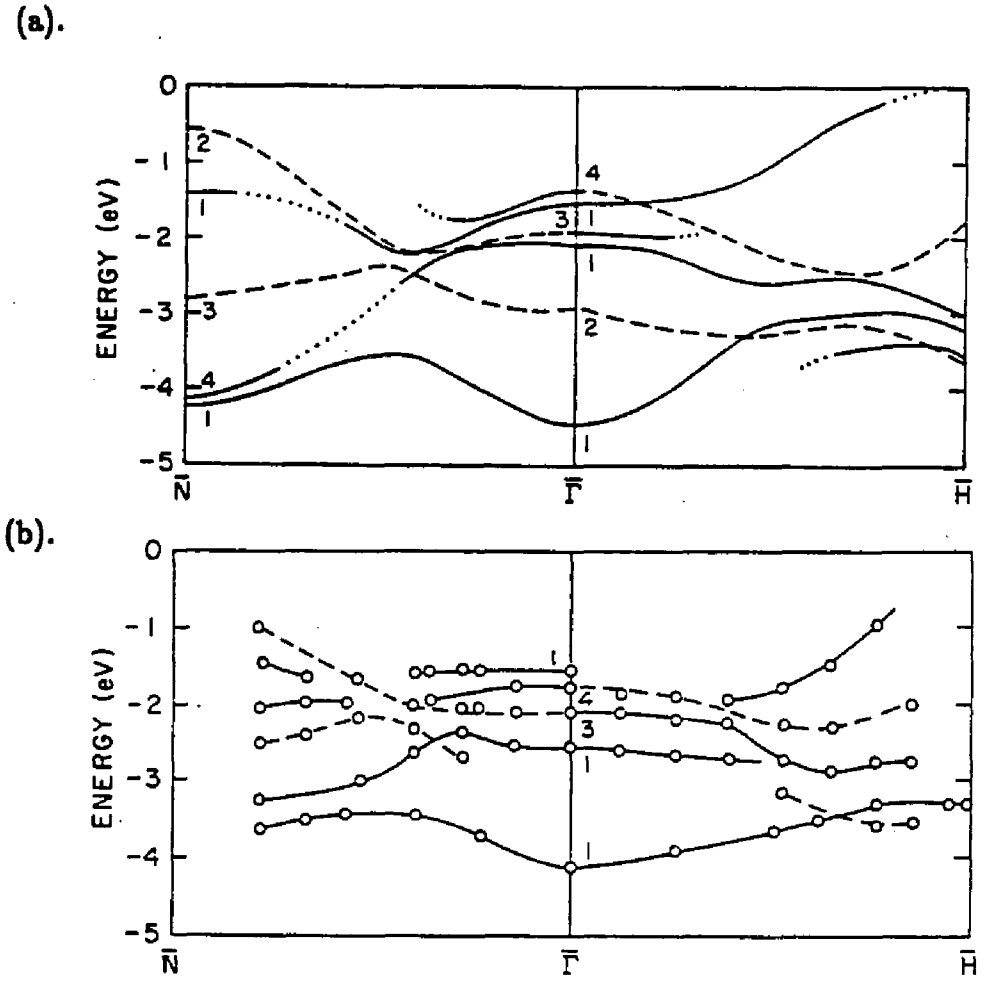

Figure 64: (a) Calculated states for a Nb film with an adsorbed Pd monolayer compared with (b) the experimental dispersion of Pd-induced states on Nb(110). States which are dotted are strongly hybridized with Nb. Solid (dashed) lines are states which are even (odd) under reflection.

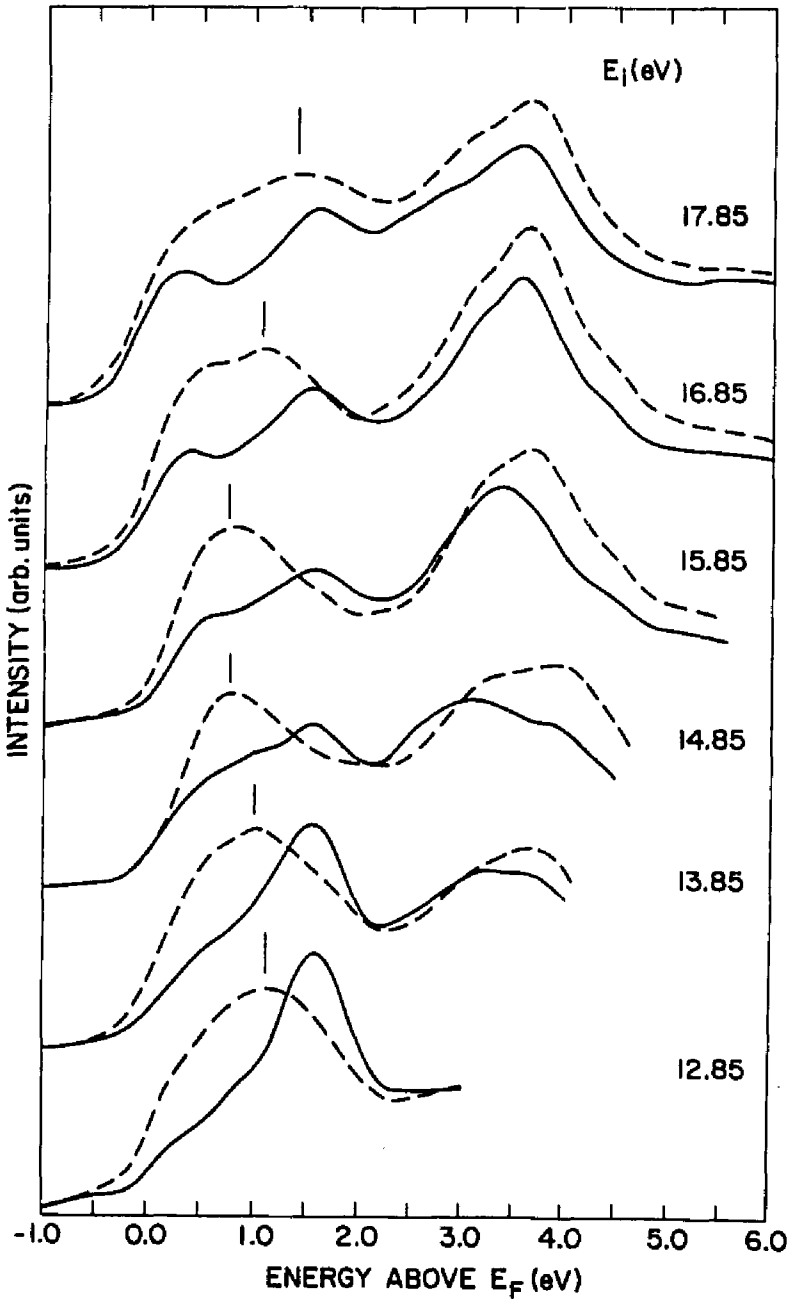

Figure 65: KRIPES spectra recorded from clean Nb(110) (dashed spectra) and from the Nb surface with a monolayer of Pd (solid line spectra). The normally incident electron beam energy with respect to the Fermi level is indicated.

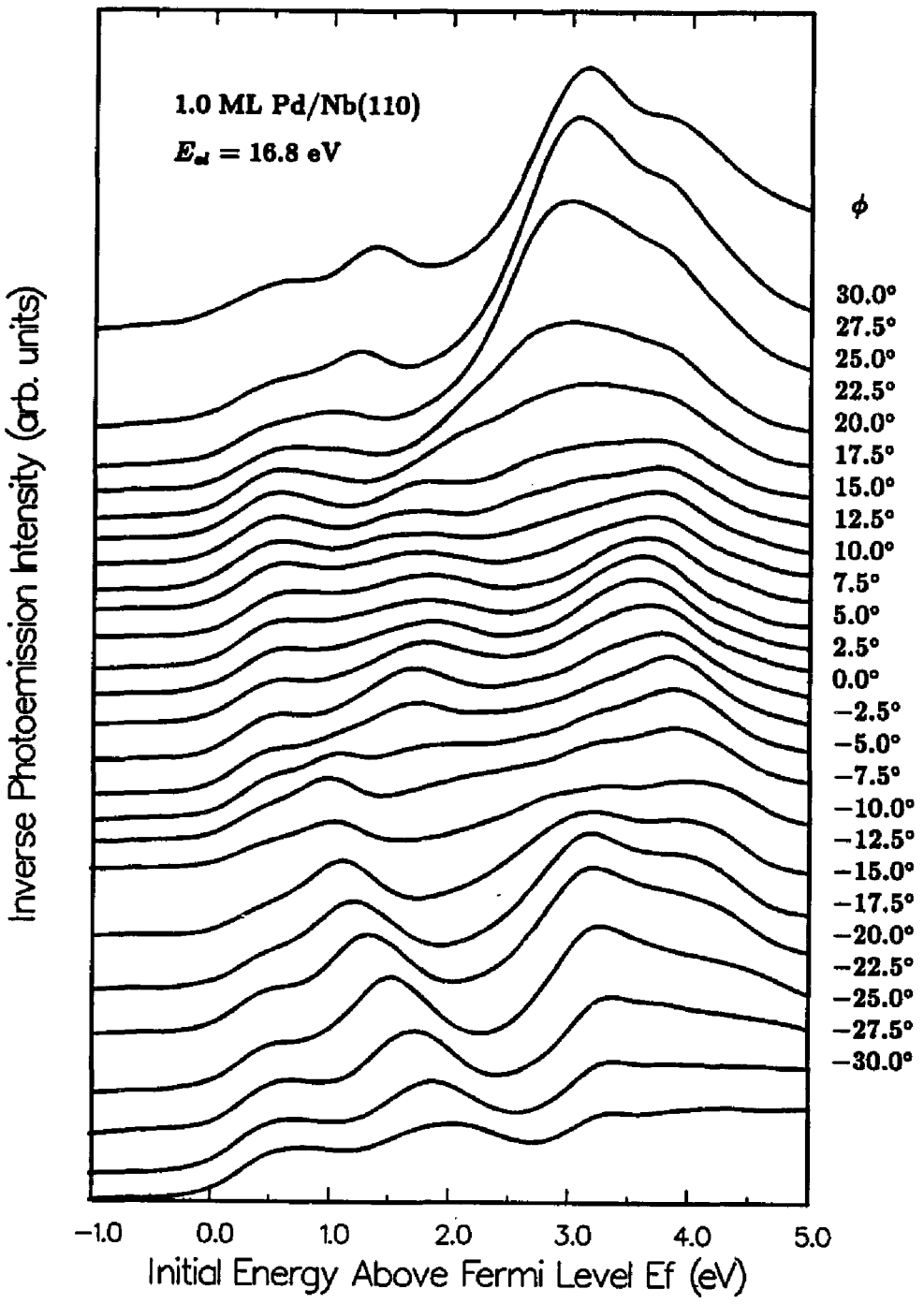

Figure 66: K-resolved inverse photoemission spectra for a monolayer of Pd on Nb(110) taken at 16.8 eV initial electron energy relative to E_F as a function of $k_{||}$ along the $\bar{\Gamma}\bar{P}$ direction.

intensity. Fig. 65 shows normal incident k-resolved inverse photoemission spectra recorded from a monolayer of Pd compared with clean Nb(110) spectra at the same electron energies. These spectra are dominated by two features, at 1.6 eV and 3.6 eV above the Fermi level. The feature localized at E_F+1.6 eV is an interface state and the feature at E_F+3.6 eV is the Nb(110) bulk Σ_4 state which splits into two features as $k_\perp$ moves away from the Γ point. The most important phenomenon is that the 1.6 eV state is localized in the metal-metal interface. To our knowledge this is the first experimental evidence for an interface state in a metal-metal system.

During the inverse photoemission experiment, we found that the intensity of the interface state peaks at the values of $k_\perp$ corresponding to 12.8 eV and 19.8 eV. This observed variation in strength of the interface state as a function of $k_\perp$ can be explained in terms of the bulk band structure of Nb along the Σ direction of the Nb(110) surface Brillouin zone. The values of $k_\perp$ for which the intensity of the interface state peaks (E_{el} = 12.8 eV and E_{el} = 19.8 eV) coincide with the Nb(110) bulk Σ_1 state in the reduced-zone scheme. The Nb(110) Σ_1 band, from which this interface state is mainly derived, comes closest to the interface state at these two points and its intensity is transferred into the interface state at these values of $k_\perp$. In other words, comparing the interface state intensity as a function of $k_\perp$ with the substrate Nb(110) bulk band structure obtained using the same techniques, we show that the intensity of interface state for monolayer Pd on Nb(110) peaks at the value of $k_\perp$ for which it lies closest to the substrate bulk band from which it is derived. Similar behavior was observed previously for an unoccupied surface state on Cu(001) by Johnson *et. al.* [139]. The widths of the interface state intensity peaks are related to the decay lengths of the interface state into the bulk of substrate. An example of deriving the surface-state decay length from a photoemission experiment data on Al(111) by a simple two-plane-wave model can be found in Kevan's paper [140].

The interface states should exhibit a two-dimensional band dispersion $E(k_\parallel)$. Like surface states, interface states can have very different character, depending on their localization near the interface and the nature of the substrate bulk band from which they are derived. It is well established from angle-resolved photoemission studies that near the center of the zone electronic antibonding states disperse towards the Fermi level with negative effective masses. Fig. 66 shows k-resolved inverse photoemission spectra for a monolayer of Pd on Nb(110) taken at 16.8 eV initial electron energy relative to E_F as a function of $k_\parallel$ along $\bar{\Gamma}\bar{P}$ direction. It is noted that the dispersion curve of the interface state is very similar to that

of the Nb bulk band from which the interface state is derived. Let us take a closer look at the dispersion relation of the interface state as a function of $k_{\|}$ with 16.8 eV electron energy for a monolayer of Pd on Nb(110). As the incident angle of electron beam varies from $\bar{\Gamma}$ to $\bar{P}$, we found that the interface state disperses toward the Fermi level E_F, which indicates that the interface state observed for the Pd monolayer has antibonding character. In summary, it is confirmed by k-resolved inverse photoemission that an antibonding interface state derived from the Nb bulk *d*- band appears above the Fermi level after a monolayer of Pd is deposited onto the Nb(110) substrate at room temperature.

It should be mentioned that the observed interface state overlaps the substrate valence bands and indeed is predominantly derived from those bands in agreement with the theoretical calculations of Kumar and Bennemann[10]. However, the interface nature of the Pd-induced band is confirmed by the lack of dispersion with the $k_{\perp}$, which indicates that this state is indeed two-dimensional and localized within the region of the interface. Because of the overlap with the substrate bands the state might more appropriately be referred to as an "interface resonance".

7.5. Surface, Interface and Image States

K-resolved inverse photoemission, like angle-resolved photoemission, is well suited to measure the energy E and momentum $\hbar\vec{k}$ of electrons in a solid. In particular, two-dimensional systems such as surfaces and interfaces are a very rich field of study. The nature of electronic surface, interface, and image states represents a current scientific frontier. In this section, we will discuss the electronic structure of two-dimensional states such as surface, interface and image states of Pd overlayers on Nb(110).

A surface state is a solid-vacuum interface state which is determined by the boundary condition of the image potential at the solid surface. It is noted from photoemission studies that the (111) surface of all the noble metals supports a Shockley-type surface state at the bottom of the *s-p* band gap. These surface states have binding energies close to the Fermi level and they disperse towards the vacuum level near the center of the zone. Recent theoretical and experimental studies have shown that a Shockley-type surface state also exists on the (111) surface of some transition-metals. Unlike the (111) surface of the noble metals, the Shockley-type surface states are unoccupied at the center of the zone of the (111) transition-metal surfaces. Our inverse photoemission results on thick Pd(111) layers on Nb(110) clearly show this anticipated Shockley state at the bottom of the L_2, L_1 band gap. Hulbert and Johnson [141] have demonstrated that measurements of the binding energies of these Shockley-type surface state in principle yield information about the position of the image plane.

The image state, a new class of unoccupied surface state which is derived from the long-range image potential, has led to the great interest in the factors that determine the binding energies of surface states in general. The phase analysis model has been considered by a number of authors [141], who treated the states as electron waves undergoing multiple reflections between the infinite crystal barrier on one side and the attractive image potential on the other. Assuming the phase change on reflection from the crystal is Φ_C and the image potential barrier is Φ_B, then stationary states exist for energies such that the total phase change satisfies the following condition:

$$\Phi = \Phi_C + \Phi_B = 2\pi n \quad , \quad n = 1, 2, \cdots \tag{7.5.1}$$

For $n = 0$, the phase model predicts bound states several eV below the vacuum level that can be identified with the standard Shockley or crystal-derived surface states. For $n \geq 1$, the image states near the vacuum level are predicted. These authors demonstrated that

the binding energy of surface states is a multibranch function of the position of the image plane. Therefore both the $n = 0$ crystal-derived and $n \geq 1$ image states can be predicted for a given image plane position. In this approach the energy levels of the image-potential state can be written as

$$E(k_{\|}) = E_v - e_n + \hbar^2 k_{\|}^2 / 2m \tag{7.5.2}$$

where the binding energy $e_n(Ry)$ is given by the series

$$e_n(Ry) = \frac{1}{16(n+a)^2} \quad , \; n = 1, 2, \cdots . \tag{7.5.3}$$

The quantum defect parameter a can range between $-\frac{1}{2}$ and $+\frac{1}{2}$ depending on the phase relations Φ_C for electrons scattering in the surface region. By fitting the edges of the band gap to the experimental results of Himpsel and Eastman [142], this model predicts a binding energy of 1.28 eV above the Fermi level for the $n = 0$ crystal-derived surface state and 0.56 eV below the vacuum level for the $n = 1$ image state. The inverse photoemission results on Pd(111) show good agreement between this model prediction and the experiments.

The interface states of a metal-metal system, which give great insight regarding the bonding of the two metallic components, represent another interesting field and are attracting more and more attention. In the photoemission studies of Ni, Pd, and Pt monolayers on Nb(110), the adsorbate derived features which reside at the upper edge of the *d*- band are observed, whereas these features are not seen for either clean bulk adsorbate or substrate materials. Together with their behavior as a function of adsorbate layer coverage we strongly suggest that these structures are electronic bonding interface states which are due to the hybridization of bulk *d*- states or derived from the adsorbate metal at the metal-metal interface. Houston and Feibelman have conducted photoemission studies and theoretical calculations on the interface state in the Cu/Ru(0001) system [143]. Their angle-resolved photoemission results showed a state -1.5 eV below the Fermi level which appears localized in the Cu and outermost Ru layers. By surface linearized, augmented plane-wave calculations they suggested that the E_F-1.5 eV state is the antibonding partner of a pair of Cu(3*d*)-Ru(4*d*)-derived interface states. This work needs to be confirmed by experimental measurements of the band structures of this interface state.

7.6. Summary

This is the first time, to our knowledge, that a metal-metal system has been studied by k-resolved inverse photoemission. By $\vec{k}$-dependent and $E\left(\vec{k}\right)$-dependent probes of the unoccupied electronic states for Pd overlayers on Nb(110), several significant results have been acquired.

Our experiments show that a Pd-induced unoccupied electronic state at 1.6 eV above the Fermi level for a Pd monolayer on Nb(110) is mainly derived from the *d*- states of bulk Nb. This state was not observed for either the bulk Pd(111) or for the substrate Nb(110). By varying the $k_\perp$ with $k_\parallel$ fixed, we proved that this state is localized in the interface region between the Pd layer and the Nb(110) substrate. By varying $k_\parallel$ with E_{el} fixed, we found that this interface state has antibonding character. Together, we report the first experimental evidence of an interface state in a metal-metal system. The binding energy of the interface is shown to be very sensitive to the geometrical structure and bonding of the Pd-Nb interface. After the structural phase transition of the Pd layer from commensurate (110) to incommensurate (111), the interface state shifts 0.3 eV to higher binding energy. This indicates that the interface bond between the two metals weakens as the thickness of the Pd overlayers increases. The intensity of the interface state is found to peak near the points in the Brillouin zone where it coincides with the bulk Σ_1 points in the reduced-zone scheme. In other words, we show that the antibonding interface state peaks in intensity at the value of $k_\perp$ for which it lies closest to the bulk Nb *d*- band from which it is derived.

The discovery of the antibonding interface state above the Fermi level confirms a rather simple picture of *d-d* hybridization between the late transition-metal overlayer and the early transition-metal substrate with a bonding level below E_F and an antibonding level above E_F.

Appendix A.
Publications

1. Xiaohe Pan, M. W. Ruckman, C. Zhang, and Myron Strongin, "Observation of novel Ni/Nb and Ni/Ta surface compounds produced by heat treatments", Materials Lett. 4(3), 125 (1986).
2. M. L. Shek, Xiaohe Pan, Myron Strongin, and M. W. Ruckman, "Interaction of oxygen with sodium at 80 K and 20 K", Phys. Rev. B34, 3741 (1986).
3. Xiaohe Pan, S. Raaen, M. I. Florit, S. L. Qui, and Myron Strongin, "Observation of bulk Ta oxidation formation below 30 K", To be published on Phys. Rev. B.
4. Xiaohe Pan, M. W. Ruckman, and Myron Strongin, "Electronic structure and chemical properties of Pt overlayers on Nb(110)", Submitted to Phys. Rev. B.
5. Xiaohe Pan, M. W. Ruckman, and Myron Strongin, "Structure dependent modification of the electronic states of Ni/Nb(110)", Submitted to Phys. Rev. B.
6. M. W. Ruckman, Xiaohe Pan, and Myron Strongin, "Synchrotron radiation photoemission studies of CO chemisorption on Pt/Ta(110) and Ni/Ta(110)", J. Vacuum Science and Technology, A, December, (1986).
7. M. L. Shek, Xiaohe Pan, and Myron Strongin, "Effects of Na on the interaction of CO with Ta(110)", J. Vacuum Science and Technology, A, December, 1986.
8. S. L. Hulbert, Xiaohe Pan, and P. D. Johnson, "Inverse photoemission observation of the shape resonance", To be published on Phys. Rev. B.
9. Xiaohe Pan, P. D. Johnson, S. L. Hulbert, and Myron Strongin, "K-resolved inverse photoemission studies of Pd overlayers on Nb(110)", Submitted to Phys. Rev. Lett.
10. Xiaohe Pan, P. D. Johnson, and Myron Strongin, "K-resolved inverse photoemission studies of hydrogen chemisorption on Nb(110)", Manuscript in preparation.

Appendix B.
Reports

1. Xiaohe Pan, R. Corderman, F. E. Loeb, and Myron Strongin, "Photon desorption studies of synchrotron materials", *NSLS Annual Report*, 107, (1984).
2. Xiaohe Pan, M. L. Shek, and Myron Strongin, "Studies of the low temperature oxidation of Ta", *NSLS Annual Report*, 81, (1985).
3. Xiaohe Pan, M. L. Shek, and Myron Strongin, "Studies of CO adsorption on Ta at low temperatures", *NSLS Annual Report*, 83, (1985).
4. M. L. Shek, Xiaohe Pan, and Myron Strongin, "Studies of Na core level shifts in solid krypton supported on Ta, Pt, and Na", *NSLS Annual Report*, 85, (1986).
5. M. L. Shek, Xiaohe Pan, and Myron Strongin, "Studies of Ni_3Al", *NSLS Annual Report*, 87, (1986).
6. Xiaohe Pan, M. W. Ruckman, M. L. Shek, and Myron Strongin, "Photoemission studies of Pt and Ni overlayers on Ta(110)", *NSLS Annual Report*, (1987).

Appendix C.
Presentations

I. **Annual Meeting of the American Physics Society, 31 March - 4 April, 1986, Las Vegas, Nevada:**

1) "Pt and Ni overlayers on Nb(110): Electronic structure and chemical properties", Xiaohe Pan, M. L. Shek, M. W. Ruckman, C. Zhang, and Myron Strongin.
2) "Observation of bulk Ta oxide formation below 30 K", S. Raaen, Xiaohe Pan, M. L. Shek, M. I. Florit, S. L. Qui, and Myron Strongin.
3) "The problem of photoemission from supported metal clusters", Myron Strongin, Xiaohe Pan, V. Murgai, S. Raaen, and P. H. Citrin.
4) "Interaction of oxygen with Na at 80 K", M. L. Shek, Xiaohe Pan, and Myron Strongin.

II. **Annual Meeting of the American Vacuum Society, October 27 - 31, 1986, Baltimore, Maryland:**

1) "Synchrotron radiation photoemission studies of CO chemisorption on Pt/Ta(110) and Ni/Ta(110)", Xiaohe Pan, M. W. Ruckman, M. L. Shek, and Myron Strongin.
2) "Effects of Na on the interaction of CO with Ta(110)", M. L. Shek, Xiaohe Pan, and Myron Strongin.

III. **Annual Meeting of Materials Research Society, December 1 - 6, 1986, Boston, Massachusetts:**

1) "Modification of the properties of metal overlayers on Nb(110) and Ta(110)", M. Ruckman, Myron Strongin, and Xiaohe Pan.

IV. **Annual Meeting of the American Physics Society, 16 - 20 March, 1987, New York, New York:**

1) "Inverse photoemission studies of the Nb-Pd interface", Xiaohe Pan, P. D. Johnson, S. L. Hulbert, and Myron Strongin.
2) "Inverse photoemission from hydrogen adsorbed on Nb(110)", Xiaohe Pan, P. D. Johnson, and Myron Strongin.

References

1. Ralf Vanselow, (Ed.) *Chemistry and Physics of Solid Surfaces*, Vol. II, (CRC Press, Inc. 1979).
2. Gabor A. Somorjai, *Chemistry in Two Dimensions Surfaces*, p194, (Cornell University Press, Ithaca and London, 1981).
3. J. R. Anderson, (Ed.) *Chemisorption and Reaction on Metallic Films*, Vol. I, (Academic Press, 1971).
4. M. W. Ruckman, P. D. Johnson, and Myron Strongin, Phys. Rev. B31, 3405, (1980).
5. D. Prigge, W. Schlenk, and E. Bauer, Surf. Sci. 123, L698, (1982).
6. Shen Xinyin, D. J. Frankel, *et al.*, Phys. Rev. B32, 2120, (1985).
7. J. W. Sachlter, M. A. Van Hove, J. P. Biberian, and G. A. Somorjai, Phys. Rev. Lett. 45, 1601 (1980).
8. M. A. Pick, J. W. Davenport, Myron Strongin and G. J. Dienes, Phys. Rev. Lett. 43, 286 (1979).
9. Myron Strongin, M. El-Batanouny, and M. Pick, Phys. Rev. B23, 3126 (1980).
10. Vijay Kumar and K. H. Bennemann, Phys. Rev. B28, 3138 (1983).
11. M. El-Batanouny, D. R. Hamann, S. R. Chubb, and J. W. Davenport, Phys. Rev. B27, 2575 (1983).
12. M. W. Ruckman and Myron Strongin, Phys. Rev. B29, 7105 (1985).
13. H. P. Bonzel, J. Vac. Sci. Technol. A2, 866 (1984).
14. J. E. Crowell, E. L. Garfunkel, and G. A. Somorjai, Surf. Sci. 121, 303 (1982).
15. A. J. Melmed, J. Appl. Phys. 38, 1885 (1967).
16. John F. O'Hanlon, *A User's Guide to Vacuum Technology*, (John Wiley & Sons, 1980).
17. C. M. Van Atta, *Vacuum Science and Engineering*, (McGraw-Hill Book Company, 1965).
18. J. M. Poate, K. N. Tu and J. W Mayer, *Thin Films - Interdiffusion and Reactions*, (The Electrochemical Society, Inc. 1978).
19. L. I. Maissel and R. Glanz, (Ed.) *Handbook of Thin Film Technology*, (McGraw Hill, New York, 1970).

20. M. G. Chopra, *Thin Film Phenomena*, (McGraw, Hill, New York, 1969).

21. M.-G. Barthes-Labrousse and G. E. Rhead, Surf. Sci. 116, 217 (1982).

22. C. Argile and G. E. Rhead, J. Phys. C: Solid State Phys. 30, L193 (1982).

23. E. E. Chaban and Y. J. Chabal, Rev. Sci. Instrum. 54, 1031 (1983).

24. Guy Kendall White, p293, p294, p316, *Experimental Techniques in Low-Temperature Physics*, (Oxford, At the Clarendon Press, 1959).

25. D. K. C. MacDonald, Handb. der Physik, 14, 137 (1956).

26. L. Towle, Canad. J. Phys. 34, 418 (1956).

27. D. K. C. MacDonald and W. B. Pearson, Acta Met. 3, 392, 403 (1955).

28. C. J . Davisson and L. H. Germer, Phys. Rev., 30, 705, (1927).

29. M. A. Van Hove and S. Y. Tong, *The Structure of Surfaces*, (Spring-Verlag, 1984).

30. G. Wulff, Krist. Z, p275-311 *The Nature of the Surface Chemical Bond*, edited by T. N. Rhodin and G. Ertl, (North-Holland, Amsterdam, 1979).

31. Hassan Windawi and Floyd F. -L. Ho, *Applied Electron Spectroscopy for Chemical Analysis*, (John Wiley & Sons, 1982).

32. Michael Thompson, Mark D. Baker, Alec Christie, and Julian F. Tyson, *Auger Electron Spectroscopy*, (John Wiley & Sons, 1985).

33. Kenneth D. Sevier, *Low Energy Electron Spectrometer*, p17, (Wiley-Interscience, John Wiley & Sons, Inc. 1972).

34. F. J. Himpsel, *Angle-resolved Measurement of the Photoemission of Electrons in the Study of Solids*, Advances in Physics, 32, No.1, 1-51 (1983).

35. D. Briggs, *Handbook of x-ray and Ultraviolet Photoelectron Spectroscopy*, (Heyden, 1977).

36. J. H. D. Eland, *Photoelectron Spectroscopy*, (Butterworths, 1984).

37. M. Cardona and L. Ley, *Photoemission in Solids – General Principles*, (Springer-Verlag Berlin Heidelberg, 1978).

38. R. H. Williams, G. P. Srivastava and I. T. Mcgovern, *Photoelctron Spectroscopy of Solids and Their Surfaces*, Rep. Prog. Phys., 43, 1358 (1980).

39. J. Hermanson, Solid State Commun. 22, 9 (1977).

40. Bodie E. Dougals and Charles A. Hollingsworth, *Symmetry in Bonding and Spectra – An Introduction*, (Academic Press, Inc. 1985).

41. J. W. Davenport, J. Vac. Sci. Technol. 15 433 (1978).

42. J. W. Davenport, Phys. Rev. Lett. 36, 945 (1976).

43. J. Stohr and R. Jaeger, Phys. Rev. B26, 4111 (1982).

44. N. J. Shevchik, J. Electron Spec. and Related Phenomena, 14, 411 (1978).

45. D. E. Eastman, J. J. Donelon, N. C. Hien, and F. J. Himpsel, Nucl. Instr. Methods, 172, 327 (1980).

46. S. P. Weeks, J. E. Rowe, S. B. Christman, and E. E. Chaban, Rev. Sci. Instrum. 50, 1249 (1979).

47. Herman Winick and S. Doniach, *Synchrotron Radiation Research*, (Plenum Press · New York and London, 1980).

48. C. Kunz, *Synchrotron Radiation*, (Springer-Verlag, Berlin Heidelberg New York, 1979).

49. M. R. Howells, Proc. Conf. on "Synchrotron Radiation Instrumentation", Gaithersburg, Md. (1979).

50. C. T. Chen, E. W. Plummer, and M. R. Howells, Nucl. Inst. Meth. 222, 103 (1984).

51. P. D. Johnson and J. W. Davenport, Phys. Rev. B31, 7521 (1985).

52. V. Dose, Surf. Sci. Rep. 5, 337, (1985).

53. N. G. Stoffel and P. D. Johnson, Nuclear Instruments and Methods in Phys. Research, A234, 230 (1985).

54. L. F. Mattheiss, Phys. Rev. B1, 373 (1970).

55. J. R. Anderson, D. A. Papaconstantopoulos, J. W. McCaffrey, and J. E. Schirber, Phys. Rev. B7, 5115 (1973).

56. K. M. Ho, Steven G. Louie, James R. Chelikowsky, and Marvin L. Cohen, Phys. Rev. B15, 1755 (1977).

57. N. Elyashar and D. D. Koelling, Phys. Rev. B15, 3620 (1977).

58. I. Lindau and W. E. Spicer, Phys. Rev. B10, 2262 (1974).

59. R. J. Smith, Solid State Comm. 37, 725 (1981).

60. R. J. Smith, G. P. Williams, J. Colbert, M. Sagurton, and G. J. Lapeyre, Phys. Rev. B22, 1584 (1980).

61. I. Petroff and C. R. Viswanathan, Phys. Rev. B4, 799 (1971).

62. Alex Zunger, G. P. Kerker, and Marvin Cohen, Phys. Rev. B20, 581, (1979).

63. M. El-Batanouny, Myron Strongin, and G. P. Williams, Phys. Rev. B27, 4580 (1983).

64. P. R. Norris, Phys. Lett. 45A, 387 (1973).

65. J. A. Tagle, E. T. Arakawa, and T. A. Callcott, Phys. Rev. B21, 4552 (1980).

66. R. J. Smith, J. Anderson, J. Hermanson and G. J. Lapeyre, Solid State Communication, 21, 459 (1977).

67. S. G. Louie, Phys. Rev. Lett. 40, 1525 (1978).

68. S. L. Hulbert, P. D. Johnson, and M. Weinert, Phys. Rev. B34, 3670 (1986).

69. G. Broden, T. N. Rhodin, C. Brucker, R. Benbow, and Z. Hurych, Surf. Sci. 59, 593 (1976).

70. Y. Iwasawa, R. Mason, M. Textor, and G. A. Somorjai, Chem. Phys. Lett. 44, 468 (1976).

71. Carl J. Ballhausen and Harry B. Gray, *Molecular Electronic Structures – An Introduction*, (The Benjamin/Cummings Publishing Company, Inc. 1980).

72. Swapan K. Saha and Badal C. Khanra, Phys. Rev. B31, 5521 (1985).

73. G. Doyen and G. Ertl, Surf. Sci. 43, 197 (1974).

74. H.-J. Freund and E. W. Plummer, Phys. Rev. B23, 4859 (1981).

75. D. Saddei, H.-J. Freund, G. Hohlneicher, Surf. Sci. 95, 527 (1981).

76. G. Alefeld and J. Volkl, (Ed.)*Hydrogen in Metals I: Basic Properties*, (Springer, New York 1978).

77. T. Schober and H. Wenzl, p.11, in *Hydrogen in Metals II: Topics in Applied Physics*, edited by G. Alefeld and J. Volkl, (Springer, Berlin, 1978).

78. R. J. Smith, Phys. Rev. Lett. 45, 1277 (1980).

79. R. J. Smith, Phys. Rev. B21, 3131 (1980).

80. F. Greuter, I. Strathy, E. W. Plummer, and W. Eberhardt, Phys. Rev. B33, 736 (1986).

81. D. J. Peterman, D. K. Misemer, J. H. Weaver, and D. T. Peterson, Phys. Rev. B27, 799 (1983).

82. K.-M. Ho, H.-J. Tao, and X.-Y. Zhu, Phys. Rev. Lett. 53, 1586 (1984).

83. B. Feuerbacher and R. F Williams, Phys. Rev. Lett. 36 1339 (1976).

84. V. Murgai, Shang-Lin Weng, Myron Strongin, and M. W. Ruckman, Phys. Rev. B28, 6116 (1983).

85. D. Prigge, W. Schlenk, and E. Bauer, Surf. Sci. 123, L698 (1982).

86. J. H. Weaver, D. W. Lynch, and C. G. Olsen, Phys. Rev. B7, 4311 (1973).

87. J. kolaczkiewicz and E. Bauer, Surf. Sci. 160, 1 (1985).

88. Ernst Bauer, p39, *The Chemical Physics of Solid Surfaces and Heterogeneous Catalysis*, Edited by D. A. King and D. P. Woodruff, (Elsevier, 1984).

89. Charles F. Brucker and Thor N. Rhodin, Surf. Sci. 86, 638 (1979).

90. G. Blyholder, J. Phys. Chem. 68, 2772 (1964).

91. Paul S. Bagus, Constance J. Nelin, Charles W. Bauschlicher Jr., Phys. Rev. B28, 5423 (1983).

92. G. W. Graham, J. Vac. Sci. Technol. A4, 3, 760 (1986).

93. J. W. Schlenk and E. Bauer, Surf. Sci. 93, 9 (1980).

94. C. L. Allyn, T. Gustafsson, and E. W. Plummer, Solid State Comm. 24, 531 (1977).

95. E. W. Plummer, W. R. Salaneck and J. S. Miller, Phys. Rev. B18, 1673 (1978).

96. K. Schonhammer and O. Gunarson, Solid State Commun. 23, 691 (1977).

97. O. Gunnarson and K. Schonhammer, Phys. Rev. Lett. 41, 1608 (1978).

98. S. -S. Sung and R. Hoffman, J. Am. Chem. Soc. 107, 578 (1985).

99. O. Gunnarson and K. Schönhammer, Phys. Rev. Lett. 41, 1608 (1978).

100. M. El-Batanouny and Myron Strongin, Phys. Rev. B31, 4798 (1985).

101. M. Sagurton, Myron Strongin, F. Jona, and J. Colbert, Phys. Rev. B28, 4075 (1983).

102. E. Bauer, Appl. Surf. Sci., 11/12, 479 (1982).

103. P. M. Williams, P. Butcher, and J. Wood, Phys. Rev. B14, 3215 (1976).

104. D. T. Pierce and W. E. Spicer, Phys. Rev. B25, 581 (1970).

105. R. Glanberg and W. Gudat, W. Radlik, W. Braun, Phys. Rev. B31, 1754 (1985).

106. W. Eberhardt and E. W. Plummer, Phys. Rev. B21, 3245 (1980).

107. David R. Penn, Phys. Rev. Lett. 42, 921 (1979).

108. S. Hufner and G. K. Wertheim, Phys. Lett. 47A, 349 (1974).

109. R. J. Smith, J. Anderson, J. Hermanson, and G. J. Lapeyre, Solid State Commun. 21, 459 (1977).

110. P. C. Kemeny and N. J. Shevckik, Solid State Commun. 17, 255 (1975).

111. Gary G. Tibbetts and Williams F. Egelhoff, Phys. Rev. Lett. 41, 188 (1978).

112. C. E. Moore, *Atomic Energy Levels*, U.S. National Bureau of Standards Circular No. 467 (U.S., GPO, Washington, D.C., 1949, 1952, 1958).

113. R. W. Gurney, Phys. Rev. 47, 479 (1935).

114. M. Strongin, M. El-Batanouny, and M. Pick, Phys. Rev. B22, 3126 (1980).

115. M. El-Batanouny, M. Strongin, G. P. Williams, and J. Colbert, Phys. Rev. Lett. 46, 269 (1981).

116. W. Eberhardt, F. Greuter, and E. W. Plummer, Phys. Rev. Lett. 46, 1085 (1981).

117. F. Greuter, I. Strathy, and E. W. Plummer, Phys. Rev. B33, 736 (1986).

118. R. C. Evans, *An Introduction to Crystal Chemistry*, (Cambridge University Press, Cambridge, 1978).

119. C. T. Liu and J. O. Stiegler, Science, 226, 636 (1984).

120. R. P. Messmer and C. L. Briant, Acta Metall. 30, 457 (1982).

121. A. Franciosi, J. H. Weaver, D. G. O'Neill, *et al.*, J. Vacuum Sci. Technol. 21 624 (1982).

122. O. Bisi and C. Calandra, J. Phys. C14, 5479 (1981).

123. Y. J. Chabal, D. R. Hamman, J. E. Rowe and M. Schluter, Phys. Rev. B25, 7598 (1979).

124. L. Ley and M. Cordona, *Photoemission in solid II – Case Studies*, (Spring, Berlin, 1979).

125. J. W. Cooper, Phys. Rev. 128, 681 (1982).

126. Xiaohe Pan, M. W. Ruchman, C. Zhang, and Myron Strongin, Materials Lett. 4, 125 (1986).

127. P. A. Beck, Advan. X-ray Anal. 12, 1 (1969).

128. W. B. Pearson, *Handbook of lattice spacings and structures of metals*, Vol. 2, p326 (Pergamon, Oxford, 1967).

129. J. R. Chelikowsky, Surface Sci. 139, L197 (1984).

130. A. R. Miedema, Z. Metallk. 69, 455 (1978).

131. A. K. Sinha, Trans. Metall. Soc. AIME, 245, 911 (1969).

132. C. T. Liu and H. Inouye, Metall. Trans. 10A, 1515 (1979).

133. C. T. Liu, Intern. Metall. Rev. 29, 168 (1984).

134. M. A. Pick, J. W. Davenport, Myron Strongin, and G. J. Dienes, Phys. Rev. Lett. 43, 286 (1979).

135. Jeffrey Colbert's Ph.D. thesis (unpublished data).

136. G. P. Williams, M. El-Batanouny, J. Colbert, E. Jensen, and T. N. Rhodin, Phys. Rev. B25, 3658 (1982).

137. Shang-Lin Weng and M. El-Batanouny, Phys. Rev. Lett. 44, 612 (1980).

138. P. D. Johnson, S. L. Hulbert, R. F. Garrett, and M. R. Howells, Rev. Sci. Instrum. 57, 1324 (1986).

139. S. L. Hulbert, P. D. Johnson, R. F. Garrett, Phys. Rev. B33, 7326 (1986).

140. S. D. Kevan, N. G. Stoffel, and N. V. Smith, Phys. Rev. B31, 1788 (1985).

141. S. L. Hulbert, P. D. Johnson, N. G. Stoffel, W. A. Royer, and N. V. Smith, Phys. Rev. B31, 6815 (1985).

142. F. J. Himpsel and D. E. Eastman, Phys. Rev. B18, 5236 (1978).

143. J. E. Houston, C. H. F. Peden, Peter J. Feibelman, and D. R. Hamann, Phys. Rev. 56, 375 (1986)